Royal Holloway College

(University of London)

INTERACTION OF CO_2 LASER RADIATION WITH DENSE PLASMA

WASFI SHARKAWY ABDEL-RAOOF
B Sc., M Sc.

This thesis is submitted in partial fulfilment of the requirements for the degree of Doctor of Philosophy in the University of London.

April 1980

TO MY DAUGHTER

REHAM

A B S T R A C T

The instabilities which occur in the interaction of CO_2 laser radiation with a dense plasma have been studied.

A TEA CO_2 laser provided pulses of up to 30 joules of energy with a duration of 50 nanoseconds. By focussing the radiation on to a plane target a focal spot of about 180 micrometers diameter was formed with a irradiance of 10^9 to 10^{12} W cm^{-2}. The scattered radiation was collected by a laser focussing lens and analysed with a grating spectrometer.

Linear relationships have been found between the incident irradiance and the back scattered energies at ω_o, $\frac{3}{2}\omega_o$ and $2\omega_o$. This is in contrast to the results of other workers who have found quadratic relations at high irradiance. The back scattered energies were of the order of 0.1 at ω_o, 10^{-7} at $\frac{3}{2}\omega_o$ and 10^{-5} at $2\omega_o$, compared with the incident energy.

The spectrum of ω_o shows a displacement to longer wavelength which is attributed to stimulated Brillouin scattering, there being an ion acoustic wave which is driven by the laser radiation. A similar displacement occurs in the $2\omega_o$ spectrum and is attributed to the scattering of plasmons from the ion acoustic wave. The measured displacement is in agreement with a theory due to Silin. Fine structure also exists in the $2\omega_o$ spectrum, a shoulder being found on the red side of the line and this may result from a non-Maxwellian electron temperature distribution. There is also a satellite which is displaced towards longer wavelengths by about 0.1 micrometers from the precise value of $2\omega_o$. Explanations of this feature are offered.

The self generated magnetic field has been measured and its effect on the interactions have been examined. The plasma temperature has been determined by X-ray measurements and compared with the values estimated from the scattered spectrum.

C O N T E N T S

CHAPTER I

INTRODUCTION

CHAPTER II

THEORY OF LASER PLASMA INTERACTION

CONTENTS
(continued)

CONTENTS
(continued)

CHAPTER IV

EXPERIMENTAL APPARATUS AND METHODS

CHAPTER V

EXPERIMENTAL RESULTS

C O N T E N T S
(continued)

CHAPTER VI

DISCUSSION OF EXPERIMENTAL RESULTS

CHAPTER VII

APPENDICES

APPENDIX A1

.....

LIST OF FIGURES

LIST OF FIGURES(CONTINUED)

LIST OF FIGURES(CONTINUED)

LIST OF FIGURES(CONTINUED)

LIST OF FIGURES(CONTINUED)

* * * * * * * * * * * * * * * * * * *

LIST OF TABLES

* * * * * * * * * * * * * * * * * * *

A C K N O W L E D G E M E N T S

I would like to express my appreciation to my supervisor, Dr. E.R. Wooding for his invaluable guidance and helpful discussions. I am also grateful to Mr. D. Brown for many informative discussions. I also convey my thanks to Professor D.W.O. Heddle for allowing me the use of the facilities of the department. Lastly the help of Mr. J. Elazar is acknowledged during the magnetic field measurements.

I gratefully acknowledge the help of the following persons: Mr. J. Henley, Mr. G. Waters, and Mr. L. Ellison for the technical assistance during the experiment. Thanks to Mr. B. Tate for his photographic expertise; thanks to Mrs. P. Hill for typing the thesis; and to Mr. N.A. Sayed for his diverse assistance. Special thanks are due to my wife for her encouragement and for tolerating my long hours of working.

I am grateful to Professor Allan Offenberger for the loan of equipment. The financial support of the Education office of the Egyptian Government in London is gratefully acknowledged.

CHAPTER 1

1.1 INTRODUCTION

Laser radiation of high intensity focussed onto any material causes ionization and generates high density plasma. The radiation from lasers producing several joules of energy in pulses of nanosecond duration or less may be focussed into a volume of the order of 10^{-6} cm^3; the resulting high irradiance producing a strong electric field, high temperatures and the possibility of a wide range of non-linear processes. In principle, it opens a promising new front of attack on the long standing problem of how to produce the ultra high temperature plasma needed to maintain thermonuclear or fusion reactions under controlled conditions.

In 1963 the Q-switched ruby laser became available (McClung and Hellwarth) and could produce pulses of up to 30 MW power. These pulses were capable of producing plasmas which expanded at 2×16^6 cm sec. (Read y (1963)). Ion energies of 1 Kev were obtained with 5.4 MW ruby laser pulses (Linlor (1963)).

In 1963, Basov and Krokhin presented calculations on the feasibility of using a laser to heat a dense deuterium plasma to thermonuclear temperatures, (also Basov 1964) with greater details and Dawson (1964).published similar calculations. Communications indicated that higher powers than were available would be necessary to produce thermo-

nuclear temperatures. Subsequent calculations (Nuckolls et al 1972) have shown the possibility of producing thermonuclear reactions by compressing and heating deuterium tritium pellets with an intense laser.

To achieve efficient heating it is necessary to understand the physics of interaction of radiation with a plasma, the heating processes and the way which energy can be dissipated. Some of the physical processes have been known for some time. For example, Stern (1965) has shown that non linear phenomena occurred with relatively long ($\leq$ 3 cm) wavelength radiation.

1.2 LASER PRODUCED PLASMA

1.2.1 Gas Breakdown

Observations of laser induced breakdown in gases were first reported by Maker in 1963. A spark was formed when a laser pulse of a few megawatt power was focussed in atmospheric air and was accompanied by a loud click. The mechanism of this spark was subsequently shown to be similar to breakdown by microwave radiation and is often referred to as optical frequency breakdown. The essential feature is that the gas which is normally a transparent and non-conducting medium becomes ionized by laser light and absorbs energy strongly from the beam. Rapid local heating occurs, leading to the production of a dense, strongly ionized plasma.

Gas breakdown can be observed at atmospheric pressure

but direct photoionization of the gas is impossible. For example, the ionization potential of argon is 15.8 eV, whereas the energy of a CO_2 laser quantum is only 0.117 eV.

In the classical theory the electrons oscillate in the wave field with mean energy of

$$\frac{e^2 E^2}{m\omega^2}$$

and lose energy when it collides with an atom. The rate at which energy is gained from the electric field is given by

$$\frac{d\mathcal{E}}{dt} = eE\,V$$

where V is the mean velocity.

The effective field given by MacDonald (1966) is

$$E_o^2 = E^2 \frac{\nu_c^2}{\nu_c^2 + \omega^2}$$

$$\frac{d\mathcal{E}}{dt} = \frac{e^2 E^2}{2\,m\omega^2} \nu_c \frac{\omega^2}{\omega^2 + \nu_c^2}$$

where $\nu_c = N_o v \sigma$ is the effective collision frequency between electrons and ions, N_o the number of atoms cm^{-3}, v is the electron velocity and σ is the collision cross-section.

For $\omega^2 \gg \nu_c^2$

Then

$$\frac{d\mathcal{E}}{dt} = \frac{e^2 E^2}{2\,m\omega^2} \nu_c$$

$$\frac{d\mathcal{E}}{dt} = \nu_c \frac{\hbar^2\omega^2}{\mathcal{E}} \frac{I(t)}{I_o}$$

where the intensity of the radiation is

$$I(t) = \frac{E_c^2}{(8\pi)}$$

and $$I_o = \frac{m c \hbar^2 \omega^4}{4\pi e^2 \mathcal{E}}$$

The total gain in energy

$$\frac{d\mathcal{E}}{dt} dt = \frac{K}{\alpha} \chi$$

where K is the number of ions generated during the time of the laser pulse, χ is the ionization energy, and α is a factor to take into account the energy losses.

$$\frac{\nu_c \hbar^2 \omega^2}{\mathcal{E} I_o} \int_o^t I(t)\, dt = \frac{K\chi}{\alpha}$$

The time averaged threshold for breakdown given by Ramsden (1964) and Morgan (1975) is

$$I_{th} = \frac{m c K \omega^2 \chi}{4\pi e^2 \sigma V N_o t}$$

which shows the importance of the different factors.

1.2.2 Laser Produced Plasma in a Solid Target

Plasma may also be produced by a laser beam irradiating a solid target. In this process there is no threshold as in the case of gas, radiation being absorbed at any intensity. However, the interaction between the light and the target now takes place initially in a thin surface layer and produces a very steep density gradient which may not absorb light efficiently.

Most theoretical work has attempted to explain the heating mechanisms involved when a laser beam is focussed

on the surface of a solid in vacuum and the subsequent melting, vaporization and ionization. The beginning of the interaction is considered first where energy is absorbed from the radiation field, causing evaporation and ionization of the solid. There are three possible absorption processes: absorption by phonon production in the solid; multiphoton absorption and absorption by free electrons.

1.3 THERMAL CONDUCTIVITY

When laser light falls on an opaque material some of it is reflected and the rest is absorbed by electrons in the conduction band. Energy is then transferred from these electrons by collision with other electrons and with phonons, so that the solid tends to reach an equilibrium at a higher temperature.

1.3.1 Evaporation

The next stage in heating a solid target begins when phonons are produced by the absorbed radiation when the target temperature is raised to boiling point. Assuming that all the laser energy is converted into heat within a volume equal to the (focal spot area) x (the depth of penetration), then the time required to vaporise the volume is that in which the specific energy absorbed equals the specific heat of vaporisation. In an optically opaque solid (Afanasyev et al 1966), the laser radiation is strongly absorbed on the surface of the solid into its

vibrational levels, producing heat, but the interior of the solid is heated by a thermal conduction wave which penetrates to a depth

$$1 \simeq (Kt)^{\frac{1}{2}} \text{ cm}$$

where K = thermal diffusivity $cm^2\ sec^{-1}$

t = time for absorption of sufficient energy for vaporisation in seconds

For a material in which all the light is absorbed in a length < 1, the time for vaporisation is

$$t = \frac{\Omega^2 \rho^2 K}{I^2_{(cgs)}}$$

where

Ω = specific heat of evaporation in ergs $gram^{-1}$

ρ_o = material solid density gm cm^{-3}

$I_{(cgs)}$ = laser radiation flux density ergs sec^{-1} cm^{-2}

In the case of weakly absorbing material, the time required for evaporation becomes

$$t = \frac{\rho_o \Omega}{I_{(cgs)} \alpha}$$

where α is the absorption coefficient for the radiation in the solid cm^{-1}.

1.3.2 Multiphoton Ionization

For laser flux greater than 10^9 W $cm.^{-2}$ possibilities of multiphoton absorption must be considered. If a sufficient number of photons are absorbed so that their

cumulative energy exceeds the ionization potential of the atom, multiphoton ionization occurs.

The multiphoton ionization probability for atoms is similar to that for gases. These were discussed by Bunkin and Prakhorov (1964) and Gold and Bebb (1965). Calculations have been made of the multiphoton photo current from metals by Silin (1971) and experimental observations were reported by Farkas et al (1972).

1.4 PLASMA HEATING

There are many models describing the plasma heating process. The first was reported by Basov and Krokhin (1964). Similar work was published by Dawson (1964). These models describe the processes involved in the heating of a volume of plasma, having dimensions of the focal region of the laser beam. The heating process then involves the absorption of photons by electrons in the field of the ions. High absorption takes place at densities below the critical density.

The plasma absorption coefficient K resulting from inverse Bremsstrahlung is:-

$$K = \frac{1.17 \times 10^{-8} \, Z \, n_e^2 \ln\Lambda}{3 \, \omega_o^2 \, (kT)^{3/2}} \quad \frac{1}{\left[1 - (\omega_p^2/\omega_o^2)\right]^{\frac{1}{2}}} \quad cm^{-1}$$

where kT in eV

Z is the atomic number

when $\omega_o = \omega_p$

The absorption length $\frac{1}{K} = 9.7 \times 10^{-3}$ cm

which is of the same order as the dimensions of the laser focal spot.

The electron ion thermalization time is

$$t_{ei} = \frac{1.05 \times 10^{13} A}{n_e Z \ln\Lambda} T_e^{3/2}$$

where T_e in KeV

and A = atomic weight of the ions.

This gives $t_{ei} = 7 \times 10^{-8}$ sec for a CO_2 laser with a carbon target which is small compared with the reciprocal plasma expansion velocity. When the plasma is fully ionized, the only significant radiation is Bremsstrahlung, the radiated power being given by:-

$$P_B = 4.9 \times 10^{31} Z n_e^2 T^{\frac{1}{2}} \quad W\ cm^{-3}$$

where T in KeV.

The amount of radiation losses by Bremsstrahlung from the whole plasma is of the order of 10^4 W which is negligible, compared to the laser power required to produce the plasma.

Laser power = $\frac{d}{dt}$ (thermal energy + expansion energy)

Plasma thermal energy = $\frac{3}{2} KT_e (n_e + n_i)$

n_e = number of electrons

n_i = number of ions

Assuming that uniform density and temperature are maintained throughout the plasma and that the velocity increases linearly from the centre to the edge of the plasma:-

$$\frac{d}{dt} \text{ (expansion energy)}$$

$$= P\ 4\pi r^2 = \frac{3}{10} n_i m_i \frac{d}{dt}\left(\frac{dr}{dt}\right)^2$$

where p is the pressure and r is the radius of the plasma at time t.

The plasma pressure, in terms of temperature and radius, is

$$p = \frac{3(n_e + n_i)\, KT}{4\pi r^3}$$

the temperature is determined by the conservation of energy equation:-

$$\frac{3}{2}(n_e + n_i)\, K \frac{dT}{dt} = -p\, 4\pi r^2 \frac{dr}{dt} + Q$$

Q is the rate at which plasma absorbs energy

$$Q = \frac{r^2}{R} W (1 - e^{Kr}) \qquad r \leq R$$

$$Q = W (1 - e^{-Kr}) \qquad r \geq R$$

where R is the focal spot radius

W is the laser power

These equations can be solved for the plasma radius and temperature, the solution depending on the assumed dependence of the laser power on time. Haught and Polk (1966) have calculated the radius, velocity temperature and average energy of a plasma produced by different forms of the irradiating laser power W.

Although thermal energy is lost by the plasma in the long pulse mode, due to gas dynamical expansion, the plasma continues to absorb laser radiation and convert it to thermal energy until the plasma becomes transparent, ie when

$$K_o\, r = 1$$

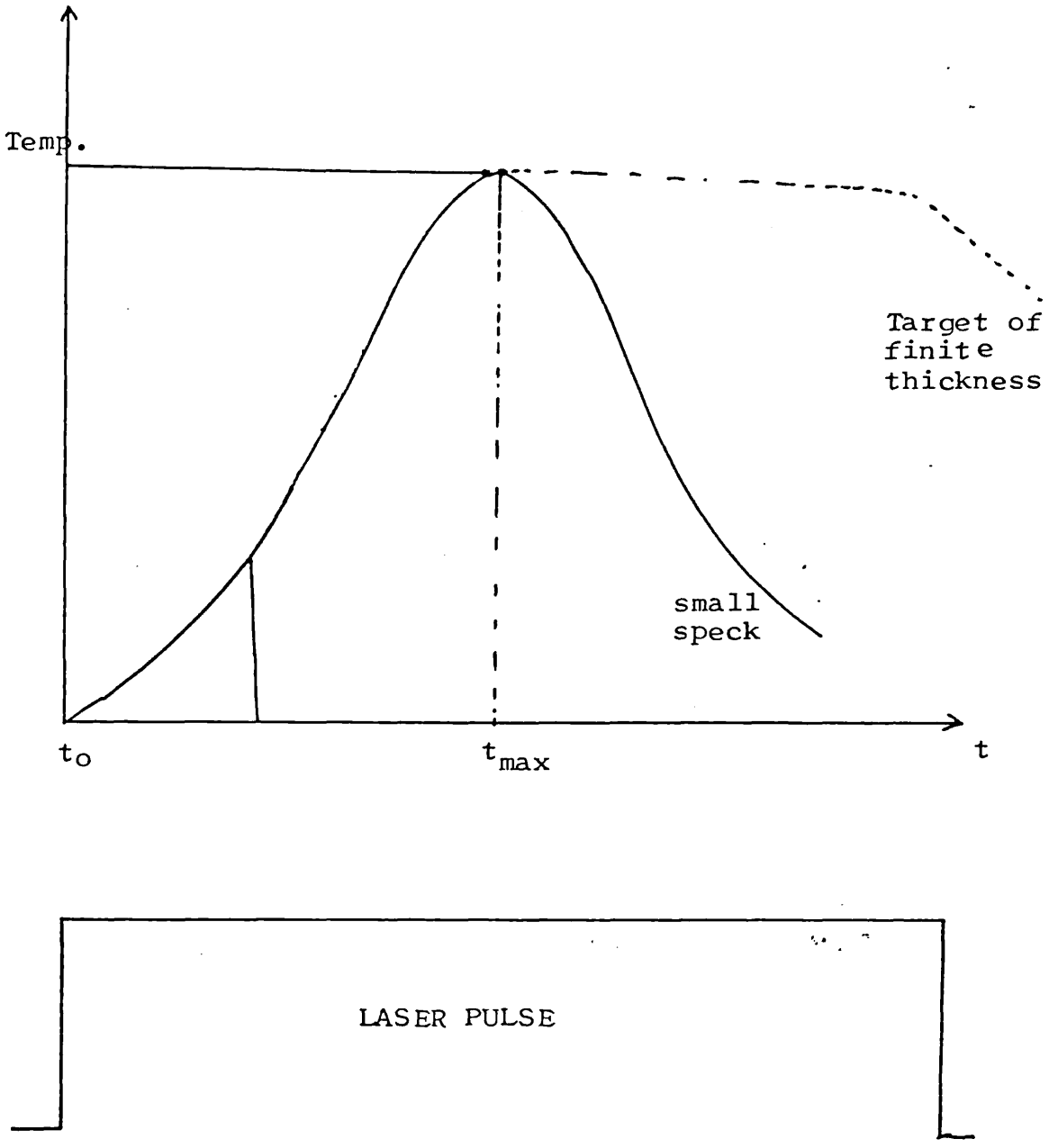

Figure 1.1
Plasma Heating Time history

Dawson (1964) shows that during the period of absorption three quarters of the energy is converted into expansion energy, that the temperature increases until the plasma density becomes so low that it is transparent to laser radiation. Haught and Polk (1966) obtained a temperature-time profile, shown in Figure 1.1., which shows the relation between the temperature and time during the laser pulse for the spherical expansion of a speck of plasma. If the pulse length is longer than t_{max}, the plasma becomes transparent at time t_{max}, so the extra laser energy is superfluous and the plasma cools.

Dawson obtained

$$t_{max} = \frac{7.3 \times 10^{-10} \, n^{2/3} \, A^{5/16} \, (1 + \frac{1}{Z})^{1/6}}{Z^{1/6} \, (\pi I)^{4/9}} \quad \text{sec}$$

where A = atomic weight

I = laser irradiance W cm^{-2}

a time typically of the order of 1 n sec.

The dependence of the maximum attainable temperature on laser radiation flux is

$$K \, T_{max} \propto I^{5/9}$$

1.4.1 Plasma Formed From a Finite Thickness Target

If pulses longer than t_{max} interact with a finite thickness target, the temperature profile is shown by the dotted line in Figure 1.1. The high temperature plasma is replaced by newly ionized cool opaque plasma boiled off the new surface of the target.

For a laser pulse lasting several nanoseconds focussed onto a solid target, the one-dimensional model is not appropriate. Lateral expansion was first taken into account by Nemchinov (1967). Puell (1970) considered a model in which the three separate regions are distinguished, as shown in Figure 1.2. Ionization occurs on the surface of the target and a layer of plasma is formed with a thickness of the laser radiation absorption length in the plasma. Therefore the plasma temperature increases and the density decreases by increasing the ionization to reach the critical density (10^{19} in the case of a CO_2 laser). Meanwhile, the high temperature in this layer increases the plasma pressure and drives a thermal expansion into the vacuum, so that the electron density falls and the radiation can penetrate further into the solid. The density of the plasma falls rapidly with distance from the target surface.

The different regions of plasma were classified by Puell (1970) who considered a model in which the separate regions are distinguished, as shown in Figure 1.2.

(1) Cooling expanding plasma which is optically transparent.

(2) A hot dense core of plasma where the laser radiation is absorbed.

(3) The boundary of the laser radiation absorption region where the electron density equals the critical electron density.

(4) A region of very dense plasma, shock compressed and heated by thermal conduction.

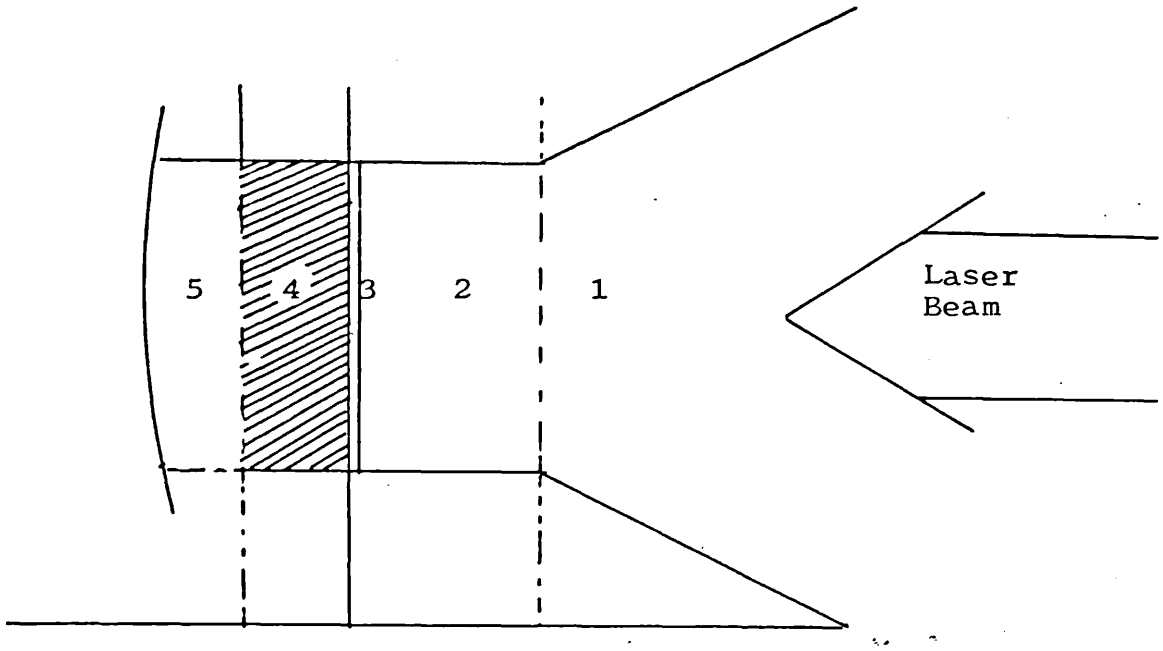

Figure 1.2.

Plasma regions created by laser pulse

(1) expanding plasma

(2) A hot dense core

(3) Boundary of the absorbing region

(4) A region of very dense plasma

(5) The undisturbed material.

(5) The undisturbed material.

1.5 REFLECTIVITY OF PLASMA BOUNDARY

When the incident laser radiation approaches the critical density, it reflects since plasma frequency ω_{pe} is much greater than laser frequency ω. Also ω is much greater than the effective collision frequency ν_{ei}. The reflection coefficient given by Kidder (1971) is:-

$$R = \frac{1}{1 + \frac{2\nu_{ei}}{\omega_{pe}}}$$

The penetration depth $d = \frac{c}{2\omega_{pe}}$

The laser light passes through different layers of electron density where it is, to some extent, absorbed. Dawson et al (1968) calculated the overall reflectivity of plasma for light of lower irradiance where the non-linear effects can be ignored. The problem has also been discussed by Mulser (1970).

When a plane polarized wave incident normally to the plasma boundary with the plasma density increasing monotonically from zero to the critical density at a distance Z_c where the incidence wave can be reflected back, the reflectivity is

$$R = \frac{I_r}{I_o} .$$

$$R = (I_r/I_o)_\omega = \exp(-2d)$$

where d is the optical depth of plasma to the turning point

$$\text{where} \quad d = \int_{-\infty}^{z_c} a_\omega(z)\, dz$$

$$a_\omega = \frac{\nu_{ei}\,\omega_{pe}^2}{nc\,\omega^2}$$

$$n = \left(1 - \frac{\omega_{pe}^2}{\omega^2}\right)^{\frac{1}{2}}$$

$$d = \int_0^{z_c} a_\omega(z)\, dz = \frac{\nu_{ei}\,\omega^2}{\omega_c^2}\left[1 - \left(\frac{\omega_p(z)}{\omega}\right)^2\right]$$

$$\frac{\omega_p^2(z)}{\omega^2} = \frac{n_e(z)}{n_{ec}} = \frac{z}{z_c}$$

$$d = \alpha\left(\frac{n_{ec}}{\omega}\right)^2 \int_0^{z_c} \left(\frac{z}{z_c}\right)^2 \left(1 - \frac{z}{z_c}\right)^{-\frac{1}{2}} dz$$

$$= \frac{16}{15}\alpha\left(\frac{n_{ec}}{\omega}\right)^2 z_c$$

Clearly the effective reflectivity depends very strongly on the plasma electron density profile and on the laser frequency, which means a laser with a short wavelength is often preferable for plasma heating.

The problem of the laser being incident obliquely has been discussed by Shearer (1971). The reflectivity is then

$$R = I_r/I_o = \exp\left(-2d\cos^5\theta\right)$$

where θ is the angle of incidence.

Eventually the interaction region moves out of the focus of the laser beam and the radiation intensity is too low to maintain the temperature, causing the plasma to cool. Alternatively, if the pulse is sufficiently short, then the laser pulse ends before the interaction region moves out of the focal region.

1.6 ABSORPTION OF LASER RADIATION

The absorbed laser energy creates a very high temperature and pressure in the outer region of the plasma. This leads to a blow-off of hot plasma, whose pressure compresses the cold interior. Light absorption takes place at densities below n_{ec} . For a CO_2 laser, $n_{ce} = 10^{19}$ for $\omega = \omega_p$, where ω_p is the plasma frequency $(4\pi n e^2/m)^{\frac{1}{2}}$.

The dispersion relation for an electron wave in a plasma is given by

$$\omega^2 = K^2 c^2 + \omega_p (1 + i \frac{\nu}{\omega})$$

where ν is the electron-ion collision frequency. As the wave enters the plasma and radiation is absorbed, until at $\omega = \omega_p$ the wave is reflected back. Under conditions of interest for high power laser to interact with a plasma, the collision frequency is so low that absorption will be negligibly small, although Morse and Nielson (1973) have pointed out that for a narrow range of angles of oblique incidence, significant non-anomolous absorption may occur.

At a high laser irradiance, collective processes can occur. The three wave decay process (Oraevsky and Sagdeev (1962) provides strong laser plasma interaction and the possibility of absorption by decay of the laser photon into a plasmon and a phonon (DuBois and Goldman (1965)). The conditions for decay of a wave of frequency ω_o and wave number K_o into two other waves in an infinite homogeneous plasma are the familiar sum rules of energy

and momentum of the wave

$$\omega_o = \omega_1 + \omega_2$$

$$\vec{K}_o = \vec{K}_1 + \vec{K}_2$$

The possibility of decay of the laser photon into a Langmuir plasma oscillation and an ion acoustic mode occurs when $\omega_p < \omega_o$ provides a very efficient mechanism for anomalous absorption, as discussed by many authors and verified experimentally in microwave and laser experiments, as well as in ionospheric heating. Moreover, at a density $\frac{n_c}{4}$ the decay of a laser photon into two plasmons can occur.

Classical theory explains this absorption as the generation of a plasmonwhich propagates to a region of lower density, where Landau damping converts their energy into electron thermal energy. However, for the laser intensities needed for laser fusion, strong non-linear effects can occur. These have been studied analytically by Galeev et al (1972). Qualitatively, the plasma oscillation grows to a large amplitude, leading to electron trapping at the phase velocity of the fastest growing mode about 10 v_{the}. Thus the parametric instability tends to convert the laser light into very high energy electrons. The very long mean free path of such electrons makes them couple only very weakly with the main thermal plasma, a problem which has been discussed by Kidder. Additionally, these electrons penetrate into and preheat the core, raising

its entropy and making further compression difficult. This one interesting area on which plasma physicists might speculate is possible non-linear mechanisms for thermalization of these electrons. Rosenbluth (1972) indicates that simple two stream instability should not occur as the non thermal distribution tends to be monotonically decreasing in energy. There is another important reason why the parametric instability may not provide the desired efficient coupling between laser and plasma, as a result of which other forms of parametric decay instabilities may occur at lower densities, ie before the photon reaches the critical density at which conversion to plasmons and acoustic waves occurs.

The types of parametric conversion of photons to other waves may be summarized as

$\omega_p = \omega$ photon $\longrightarrow$ plasmon + acoustic wave

$\omega_p = \frac{\omega}{2}$ photon $\longrightarrow$ two plasmon

$\omega_p^2 \geq \frac{T_e}{m_c^2}\omega^2$ photon $\longrightarrow$ plasmon + photon

$\omega_p^2 \geq \frac{T_i}{m_c^2}\omega^2$ photon $\longrightarrow$ acoustic wave + photon

The last two processes represent the parametric production of a lower energy photon, causing reflection. It is noticeable that these backscattered reactions occur at lower density than the first two, even though the growth rate is somewhat smaller so that the coupling is efficient, the photons are primarily reflected rather than absorbed, Shen (1976).

There is great interest concerning the backscattered laser radiation from the plasma and there are different explanations to determine whether the backscattering occurs and how it may saturate.

On the level of linear theory, three stabilizing effects may be considered: damping of the product waves, finite bandwidth radiation, and plasma inhomogeneity. To stabilize the decay $\nu_1 \nu_2 > \gamma^2$ (Nishikawa 1968) where γ is the growth rate, this is not an important mechanism since the damping is classical (collisional or Landau). For the laser bandwidth Rosenbluth considered $\gamma_o > \delta\omega$. Thus, the principal linear stabilization mechanism appears to result from the fact that the decay instability is not taking place in an infinite uniform plasma, but in the steeply varying density plasma.

As was noted, there are two possible three wave backscatter decay modes. Raman scattering off plasmons and Brillouin scattering of ion acoustic modes. One simple mechanism for the saturation of Raman scattering is electron heating by nonlinear processes, since $K_p \sim 2K_o$ and $K_p \lambda_D \leq 1/3$ to avoid Landau damping it follows that rather modest electron temperatures of $T_e \sim 0.05\ mc^2\ (\omega_p/\omega)^2$ will stabilize the backscatter (Rosenbluth and Sagdeev 1972). The Brillouin backscatter deposits very little energy into the plasma.

1.7 MAGNETIC FIELD

Since Krokhin and Serov (1966) announced their result of measuring D.C. magnetic field from laser produced plasma, there has been a great deal of interest in this field and its relation with resonance absorption.

Some of this theoretical work deals with the magnetic field resulting from thermo-electric currents Tidman and Shanny (1974), or as a field generated as an intrinsic part of resonance absorption, Thomson et al (1975). The latter process occurs when a plane polarized wave is oblique incident on a plasma with a density gradient, since a focussed laser spot contains rays with a variety of angles , resonance absorption is a ubiquitous phenomena for absorption of laser light. In the case of waves polarized in the plane of incidence, plasma waves are generated at the critical surface where they feed energy into the plasma. Ginzburg (1970) also stated that the incidence wave will turn back at a density

$$n = n_c \cos^2\theta$$

This absorption introduces a phase delay between electrons oscillating motion and the incidence wave, causing electrons to experience a time t average force. The force on the electron determines the D.C. magnetic field. The dispersion relation of the wave becomes

$$\omega_o^2 = \omega_{pe}^2 + \omega_{pe}\,\omega_{ce}$$

The resonance density due to the magnetic field

$$n_r = n_c \left[1 - (\omega_{ce}/\omega_o)^2 \right]$$

where ω_c is the electron cyclotron frequency. Physically the light is reflected at cut off density but its electric field tunnels into the higher density region where it appears hybrid waves are resonantly driven.

1.8 INTRODUCTION TO THE EXPERIMENT

A TEA CO_2 laser pulse was used to irradiate a solid carbon target to produce a plasma. The laser was in existence in the Department, but some modifications have been done to improve the output energy, the beam quality and the rate of firing.

To know the different mechanisms of the parametric processes stimulated in these plasma, the backscattered radiation was analysed for harmonic generation.

For an accurate analysis of the harmonic generation the laser was oscillating at 10.6 μm wavelength by inserting a diffraction grating as an end reflector in the cavity. Chapter 3 gives a full discussion of the CO_2 laser. In Chapter 4 the experimental arrangement, the spectroscopic and diagnostic techniques are explained. The results and plots are presented in Chapter 5. The discussion and analysis of the results are in Chapter 6. In Chapter 7 there is a conclusion.

CHAPTER 2

THEORY OF LASER PLASMA INTERACTION

2.1 INTRODUCTION

Laser light interacts with a plasma because the electrons and, to a lesser extent, the ions, oscillate in the electromagnetic field. The manner in which energy can be absorbed by the charged particles in the plasma is of considerable importance.

When an electromagnetic wave of small amplitude propagates through the plasma an important absorption process is inverse Bremsstrahlung which accompanies electron ion collisions. However, as the temperature of the plasma increases, the frequency of the inter particle collisions decreases and absorption, due to this process, diminishes.

If the propagating wave reaches a region where the electron plasma frequency equals the laser frequency the wave is reflected. Because the plasma is generated by focussing a short laser pulse on a solid target, the density gradient can be extremely steep, corresponding to a scale length $L = \left(\frac{1}{n}\frac{dn}{dx}\right)^{-1}$ of 10^{-4} to 10^{-2} cm. In this case, a small amplitude wave may be reflected with very little absorption, so that the fraction of the incident energy converted into random kinetic energy of the electrons and ions in the plasma is small.

When the radiation intensity increases, the absorption due to inverse Bremsstrahlung reaches a maximum value imposing a limit on the rate of heating. However, in regions where the electron density approaches the critical value, parametric interactions can occur between the incident wave and plasma electron and ion waves. Energy is then fed into these instabilities and anomalously strong absorption occurs.

If the intensity of the laser light incident on the plasma is increased sufficiently, the interaction with the plasma becomes strongly non-linear and several important effects appear. The light wave can excite some of the natural modes of oscillation of the plasma, so the energy of the laser light is converted into plasma kinetic energy.

One of the fundamental non-linear processes is the parametric generation of other modes by a large amplitude electromagnetic pump wave. This provides efficient transfer of energy from the pump wave into the excited modes. If the excited waves are purely electrostatic, they are absorbed in the plasma through various damping mechanisms, (Nishikawa (1968), Kaw and Dawson (1969) and Silin (1965)). On the other hand, if one of the excited waves is electromagnetic it can escape from the plasma leading to anomalous reflection of the incident electromagnetic wave (Rosenbluth and Sagdeev (1972), Drake et al (1974)).

A large amplitude electromagnetic pump wave propagating in a plasma leads to the growth of other plasma waves out of the background thermal noise, providing that the excited

field exceeds a threshold value. The plasma waves grow at the expense of the pump electromagnetic field.

In a non-linear medium, coupling can occur between different modes of oscillation resulting in a transfer of the energy from one mode of oscillation to another. Coupling between waves is strongest for frequencies in the vicinity of a natural resonance of the medium. Hence, it is to be expected that electron plasma waves and ion acoustic waves will be involved in many of these processes. At least three wave processes are involved if energy and momentum balance are to be satisfied with phase matching conditions.

$$\omega_o = \omega_1 + \omega_2$$

$$\bar{K}_o = \bar{K}_1 + \bar{K}_2$$

where ω_o and K_o are the frequency and wave vector of the pump wave, and ω_i, K_i ($i = 1, 2$) refer to the driven modes.

In an unmagnetized plasma the principal branches of the dispersion relation are transverse electromagnetic wave (T), electrostatic Langmuir wave (L) and electrostatic ion acoustic wave (S). The possible three wave decay processes driven by the laser light are:-

$T \longrightarrow L + S$ (parametric decay instability)

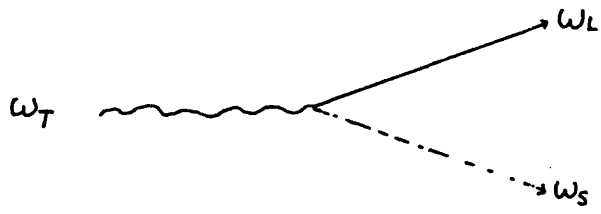

$T \longrightarrow L + L'$ (two plasmon decay)

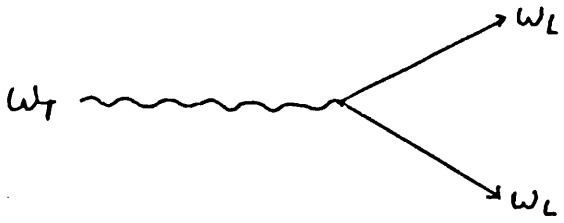

$T \longrightarrow T' + L$ (stimulated Raman scattering (S.R.S.))

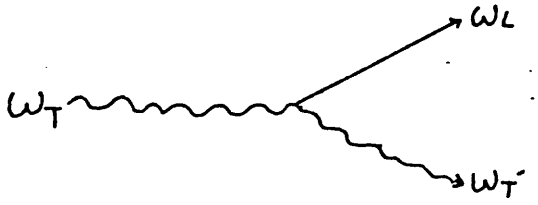

$T \longrightarrow T' + S$ (stimulated Brillouin scattering (S.B.S.))

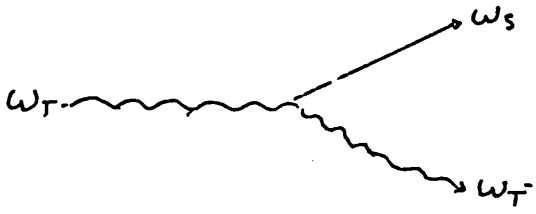

where T' represents transverse wave photons at lower frequencies than that of the laser.

The first two instabilities represent anomalous absorption mechanisms where as the stimulated scattering processes (S.B.S.) and (S.R.S.) give rise to anomalous reflectivity.

The frequencies of the wave under consideration are usually ordered as $\omega_o > \omega_{pe} >> \omega_i$, where $\omega_{pe} = \left(n_e^2/\epsilon_o\, m_e\right)^{\frac{1}{2}}$ is the plasma electron frequency and ω_i is the ion acoustic frequency. It is readily seen from the phase matching conditions that the parametric decay instability occurs near the critical density, n_{ce}, where ω_{pe} equals ω_o and $n_{ce} = \epsilon_o\, m_e\, \omega_o^2/e^2$. The two plasmon decay occurs near to the quarter critical density with ω_o equal to ω_{pe} and equal to $n_e \frac{n_{ce}}{4}$. Stimulated Brillouin and Raman scattering are possible in the underdense plasma region $n_e < n_{ce}$ (S.B.S.) and $n_e < n_{ce}/4$ (S.R.S.).

In some cases where $\bar{K} + \bar{K}_o$ or $\bar{K} \rightarrow 0$, the anti Stokes wave cannot be ignored and a four-wave process occurs. This will be described in a later section.

When laser light generates a plasma from a solid surface, the electron density rises from zero to a value above the critical density. The regions in which the various parametric processes can occur are shown below.

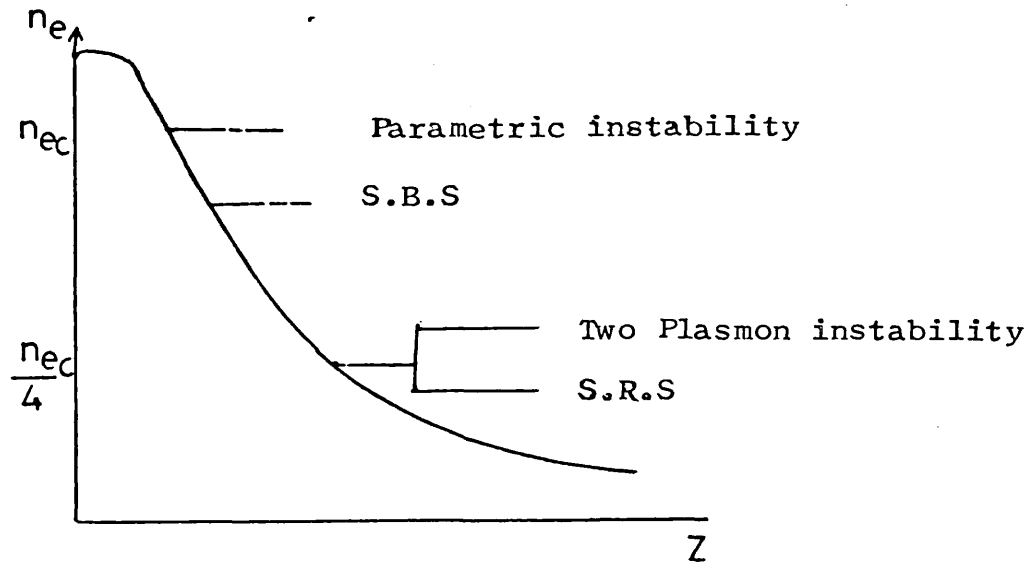

2.2 LASER PLASMA INTERACTION

The laser plasma interaction problem is concerned mainly with how the light energy couples to the plasma. For low temperature plasma the laser energy is absorbed by classical absorption (inverse Bremsstrahlung) i.e. due to inter particle collisions. However, as the temperature of the plasma increases the particle collision frequency decreases and absorption due to this process falls. When the laser light propagates in the plasma to a density where the plasma frequency equals the laser frequency ($\omega_o = \omega_{pe}(Z)$) the laser light is totally reflected with no absorption according to linear theory.

As the intensity of the incident light increases, non-linearities of the plasma become important; In particular, above a certain intensity where the light wave can excite the plasma waves. The effect of this non-linear excitation of plasma waves provides another absorption mechanism "anomalous absorption".

2.3 CLASSICAL ABSORPTION

The plasma electrons oscillate rapidly in the electromagnetic field ionizing the surrounding atoms, giving high density plasma. The wave equations of such a plasma can be obtained from Maxwell's equations

$$\nabla^2 E - \frac{4\pi n_e e^2}{m_e c^2} E = \frac{1}{c^2} \frac{\partial^2 E}{\partial t^2} \qquad (2.1)$$

For the particular case of an electro. magnetic wave in which E_y propagates in the Z direction, equation (2.1) becomes

$$\frac{\partial^2 E_y}{\partial z^2} - \frac{\omega_{pe}}{c^2} E_y = \frac{1}{c^2} \frac{\partial^2 \bar{E}_y}{\partial t^2} \qquad (2.2)$$

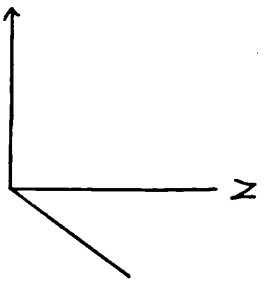

Assuming a solution of the form

$$E_y = E_o \exp\left[i(Kx - \omega t)\right] \qquad (2.3)$$

then equation (2.2) reduces to

$$K^2 = \frac{\omega^2}{c^2}\left(1 - \frac{\omega_{pe}^2}{\omega^2}\right) \qquad (2.4)$$

If the laser frequency $\omega_o > \omega_{pe}$ then the plasma frequency in equation (2.4) is real and the wave propagates through the plasma. If $\omega_o < \omega_p$, K will be imaginary and the wave amplitude decreases by a factor $1/e$ in a distance given by

$$d = \frac{c}{(\omega_p^2 - \omega^2)^{\frac{1}{2}}}$$

The electromagnetic wave is then completely reflected. The critical density at which the incident radiation is reflected is

$$n_{ec} = \frac{m_e c^2 (2\pi)^2}{e^2 \lambda^2} \qquad (2.5)$$

Beyond this density the plasma becomes opaque to the incident laser radiation.

According to linear theory the laser energy is deposited in the plasma as a result of electron-ion collisions. The absorption coefficient due to inverse Bremsstrahlung is given by Johnston and Dawson(1973) as

$$K = \frac{16\,\pi\, Z^2\, n_e\, n_i\, e^6 \ln\Lambda(\nu)}{3\,C\,\nu^2\,(2\pi\, m_e\, K_B\, T_e)^{3/2}\,(1 - \nu_p^2/\nu^2)} \qquad (2.6)$$

$$= \frac{7.8 \times 10^{-9}\, Z\, n_e^2 \ln\Lambda\ (\nu)}{\nu^2\,(K_B\, T_e)^{3/2}}\ \frac{1}{(1 - \nu_p/\nu)^{\frac{1}{2}}}$$

$K_B\, T_e$ is the electron temperature in eV

$\Lambda(\nu)$ is the minimum of $\frac{V_T}{\omega_p\, p_{min}}$ or $\frac{V_T}{\omega\, p_{min}}$

V_T is the electron thermal velocity

p_{min} is the minimum impact parameter for electron ion collisions

$p_{min} \approx$ maximum of $\frac{Z_e^2}{K_B T}$ or $\frac{\hbar}{(m_e\, K_B\, T)^{\frac{1}{2}}}$

Z_e and n_i are the ionic charge and density

e, m_e, n_e are electronic charge, mass and number density.

C is the velocity of light.

If the incident radiation is increased sufficiently the radiation electric field begins to have a significant effect

on the electron distribution which can no longer be accurately described by the electron temperature. The electrons start to oscillate in the electric field of the radiation with a velocity amplitude or quiver velocity of:-

$$V_o = \frac{e\,E_o}{m_e\,\omega} = 25\,\lambda\,(\mu_m)\,\sqrt{I}\ \text{cm/sec}$$

where λ is the laser wavelength in μ_m and I is the intensity in W/cm^2.

The ratio of the quiver velocity to electron thermal velocity V_t is known as the field strength parameter

$$\eta = V_o/V_T$$

$$V_T = (K_B\,T_e/m_e)^{\frac{1}{2}}$$

In a strong radiation field the plasma processes are governed by the quiver velocity of the electron, rather than by the thermal velocity. Then thermal velocity can be replaced by quiver velocity in equation (2.6). which leads to a non linear absorption coefficient of:-

$$K = \frac{16\,Z^2\,n_e\,n_i\,e^3\,\omega\,\ln\Lambda\,(\nu)}{3\,C\,(2\pi)^{\frac{1}{2}}\,E_o^3\,(1 - \frac{\omega p^2}{\omega 2})^{\frac{1}{2}}} \qquad (2.7)$$

The value of $\ln\Lambda$ has been calculated by various authors, eg Silin (1965), Pert (1972), and Dawson and Johnston (1973).

Since the radiation intensity is proportional to E_o^2 the absorption coefficient therefore becomes dependent on the irradiance and varies as $I^{-3/2}$. The transition from the weak to strong interaction takes place approximately when $\eta = 1$. Under these conditions, the power absorbed by the

plasma due to inverse Bremsstrahlung is a maximum.

2.4 RESONANCE ABSORPTION

When a transverse electromagnetic wave is incident, normally on the plasma boundary, it penetrates a distance Z_1 to the critical density. On the way to the critical surface it is partially absorbed and then reflected back to form a standing wave. The dielectric constant of the plasma becomes

$$\epsilon(Z_1) = 1 - \frac{\omega_{pe}^2(Z_1)}{\omega_o^2} = 0 \qquad (2.9)$$

If the transverse wave is incident obliquely on the plasma boundary it is refracted by the plasma layers according to Snells law.

$$n = \epsilon^{\frac{1}{2}}(Z) = \sin\theta$$

where θ is the angle of incidence of the wave on the plasma boundary as shown in Figure 2.1

and

$$\sin\theta = \left(1 - \frac{\omega_{pe}^2(Z_o)}{\omega_o^2}\right)^{\frac{1}{2}} \qquad (2.10)$$

This refraction increases gradually until a turning point is reached at a depth in the plasma where the plasma frequency is given by

$$\omega_p^2(Z_o) = \omega^2 \cos\theta$$

and the local plasma density is given by

$$n_t = n_c \cos^2 \theta$$

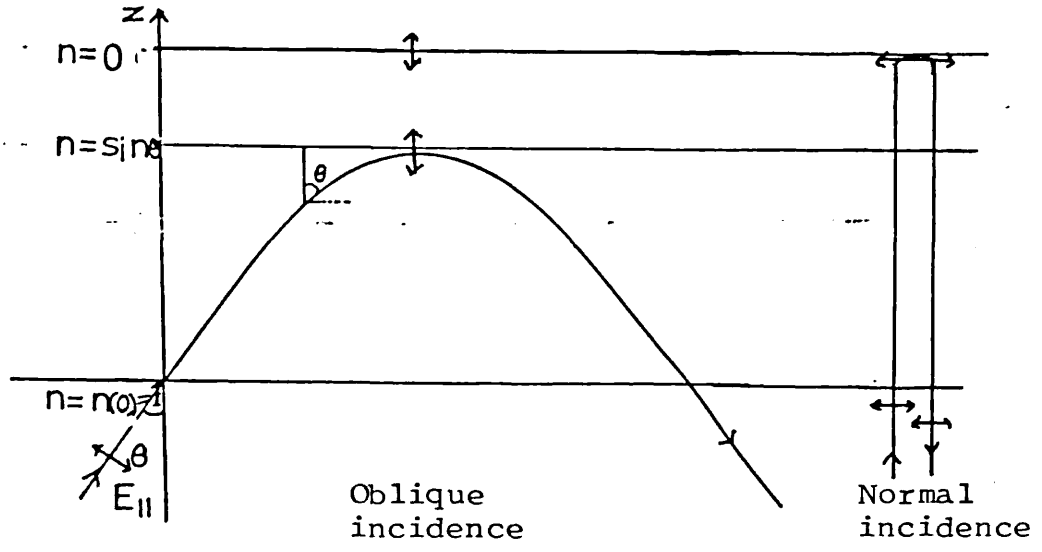

Figure 2.1

For a linear density gradient the result would be as follows.

The structure of the electric field as a function of depth in the plasma depends on the polarization of the electromagnetic wave. In the case of the electric vector of the incident radiation being normal to the plane of incidence $|E^2|$ oscillates in the region $Z < Z_1$, with Z_1 being the point where the refractive index $n = \sqrt{\epsilon}(K, \omega, Z_1) = \sin\theta$. For $Z > Z_1$ the amplitude of the electric field drops off to zero exponentially. Schematically the behaviour of E_n^2 is shown in Figure 2.2(a).

An interesting effect arises when the electric vector has a component parallel to the plane of incidence. Then, $|E_Z^2|$ oscillates in the region $Z < Z_1$ as in the case for

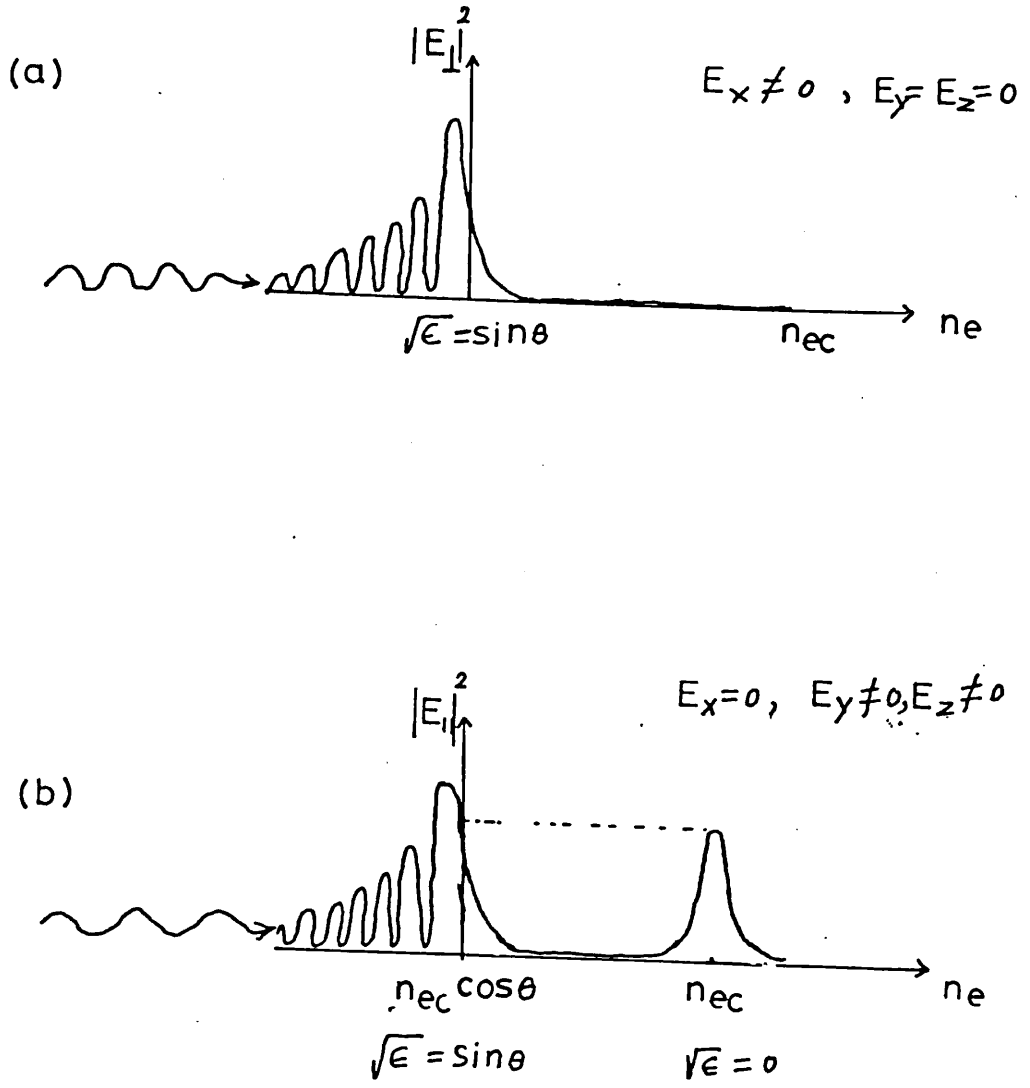
(a)
$|E_\perp|^2$
$E_x \neq 0$, $E_y = E_z = 0$
$\sqrt{\epsilon} = \sin\theta$
n_{ec}
ne
(b)
$|E_\perp|^2$
$E_x = 0$, $E_y \neq 0, E_z \neq 0$
$n_{ec}\cos\theta$
n_{ec}
ne
$\sqrt{\epsilon} = \sin\theta$
$\sqrt{\epsilon} = 0$

Figure 2.2

the electric vector normal to the plane of incidence. When the wave approaches the turning point the E-vector has a component along the density gradient and the wave can tunnel through the critical density. (Budden 1966)). Then it begins to grow and this field has a singularity at the point where $\epsilon(Z) = 0$. If collisions and temperature effects are included, the singularity does not appear. However, a sharp resonance remains. The large magnitude of the electric field leads to the excitation of plasma oscillations. These plasma oscillations transfer their energy to the electrons by Landau damping. The field at the resonance point depends on the density gradient scale length.

If linear variation of density is assumed,

ie

$$n_e = n_{ce} \left(1 - \frac{Z}{L}\right)$$

where L is the scale length

$$L = n_{ce} / \left(d n_e / d z\right)_{n_e = n_{ce}}$$

which is much greater than the wavelength of the laser light $\lambda = 2\pi / K_o$. If E(Z) is assumed to vary linearly with Z then at the point where E(Z) = 0 the magnitude of the electric field strength $|E_Z|$ becomes

$$E_r = E_o \frac{\Phi(t)}{(2\pi K_o L)^{\frac{1}{2}}} \frac{\omega_o}{\nu_e} \qquad (2.11)$$

where $t = (K_o L)^{1/3} \sin\theta$, and the function $\Phi(t)$ is a dimensionless parameter given by Ginzburg (1961) and expressed in terms of the Airy integrals as

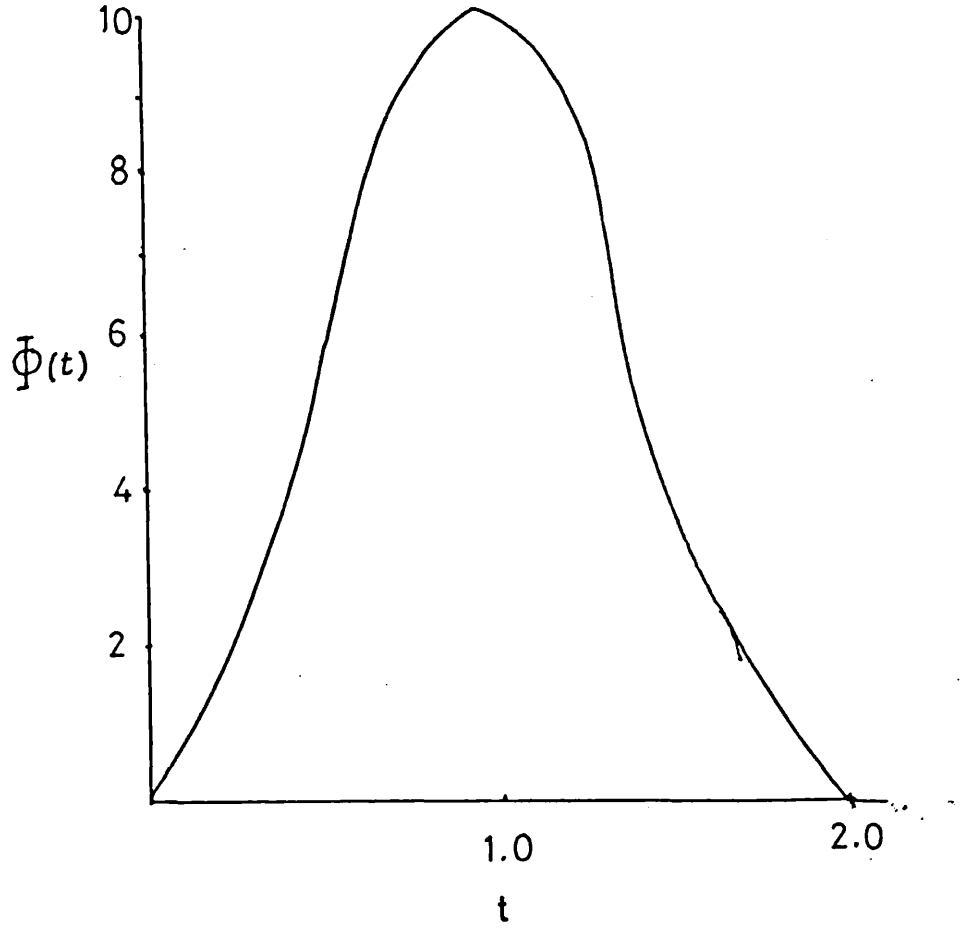

Figure 2.3

Function $\Phi(t)$ that determined the electric field strength at various position in the plasma

$$\Phi(t) = 2t\, V(t^2) \sqrt{\frac{V(t^2)}{-V'(t^2)}} \qquad (2.12)$$

with $V(t^2) = \sqrt{\frac{t^2}{3\pi}}\, K_{1/3}\left(\frac{2}{3} t^3\right)$

and $V'(t^2) = -t^2\, (3\pi)^{-\frac{1}{2}}\, K_{2/3}\left(\frac{2}{3} t^3\right)$

Where K is the Bessel function and a function of the angle of incidence θ_o, Φ is shown in Figure 2.3. Φ has a peak that depends on the wavelength of light and the density scale length of the plasma falling rapidly with t. The maximum value of the electric field is given as:-

$$E = \frac{1.2}{(2\pi K_0 L)^{\frac{1}{2}}} E_o \frac{\omega_o}{\nu} \qquad (2.13)$$

with a width in the Z direction of

$$\Delta z = \frac{\nu}{\omega_o L} \qquad (2.14)$$

Pearlman et al (1977) and Manes et al (1977) found experimentally that at oblique incidence absorption of the laser light suffers a two times enhancement if the plane of polarization is parallel to the plane of incidence, compared with the case when the plane of polarization is normal to the plane of incidence. The angle of incidence is chosen such that the turning point electron density ($n_t = n_{ce} \cos^2 \theta$) is not too far from the density n_{ce}. With the maximum angle given by the focussing lens of 7.6^o the density n_t is $0.97\, n_{ce}$. It should be mentioned

that at the surface where $\sqrt{\epsilon} = \sin\theta$ the parametric decay rate is expected to be reasonably high and the main absorption mechanisms are expected to be inverse Bremsstrahlung and resonance absorption.

Due to the absorption of large amounts of laser radiation by resonance absorptions in small regions and consequent production of a temperature gradient, these temperature and density gradients lead to megagauss magnetic fields which can, in turn, inhibit the conduction of electrons see Bezzerides et al (1977).

2.5 PARAMETRIC PROCESSES

Classical absorption due to inverse Bremsstrahlung becomes inefficient as the plasma temperature increases due to the rapid decrease of the electron-ion collision frequency. The absorption of intense radiation is then determined by collective effects in the plasma, resulting in the conversion of radiation energy into plasma waves, which in turn heat the particles.

High power laser radiation incident on these waves can drive parametric instabilities, Kaw and Dawson (1969), Kruer and Dawson (1972) and Thomson et al (1973), in which electrostatic waves or both electrostatic and electromagnetic waves are excited. (Goldman and Dubois (1965), Liu et al (1973) and Drake et al (1974).) Interaction of laser radiation with electrostatic waves results in parametric decay, oscillating two stream instabilities

which lead to an enhanced absorption at the critical surface. Resonance absorption also occurs in this region.

However, the scattering of laser radiation by density fluctuations in the plasma can lead to radiation losses of energy such as Raman and Brillouin scattering. These processes may provide useful diagnostic tools for learning about the spectrum of collective excitations and electron temperature in the region of tenuous plasma.

2.5.1 The Parametric Decay Instability

The theory of the parametric decay instability was developed by Nishikawa (1968). It occurs when the electron plasma wave frequency ω_p is equal to the incident laser frequency ω_o.

The incident transverse wave excites both a high frequency electron plasma wave ω_{pe} and low frequency ion acoustic wave ω_{pi} and then couples with these waves, provided that the matching conditions

$$\omega_o = \omega_{pe} + \omega_{pi}$$

and $$\vec{K}_o = \vec{K}_l + \vec{K}_1$$

are satisfied.

These are the energy and the momentum conservation conditions. If the intensity of the incident radiation is large enough the plasma waves ω_{pe} and ω_{pi} grow rapidly and act as a pump frequency for each other. Parametric coupling between waves makes it possible to produce beat frequencies of $\omega_o \pm \omega_{pi}$,

$\omega_o \pm 2\omega_{pi}$, $\omega_o \pm \omega_{pe}$, $\omega_o \pm 2\omega_{pe}$ and harmonics. The relative coupling of these modes depends on the intensity of the incident radiation. However, the intensity can be increased so that the growth rate is greater than the damping rate. At this point these oscillations become unstable and grow exponentially. The threshold for such an instability has been evaluated:-

$$\left(\frac{v^o}{V_{th}}\right)^2 K_o^2 L > 8\gamma\left(\frac{\nu}{\omega_{p_1}}\right)^{1/2} + 3.2\,\frac{\nu_1 \nu_e}{\omega_{p_1}\omega_o}$$

$$\gamma = [1 + (3T_i/T_e)]$$

The threshold field strength E_c given by Nishikawa for the case of $\omega_o > \omega_{pe}$ and the electron plasma and ion plasma oscillations propagate without attenuation is given by

$$E_C^2 = \frac{m_e m_i}{e^2}\,\frac{\nu_{in}}{\nu_{ei}}\,\frac{\omega_{ek}}{K^2(\omega_o - \omega_{ek})}\left(\frac{\nu_{ee}^2}{4} + (\omega_o - \omega_{ek})^2\right)^2 \qquad (2.15)$$

where ν_{ee}, ν_{ii} and ν_{ei} are electron-electron, ion-ion and electron-ion collision frequencies, and $k = \frac{e^2}{m_e m_i}(k_1 E_o)^2$.

Also $\omega_{ek}^2 = \omega_{pe}^2 + V_{th}^2 k_o^2$, where V_{th} is the electron thermal velocity. The growth rate just above threshold is

$$\gamma = -\tfrac{1}{2}\nu_{ii}\,\frac{2k(\omega_o - \omega_{pe})}{\omega_{pe}}\,\frac{\nu_{ee}}{\nu_{ee} + 4(\omega_o - \omega_{pe})^2} \qquad (2.16)$$

This rate attains a maximum when

$$\omega_o = \omega_{pe} + \frac{1}{2\sqrt{3}}\,\omega_{ek} \qquad (2.17)$$

leading to a maximum growth rate of

$$\gamma = -\tfrac{1}{2}\nu_{ii} + \frac{9}{16\sqrt{3}}\,\frac{4K}{16\sqrt{3}\,\omega_{pe}^2\,\omega_{ek}} \qquad (2.18)$$

If the field strength of the incident radiation is greater than the critical field strength E_c, the maximum growth rate of the parametric instability is given by

$$\gamma_m = \frac{\sqrt{3}}{2} \omega_{ek} \frac{m_e}{4_{mi}} \left(\frac{ek \cdot \bar{E}_o}{m_e \omega_o^2} \right)^2 \quad 1/3 \qquad (2.19)$$

This formula is valid only near the critical field strength E_c given by equation (2.15).

2.5.2 The Two Plasmon Instability

An electromagnetic wave incident on an inhomogeneous plasma may decay into two plasmons in the region of quarter critical density. The generated plasma waves may further couple with the incident wave to generate a scattered wave at a frequency $\frac{3}{2}\omega_o$. This process has been discussed by Goldman (1966), Jackson (1964) and Galeev et al (1972).

The frequency and wave number matching conditions are

$$\omega_o = \omega_{L1} + \omega_{L2}$$

$$= 2\omega'_{pe} \quad \text{at } n_{cr}/4$$

$$K_o = \vec{K}_{L1} + \vec{K}_{L2}$$

where $\omega_L'^2 = \omega_{pe}^2 + 3K^2 V_e^2$

Configuration for the wave vectors in this process is then:-

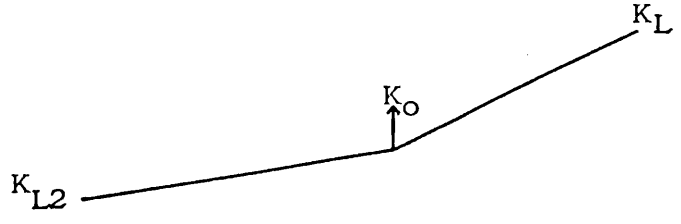

The Langmuir wave vectors are at $\pi/4$ or $5\pi/4$ to K_o and the most unstable modes occur both are at $\pi/4$ to $\vec{K}_o$, Jackson (1967).

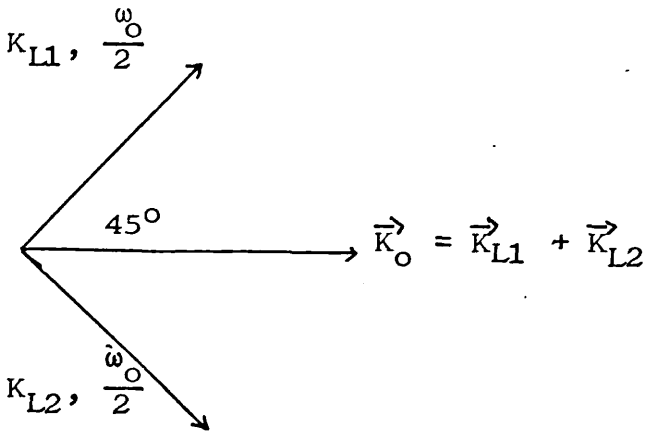

The threshold for the two plasmon instability is given by Liu as :-

$$\frac{1}{3}\left(\frac{V_o}{V_e}\right)^2 K_o L > 1$$

where V_e is the electron thermal velocity and L is the density scale length.

Since the laser energy is converted to electrostatic modes which propagate only in the plasma, this process leads to enhanced absorption.

2.5.3 Stimulated Brillouin Scattering

Laser light may be scattered from collective ion plasma oscillations, the emitted radiation:-

$$T = T' + S$$

where the laser light T is converted into light of a lower frequency T^1 and an ion acoustic wave S satisfying the conditions:-

$$\omega_T = \omega_T + \omega_S$$

$$\vec{K}_T = \vec{K}_{T'} + \vec{K}_S$$

and $\omega_S = KC_S$

As the irradiance increases, the intensity of Brillouin scattering increases.

Ion acoustic waves have wavelengths which are appreciably greater than those of electromagnetic waves but suffer Landau damping, as given by Dubois et al (1963)

$$\gamma_i = 4\pi I_m \sigma_L = \sqrt{\frac{\pi}{2}} \frac{\omega^2}{\alpha} \exp\left(-\frac{1}{2}\frac{\omega^2}{\alpha^2 K^2}\right) \qquad (2.20)$$

where $\alpha^2 = \frac{m}{M}$

This damping term is quite small since the arguement of their exponent is of the order of $- C^2$.

For Brillouin scattering the dispersion relation of the ion wave with $K \lambda_o << 1$ is independent of the plasma density, Consequently, the width of the resonance zone is principally determined by the change of the wave vector of the electromagnetic waves of the order

$$\left(dK/dz\right)^{1/2} \simeq 2 K_o C^2 L/\omega_{pe}^2 \,^{1/2} \qquad (2.21)$$

Liu (1976).

Because this width is greater than that for Raman scattering by a factor of the order (C/V_e), it is expected that the threshold for Brillouin scattering in an inhomogeneous plasma is also much lower. The threshold for Brillouin scattering is given by Liu (1976) as

$$\frac{2}{3}\left(\frac{V_o}{V_e}\right)^2 K_o L > 1$$

and is approximately $(V_e/C)^2$ lower than for Raman back scatter, or about $(V_e/C)^{3/2}$ $(V_e/V_o)^{1/2}$ lower than for Raman sidescatter. The Brillouin backscattered with $K \approx 2 K_o$ has the same threshold mentioned here.

The frequency and wave number matching conditions can be illustrated in the dispersion diagram as follows:-

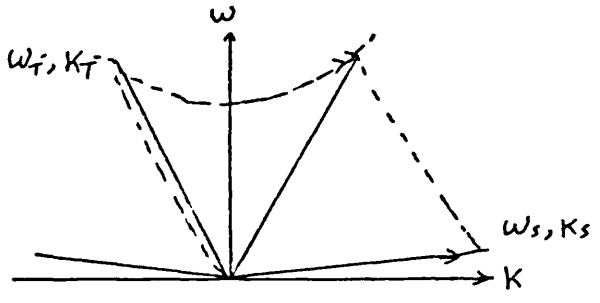

It is seen that the scattered electromagnetic wave (ω_T , K_T) propagates in the reverse direction to the electromagnetic pump wave. Then the matching conditions are satisfied at any point in the plasma from the critical surface outwards. This means that once the threshold condition for this instability is exceeded, all the laser light power converted to the backscattered wave is reflected normally from the plasma.

2.5.4 Stimulated Raman Scattering

In this process the incident light wave is scattered from a Langmuir wave with $\omega_L = \omega_p$. Consequently, the scattered light is shifted further in frequency, than was the stimulated Brillouin scattering light.

The energy and momentum conservation matching conditions are:-

$$\omega_T = \omega_{T'} + \omega_L$$

$$\vec{K}_T = \vec{K}_{T'} + \vec{K}_L$$

and may be satisfied at all densities from $\frac{n_{ce}}{4}$ outwards to the coronal region.

For inhomogeneous plasma with $n = n_o\ (1 + Z/L)$ there are two Raman scattering processes. For backscattered where $\cos\theta \gg (V_e/C)^2$ and $\omega_o = 2\,\omega_{pe}$, the threshold condition for Raman backscattered radiation given by Liu is:-

$$\left(\frac{V_o}{C}\right)^2 K_o\, L > 1$$

This may occur at $\omega_o \gg \omega_p$ as well as $\omega_o = 2\,\omega_p$ and temporally growing modes may exist. In both cases the scattered light has a very long wavelength in the direction of the density gradient. This saturation has been discussed by Liu et al (1973), Drake and Lee (1973) and White et al (1974). The Maxwell equations are used to study the temporally growing modes for underdense plasma $\omega_o = 2\,\omega_{pe}$ and $\omega_o > 2\,\omega_{pe}$ below the quarter critical density.

The threshold for instability sidescattering is

$$\left(\frac{V_o}{C}\right)^{3/2} (K_o\, L) > 1$$

2.6 HARMONIC GENERATION

Harmonics may be generated in a plasma if the plasma parameters are modulated by an incident electromagnetic wave and then further radiation interacts non-linearly with the modulated plasma. Theoretical derivations of the scattered intensity may be made by solving the equations describing coupling between plasma modes of oscillation and transverse electromagnetic waves. Alternatively, a quantum mechanical model may be set up.

Possible models consist of the coalescence of two plasmons having frequency near to ω_o, with conversion to electromagnetic radiation

$$\omega_o + \omega_o \longrightarrow 2\omega_o$$

Another harmonic that has been studied has a frequency $\frac{3}{2}\omega_o$ and may arise from an up conversion process, such as

$$\frac{\omega_o}{2} + \frac{\omega_o}{2} \longrightarrow \omega_o$$

$$\omega_o + \frac{\omega_o}{2} \longrightarrow \frac{3}{2}\omega_o$$

Higher harmonics have been detected, McClean et al (1977), but will not be discussed here.

In the following section, it will be seen that there is more than one process leading to the generation of harmonics but the matching conditions can be specified for the incident and generated waves. Also, the power and the frequency of the scattered wave may be determined.

2.6.1 Second Harmonic Generation $2\omega_o$

Second harmonic generation in laser plasma interaction has been the subject of considerable theoretical and experimental work. For example, Bobin et al (1973), Silin (1975) and Erokhin et al (1974).

In a homogeneous isotropic plasma the process of recombination of the two transverse waves with an electromagnetic wave are forbidden (Vedenov (1963)) because it is impossible to satisfy the energy and momentum conservation condition.

The generation of electromagnetic waves with frequency $\omega = 2\omega_o$ in such a plasma is possible if one of the plasma waves is a longitudinal wave. The second harmonic may be generated by recombination of a transverse electromagnetic wave t with a Langmuir wave L

$$t + L \rightarrow t'$$

Momentum and energy conservation require

$$\omega_t + \omega_L \rightarrow \omega_{t'}$$

$$K_T + K_L \rightarrow K_t$$

An alternative scheme consists of the coupling of two Langmuir waves to give transverse electromagnetic waves:-

$$l + l \rightarrow t$$

with $\omega_l + \omega_L \rightarrow \omega_t$

and $K_l + K_L \rightarrow K_t$

In an inhomogeneous plasma the conservation conditions for the waves will be satisfied at a particular position in the plasma.

2.6.1.1. Generation of 2ω in Oblique Incidence

In an inhomogenous plasma the electric field of the incidence radiation increases to a maximum amplitude near the critical surface, Ginzburg (1964). If the incidente electromagnetic wave has an electric field component in the plane of incidence, this field can excite Langmuir oscillations parallel to the density gradient. Subsequently, non linear interaction can occur between the incident oblique wave and the plasma electron oscillations in the density gradient to produce 2ω. This mode of generation has been studied by Erokhin (1969) and (1974) and Vinogradov (1973), who determined the electromagnetic fields structure to the first and second harmonic and the rate of conversion to the second harmonic.

Using a non-relativistic cold model description where the ions provide a neutralizing background, Bobin calculated the current as

$$J_2 = \frac{i e^2}{m^2 \omega_o^3} \frac{N_o}{4} \vec{\nabla} (\vec{E}_L \cdot \vec{E}_L) + \frac{1}{1 - (\omega_P/\omega_o)^2} (\vec{\nabla} N_o \vec{E}_L) \vec{E}_L \qquad (2.2$$

The second term in this equation contains $2\omega_o$.

In a uniform plasma ($\nabla N_o = 0$) so

$$J_2 = \vec{\nabla} (\vec{E}_L \cdot \vec{E}_L) \qquad (2.22)$$

Since this term is longitudinal no transverse wave at 2ω

can be generated.

In an inhomogenous plasma there is a contribution for ∇N_o which is important near the critical layer and can give rise to second harmonic generation.

2.6.1.2 Silin Theory

The theory of parametric resonance given by Silin (1973) offers the possibility of determining the dependence of the shift of the intensity maximum of the second-harmonic line due to the ion acoustic wave, so the electron temperature can be determined.

If the irradiance of the electromagnetic wave is higher than the threshold of the parametric process, the electron oscillation instabilities can come from the region around the critical density. Then the second harmonic results from coupling of the electron plasma wave excited parametrically to the incident or reflected electromagnetic wave.

$$t + l \rightarrow t$$

If the plasma frequency is slightly lower than the laser frequency $\omega_o > \omega_{pe}$, the second harmonic 2ω generated by this mechanism is shifted from the original $2\omega_o$ towards longer wavelengths.

The displacement of this harmonic towards the red can be calculated from the conservation relation. If (ω_o, K_o) is the incident laser wave, (ω_1, K_1) is the plasmon and (ω_2, K_2) is a phonon, then the energy and momentum conservation relations become:-

$$\omega_o = \omega_1 + \omega_2 \qquad \omega_1 = \omega_o - \omega_2$$

$$\vec{K}_o = \vec{K}_1 + \vec{K}_2 \qquad \vec{K}_1 = \vec{K}_o - \vec{K}_2$$

Since the interaction takes place near the critical surface and $\omega_o > \omega_{pe} >> \omega_{pi}$

then $\omega_1 = \omega_{pe} + \delta\omega$ where $\delta\omega << \omega_p$.

The plasmon ω_1 can coalesce with the photon to produce 2ω displaced from the original $2\omega_o$ by $\Delta\omega$:

$$\Delta\omega = 2\omega_o - 2\omega$$

$$= 2\omega_o - (\omega_o + \omega_1)$$

$$= 2\omega_o - (\omega_o + \omega_o - \omega_2) = \omega_2$$

ω_2 is the phonon frequency ($\omega_2 = K_2 C_s$). The second harmonic generated from the parametric process is displaced towards the red by an amount equivalent to the phonon frequency.

The wave vector conservation relation for the second harmonic is

$$K = K_o + K_1$$

$$= 2\vec{K}_o - \vec{K}_2$$

Applying the dispersion relation of the electromagnetic wave 2ω gives

$$(2\omega_o - \Delta\omega)^2 = \omega_{pe}^2 + (2\vec{K}_o - \vec{K}_2)^2 c^2$$

$$= (\omega_o - \Delta\omega - \delta\omega)^2 + (2\vec{K}_o - \vec{K}_2)^2 c^2$$

$\delta\omega \ll \omega_o$ This gives

$$4\omega_o^2 = \omega_o^2 + (2\vec{K}_o - \vec{K}_2)^2 c^2$$

Therefore

$$\left|2\vec{K}_o - \vec{K}_2\right| = \sqrt{3}\ \frac{\omega_o}{2}$$

but near the critical surface $K_o \simeq 0$, therefore

$$\vec{K}_2 \simeq \sqrt{3}\ \frac{\omega_o}{2}$$

Then the displacement of the second harmonic is

$$\Delta\omega = \omega_2\ K_2\ C_S = \sqrt{3}\ \frac{\omega_o}{C} C_S$$

Therefore

$$\omega_o\ C_S = \omega_{Li}\ V_{Te}$$

where ω_{Li} is the ion Langmuir frequency and V_{Te} is the electron thermal velocity, therefore

$$\Delta\omega = \sqrt{3}\ \omega_{Li}\ \frac{V_{Te}}{C}$$

On the other hand, the above formula does not take into account the non-linear effect associated with the oscillation of the electrons in the electric field of the wave. This introduces a correction which involves mainly a high flux. The non-linear dispersion relation of the ion acoustic wave must then be introduced

$$\omega_L = K_2 \left(C_S^2 + \frac{m_e}{4m_i}\ \frac{\omega_o}{\Delta\omega_o}\ V_o^2\right)^{1/2} \qquad (2.23)$$

where V_o is the quiver velocity of the electrons, $\Delta\omega_o$ is the difference between the laser frequency and the plasma local frequency.

$$\Delta\ \omega_o(z) = \omega_o - \omega_p(z)$$

$$= \omega_o \frac{z}{2L}$$

$$= \frac{1}{2}\ \omega_o \left(\frac{c}{L\omega_o}\right)^{2/3}$$

z is the distance between the critical surface and the region where the electric field given by the Airy function becomes maximum (Ginzburg (1960)).

Then the red shift of the second harmonic backscattered wave becomes

$$\Delta\ \omega = \sqrt{3}\ \frac{\omega_o}{c}\ \left(c_s^2 + \frac{1}{4}\ \frac{m_e}{m_i}\ \frac{\omega_o}{\Delta\ \omega_o(z)}\ v_o^2\right)^{\frac{1}{2}}$$

$$= \sqrt{3}\ \omega_{Li}\ \left[\left(\frac{V_{Te}}{c}\right)^2 + \frac{1}{4}\ \frac{v_o^2}{c^2}\ \frac{\omega_o}{\Delta\omega_o}\right]^{\frac{1}{2}} \qquad (2.24)$$

The second term is the correction term which is only important at high flux.

The quiver velocity is

$$v_o = \frac{e\ E_o}{m\ \omega_o}$$

$$= 0.25\ \lambda \cdot \sqrt{I}$$

$$\Delta\ \omega = \sqrt{3}\ \omega_{Li}\left[\left(\frac{V_{Te}}{c}\right)^2 + \frac{1}{4}\left(\frac{0.25\ \lambda}{c}\right)^2\ I\ \frac{L^{2/3}}{\omega_o^{4/3}}\right]^{\frac{1}{2}} \qquad (2.25)$$

where I is W/cm^2 $\lambda\ \mu_m$

2.6.2 Four Wave Processes

In certain cases, to satisfy the conditions of momentum conservation, it is necessary to introduce a fourth wave. This wave eliminates the difference in

momentum without upsetting the energy conservation. The second harmonic 2ω generated by this method is described as "superelastic scattering" of the incident wave with plasmons containing four parametric processes, ie

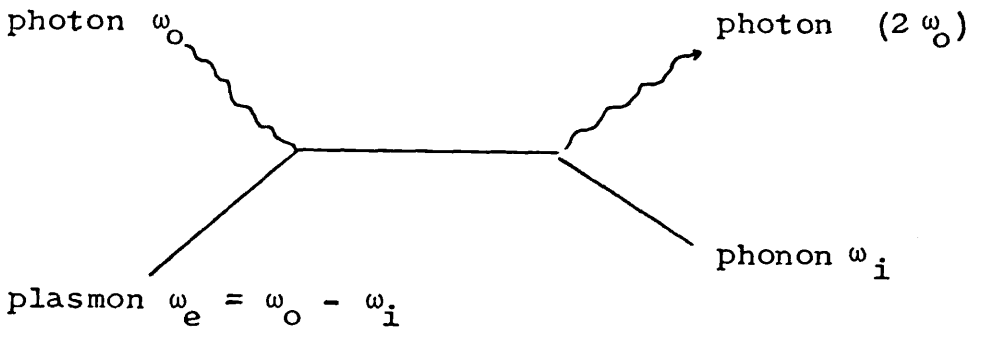

The backscattered photon must satisfy:-

$$\omega_o + \omega_e - \omega_i = 2\omega_o - 2\omega_i$$

It is seen that the second harmonic 2ω generated by this mechanism is displaced from the original $2\omega_o$ towards the red by $2\omega_i$.

Then

$$2\omega = 2\omega_o - 2\omega_i$$

Introducing the phonon allows the momentum conservation to be satisfied and there are more possibilities of plasmon interaction. However, the efficiency of a four wave process is lower compared with that of three wave process. Nguyen, Duc Long and Johnston (1975) determined the threshold growth rate.

2.6.3 Harmonic Generation at $\frac{3}{2}\omega_o$

The backscattered radiation at $\frac{3}{2}\omega_o$ of the incident laser frequency is generated at a region of quarter critical

density, where $\omega_o = 2\omega_{pe}$, by the coupling between the incidence or backscattered ω_o of the incident laser wave ω_o and plasmons at frequency $\frac{\omega}{2}$. There are two possibilities of parametric instabilities in this mechanism; the two plasmon instability near $\frac{n_c}{4}$ or stimulated Raman scattering.

If $(\omega_o, \bar{K}_o)$, $(\frac{\omega_o}{2}, \bar{K}_p)$ are the frequency and the wave number for the incident photon and plasmon respectively, these photon and plasmon can be coupled to give a photon $(\frac{3}{2}\omega, \bar{K})$. The interaction geometry is given by Jackson (1967). In the case of the two plasmon instability, it has been shown in section 2.5.2, with matching conditions

$$\bar{K}_o = \bar{K}_{p1} + \bar{K}_{p2}$$

$$\omega_L = 2\omega_e$$

The two plasmon coupling processes are generated by interactions to satisfy the following condition.

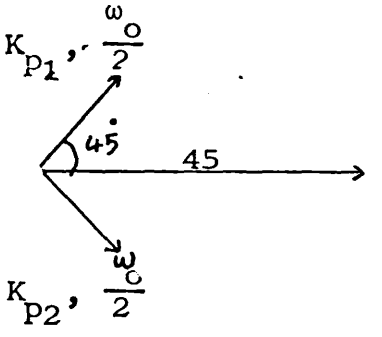

$$K_o = K_{p1} + K_{p2}$$

$$K_o^2 = 2K_p^2$$

For Raman backscattering:-

$$\omega_o = 2\omega_p = 2\omega_R$$

and $$K_R = 3K_e^2 V_o^2/C^2$$

$$\omega^2 = \omega_p^2 + K^2C^2$$

$$\omega_e^2 = \omega_p^2 + 3K_e^2V^2$$

leading to:-

$$\omega_o^2 = 4\omega_p^2 \frac{\left[1 - 2\,(V_e/C)\,\sqrt{3}\right]}{\left[1 - 2\,(V_e/C)\,\sqrt{3} - 9\,(V_e/C)^2\right]} \qquad (2.26)$$

This means that the corresponding density is slightly smaller than $\frac{n_{ce}}{4}$. This relationship holds whether or not there is coupling with either two plasmon resonance or up conversion. In the latter case the angle between the two K_o should have a value $\simeq 70^o$ to make $^{Ve}/_C$ small and, for the case of Raman up conversion it is

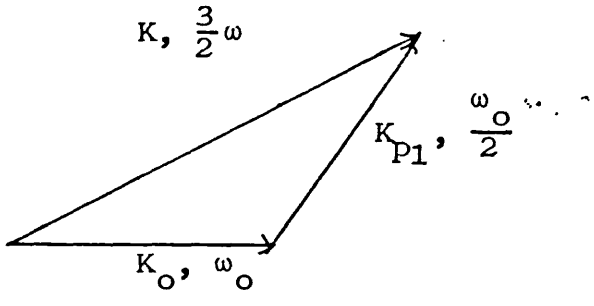

with $K^2 = K_p^2 + 2K_o$.

The dispersion relations for the waves are given as follows

$$(\tfrac{3}{2}\,\omega_o)^2 = \omega_p^2 + (K_p^2 + 2K_o^2)\,C^2$$

$$\omega_o^2 = \omega_p^2 + K_o^2\,C^2$$

$$(\tfrac{\omega_o}{2})^2 = \omega_p^2 = 3K^2\,V_e^2$$

where $$K_o^2 = \frac{\omega_o^2 - \omega_p^2}{C^2}$$

and $$K_p = \frac{\frac{\omega_o^2}{4} - \omega_p^2}{3\,V_e}$$

From these equations, we get

$$\omega_o^2 = 4\,\omega_p^2 \frac{c^2 + 3\,v_e^2}{c^2 - 3\,v_e^2} \qquad (2.27)$$

which means $\omega_o > 2\,\omega_p$ and the corresponding density is slightly smaller than the quarter critical density.

In fact, the two plasmons can be generated with geometry different from the previous, ie

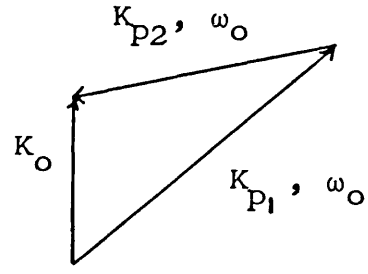

The incident photons produce a plasmon $(\omega_1, \bar{K}_{p1})$ in the forward direction and $(\omega_2, \bar{K}_{p2})$ in the backward direction to the incident. This necessitates $(K_{p1}) > (K_{p2})$ according to the dispersion relation between the waves $\omega_1 > \omega_2$. Moreover, the plasmon can interact either with the incident photon or with the backscattered photon to produce a scattered wave at $\frac{3}{2}\,\omega$ in variable directions.

2.7 CONCLUSION

It has been shown in this chapter some of the different linear and non-linear mechanisms which are responsible for absorbing the laser light. There are also some processes that may cause undesirable reflection of the incident laser irradiance. There are also, in this chapter, some of the main mechamisms which are responsible for the harmonic

generation. This kind of phenomena is very complicated and from a theoretical point of view not yet well known. Some of these harmonics have been known, Bobin et al (1973) and Yamanaka et al (1974), but it is difficult to determine the respective contribution of the different modes.

In Chapter 5, observations of some of these harmonics will be presented and their relation with the different parametric processes will be discussed in Chapter 6. This harmonic can give us some information about the plasma parameters, temperature and density.

CHAPTER 3

THE T.E.A. CO_2 LASER

3.1 INTRODUCTION

Since the first successful operation of a T.E.A. CO_2 laser was announced in 1969 (Dumanchin and Rocca Serra, 1969, Beaulieu, 1970), there has been a rapid and spectacular increase in the energies available from such a device from 30 mJ per pulse in the pin laser of Beaulieu (1970) to 2 KJ per pulse in the electron beam sustainer laser of Dougherty et al (1972) to the recent most powerful laser at Los Alamos of 10 KJ per pulse.

Table 3.1 illustrates the development of the CO_2 laser.

Theoretical predictions (Nuckolls/Los Alamos 1972) indicate that multi kilojoule pulses of a nanosecond or shorter duration are required to achieve laser-fusion. A short pulse length is required for sufficiently rapid heating of the thermonuclear fuel to fusion ignition temperature (10^8 K) before significant expansion and cooling take place.

Until a few years ago, it was generally assumed that the most powerful lasers would be solid state and the neodymium glass laser is currently regarded as the most convenient system for the possibility of laser-fusion because of the high-power short-duration pulse which can be focussed in a small area in that time.

TABLE 3.1

Year	Author	Discharge Type	Efficiency	Energy	Power
1968	Hill	Axial discharge		5J	
1969	Dumanchin et al	Transverse discharge		0.25 J/pulse	
1970	Beaulieu	Transverse discharge		1 J/pulse	
1970	Dumanchin et al	Transverse double discharge	3%	130 J	
1972	Dougherty et al	" " "	5%	2 K J	100 M W
1973	Martin et al	UV pre-ionized transverse discharge	4.5%	300 J	1 G W
1976	Bugoev et al	Fast electrons	33%	500 J/100 n sec	
1977	Datskevich et al	Non self-sustaining discharge		7.5 K J/ μ sec	
1978	Los Alamos	Electron beam		400 J/1 n sec or 10 K J/100 n sec 8 beam	

By 1970, lasers with gaseous media consisting of CO_2 or Iodine had attracted increasing interest in the USA, USSR, and Federal Republic of Germany. 3 μm wavelengths from a fluoride laser were achieved in 1975 at the Sandia Laboratories and Los Alamos Scientific Laboratories.

To achieve high pulse repetition rate necessitates rapid cooling of the active medium; something more easily achieved in a gas than a solid. Comparison of gas lasers with the Nd glass laser is made in table 3.2.

The most recent experimental results of the Los Alamos Scientific Laboratory have given rise to increased optimism about the suitability of the CO_2 laser for scientific demonstrations of fusion. These results indicate a much more efficient coupling of the laser radiation to the fuel pellet than had been anticipated. The CO_2 laser offers the advantage of a replaceable active medium which, in turn, permits a high repetition rate, a good optical quality beam and, at several atmospheric pressures, the capability of a relatively high efficiency in amplifying multi frequency short laser pulses.

3.2 ELEMENTARY THEORY OF THE CO_2 LASER

Infrared laser emission from CO_2 was first reported by Patel et al (1964) in a pulsed discharge through pure CO_2. By the time a more complete report of this work had been published (Patel, 1964), a much more efficient system, based on the transfer of vibrational energy from nitrogen to the carbon dioxide molecule, was made possible.

The vibrational energy levels of the CO_2 molecule

TABLE 3.2

HIGH POWER LASERS CONSIDERED FOR THERMONUCLEAR FUSION

	Nd-glass	CO_2	HF	I
Output energy	200-300Jin 1 nsec	400 J in 1 nsec	4.5 KJ in 20 nsec	300 J in 1 nsec
Wavelength	1.06 μ_m	10.6 μ_m	2.6 to 3.3 μ_m	1.315 μ_m
Bandwidth	1.2×10^{11} Hz	3×10^{9} Hz	2×10^{10} Hz	2×10^{10} Hz
Pulse Length:				
Theoretical	10 psec	300 psec	50 psec	50 psec
Experimental	16 psec	400 psec	1000 psec	300 psec
Intensity Damage Power for 1 nsec pulse:				
Theoretical	10^{12} Wcm^{-2}	10^{11} Wcm^{-2}	10^{12} Wcm^{-2}	10^{12} Wcm^{-2}
Experimental	2×10^{10} Wcm^{-2}			
Self Focussing Energy	1-2 Jcm^{-2}	10^{2} Jcm^{-2}	10^{2} Jcm^{-2}	10 Jcm^{-2}
Efficiency (%)	5×10^{-4}	2×10^{-2}	2	5×10^{-3}
Reference	Simmons et al (1975)	Los Alamos	Sandia Laboratory	Brederlow et al (1975)

relevant to laser action are represented in Figure 3.1. The CO_2 molecule has three vibrational modes, each giving rise to a series of energy levels: these are the symmetric stretch mode (frequency $\nu_1 = 1388.2\ cm^{-1}$), where the two oxygen atoms move in opposite directions while the carbon atom is stationary, the bending mode with frequency $\nu_2 = 667.4\ cm^{-1}$, where the oxygen atoms vibrate perpendicular to the molecular axis, and the asymmetric stretching mode (frequency $\nu_3 = 2349.2\ cm^{-1}$) where the oxygen atoms move together while the carbon atom moves in the opposite direction.

Each vibrational level has a set of rotational energy levels associated with it which, for clarity, are only shown on the upper and lower laser levels.

Any arbitrary vibrational state of the molecule can be described by the number of excited quanta in each normal mode using the notation $(n_1\ n_2^L\ n_3)$ where n_1, n_2, n_3 are the asymmetric stretching modes respectively.

The superscript L and the quantum number of the degenerate vibration takes the value $L = n_2, n_2 - 2 \ldots 1, 0$ where each L gives rise to a sublevel, when $n_2 = 1$, $L = 1$, when $n_2 = 2$, $L = 2, 0$ and the two sublevels resulting from these states would be written (01^10) and (02^20), (02^00) respectively.

In the CO_2 molecule, the vibrational levels 10^00 and 02^00 which consist of the sublevels (02^00), (02^10) have nearly the same energy resulting in perturbation of both these levels,

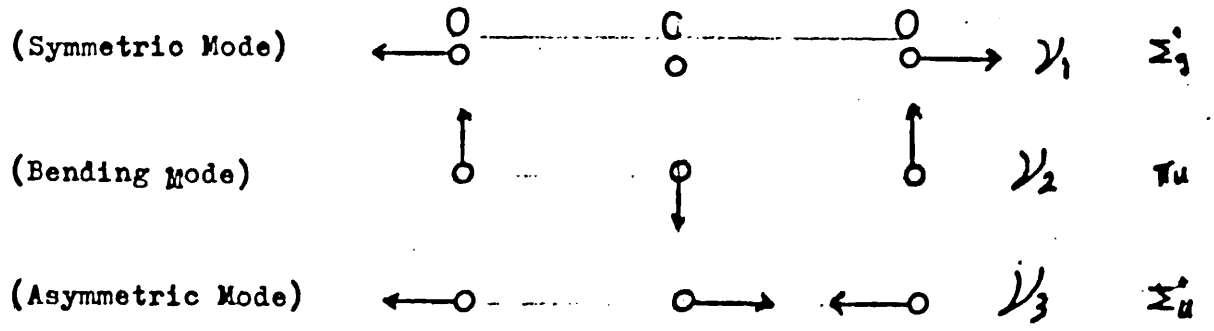

Normal Mode of Vibrations of The Co_2 Molecule

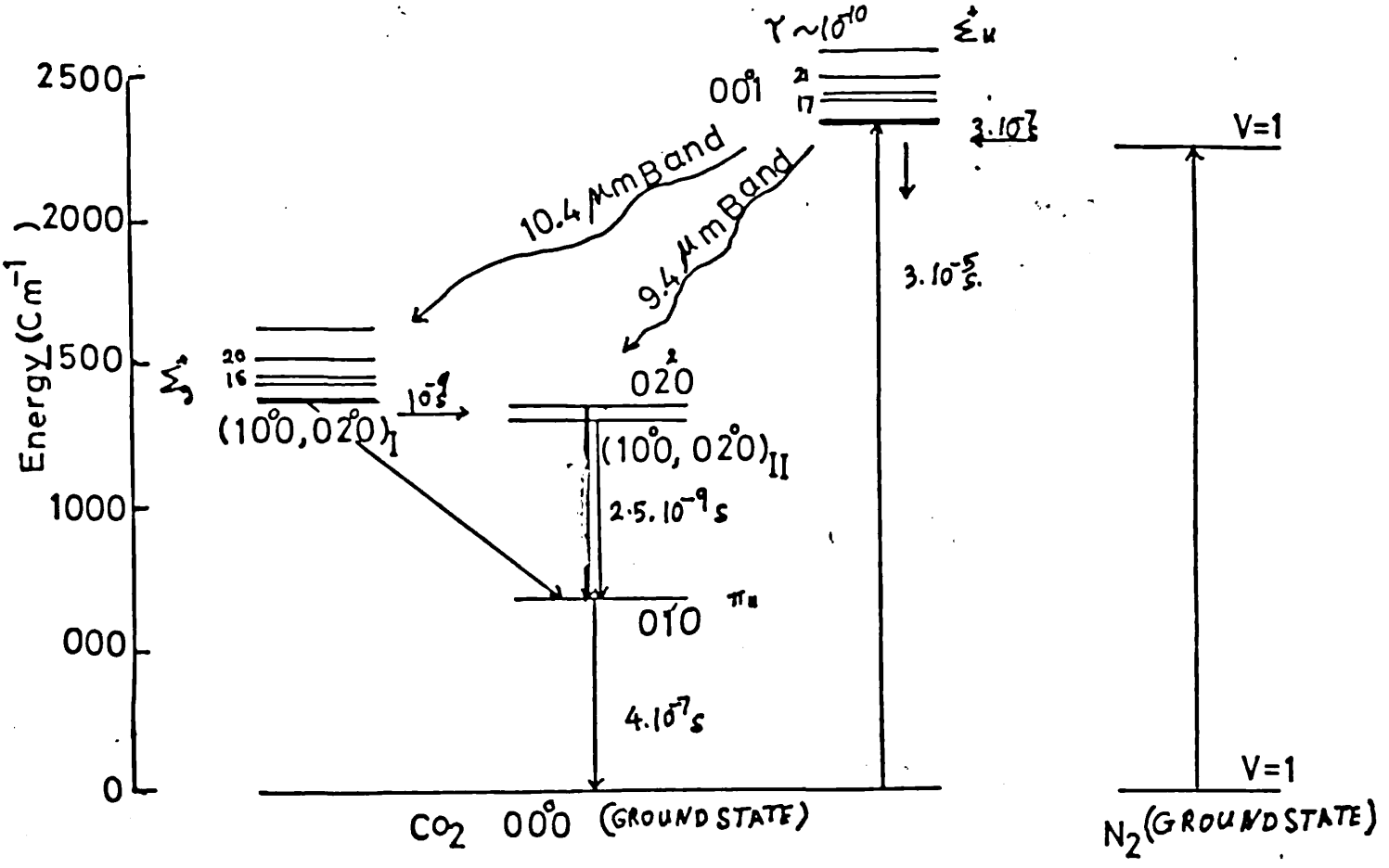

Figure 3.1

Energy Level Diagram of The vibrational and Rotational relevant to IO μm Co_2 Laser Emission.

as first discussed by Fermi (1931), and hence called "Fermi resonance". Perturbations of this type occur only between levels with the same L (Dawson, 1964) and, as a result, the two levels $10^{0}0$ and $02^{0}0$ repel each other and appear in positions different from those expected.

A series of rotational levels are superimposed on each of these vibrational states. The quantum number of these levels is given the label J. Transitions occur between pairs of rotation-vibration levels, according to the selection rules (Willett, 1974).

$\Delta L = 0$	n_2	:	even	n_3	odd	$J = \pm 1$
$\Delta L = 1$	n_2	:	odd	n_3	even	$J = 0, \pm 1$

where L denotes the vibrational angular momentum of the molecule, J is the rotational quantum number of the laser lower level, these rules giving rise to many possible transitions corresponding to radiation of 9 to 11 micrometres wavelength.

The lowest vibrational energy level of nitrogen (N_2) is also shown in the diagram. This level is metastable and within 18 cm^{-1} of the CO_2 ($00^{0}1$) level, permitting a nearly resonant de-excitation to occur by collision with the ground state of the CO_2 molecule (Sobelev and Sokovikov, 1967, and Sharma and Brau, 1969). This excites the CO_2 molecule to the upper laser level. Hence, nitrogen can provide a vibrational energy store in the discharge.

The quantum efficiency of laser action is 40% for the

10.6 μm transition and slightly higher at 45% for the 9.6 μm transition.

3.3 EXCITATION PROCESSES

Pulsed CO_2 lasers are usually electrically excited, so electronic collisions are responsible for populating the CO_2 $(00^0 1)$ level. Population may occur directly from the ground state through inelastic collisions with the low energy electrons, or indirectly through resonant energy transfer from the first vibrationally excited level of the N_2 molecule (V = 1). When N_2 is excited in a discharge or by some other means the populations will tend to build up in excited vibrational levels of the ground state of N_2. The first excited vibrational level of this state V = 1 lies at an energy nearly coincident with that of the CO_2 $(00^0 1)$ level. Thus, energy can be transferred between N_2 (V = 1) and CO_2 $(00^0 1)$ with high efficiency when N_2 collides with CO_2.

The probability of excitation of the $(00^0 1)$ level was found by Boness and Schulz (1968) to be substantially greater than that of $(10^0 0)$ and $(02^0 0)$. Andrick et al (1969) however have shown that (010) is also strongly excited when the cross-section for excitation of the $00^0 1$ and 010 levels is 1.5×10^{-16} cm^2 and 3×10^{-16} cm^2 respectively.

The cross-section for excitation of N_2 into the (V = 1) metastable level can be very high and this leads to efficient pumping of the device. Excitation cross-sections have been studied experimentally by Schulz (1964) and Boness and Schulz (1968). For electron energies $\simeq$ 2 eV the cross-

section for the (V = 1) level is 1.5×10^{-16} cm^2 and for energies of 2.3 eV the total cross-section attains a maximum value of 3×10^{-16} cm^2.

The kinetics of the process have been extensively studied by Nighan (1970). The relative populations of the various vibrational levels of N_2 and CO_2 in a discharge are influenced by the ratio E/N of the electric field E to the total density of the neutral molecules N . For the optimum laser pumping of CO_2 - N_e - H_e mixtures E/N should be about 2.10^{-16} V/cm^2. This value is equivalent to an electron temperature of 0.8 eV, which is low compared to values occurring in self sustained glow discharges. It is therefore evident that CO_2 laser systems in which the ratio E/N can be adjusted for maximum excitation CO_2 $(00^0 1)$ - N_2 (V = 1) levels are potentially more efficient.

3.3.1 Effect of Helium

The presence of helium in the discharge with the gas mixture

(i) improves the stability of the discharge,

(ii) reduces the burning voltage of the glow discharge to a low level suitable for efficient excitation of the N_2 - CO_2 grouped upper level,

(iii) is effective in de-populating the (01^10) level by collisions and may also lower the gas kinetic temperature.

All of these effects are beneficial to higher-power laser operation, since radiative relaxation rates are orders

of magnitude smaller than those due to collisions with helium atoms and other gaseous components.

3.4 THE DOUBLE DISCHARGE T.E.A. CO_2 LASER

Many different laser configurations have been described in the literature (Dulèy , 1976, or Nighan), but one of the most energetic is the double discharge transverse electrode atmospheric pressure (TEA) laser which will be described here.

Although a glow discharge can be operated at low pressure, the same circuit and electrodes operated at atmospheric pressure produce a constricted arc which is unstable. To achieve a uniform glow discharge in any gas between the laser electrode the discharge time must be shorter than the arc formation time, i.e. the rise time of the mean discharge pulse should be about 2 μsec, which is the time necessary for corona discharge to build up between the electrodes. Also the fall time of the main discharge pulse must be short so that arc formation cannot take place. The high voltage is reduced below the breakdown voltage shortly after the peak of the main current pulse (Pan, Y-L et al, 1972). Alternatively, glow discharge may be produced by limiting the discharge current density. Dyer et al (1975) found experimentally that the arc depends strongly on the circuit parameters through $R_L = E_d/I_p$, where R is the resistive load provided by the discharge peak current, E is the steady state operating field, d is the electrode

separation and I_p is the peak discharge current.

Techniques for producing a glow discharge are:-

(a) Using a current pulse shorter than the arc formation time Johns and Nation, (1972).

(b) Distribution of the current by means of an array of ballast impedances Beaulieu, 1970 and Laflamme, 1970).

(c) Pre-ionization of the gaseous medium by creating a corona discharge by means of:-

(i) bigger electrodes Pan, Y-L et al, (1972), Dyer et al, (1972), or

(ii) a pulse of ultraviolet radiation Seguin and Tulip, (1972), Richardson et al, (1973).

(d) Sustaining the discharge by means of an external source of ionization such as an electron beam Fenstermacher et al, (1972).

3.4.1 The laser used in this study

The laser used in this work, shown in plate 3.1_a and 3.1_b consisted of a self sustaining double discharge in which a uniform ionization layer was created near the cathode before the onset of the main discharge. The design is similar to that built by Culham, U.K.A.E.A. Stamatakis, 1977) and follows that described by Dumanchin et al, 1972 and Pan et al, (1972).

The laser was in existence when the author commenced this study, but it required modification to improve its

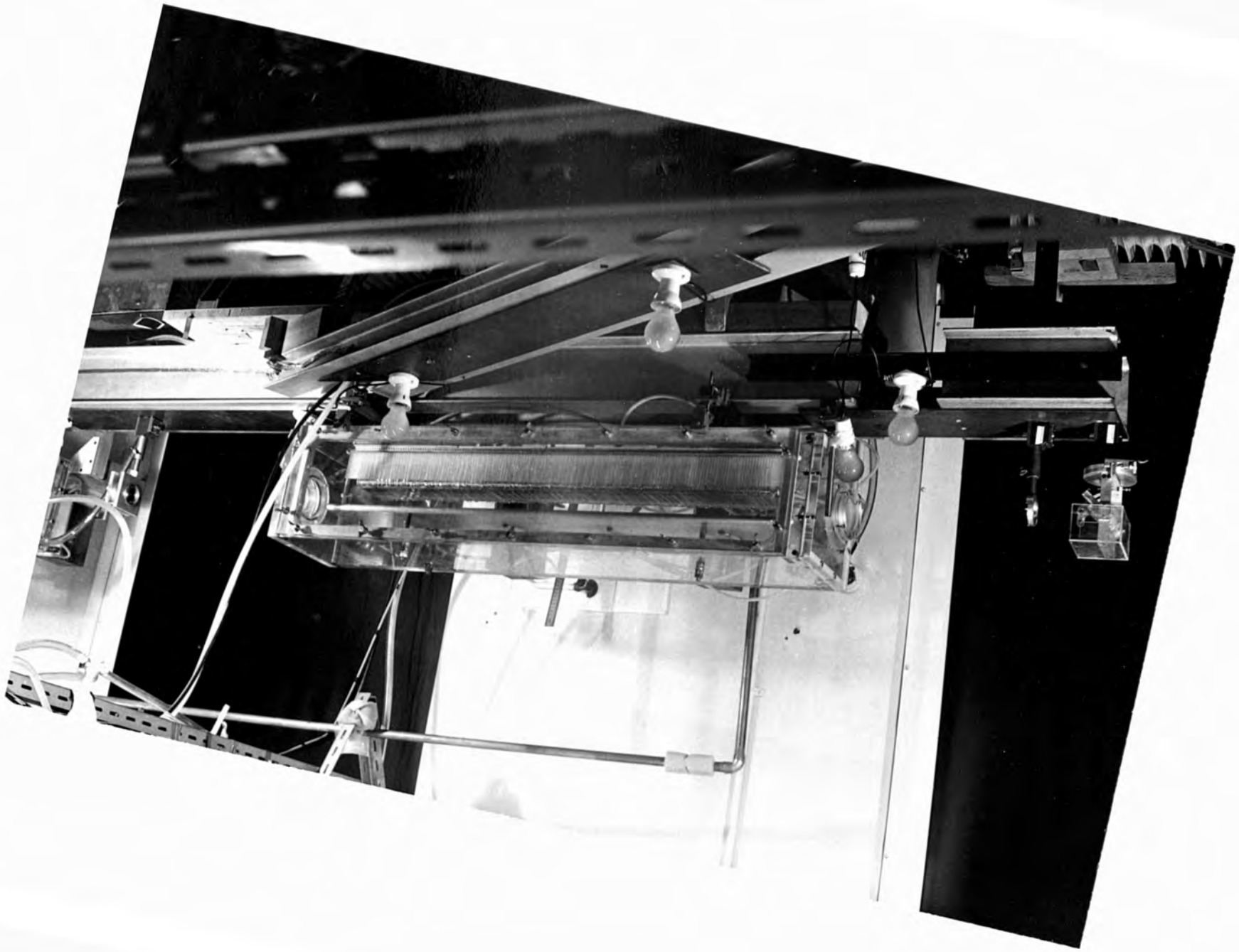

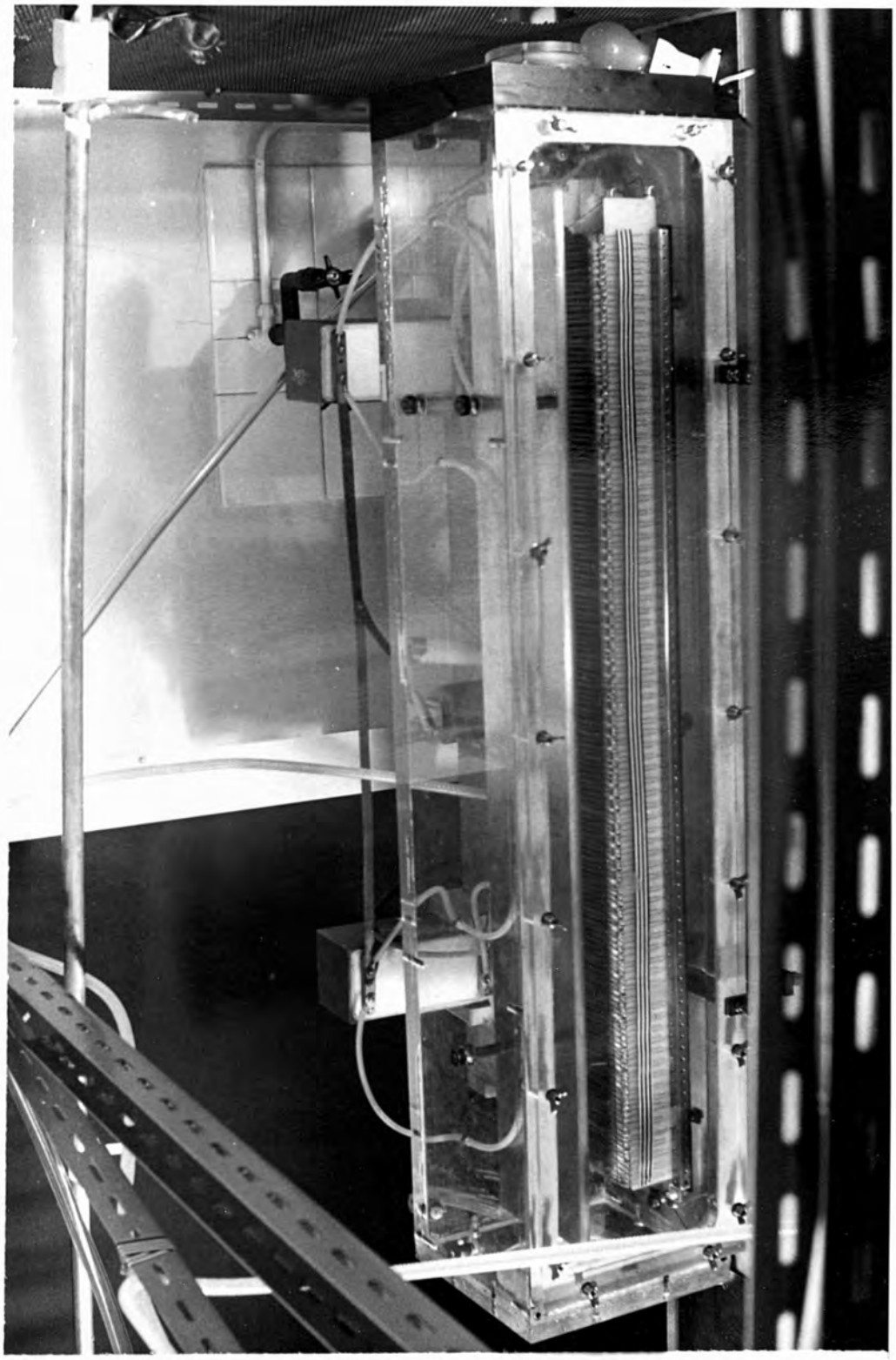

efficiency and reliability. These modifications will be discussed in the following section.

3.5 CONSTRUCTION OF THE LASER

3.5.1 The main electrodes

The laser system, as shown in Figure 3.2, consists of an oscillator and an amplifier, both built to the same design. The module, Figure 3.3a, of the laser assembly consisted of an aluminium cathode 100 cm long and 7 cm wide with a parallel anode 110 cm by 15 cm and 1.5 cm thick. The separation of the electrodes was 5 cm.

Into the cathode, 155 trigger electrodes were inserted between parallel blocks 6 mm deep, as in Figure 3.3b. The trigger electrodes shown in Figure 3.3c consist of 0.4 mm diameter nichrome wire threaded into capillary glass tubes of 4.4 mm overall diameter, 16 cm long and sealed at one end. The wires emerging from the other ends were fastened into a brass bar 2 cm x 2 cm x 100 cm long, as can be seen in plate 3.1. The bar, in turn, was connected to 1500 pf coupling capacitor C_3, as shown in Figure 3.6. The glass tubes were slightly longer than the 15 cm width of the cathode. The vertical part of the capillary was 7 ± 0.5 cm long to insulate the wire from the cathode. All the glass tubes were supported and clamped near the sealed end and also near the 90 degree bend, so that the wires in the glass tubes were at the same level at the top edge of the aluminium cathode strips. It was found that a deviation of

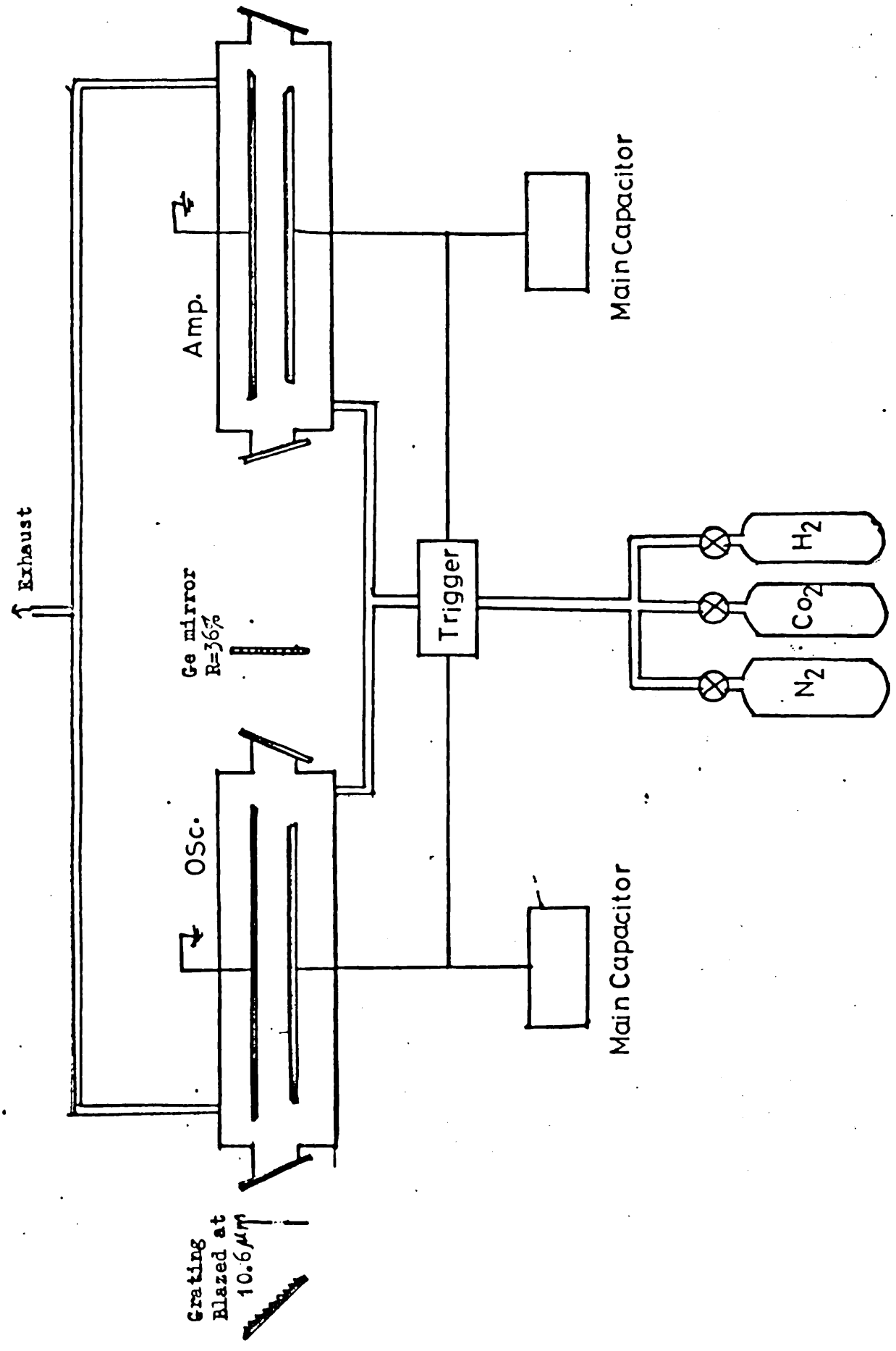

Figure 3.2
The TEA Laser

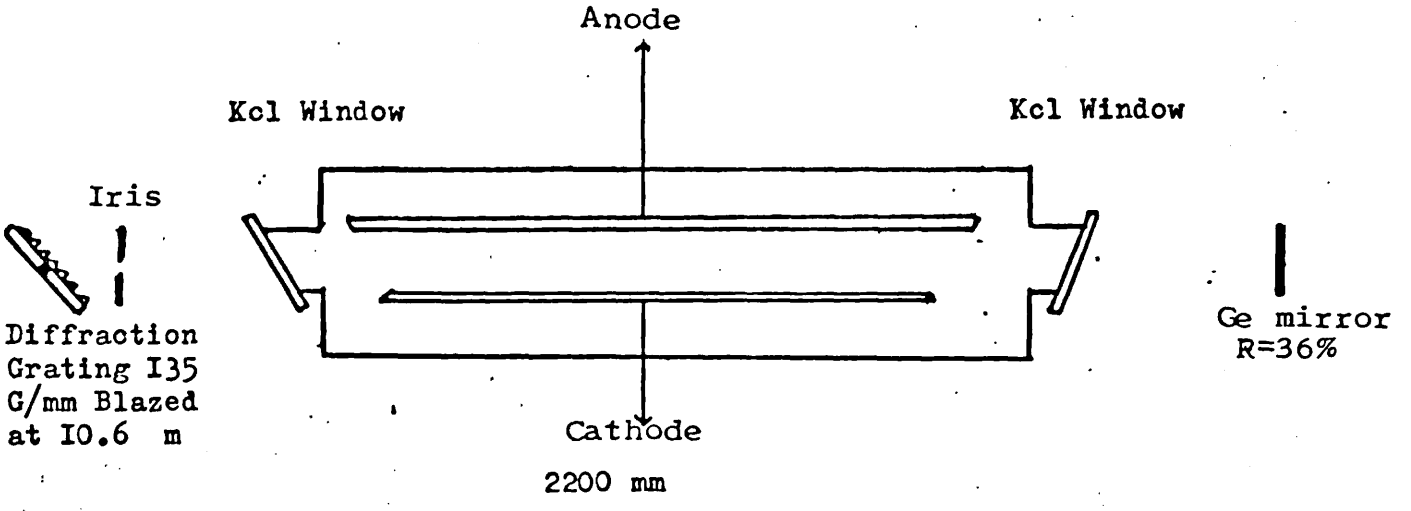

a) Laser Oscillator Cavity

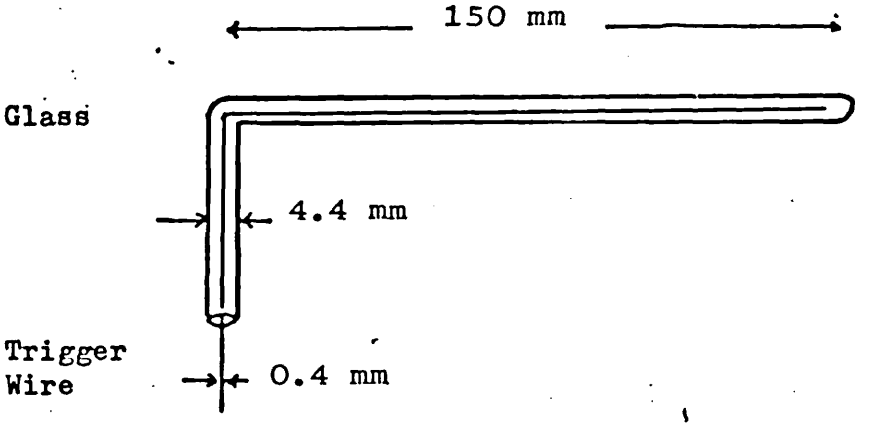

b) Trigger Electrodes

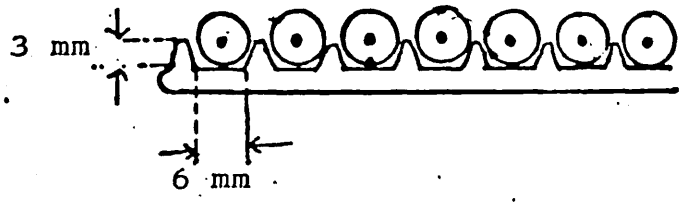

C) Trigger Electrodes In Cathode

Figure 3.3
Laser Assembly

more than 0.5 mm from this level caused arcing.

All the edges on both the cathode and anode were rounded to prevent large field gradients.

In the original design, the trigger wires were parallel to cathode length, but the laser suffered a number of faults:-

1. The capillary glass tubes broke easily, especially near the end where the trigger wire was connected to the anode. This rupture may have been caused by the inhomogeneity of the electric field distribution between the electrodes, which in turn was due to the non-uniformity of the electron density created by the trigger wire.
2. Frequent arcing occurred, possibly due to reasons mentioned above.
3. The laser output beam suffered inhomogeneity.

The operation of the laser became more reliable when the longitudinal trigger wires were replaced by transverse ones.

3.6 THE DISCHARGE CIRCUIT AND PREIONIZATION

Efficient operation of TEA CO_2 lasers requires the production of high energy density volume gas discharges in CO_2:N_2:H_2 gas mixtures. The maximum discharge density that can be achieved is, however, limited by the onset of arcing in the interelectrode volume.

To delay the arc formation the electrodes must be as

uniform as possible, parallel and well polished.

To make the discharge time short, compared to arc formation time, it is necessary to have a very low inductance electrical circuits and fast switching clean electrode surfaces.

Figure 3.4 shows, in block diagram form the discharge circuit of the laser. The energy storage low inductance capacitor C_1 and C_4 was charged to a maximum voltage of 60 kV by means of the dc power dupply. The laser was triggered with the series spark gap shown in Figure 3.5.

A pulse shaping network is shown in Figure 3.6 and consisted of an inductor $L_1 = 9\ \mu H$ and a capacitor $C_2 = 0.1\ \mu f$. When the spark gap was triggered, the electrical energy stored in the capacitor C_1 was fed into the pulse-shaping network, providing a voltage pulse across the laser electrodes. The value of this pulse is given by Dyer and James (1975) and Bushnellet al (1976) as

$$V = \frac{- V_o C_1}{C_1 + C_2} (1 - \cos \omega t)$$

$$\omega = \left(\frac{C_1 + C_2}{L_1 C_1 C_2} \right)^{\frac{1}{2}}$$

where V_o is the initial voltage of C_1.
For the components value quoted, the voltage V attains its peak value at

$$V_{peak} = 1.15\ V_o$$

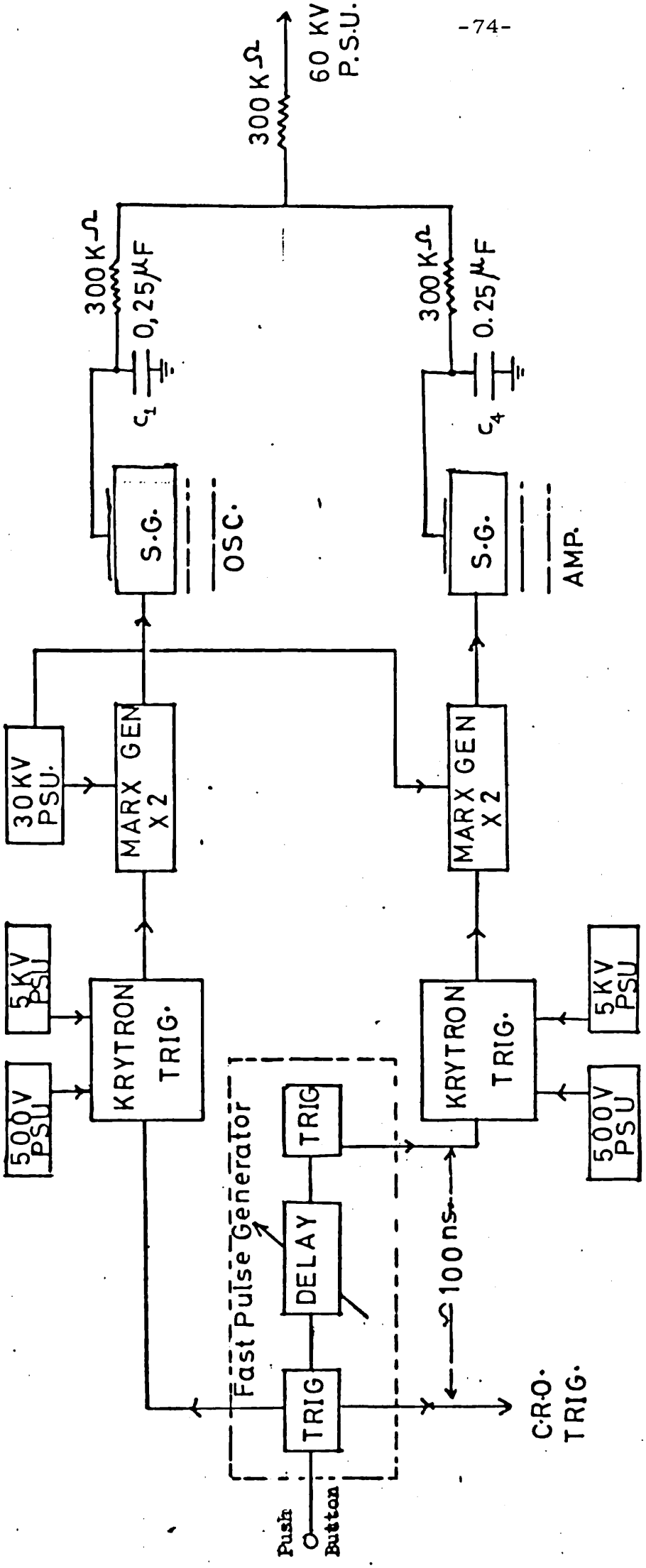

Figure 3.4.

A block diagram of the discharge circuit of the laser.

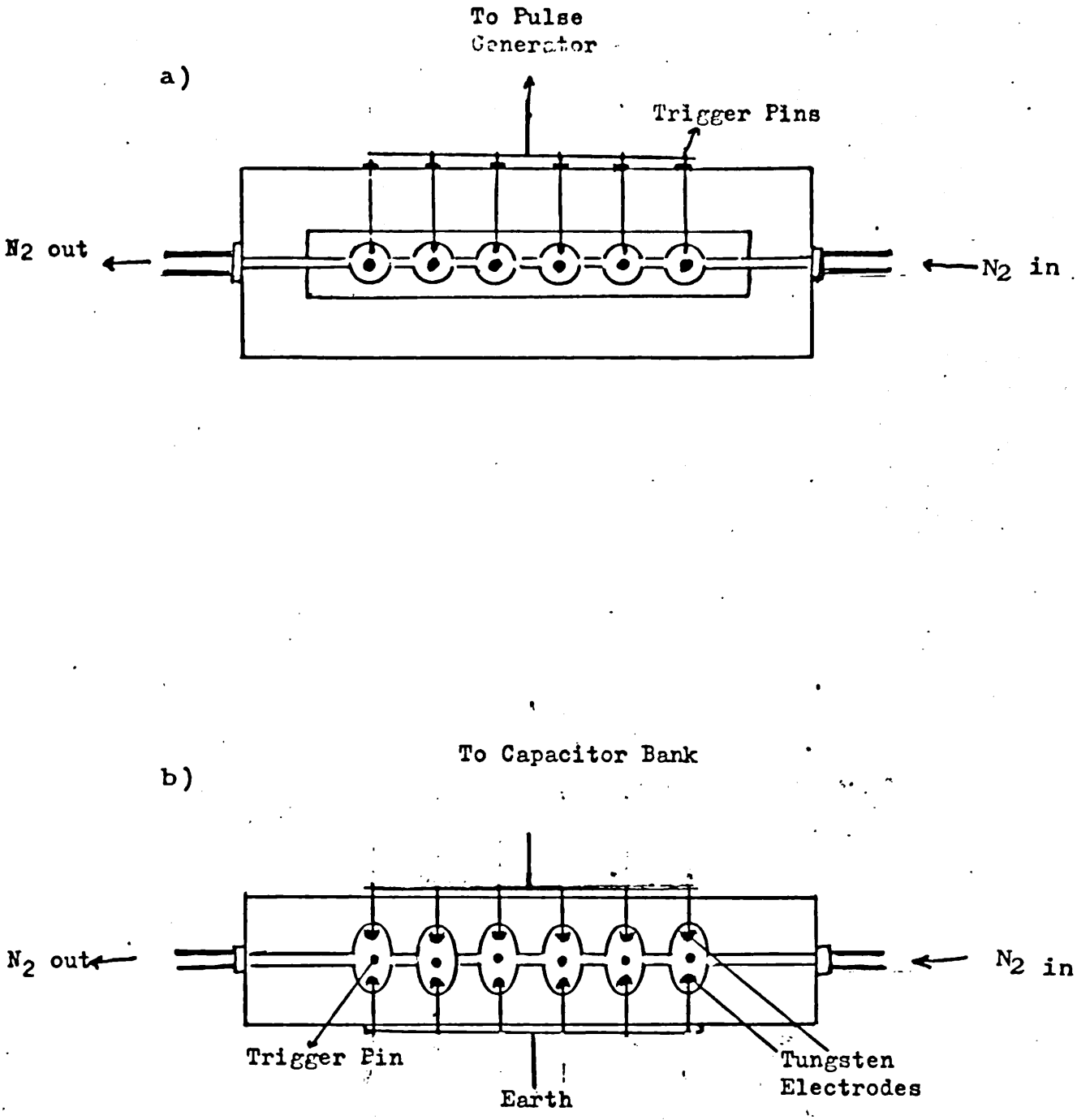

Figure 3.5.

Spark Gap Assembly

a) Side view,

b) Top view.

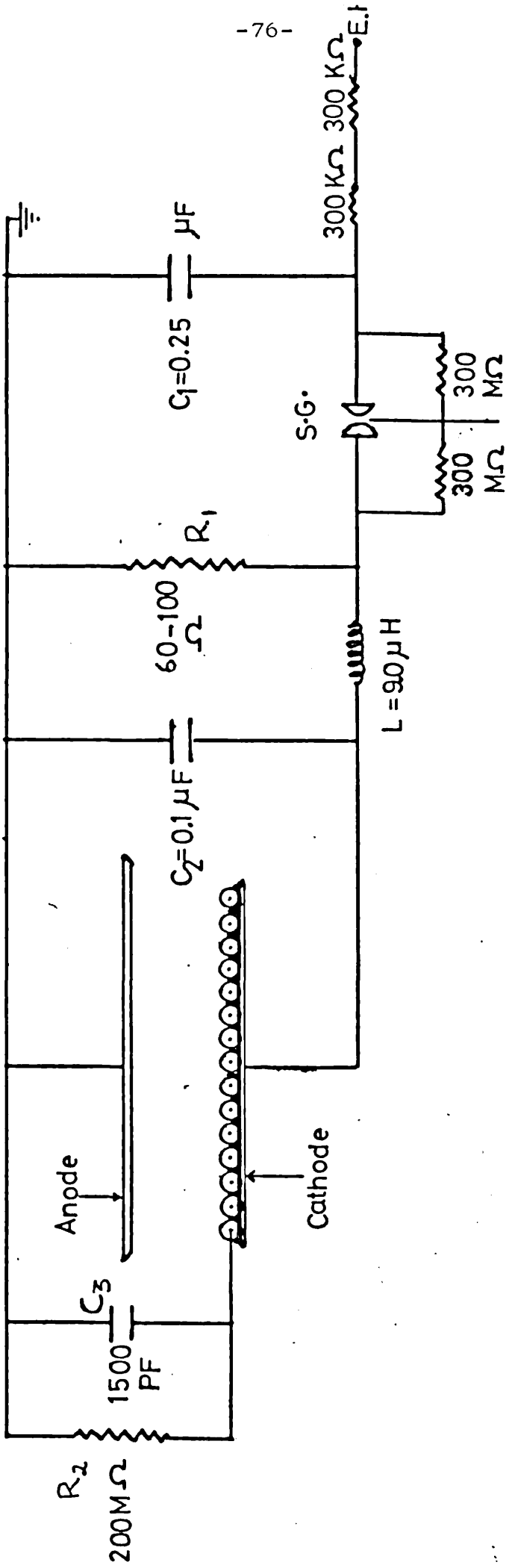

Figure 3.6

Schematic diagram of the double discharge laser and electrical circut.

at a time

$$t = \pi \left(\frac{L_1 \, C_1 \, C_2}{C_1 + C_2} \right)^{\frac{1}{2}} \simeq 2.5 \ \mu s$$

after closing the spark gap.

This delay in establishing the peak voltage across the laser cavity has been adjusted to match the time required to establish the corona discharge between the trigger electrodes and the cathode. This is responsible for creating the necessary pre-ionization for the initiation of the glow discharge between the anode and the cathode.

The earth reference resistance R_1 in Figure 3.6 has a value of between 60 - 100 ohm, so that the time constant R_1C_1 should be greater than the pulse duration time. The resistance R_1 controls the decay of the voltage waveform, but also causes an ohmic loss. It is noticed experimentally that the resistance R_1 plays a major part in the arcing problem. When R_1 is too high an arc occurs, but if it is too low the laser energy dropped as a result of reducing the input electrical energy. The optimum performance was found when R_1 was between 70 and 80 ohm.

The duration of the pre-ionizing discharge is controlled by the capacitor C_3 and the resistance R_2 which controls the duration of the corona discharge. The value of C_3 is nearly three times the capacity between the grooved cathode plate and the trigger wires in their glass tubes, as has been measured by Pan et al (1972) in a similar arrangement. They found that an average current of 13 Amp at 30 kV was required to charge the capacitors in 1.3 μs, and an average

current of 37 Amp at 60 kV to charge the capacitors in 1 μ sec.

Figure 3.7 shows a typical current pulse on the main discharge. It is displayed on a Tektronix oscilloscope 7904, using a current probe Tektronix CT-5 on the anode to earth leads. Glow discharges at atmospheric pressure were obtained repeatedly for the gas mixture CO_2:N_2:H_e 1:1:6 and electrical input energies of up to 450 Joules.

3.7 CONTROL CIRCUIT DESCRIPTION

There are three main units shown in Figure 3.4:

3.7.1 The EHT Generator

The EHT generator consists of a 5 KVA transformer delivering current of 10 mA and through high voltage silicon diodes up to 60 KV. This power supply charged the capacitor bank C_1 (= 0.25 μf) through current limiting resistor R = 300 KΩ. This resistor also protects the rectifiers when the spark gap becomes short circuited.

3.7.2 The Spark Gap

The spark gap shown in Figure 3.5 is pressurized with nitrogen at 3.5 to 4 Kg/cm^2. It is triggered by a 60 KV pulse derived from the Marx generator.

3.7.3 Fast Pulse Generator

This unit initiates the laser pulse after the push-button is depressed.

A trigger pulse is generated which, in turn, triggers the Krytron and, simultaneously, the oscilloscope.

There is a delay of about 100 n sec between triggering the oscillator and the amplifier circuits.

3.8 THE LASER GAS SUPPLY

The gas enclosure has dimensions 1250 mm x 28 mm x 250 mm and consists of 20 mm thick perspex sheet. The three gases - helium, carbon-dioxide and nitrogen - were contained in high pressure cylinders, each connected to its respective gas flow meter (Rotameter) which had been calibrated for the specific gas. The gas supply system is shown in Figure 3.2. To mix the gases before they enter the laser, the outputs of the three flow meters were connected to a manifold and the mixed gas runs through a plastic hose to the laser. The connections to the oscillator and the amplifier were in parallel. Originally, the flow to the amplifier was in series with the oscillator, but the time taken for running the gas before firing the laser was twice as long as with the series arrangement. This parallel connection was also found to give a more uniform glow discharge.

3.9 THE LASER OPTICAL CAVITY

Single mode operation of the laser is required to resolve fine spectral structure in the light scattered

from the plasma. The divergence of the beam should be as low as possible for the smallest focal area on the target.

The optical cavity was designed to meet these experimental requirements. The cavity of the laser is shown in Figure 3.3. The oscillator container had two 7.5 cm diameter KCl windows (Damage threshold 17 J/cm^2) set up at the Brewster angle to the optical axis. The resonant cavity consists of a plane grating and a plane mirror. The grating is a frequency selective element operated as the rear reflector. The output wavelength of the CO_2 laser can be tuned from 9.4 to 10.6 μm by turning the Littrow mounted diffraction grating about an axis parallel to the grooves. The incident angle is related to the wavelength by the usual law

$$n \lambda = 2 d \sin \theta$$

The mirror mount angle θ for the grating is 45^o 40' to the optical axis.

The grating was 50 mm x 25 mm standard plane master ruling grating (P.T.R.), with 135 grooves/mm ruled parallel to the 25 mm side. It was blazed at 10.6 μm, had 98% reflectivity and damage threshold $>$ 10 $Joule/cm^2$. The plane mirror at the exit of the oscillator was a coated 50 mm diameter 36% reflectivity Germanium plate.

3.10 DIAGNOSTICS OF THE LASER

To assist with interpretation of the experimental results measurements of the irradiance, power, p, and energy, W, of the laser pulse are required. Also the wavelength and line width must be determined. The irradiance I_o is given by

$$I_o = \frac{p}{r^2}$$

where r is the radius of the focal spot and p is the peak power of the laser pulse which can be obtained from the energy, W_o

$$p = \frac{W_o}{T}$$

T is the full duration of its half peak maximum (FWHM), a value which neglects the energy in the tail of the laser pulse.

Measurements of these quantities were carried out in separate experiments using the techniques described in the following sections.

3.10.1 Electrical Characteristics

Figure 3.7 shows a typical current pulse on the main discharge. It is displayed on a 7904 Tektronix oscilloscope using a Tektronix current probe model CT-5 (1000 Amp peak AC 20 Hz to 1.2 k Hz) using the 1000:1 ratio on the anode to earth leads, and 10 m Amp:1 mV ratio to the oscilloscope which gives 1 k Amp at one lead to the anode.

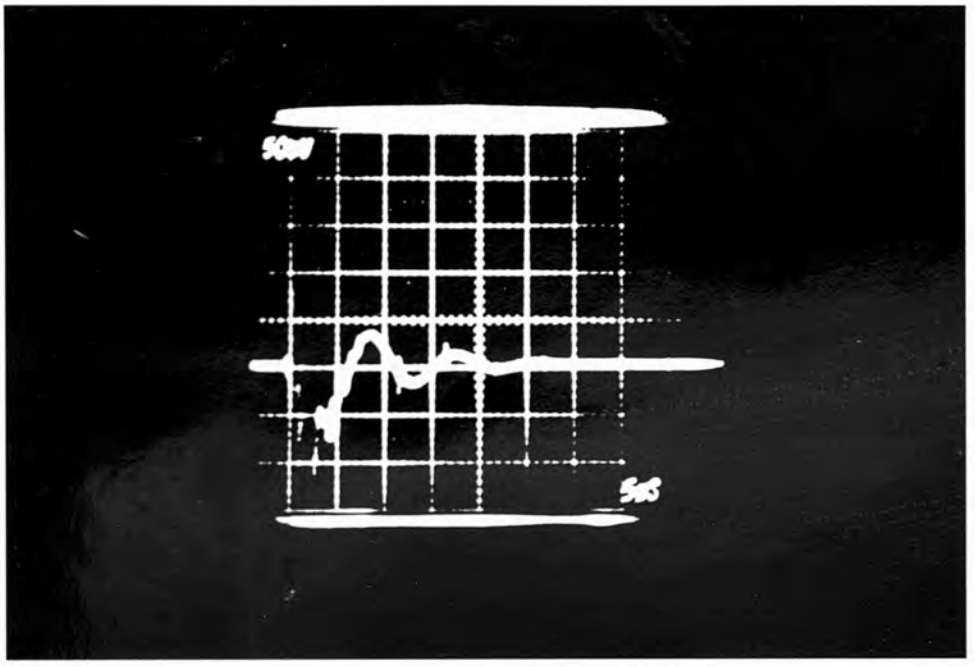

50 mv 5 μsec.

Figure 3.7.

Current Pulse on The Main Discharge

3.10.2. The Radiation Pulse

The radiation pulse was characterized by its energy, power and duration. The energy was measured with the aid of a Gen Tec calorimeter model ED500; its characteristics being shown in Table 3.3. The current from the calorimeter was displayed on an oscilloscope. If the energy were greater than 10 J Mylar filters were used to reduce the power before the damage threshold.

The pulse shape was recorded and the peak power was measured using calibrated photon drag detectors (Rofin model 7411 and 7415) with response time less than 1 n sec. The radiation pulse shape is shown in Figure 3.8 when the gas mixture consisted of $N_2:CO_2:He$ in the ratios 1:1:6. The radiation consists of a 40 n sec (FMHW) main pulse followed by one μsec low power tail. It was found that the pulse peak occurred 2 μsec after the laser trigger pulse and 400 n sec after the peak of the discharge current. The power of the long tail increases with the flow of the nitrogen as shown in Figure 3.9 and also it disappears if the electric energy is below 150 Joules, Since the excited nitrogen is no longer able to transfer energy to the CO_2 (001) level at sufficient rate to maintain the same level of population inversion.

In normal operation the maximum energy achieved with a gas mixture of $CO_2:N_2:H_2$ - 1:1:6 - is about 30 Joule with half the energy being in the main pulse. These energies could be maintained at a firing rate of two shots per minute.

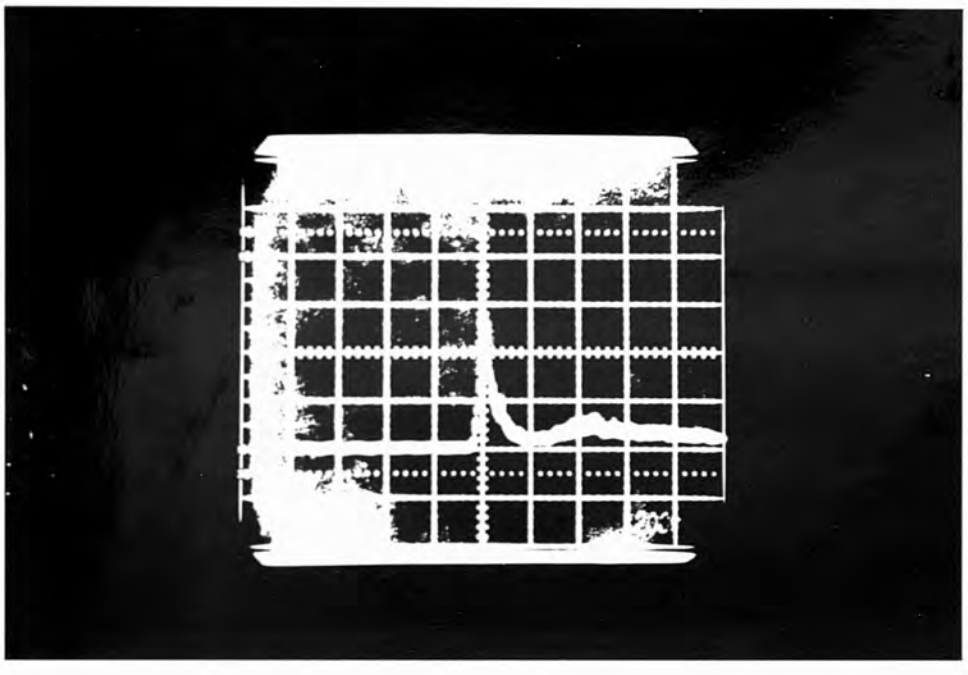

200 nsec.

Figure 3.8.

Laser Pulse With Gas Composition

N_2 : Co_2 : He ; 1 : 1 : 6 .

a)

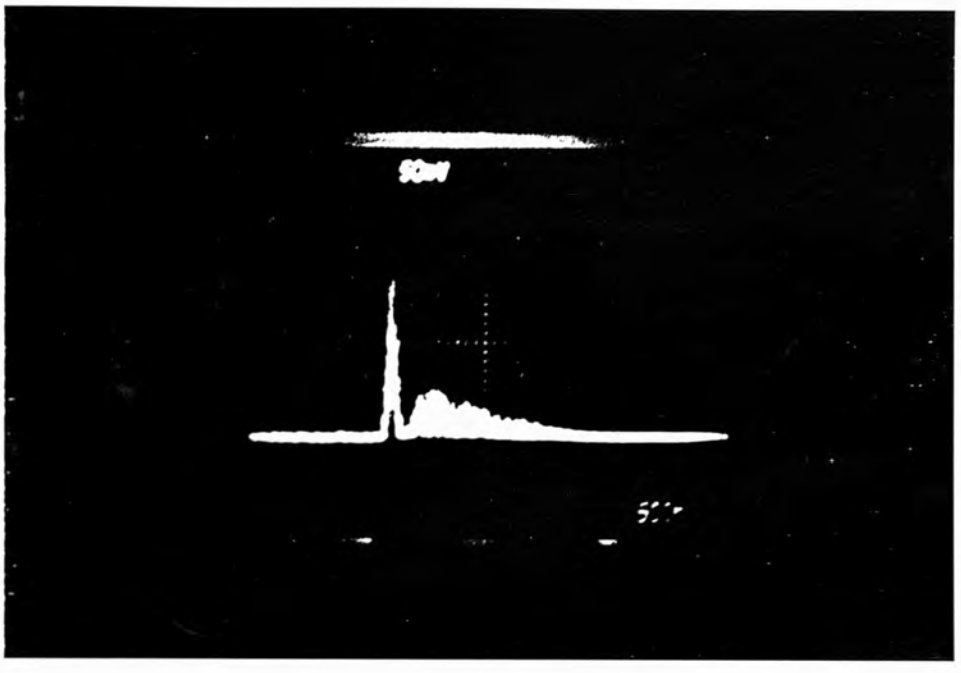

500 n sec.

b)

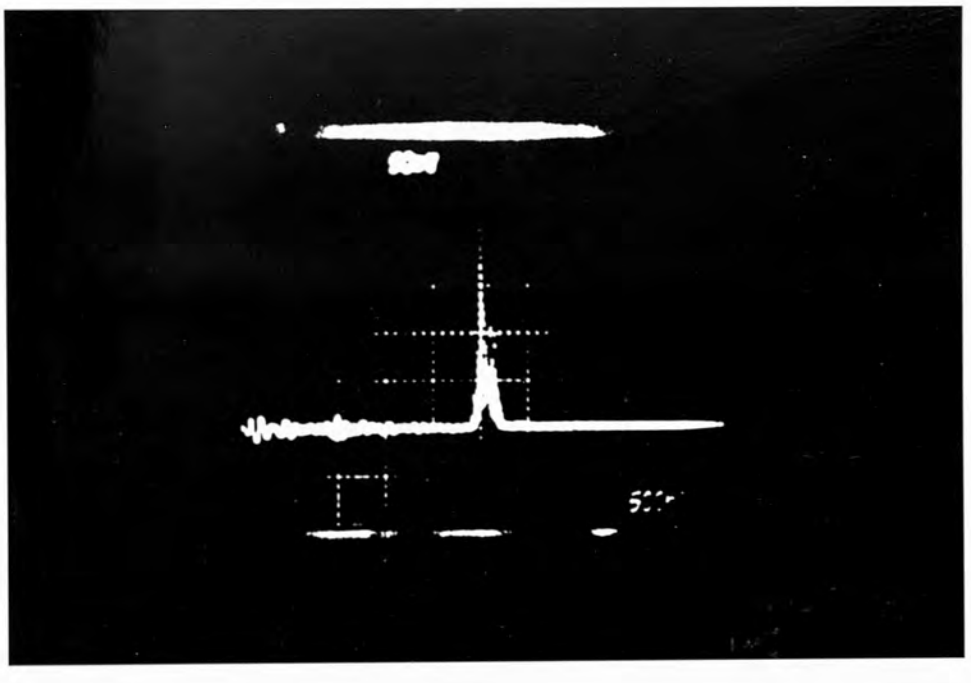

500 n sec.

Figure 3.9.

Laser Pulse

a) N_2 : Co_2 : He; 2: 1 :6

b) With Low Electric Input Energy.

TABLE 3.3

Detector	Detector Size	Response time	Responsivity at 10.6 m	Output Impedance	Maximum power or energy	Linear range	Operating temperature	Wavelength range
Photon drag detector Rofin 7411	4 x 4 mm	<1 n sec	0.19 V/MW into 50 Ω	50 Ω	8 MW	2.4 MW	Room temp	9 to 15 μm
Photon drag detector Rofin 7415	8 mm diameter	1 n sec	0.16 V/MW	50 Ω	25 MW	23 MW	Room temp	9 to 15 μm
Gold-doped Germanium detector	2 mm diameter	20 - 30 n sec	1.0 V/KW	50 Ω	100 W	100 W	77°	0.5 to 10.6 μm
Joulemeter GenTec ED-500	48 x 48 mm	10 milli seconds	1.7 V/Joule	1 mΩ	10 W or 12 Joule		Room temp	0.3 to 30 μm
Golay detector	6 mm	0.3 sec	2×10^5 V/W	3.5 kΩ	$1\ 10^{-4}$ W		Room temp	5 to 25 μm

3.10.3 The area of the focal spot

The intensity on the focal spot depends on the angular divergence Ø of the laser beam and on the focal length F of the lens, shown in Figure 3.10. If the lens is free of geometrical abberation, the intensity distribution in the vicinity of the Gaussian focus is determined by diffraction. The focal spot is an Airy of disc radius r

where $$r = 1.22 \frac{\lambda F}{D} = 1.22 \lambda f$$

F is the focal length of the lens

D is the lens diameter or the diameter of the laser beam falling on the focussing lens

f is the numerical aperture $\frac{F}{D}$

λ is the wavelength of the incident radiation

The effective length of the focal region is

$$L = \pm \frac{\lambda \text{Ø}}{r} = \frac{\pi r^2}{\lambda}$$ as shown in Figure 3.10.

Three methods were used to measure the focal spot size. To determine the focal spot size and position, three 500μm diameter holes were drilled in a 1 mm thick aluminium plate on the corners of a 90° triangle, as shown in Figure 3.11. With the diaphragm immediately before the focussing lens, the laser was fired at half energy. The resulting image of the three holes was burned on an exposed Polaroid film mounted on the target holder. By recording the height of

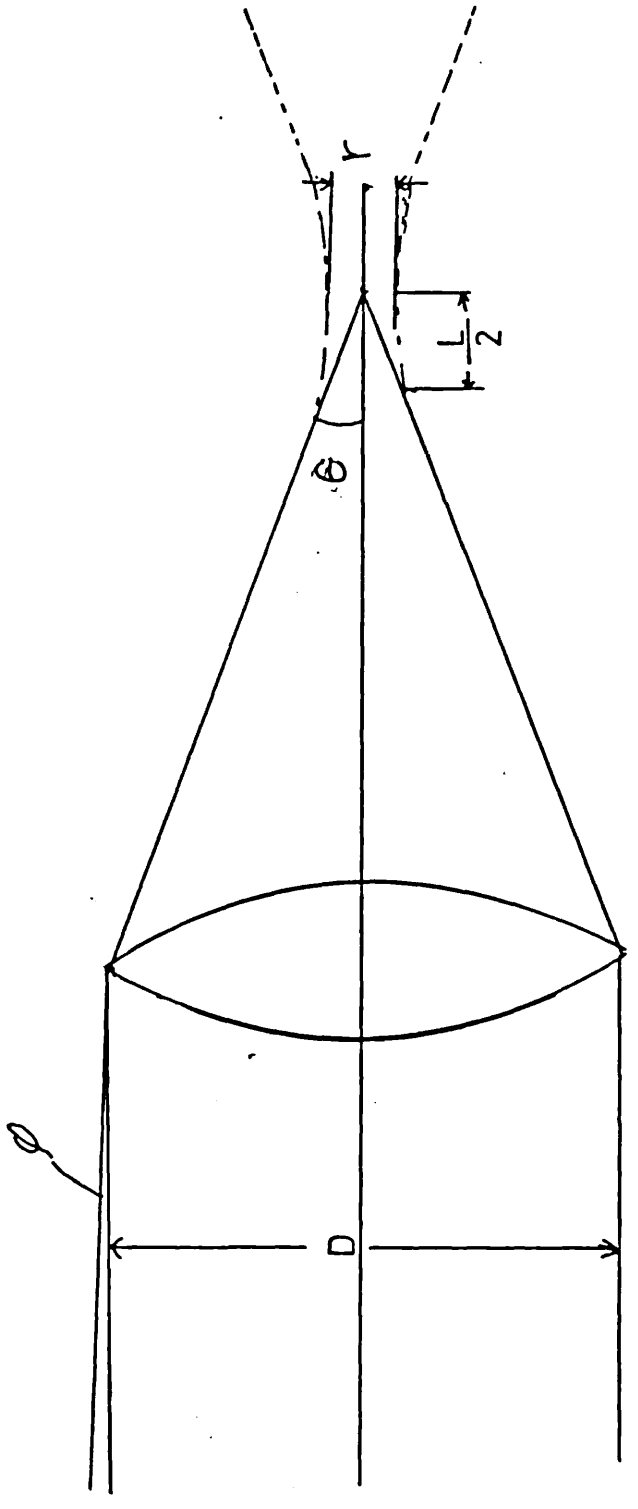

Figure 3.10

Diffraction limited focus

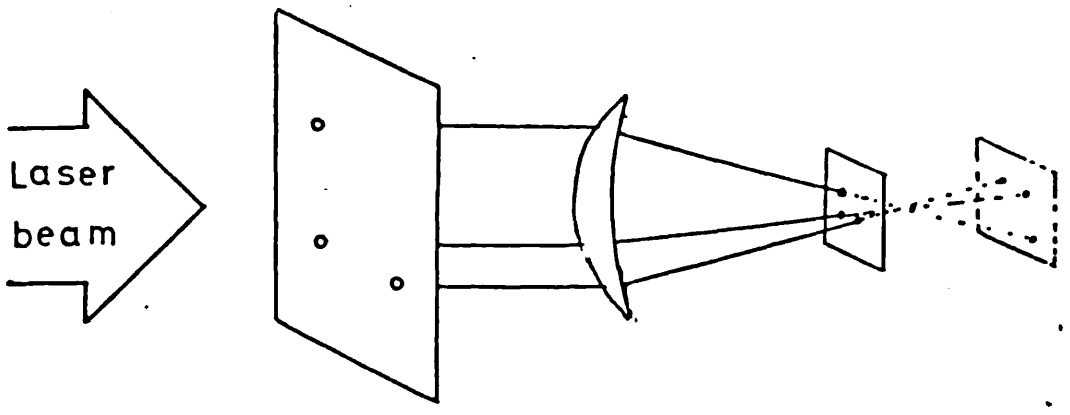

Figure 3.11

Hartmann diaphram

image separation and the displacement of the target along the optical axis at each shot, the relation between them was plotted in a graph shown in Figure 3.12. The interception of the line with x-axis (optical axis) gives the focal spot position.

The other method of determining the focal spot size is by means of the X-ray pinhole camera, which is described in section 4.5. The X-ray pinhole photograph is shown in Figure 3.13a. The microdensitometer tracing of this photograph is shown in Figure 3.13b. From this figure, combined with the camera magnification Figure 3.13_a, showed that the spatial dimensions of the emitting volume were $\geq$ 150 μ_m.

Another estimate of the focal spot size was made from the diameter of the crater burned into a target. Figure 3.14 shows the crater left in the carbon target by the laser pulse. The photograph was taken under an optical microscope with magnification of 33 times. The size of the spot from this technique is 200 μm.

3.10.4 Laser divergence

To restrict the laser transverse modes of oscillation, an iris diaphram, D_1, was placed in the cavity. This diaphram also reduces the laser divergence.

The divergence was determined by measuring the diameter of the beam at two distances 4 meters apart. Images were formed on burn paper, as shown in Figure 3.15. The measured divergence is 1 m radian, which leads to a small diameter of the focussed laser spot.

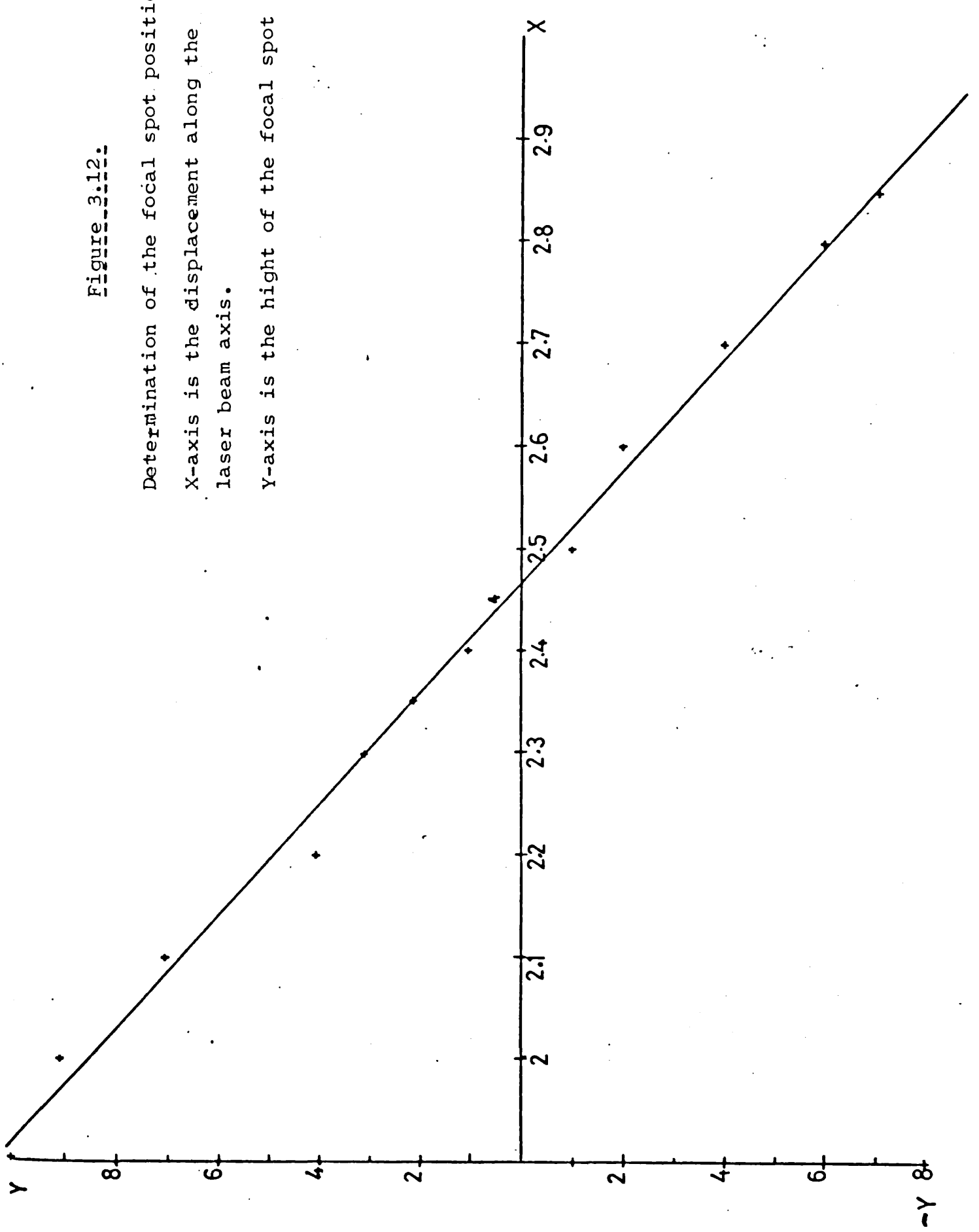

Figure 3.12:

Determination of the focal spot position.

X-axis is the displacement along the laser beam axis.

Y-axis is the hight of the focal spot

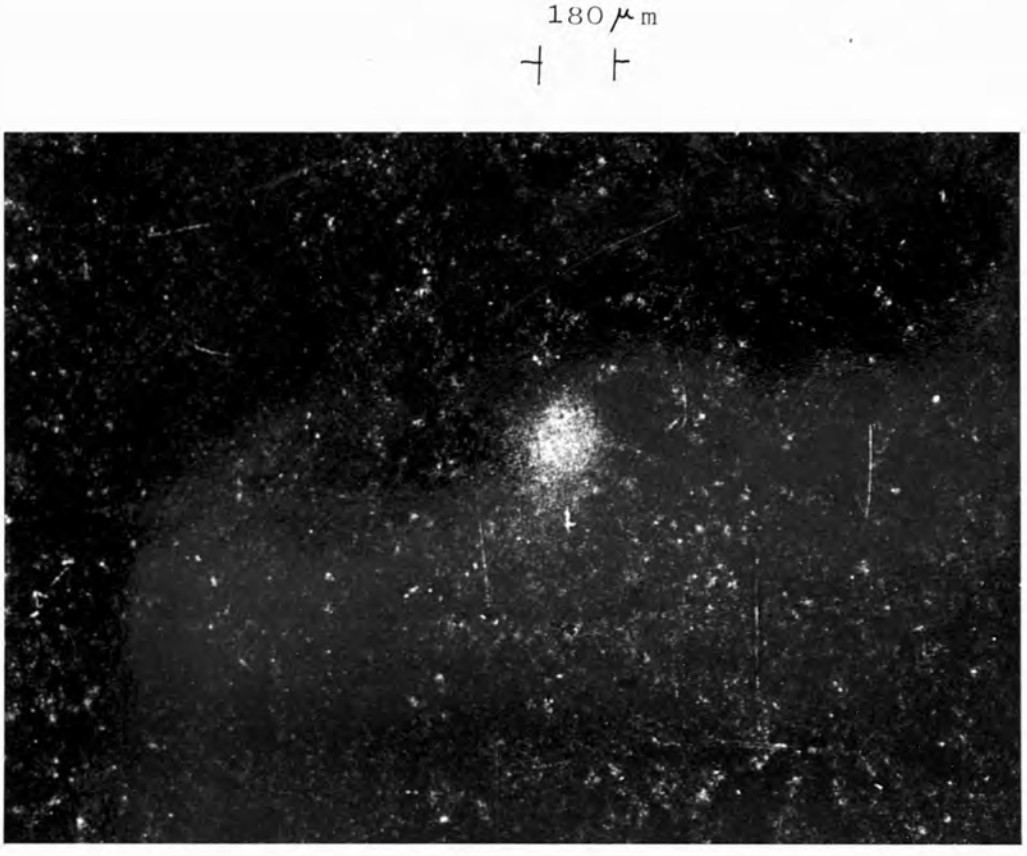

Figure 3.13a

The X-ray Pinhole Photograph.

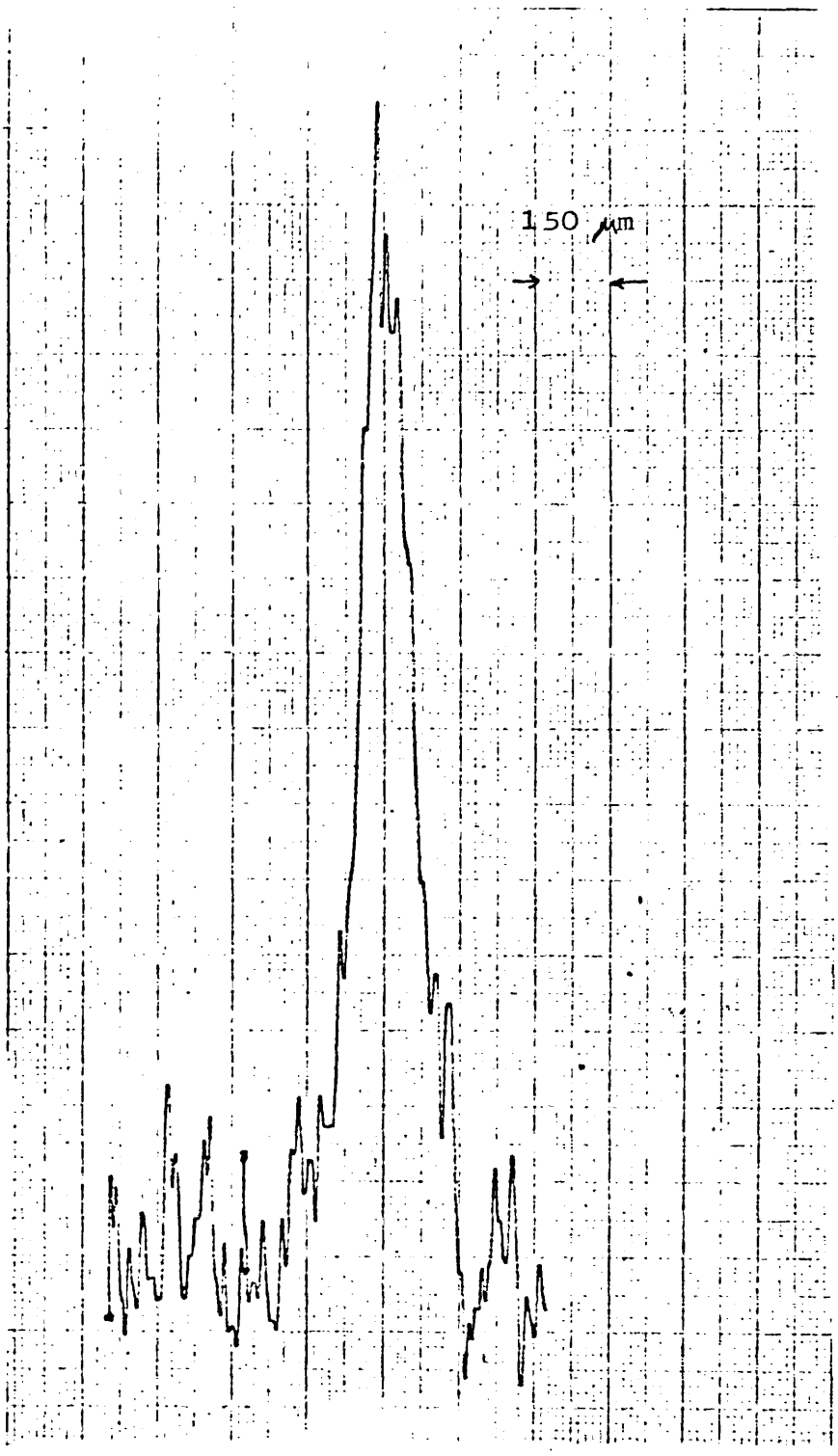

Figure 3.13b

The Microdensitometer Tracing

of The X-ray Photograph

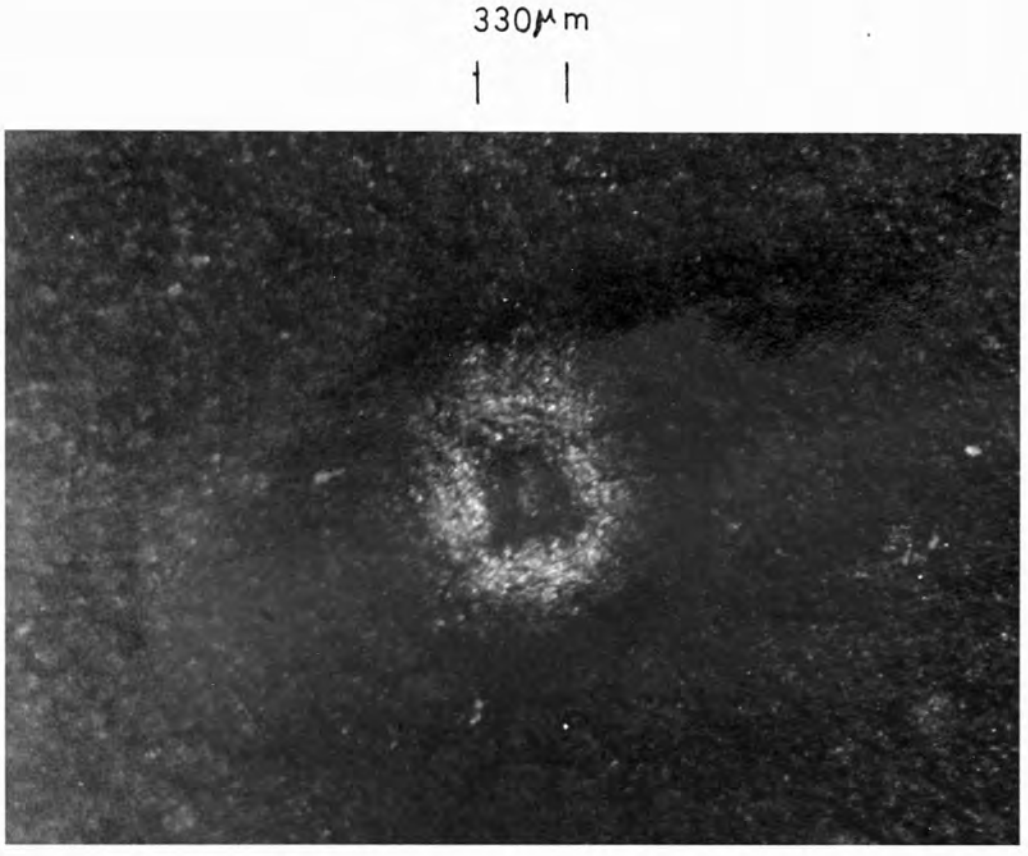

Figure 3.14

Photgraph of the crater left in the target by the laser pulse taken under optical microscope.

Figure 3.15.

The two images used for determine the beam divergence
Left side image is formed at a distance d=0
From the diaphram; Right side is at 4000mm

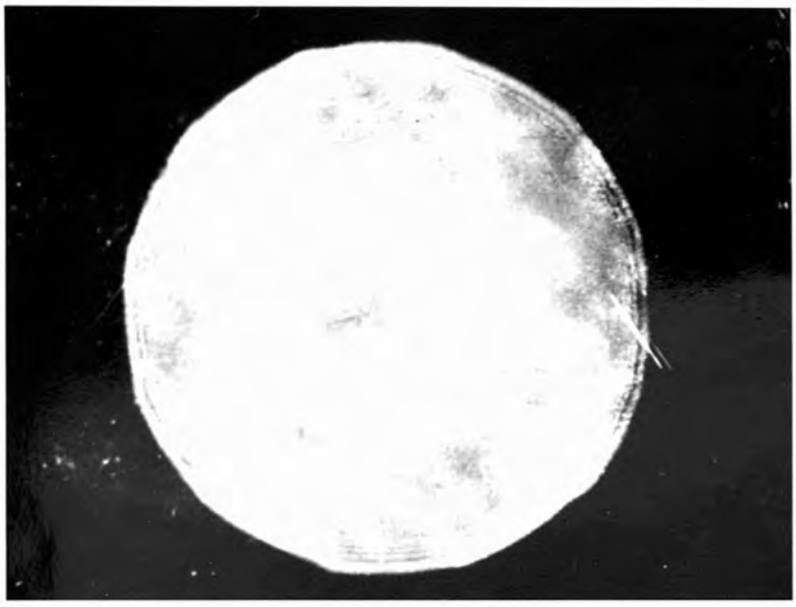

Figure 3.16.

Beam quality before the target chamber

3.10.5 Beam quality

Examples of the beam as it leaves the laser and approaches the target chamber are shown in Figure 3.16. It is seen that the beam quality is good, and there are no fringes or hot spots. There had been considerable improvement on changing from longitudinal to transverse trigger electrodes in both oscillator and amplifier.

3.11 SUMMARY OF THE LASER CHARACTERISTICS

It was found possible to operate the laser for long periods without extensive readjustment. Up to 500 shots could easily be ontained in one day. After about two weeks (5000 shots) of continuous running it was found that the energy fell off but realignment and cleaning of the electrodes produced full energy.

The maximum energy obtained was 30 Joules, but it was then found that the tail of the pulse contained a small bump. Table 3.4 shows the important characteristics of the laser.

TABLE 3.4

Description of the laser pulse shape

	Minimum	Maximum
Energy total	3 Joule	30 ± 3 Joule
Peak power	5×10^7 Watt	7.5×10^8 Watt
Pulse duration	50 n sec	40 n sec
Total pulse duration	disappears at low electrical energy Ω low N_2	5 μ sec
Wavelength	10.6 μm	
Linewidth	150 Å	200 Å

CHAPTER 4

EXPERIMENTAL APPARATUS AND METHODS

4.1 INTRODUCTION

Radiation from the laser was focussed on to solid targets which were enclosed in an evacuated interaction chamber. The chamber was fitted with eight windows which permitted several diagnostic devices to be installed and allowed the scattered radiation to be measured.

The arrangement of the interaction chamber and the associated diagnostics are represented in Figures 4.1(a) and 4.1(b).

It was seen in Chapter 2 that the region of the plasma where the interaction occurs is a small fraction of a millimeter in diameter, the electrons density increasing from zero to be above the critical value in a distance equal to a few laser wavelengths. The temperature is several hundred electron volts, and there are intense electric and magnetic fields. These special conditions are conducive to the generation of various parametric instabilities, as discussed in Chapter 2. However, under these extreme conditions, the methods of investigating the plasma are restricted almost entirely to optical ones; the most useful technique being emission spectroscopy.

By studying the spectra of the radiation scattered from the plasma, it is possible to deduce the frequencies

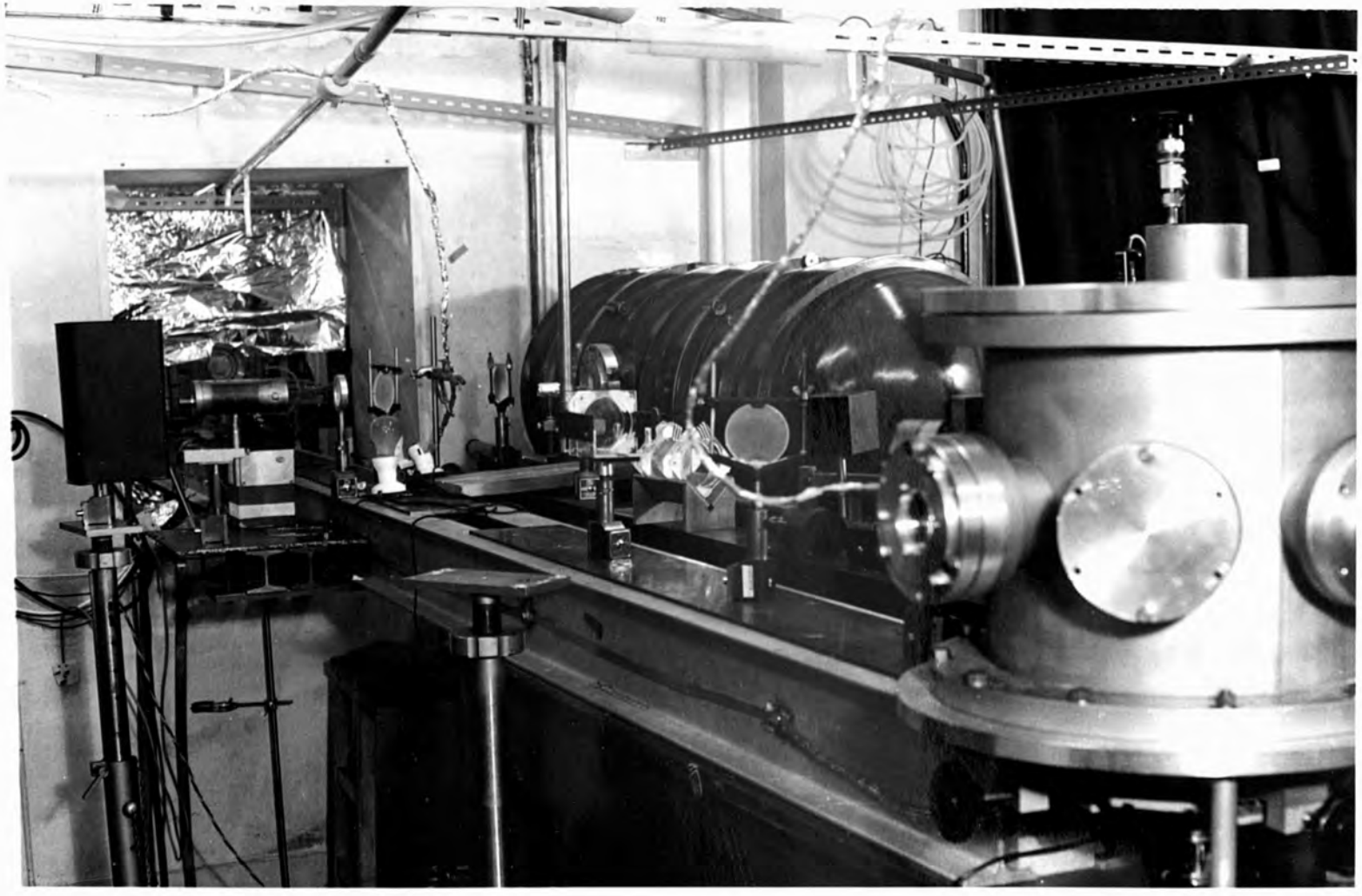

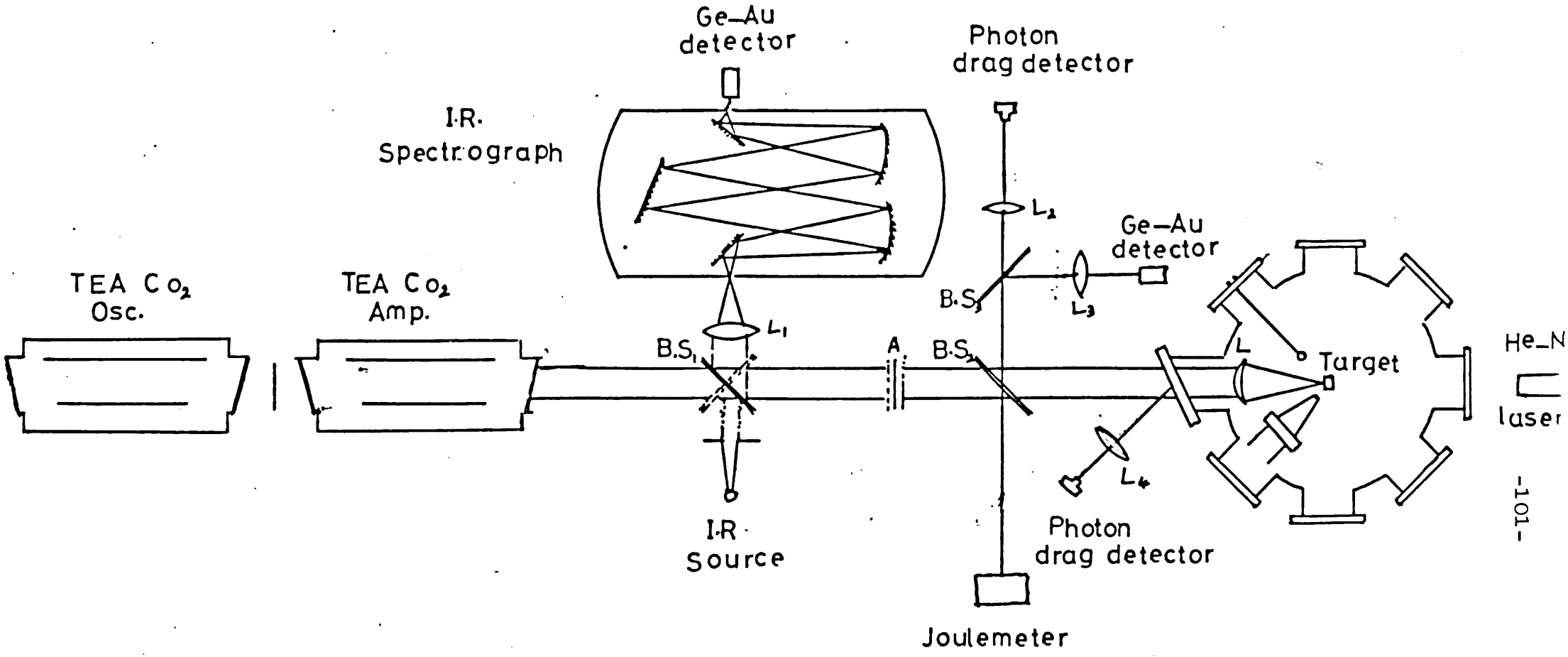

Figure 4.1b:

Laser system and interaction diagnastics

B.S.- beam splitter, L- lens, B.S$_1$.- movable beam splitter, A- attenuators.

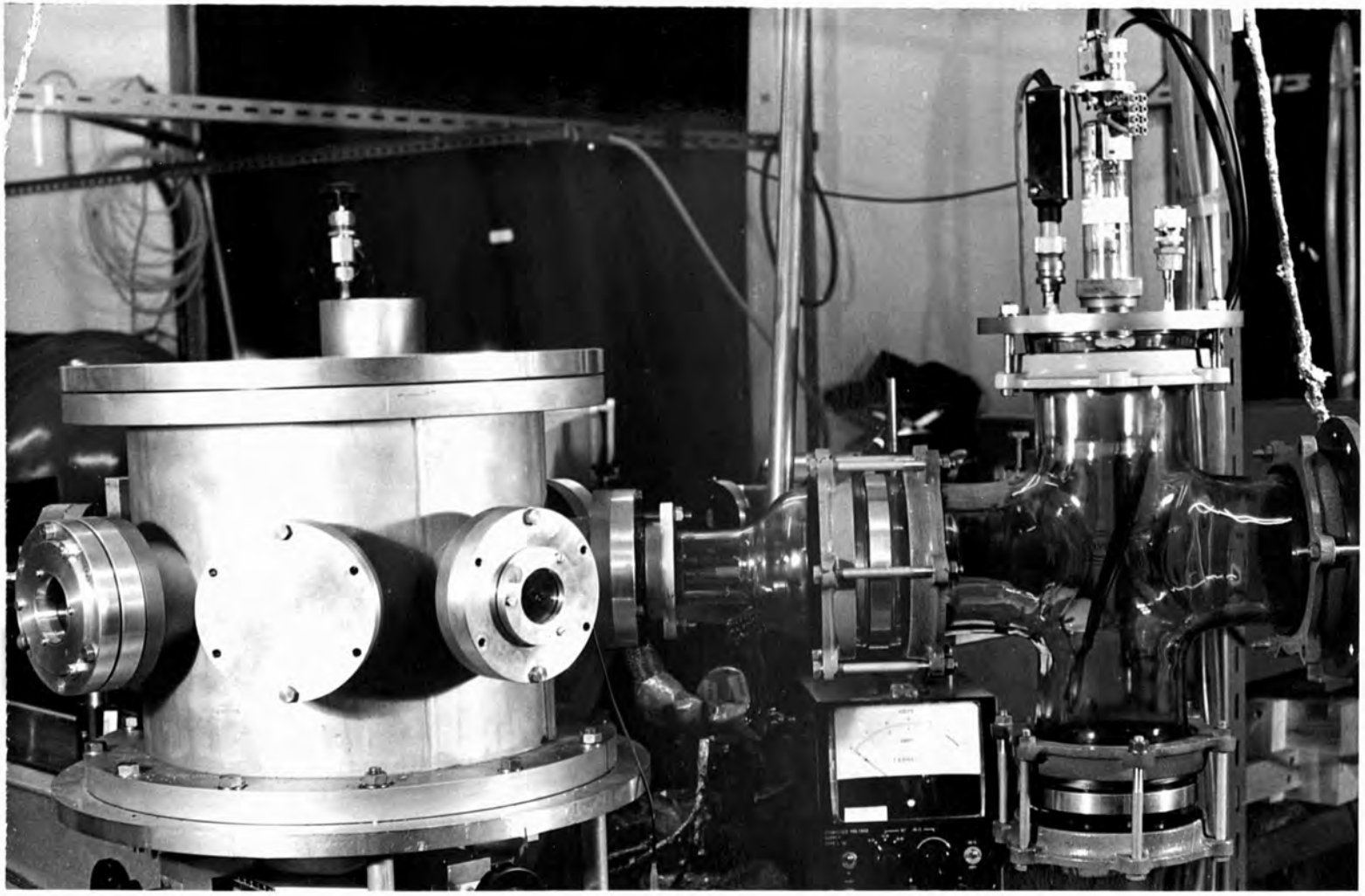

of the wavelength of the waves and instabilities which are generated within the plasma. The scattered radiation is spectrally dispersed and measured with appropriate detectors.

4.2 THE INTERACTION CHAMBER AND VACUUM SYSTEM

The interaction of laser radiation with the target occurred in the interaction chamber shown in Figure 4.2 and Figure 4.3, which was fixed at 400 cm distance from the end face of the amplifier. This distance also enhanced the homogeneity of the laser beams.

The chamber consisted of an alloy tube of 32 cm internal diameter, 30 cm height and wall thickness of 1 cm. There were eight windows, each 7 cm diameter, placed at 45 degree angular spacing around the periphery. The lid of the chamber was removable for adjusting the target or introducing diagnostic devices.

The target was mounted on a pillar, as shown in Figure 4.4, which could be positioned at the centre of the chamber by three external micrometers. The target could thus be moved vertically, and parallel or perpendicular to the laser beam in the horizontal plane.

The entrance window consisted of a 75 mm diameter, 5 mm thickness potassium chloride flat. It was fixed at 25^{o} to the optical axis to reflect stray light out of the system. This flat also acted as a beam splitter for monitoring the incident laser pulse energy.

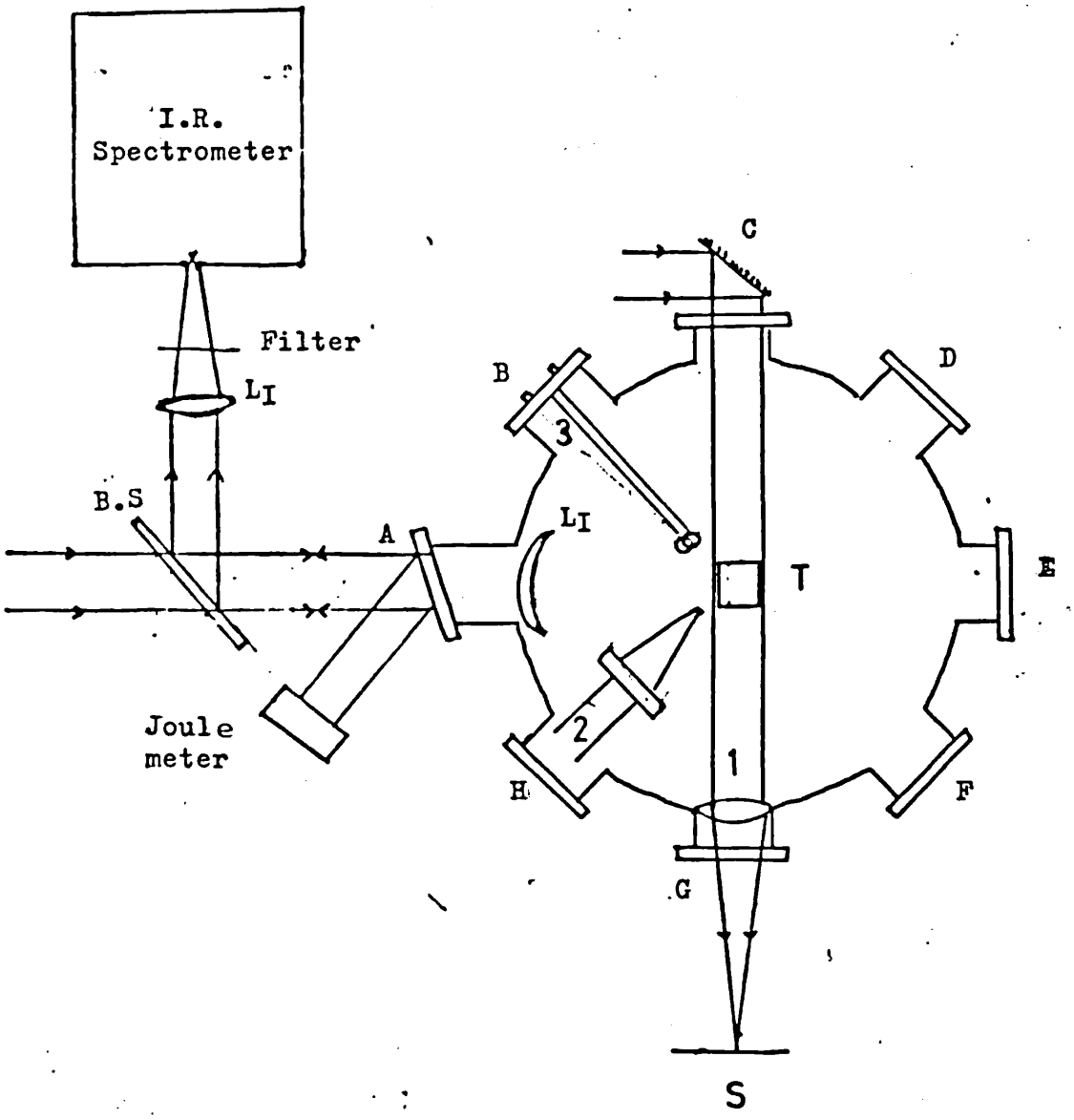

Fig. 4.3. Interaction Chamber with plasma diagnostic apparatus

L_I- Ge. Meniscus lens(F=125mm)

L_2- Kcl. Lens (F=200mm)

A- Entrance window (Kcl)

B- Magnetic probe

C-G Shadow graph technique

H- X-ray pinhole camera

T- Target

Radiation from the laser was focussed into the interaction chamber by means of a 125 mm focal length germanium miniscus lens of 70 mm diameter (f 1.7). However, a beam diameter of 35 mm results in a numerical aperture of f 3.6. The lens was initially anti-reflection coated for 10.6 μm wavelength, but the coating was damaged after a large number of laser shots. A replacement lens was protected by polythene pellicles.

The target position was checked before each laser shot by using shadow optics, as shown in Figure 4.3. This optical system consists of a beam of parallel light which passed through window C and emerged from window G in Figure 4.3. A 30 cm focal length lens imaged the target onto the screen S.

The vacuum system, which reduces the gas pressure in the interaction chamber to between 10^{-4} and 10^{-6} torr, is also indicated in Figure 4.4. It consists of a high speed rotary pump (Edwards ISC 50 B), diffusion pump, water cooled (Edwards) with mercury vapour trap, and liquid nitrogen cooled trap.

4.3 ALIGNMENT OF THE LASER AND OPTICAL SYSTEM

The optical components must be carefully aligned before each experiment to achieve optimum beam quality and high irradiance. The smallness ($\simeq 200\mu_m$) of the scattering region makes imaging and focussing onto the monochomator slit very critical. The particular laser line must be

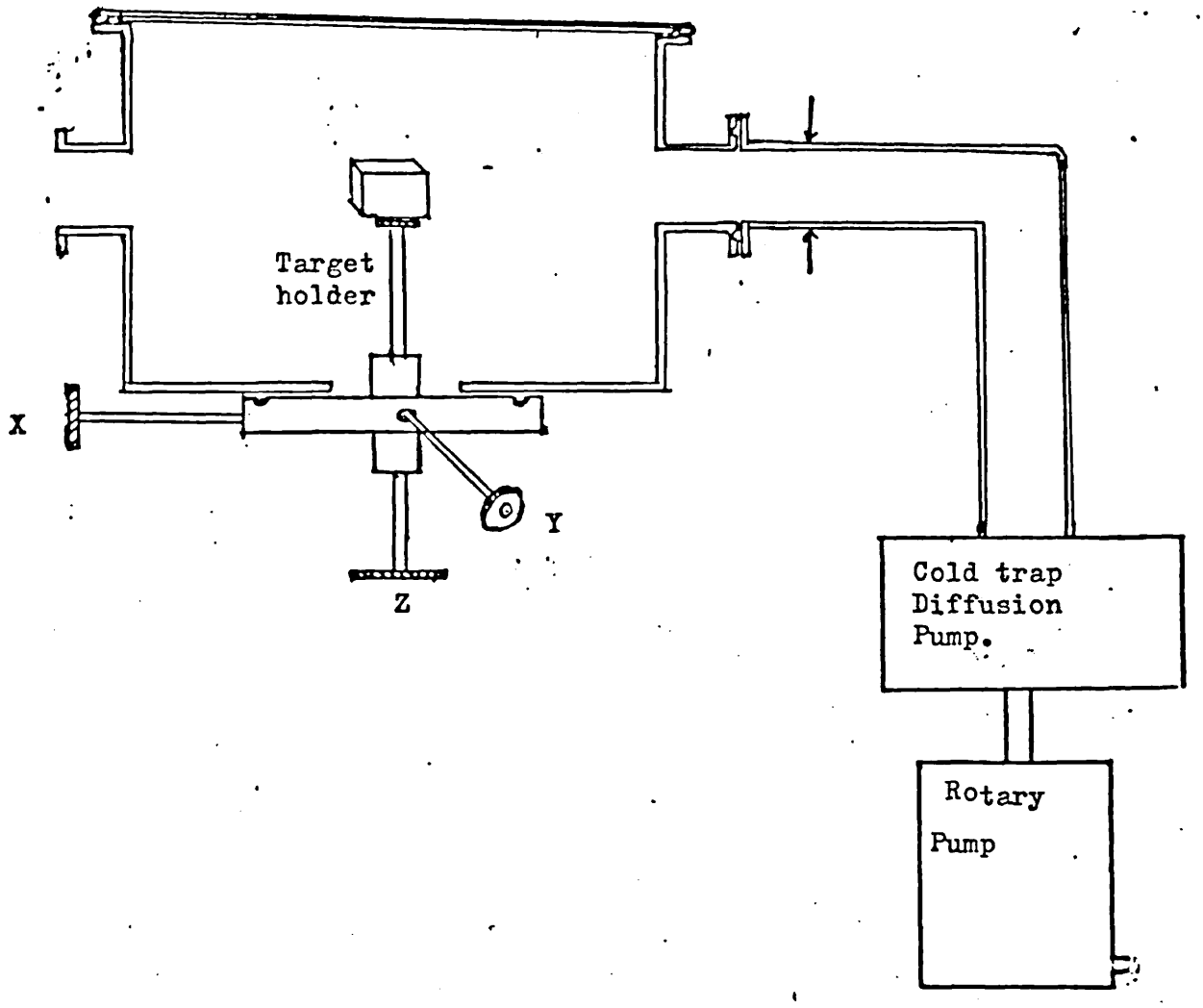

Fig. 4.4. Design of interaction chamber
and vacum system.
X,Y and Z are micrometers to
move the target in the dimension
With respect to laser beam.

selected and the beam must be directed and focussed at the desired position on the target. Also, the diagnostic devices need to be aligned to view the hottest region of the plasma. Methods were developed to facilitate all of these adjustments.

The alignment was achieved by using the He-Ne laser illustrated on the right hand side of Figure 4.1_b. Firstly, the laser resonator, with the end reflector grating, is aligned. To select the 10.6 μ_m line the grating was aligned horizontally to the optical axis and then set up vertically at the blaze angle (45^o) by micrometer. After preliminary alignment with the He-Ne laser the CO_2 laser has to be further aligned by firing and adjusting the grating to achieve maximum energy consistent with a uniform burn pattern on a blackened paper*. The wavelength was verified by reflecting part of the beam into the spectrometer slit, which was set at the (calibrated) position of 10.6 μ_m wavelength.

The rest of the optical set-up can be aligned easily by the He-Ne laser. The incident and back scattered optical components and detectors can be aligned by reflecting a portion of He Ne laser beam through them. To get the image of the hottest point of the plasma into the entrance slit of the spectrometer, the optical components must be aligned, primarily by He-Ne laser, and finding by focussing the

* (Exposed Polaroid film or "footprint paper" obtained from Messrs Roditi were used for this purpose.)

backscattered radiation of the CO_2 onto burn paper mounted on the entrance slit of the spectrometer. By moving the beam splitter BS_1 (C in Figure 4.1) and the focussing lens (F in Figure 4.1) the image of the plasma can be focussed onto the entrance slit of the spectrometer.

4.4 PLASMA DIAGNOSTICS

By studying the spectra of the back scattered radiation it is possible to obtain some valuable information on the plasma interaction processes. The radiation was dispersed on a grating spectrometer and its intensity was determined with a photon drag detector or a gold doped germanium detector, depending on the wavelength of the radiation under study. The characteristics of these detectors have been given already in Table 3.3 The method of calibrating the spectrograph is described below.

Other information that is required is the dimension of the plasma, its temperature and the magnitude of any magnetic field that may be generated.

4.4.1 Spectroscopy of the scattered radiation

To resolve the spectral radiation a Czerny-Turner monochromator (RRE no 716) was used with various gratings, as shown in Table 4.1. The spectrometer had a focal length of 2 m and an aperture of f5.

To calibrate the monochromator against the wavelength, radiation from a Globar infrared source was absorbed by

TABLE 4.1

Gratings for Spectrometer

Size	Grooves/mm	Blaze Angle	Blaze	Dispersion Theoretical	Dispersion Measured	Resolution Theoretical	Resolution Measured
150 x 150 mm^2	100/mm	30^o	10 μm	11 $\overset{o}{A}$/mn	20 $\overset{o}{A}$/mn	8 $\overset{o}{A}$	10 $\overset{o}{A}$
100 x 60 mm^2	60/mm	8 - 38	5 μm	12 $\overset{o}{A}$/mn	20 $\overset{o}{A}$/mn	$\simeq$ 9 $\overset{o}{A}$	10 $\overset{o}{A}$

material of known spectral absorptance. The radiation from the source was focussed on the entrance slit by an f5 lens L_1 of 200 mm focal length. Two absorber materials were used to calibrate the monochromator against the wavelength, the absorption spectra are shown in Figure 4.5. One was a polystyrene film for the range of wavelengths near to 10 μm, and a polyethyline film for the range of the wavelength between 5 μm and 7 μm. To calibrate the monochromator for the wavelengths 10.6, 7.07 and 5.3 μm, narrow band pass filters were used. During spectral calibration the spectra were detected by means of a Golay cell with diamond window and the output signal was recorded by a chart recorder.

The dispersion and resolution of the grating shown in Table 4.1 were measured experimentally by using narrow band pass filters.

The experimental method of the spectroscopic measurement and investigation of the backscattered radiation are summarized in the following sections.

4.4.2 Spectroscopy of radiation at ω_o

A portion of the calibrated backscattered light was sampled with a beam splitter 3 meters upstream from the target, as shown in Figure 4.1, and the target hot spot was imaged with 5x magnification onto a crossed 500 μm slit at the entrance to 2 m grating spectrometer with a measured instrumental resolution of 20 Å. The backscattered spectrum was analysed and the profile of the laser radiation and the

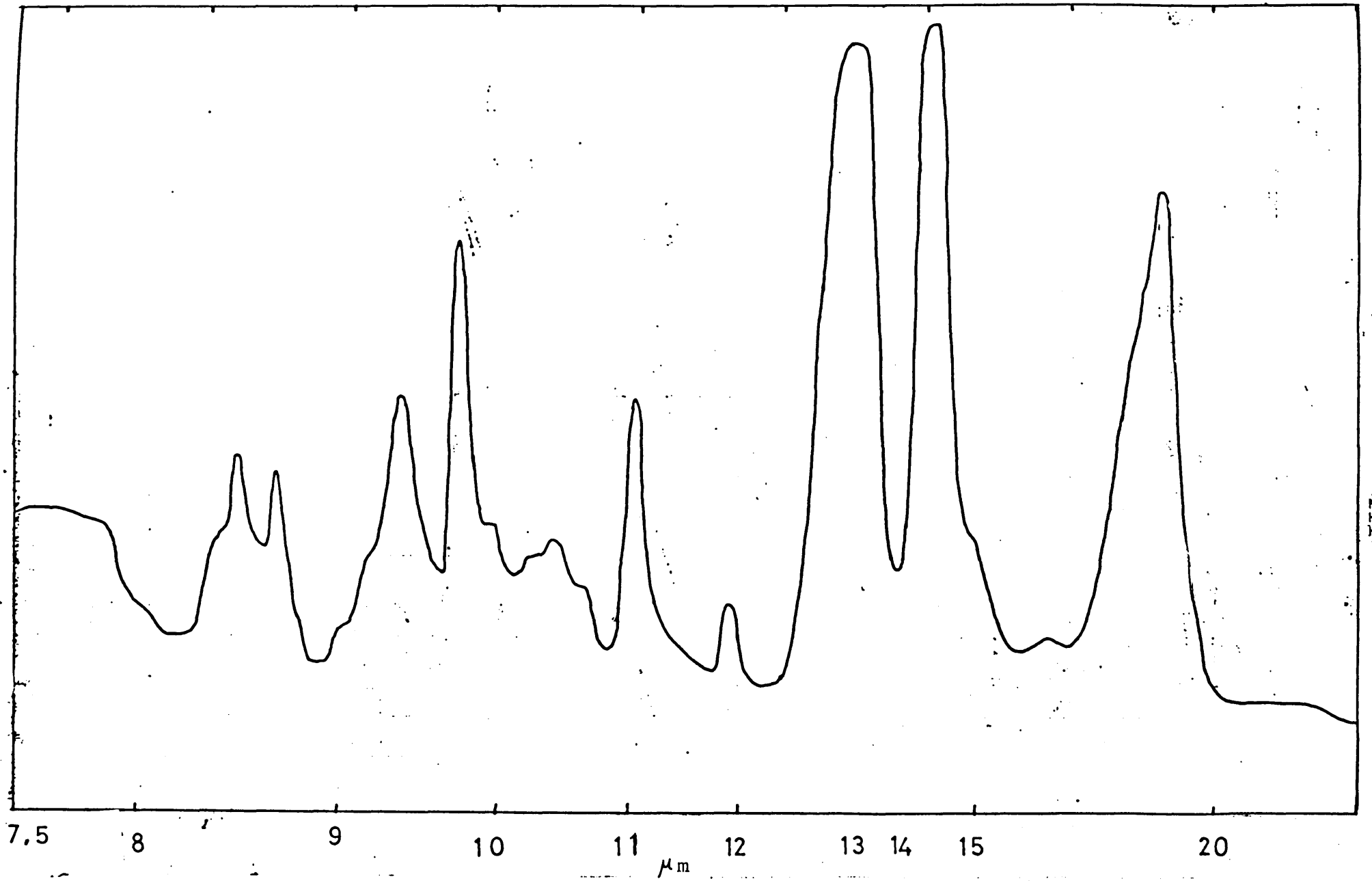

Figure 4.5.

Absorption spectra of the polystyrene film

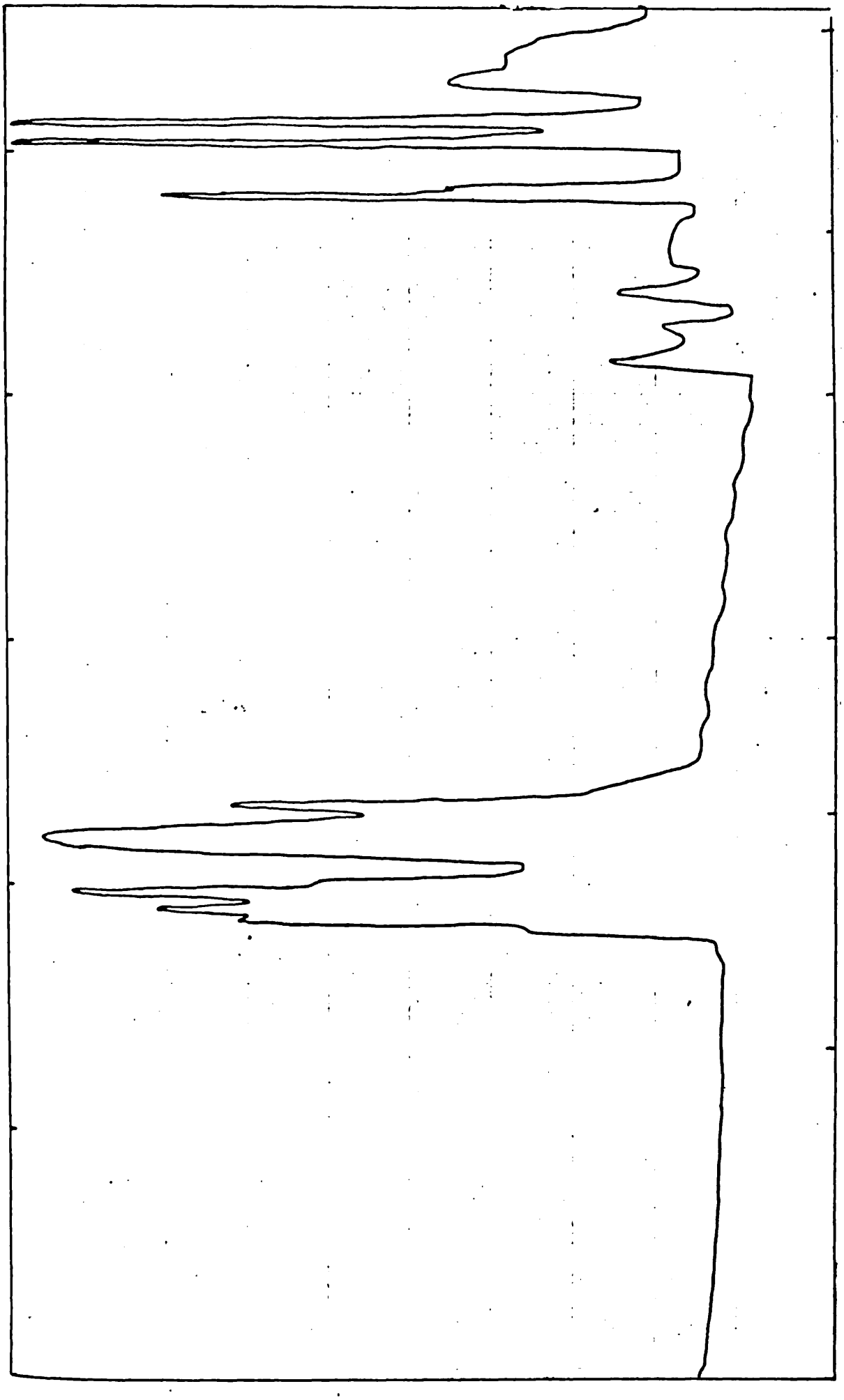

Figure 4.5.

Absorption spectra of the polyethylene film

fundamental backscattered ω_o, are shown in Figure 4.6. The line profile has been drawn by shot by shot method. Every point on the line profile is the average of 15 - 20 shots, with bars indicating the standard error. The signal was detected by photon drag detector on the exit slit of the spectrograph.

4.4.3 Spectroscopy of radiation at $2\omega_o$

The dependence of the radiation scattered back through the focussing lens at the frequency of the second harmonic as a function of the incident laser power is shown in Figure 4.7. The measurements were carried out in the same manner as those of ω_o, which were described in section 4.4.1, but with a 5.3 μm pass band optical filter to reject other grating orders. The signal was detected at this wavelength by means of a gold doped Germanium detector which had a D* of 10^{10} m $Hz^{\frac{1}{2}}$ W^{-1} cooled to 77° K. The linearity of the detector was checked and its responsivity was calibrated against the photon drag detector and is listed in Table 3.3.

The spectrograph grating used had 60 grooves per mm and was blazed for 5 μm. The incident laser power was monitored by a photon drag detector. As before, each point in the spectrum profile of 2ω , Figure 4.8, is the average of 20 successful shots with a clean target surface.

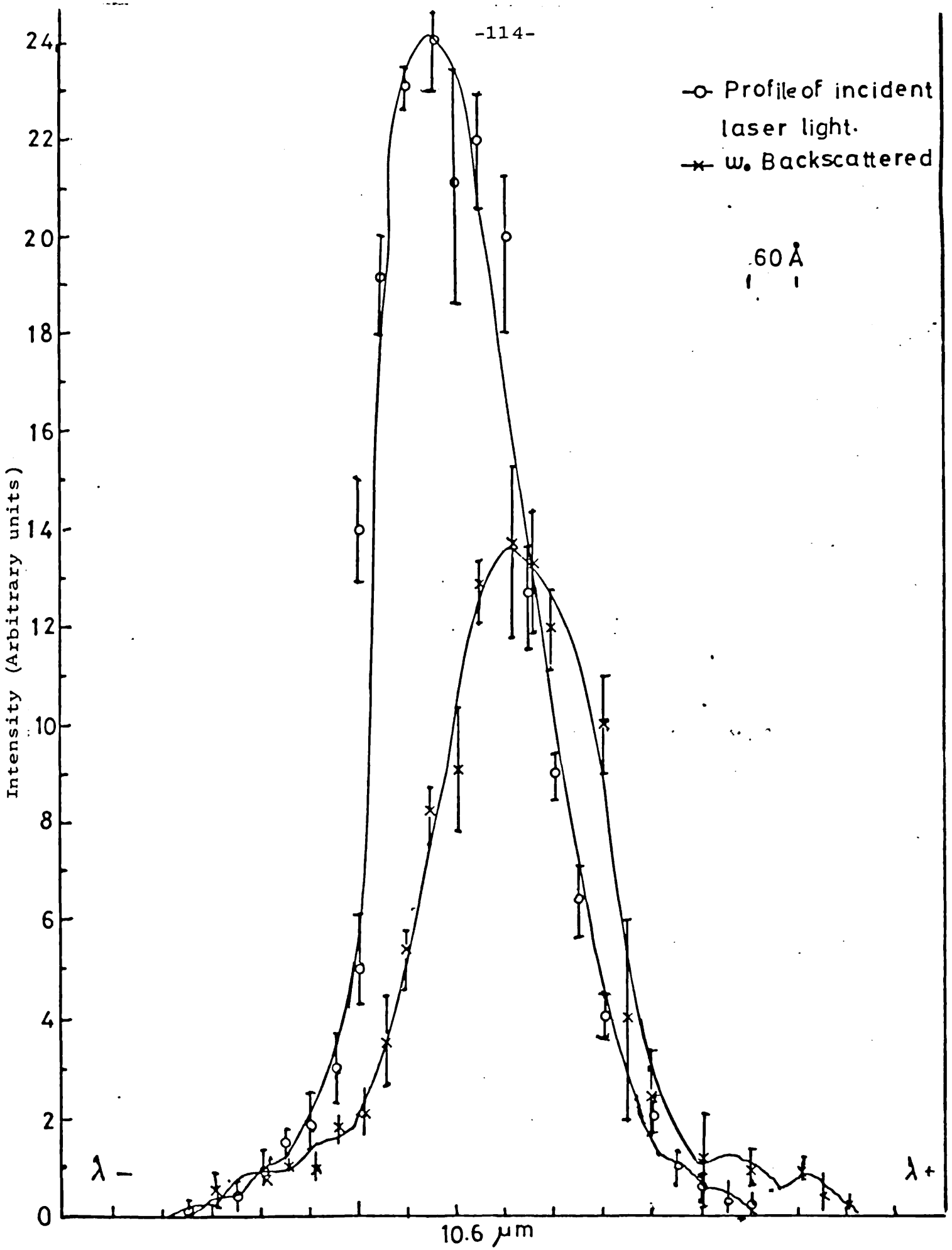

Figure 4.6.

Profile of incident and backscattered ω_o

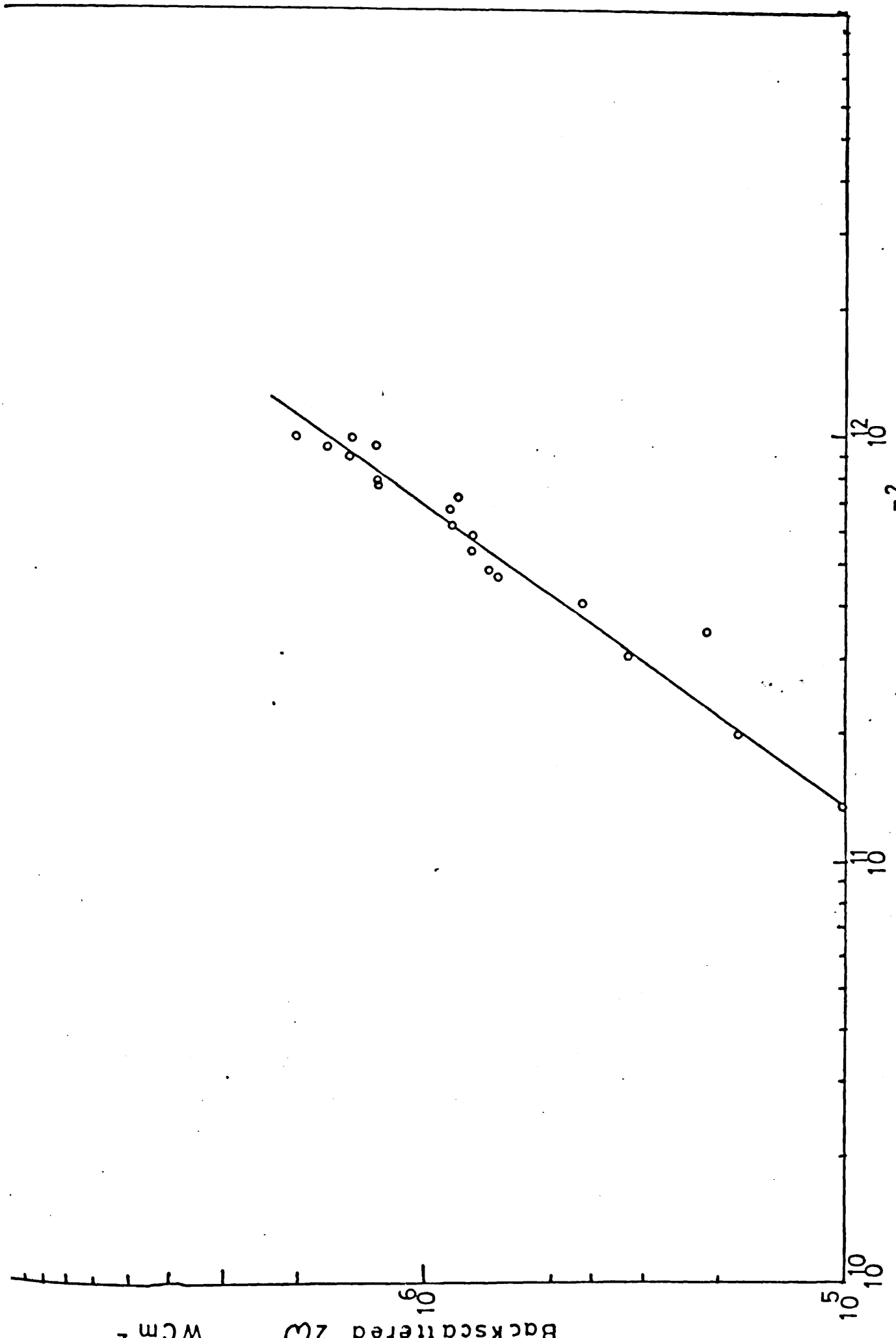

Figure 4.7.

Backscattered Intensity at 2ω vs. Irradiance.

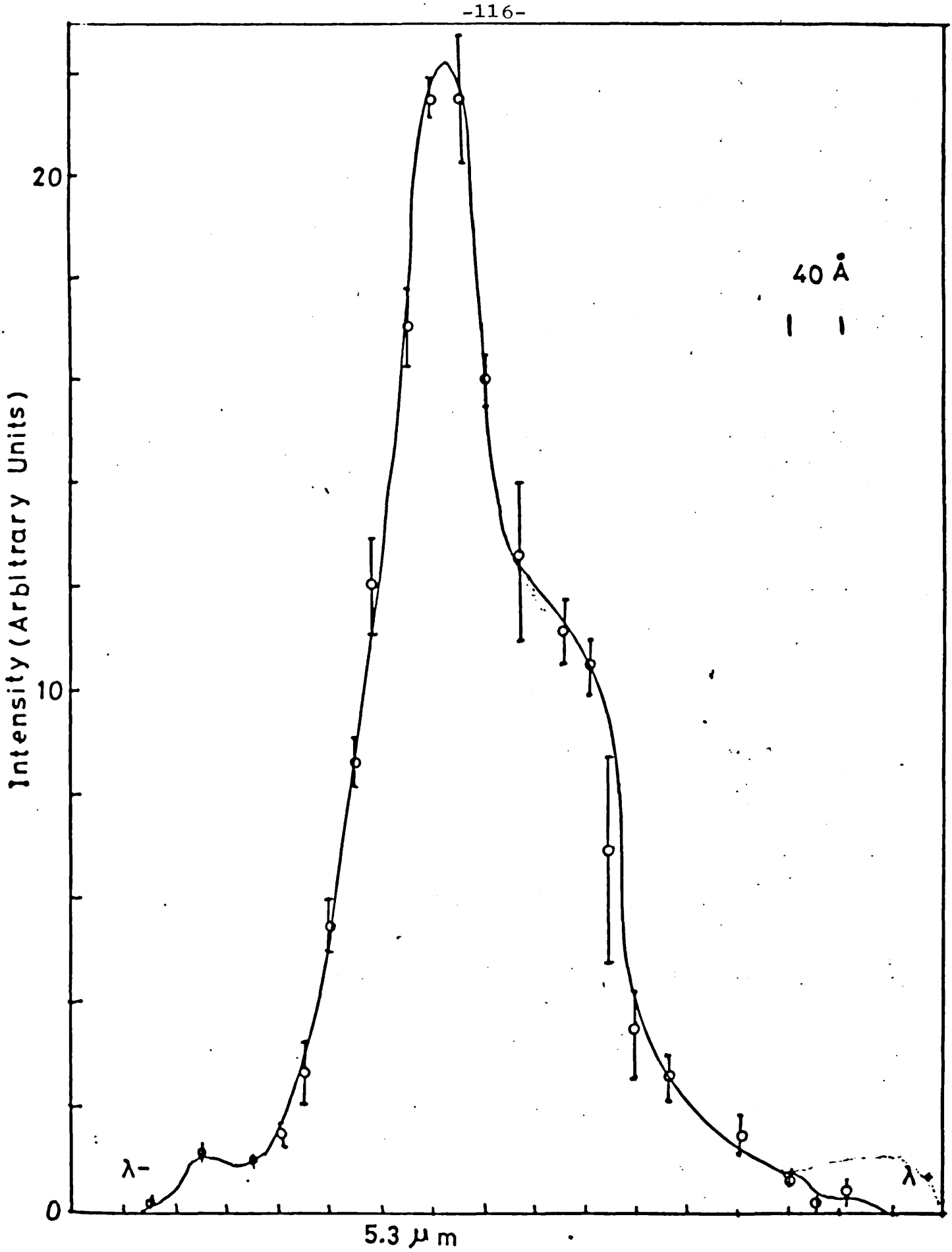

Figure 4.8.

Profile of the Backscattered
$2\omega_o$($I = 8\ 10^{11}$ W cm^{-2}

4.5. PLASMA TEMPERATURE

In addition to studying laser plasma interaction, it is possible to determine many plasma properties by analysing the radiation emitted from the plasma. Because the temperature is so high, much of the radiation is in the X-ray region.

Three methods were used to determine the plasma temperature. An estimate was made from the Brillouin scattered spectrum, the intensities of the X-ray contained in two spectral ranges were recorded with a pinhole camera and X-ray intensities were determined with scintillators and photomultipliers.

4.5.1 Temperature determined from the Red Shift of ω_o

Radiation is emitted in the vicinity of ω_o as a result of the incident laser radiation driving ion acoustic waves and then being scattered from these waves. The dispersion relation of an ion acoustic wave is

$$\omega = k\left(\frac{K_b T_e + K_b T_i}{m_i}\right)^{\frac{1}{2}} = k C_s$$

This wavelength is then Doppler displaced as the plasma expands at velocity v.

Hence $\dot{\omega} = \omega_o - 2 k C_s$

The radiation is observed after refraction in the plasma (of refractive index n). Hence the wavelength displacement

from ω_o is

$$\Delta\lambda = \frac{c(\omega_o - \omega')}{n2\pi\omega_o^2}$$

A plot of the displacement was made and is shown in Figure 4.9. against irradiance.

4.5.2 X-ray Measurements

The electron temperature was determined by the foil absorption technique, first suggested by Jahoda et al (1960), in which the relative transmission of two thin foils for continuum is measured.

The X-ray continuum varies as exp $(- E/T_e)$. The transmission coefficient of a metal foil depends on the energy of the incident radiation but a particular thickness has a cut off energy E_c, below which it is opaque. Hence, if the same radiation is incident on two foils of different thicknesses, the two cut off values E_{c1} and E_{c2} permit an estimation to be made of the spectral range.

The intensity of the X-ray transmitted by a foil of thickness d and mass absorption coefficient $\mu(E)$ is given by

$$I_T(E)\,dE = \Omega\ I_o(E)\ \exp^{-\mu(E)d}\,dE$$

where Ω is the solid angle subtended by source at the foil aperture, as in Figure 4.16.

Continuum radiation due to free-free and free-bound transition is represented by,

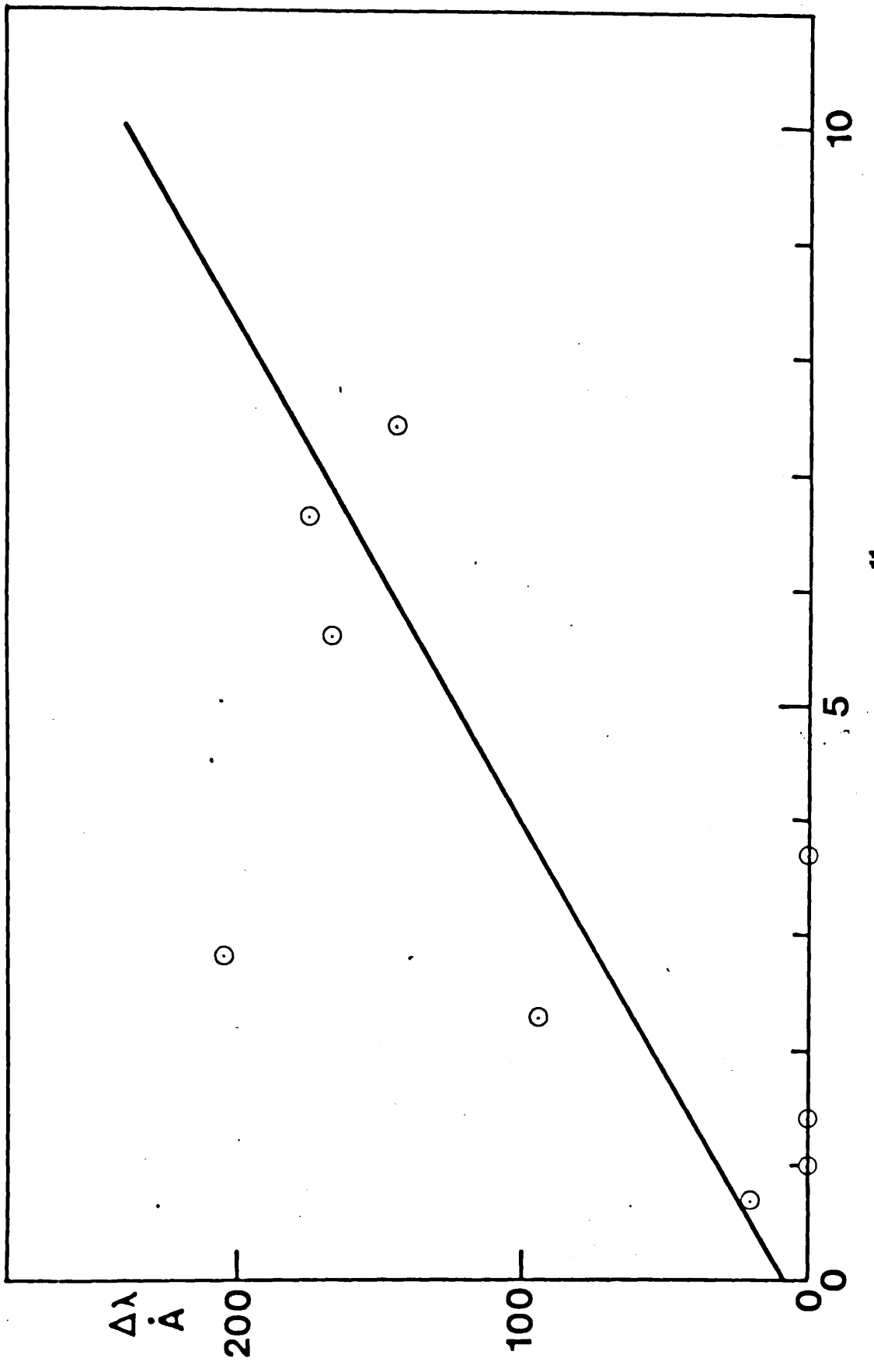

Figure 4.9:

Displacement of Backscattered ω_o vs Irradiance.

$$I_o(E)\,dE = f(z_1, T_e)\exp^{-E/T_e}\,dE, \text{erg sec}^{-1}\ \text{sterad}^{-1}$$

where f is a function dependent on Z and T_e given by Mandelshtam et al (1966) as

$$f = 7.58 \times 10^{-15}\, n_e^2\, V \left[\sum f_p\, z_p^2 + \sum f_p(\chi_H/T_e)\right.$$
$$\left.\sum(\chi_{p,n}/\chi_H)^2(\mathcal{E}_n)\, e^{\chi_{n,p}/T_e}\right]$$

n_e = plasma electron density cm^{-3}

V = volume of the emission source

z_p = the ion charge

f_p = fractional abundance ($f_p = n_p/n_e$)

n_p = ion density cm^{-3}

χ_H = ionisation potential of hydrogen (eV)

$\chi_{p,n}$ = ionisation potential (in eV) from nth shell for recombining electron

$\mathcal{E}_n$ = number of free states in n shell

If the region of the plasma hot spot is viewed by two detectors shielded by two different foils, then the ratio R of the observed intensities I_{T1} and I_{T2} in each detector may be written very approximately

$$R = \frac{I_{T1}}{I_{T2}} = \frac{E_1 \exp^{(-E/T_e)}\,dE}{E_2 \exp^{(-E/T_e)}\,dE} = \exp\left[(E_{c2} - E_{c1})/T_e\right]$$

where E_{c1} and E_{c2} are the cut off energies of the two different foils. Hence, a measurement of the ratio R with two foils of known cut off energies permits an estimation of the electron temperature T_e to be made.

Elton (1969) has published values of the ratio of the integrated Bremsstrahlung emission I_T transmitted through foils of material to the total incident flux I_o, i.e.

$$I_T/I_o = \int dE \exp(-E/KT_e - \mu d\ell) / \int dE \exp[-E/KT_e]$$

This ratio has been determined for values of foil thickness, d, and temperature KT_e, as shown in Figure 4.10. From such graphs the variations of I_T/I_o against the temperature T_e for particular foils were determined. Then the relative transmitted intensities of two different thicknesses may be obtained,

$$\frac{I_{T1}}{I_o} \Big/ \frac{I_{T2}}{I_o} = I_{T1}/I_{T2}$$

and plotted against the variations of temperature, as shown in Figure 4.11. The range of temperatures of interest is from one hundred to a few thousand electron volts. From such a plot and measurements of the transmitted intensities with two foils, the electron temperature T_e may be deduced.

To analyse the X-ray emitted from the plasma, two methods for time and space integrated spectra were used.

Thin aluminium foils combined with mylar were mounted in front of the pinhole and the scintillator, to select the required X-ray energy, Johada et al (1960). These foils are transparent and show cut off energy $E_c = h\nu_c$, which is defined by $\mu(h\nu_c)\, d = 1$, where μ is the photon absorption coefficient and d is the foil thickness. The absorption coefficients were taken from Elton and Anderson (1967) and

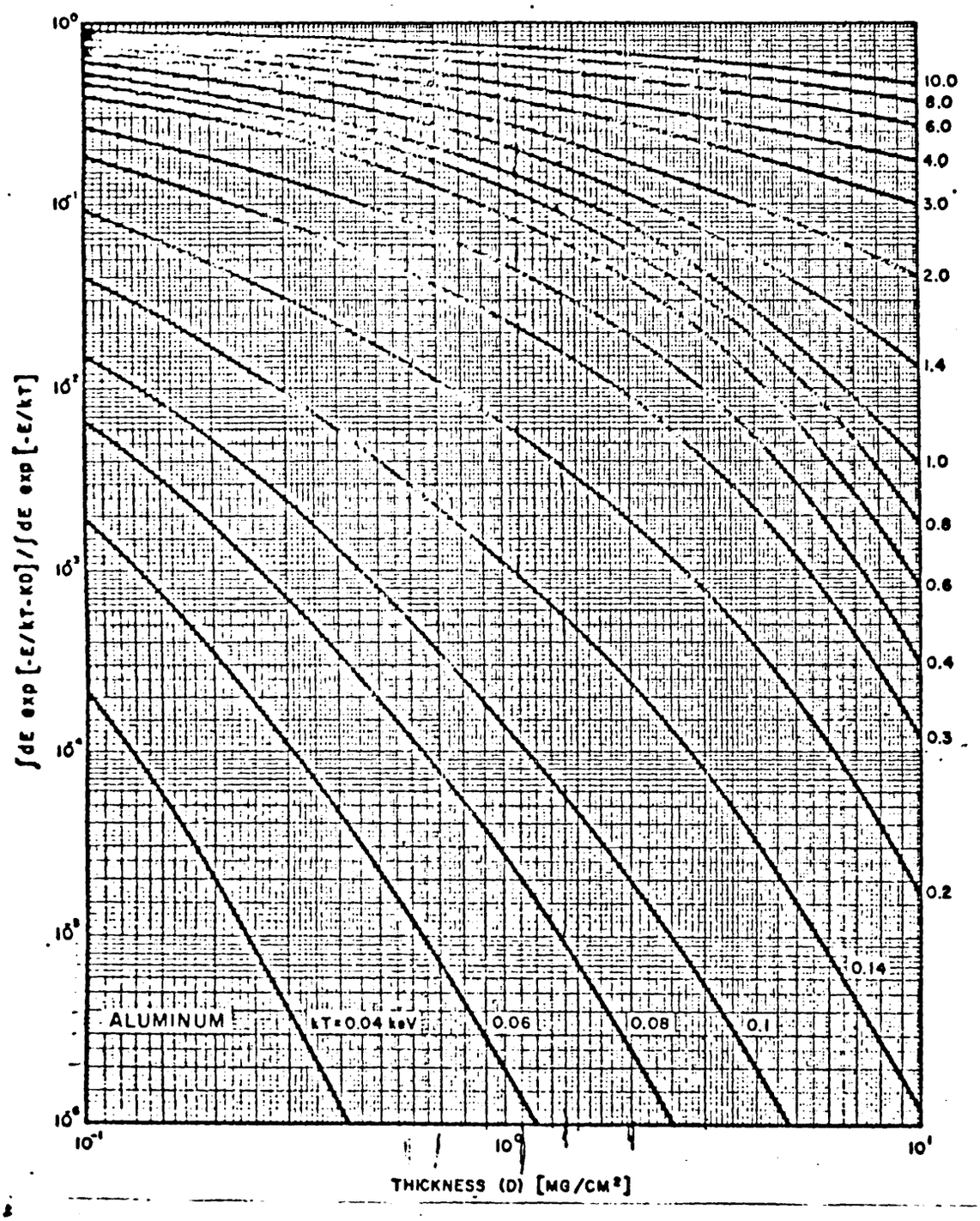

Figure 4.10.

Ratio of integrated Bremsstrahlung emission I_T transmitted through aluminum foils of different thickness to the total incident flux I_O.

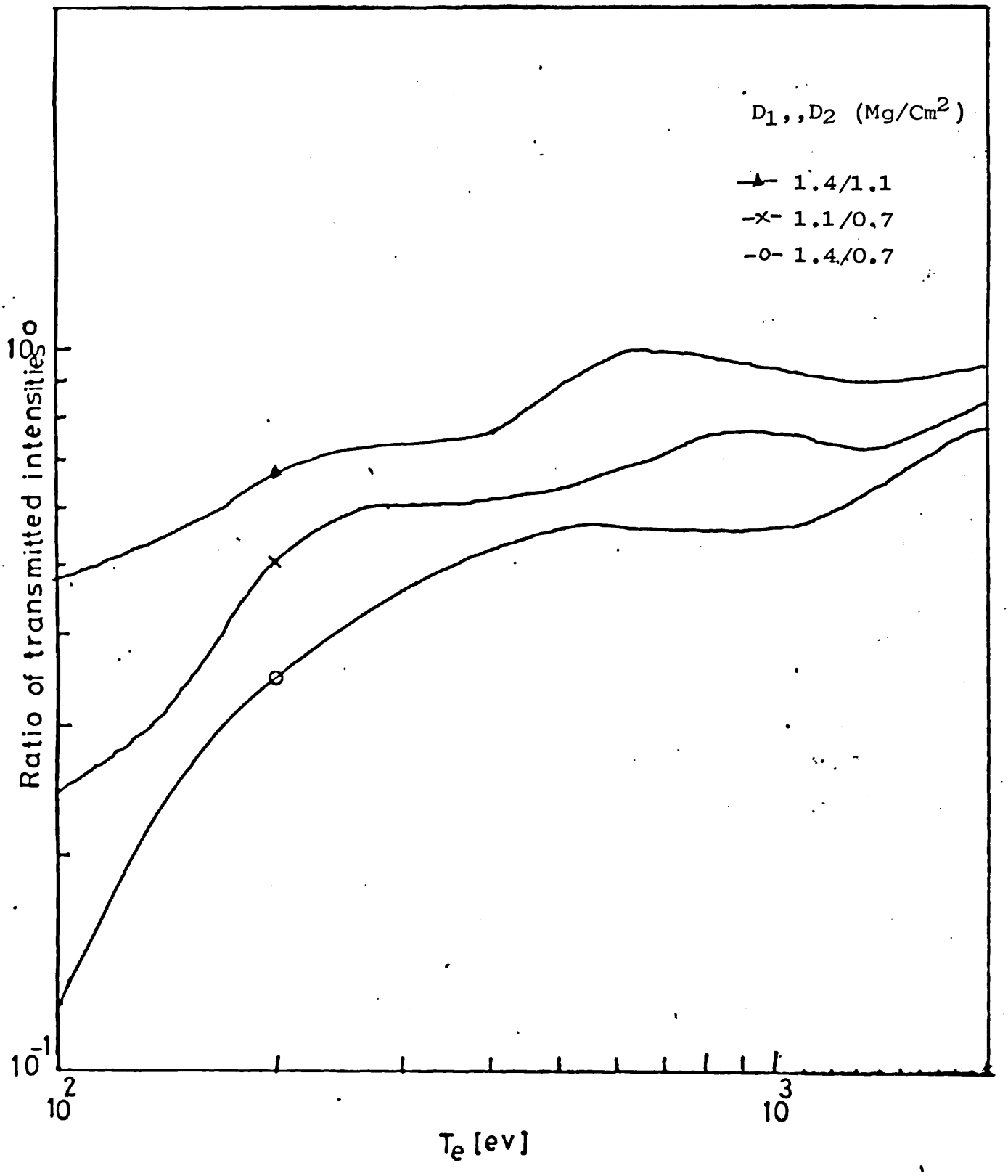

Figure 4.11.

Ratio of Bremsstrahlung radiation transmitted through different thicknesses of aluminum foils Versus temperature

Donaldson (1978). The foil with the lower cut off energy is 3 μ_m thick and the higher cut off energies are 6 μ_m and 8 μ_m thicknesses, as shown in Table 4.2.

TABLE 4.2

Foil thicknesses μ_m	mg/cm^2	Lower cut off energy (keV)	Upper cut off energy (KeV)	Absorption Coefficient
3	0.8	0.8	2.2	2×10^3
6	1.6	1.0	4	8×10^2
8	2.4	1.6	5	5×10^2

The arrangement of each pair of foils which are used as an X-ray absorber in each experiment run are

Foil A_1 0.35 mg/cm^2 mylar + 1.5 mg/cm^2 aluminium
Foil B_1 0.35 " " " + 0.8 mg/cm^2 "
for one run of experiments and
Foil A_2 0.35 mg/cm^2 mylar + 1.6 mg/cm^2 aluminium
Foil B_2 0.35 " " " + 2.4 mg/cm^2 "

Energy was absorbed through depth of the mylar, whereas it would have been totally absorbed in the surface of the aluminium , which would then have ablated. The aluminium coating was needed to prevent visible light exceeding the photographic emulsion. By choosing the foil material and thicknesses, a given range of X-ray energies were detected.

Hence, the technique based on the bandpass filter of aluminium with mylar was chosen to selected wavebands below

9 Å. Selecting the waveband required is done by choosing the appropriate absorber, and the positions of the waveband are determined by the value $\mu(\lambda)d$.

Since the plasma emitted a considerable amount of line radiation in the region of the L edge of the aluminium foil, it was necessary that the combination of foils should be opaque to visible light. To mask the continuum radiation in the region below 9 Å the mylar foils were used in combination with the aluminium foils, since they were strongly absorbed in the region of the aluminium L edge, as shown in Figure 4.12.

The X-ray absorption in matter, low for combination of two different foils, becomes

$$I_T(\lambda) = I_o(\lambda)\, e^{-\mu_M(\lambda)d_M - \mu_{Al}(\lambda)d_{Al}}$$

where the subscript, M, denotes the mylar and A denotes the aluminium. Since we are using constant thickness of mylar and different thicknesses of aluminium, as illustrated in the previous section, then the relative intensities transmitted through two different combinations will depend mainly on the aluminium foils, as

$$I_{T1}/I_{T2} = \exp\left[\mu_{A2}(\lambda)d_{A2} - \mu_{A1}(\lambda)d_{A1}\right]$$

where A_2 is the high cut off energy and A_1 is the low cut off energy aluminium foils.

To analyse the X-ray emitted from the plasma, two methods for time and space integrated spectra were used.

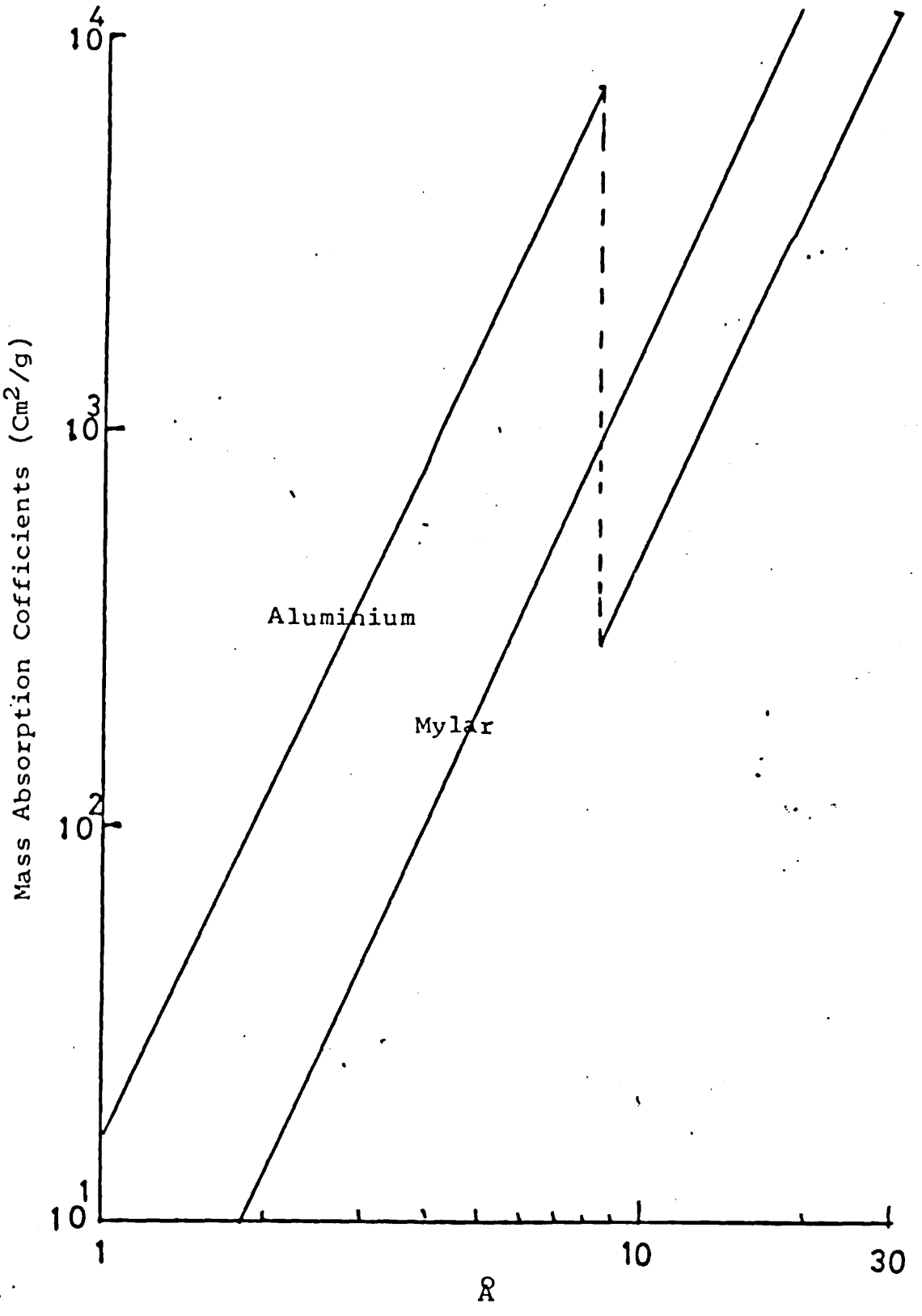

Figure 4.12.

Mass Absorption Coefficients for

Aluminium and Mylar

4.5.2.1 The Pinhole Camera

Spatially resolved measurements of the X-ray emission from the laser produced plasma were made with the aid of an X-ray camera. This camera had twin pinholes 3 mm apart, as shown in Figures 413 and 4.14. Time integrated two images were recorded simultaneously. The radiation from each pinhole passed through different foils. The pinholes were interchangeable and of diameter 25, 50 or 100 μm. Independent X-ray filters were placed over the two pinholes, as shown in Figures above. The body of the camera consisted of a truncated aluminium cone in the end of which were mounted the pinholes and the X-ray absorber filter. The conical shape caused least obstruction in the interaction chamber. The film holder was threaded onto the base of the camera 70 mm from the pinhole. The camera was mounted at 45 degrees to the laser beam axis, 15 mm from the target, resulting in a magnification of 4.7 times. Two images were recorded on Kodak No-screen film, so that the X-ray distribution in the image could be determined after microdensitometer measurement. An example of the pinhole image is shown in Figure 4.15. The resolution of the camera was calculated as 30μ_m, Donaldson et al (1973), which provides nearly six image points across the plasma diameter.

4.5.2.2 Scintillator and Photomultiplier

An alternative method of measuring X-ray intensities consists of a plastic scintillator and a photomultiplier, as shown in Figure 4.16. The scintillator was a plastic

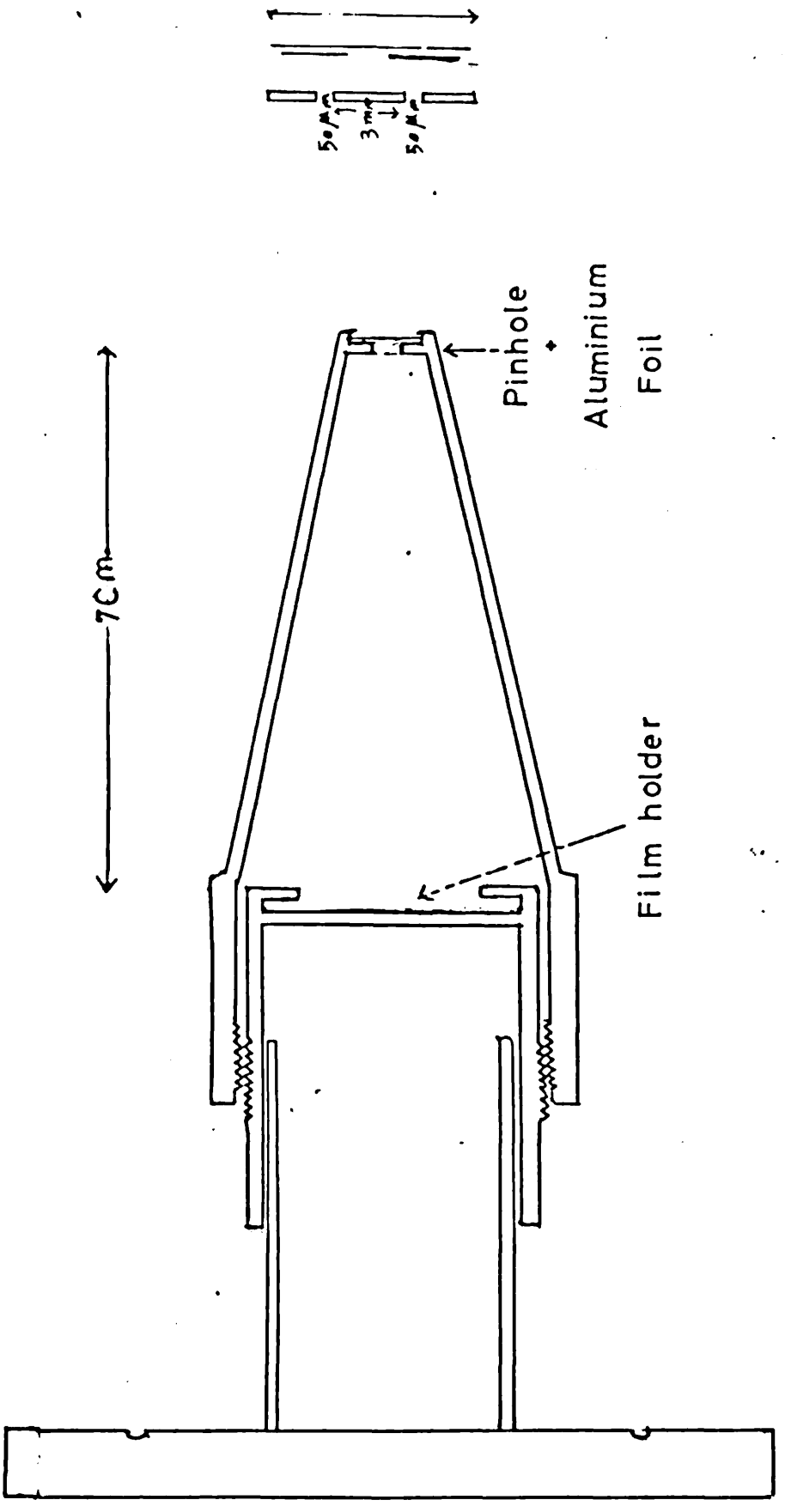

Figure 4.13.
X-ray Pinhole Camera

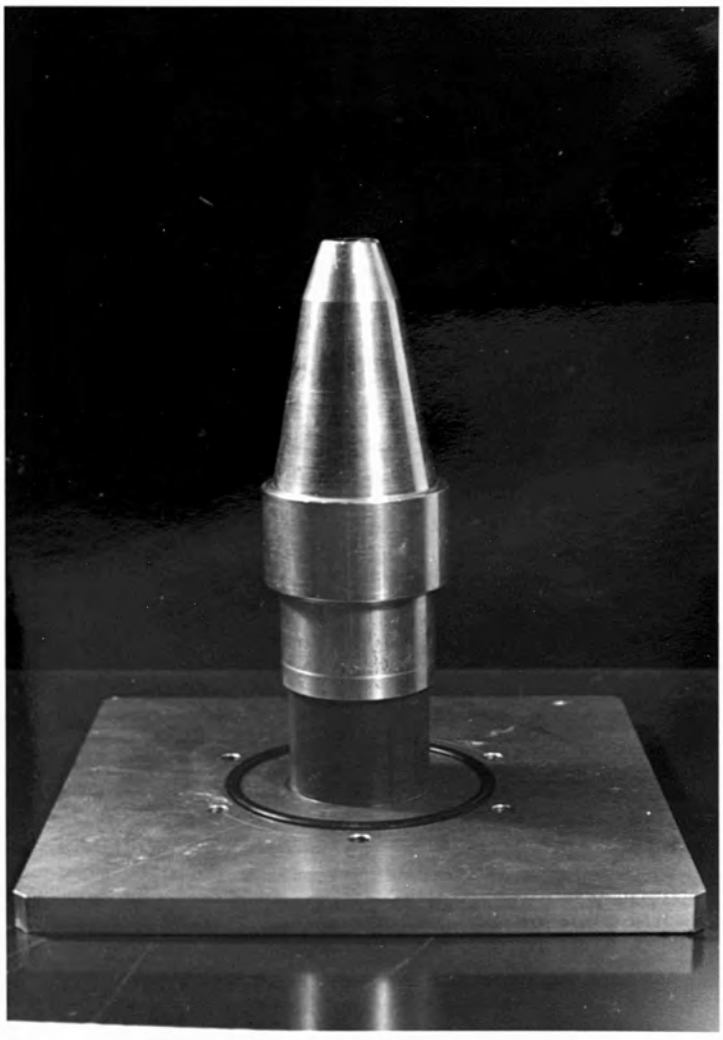

Figure 4.14.

X-ray pinhole camera

180 μ m

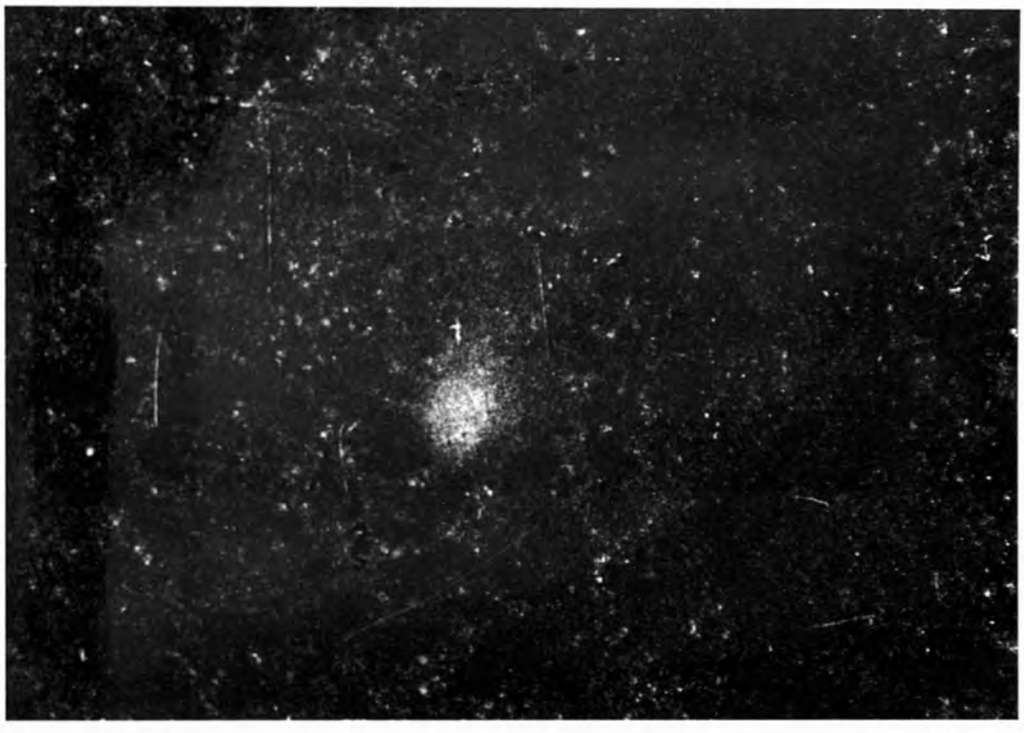

Figure 4.15$_a$.

X-ray pinhole image

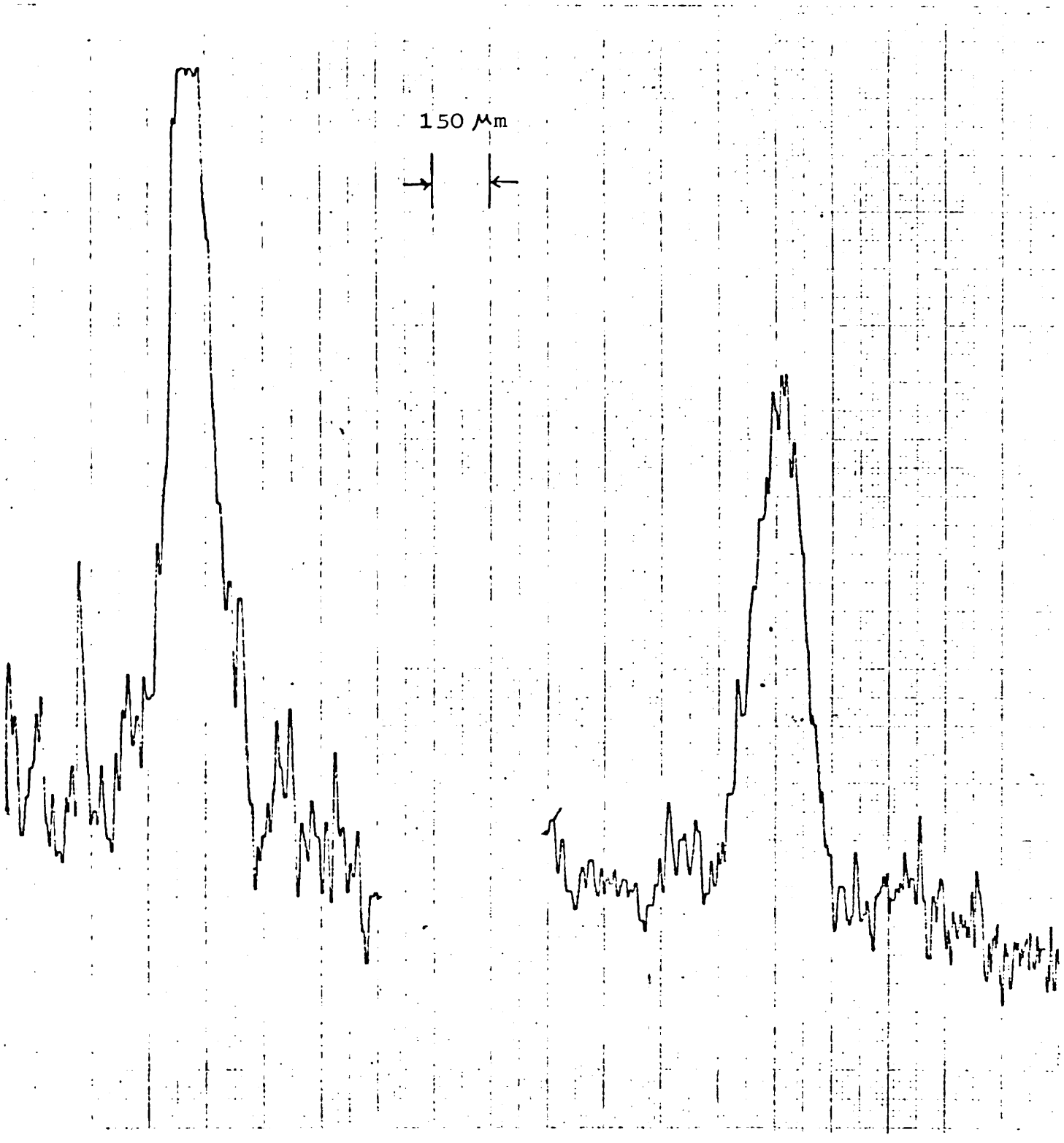

Figure 4.15b

Microdensitometer trace for The X-ray images

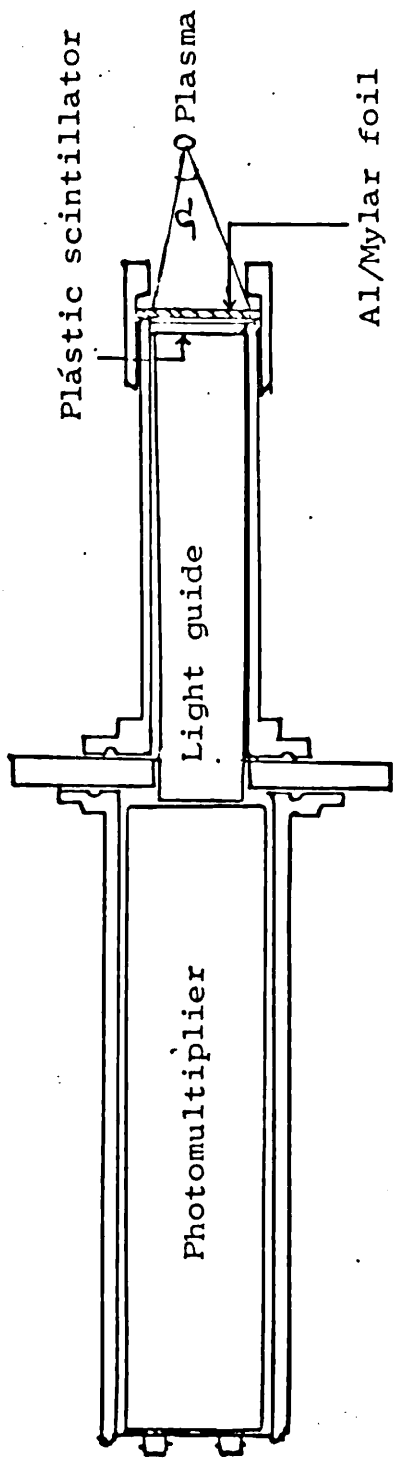

Figure 4.16: Photomultiplier/Scintillator Detector

disc, NE102 Nuclear Enterprises, shielded by thin foils. The scintillator was connected through a 20 mm diameter, 100 mm length, perspex light pipe to a photomultiplier, EMI type 9592B CS20 photocathode. The light pipe was coated with silver to stop the strong light reaching the photomultiplier. The optical pipes were connected to their respective photomultipliers outside the vacuum chamber by using optical cement of refractive index, near to that perspex light pipe. The acceptance angles of the foil windows at the end of the light pipe were defined by 2 cm diameter apertures 10 cm from the focal region of the target, as shown in Figure 4.16. The intensity of line radiation transmitted through the foils was negligible, compared with that of the X-ray continuum.

To detect two signals at one laser shot, with two different thicknesses of absorber, the two scintillators must view the same volume of plasma, therefore the scintillators were mounted at the 45 degree windows from the laser axis, as shown in Figure 4.17.

4.6 MAGNETIC FIELD MEASUREMENT

The magnetic probes which have been used for measuring pulsed magnetic fields in plasmas, Lovberg (1965), may also be used to study the fields spontaneously generated in laser produced plasma, Stamper et al (1971), Bird et al (1973). A recurrent problem is the stray field generated by spark gaps and capacitor banks, but this effect may be overcome by using two coils in such a way that they

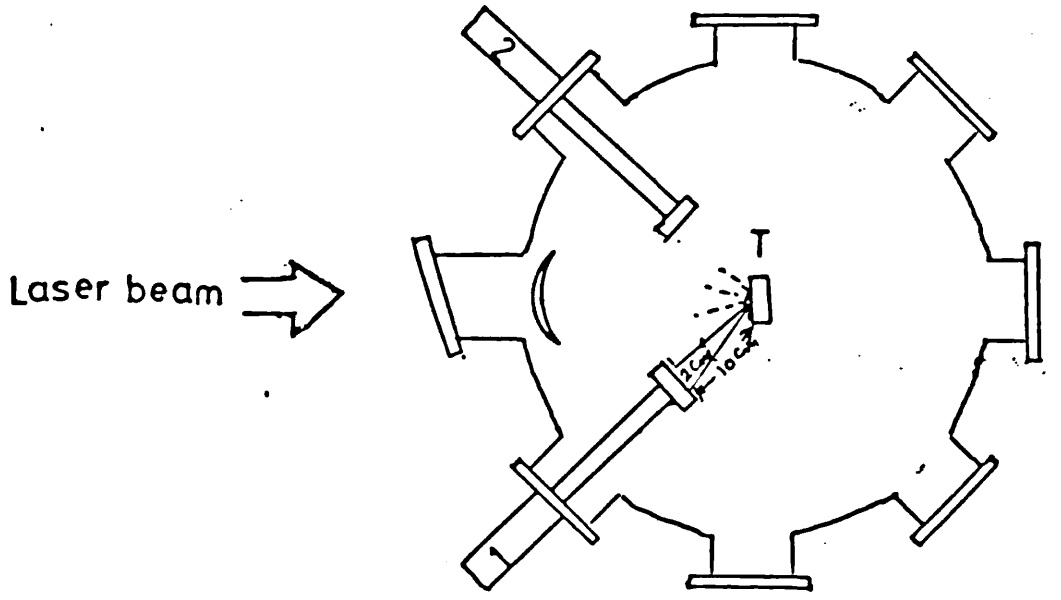

Fig. 4.17

Plasma diagnostic apparatus

1 & 2 photomultiplier/Scintillator detector 1

T Target.

compensate against electrical interference, Serov et al (1975). Compensation was achieved by winding two coils in antiphase and connecting them individually to two co-axial cables, as shown in Figure 4.18. The cables were then joined together at the same distance from the inter-action chamber, where the interfering signals were negligible. (See Appendix I for theory and details.)

The probe consisted of two identical single turn coils of loop diameter 2 mm from copper wire of thickness 0.1 mm situated in close proximity, with axes parallel, but winding directions opposed. The coils were connected to two 50 ohm cables which are joined at that distant end, as shown in Figure 4.18. The coils were compared with PTFE and encapsulated in plastic to reduce the photo-emission signal resulting from X-ray, UV radiation and particles striking the probe surface.

The signal at the oscilloscope from one coil is:-

$$N_1 + nA \frac{dB}{dt} = V_1$$

where N_1 is the noise of the cable, n the number of turns and A is the area.

The signal from the other coil is

$$N_2 - nA \frac{dB}{dt} = V_2$$

Using identical cables, connected as shown in Figure 4.18b,

$$N_1 = N_2$$

If the signal were fed to a differential amplifier in the

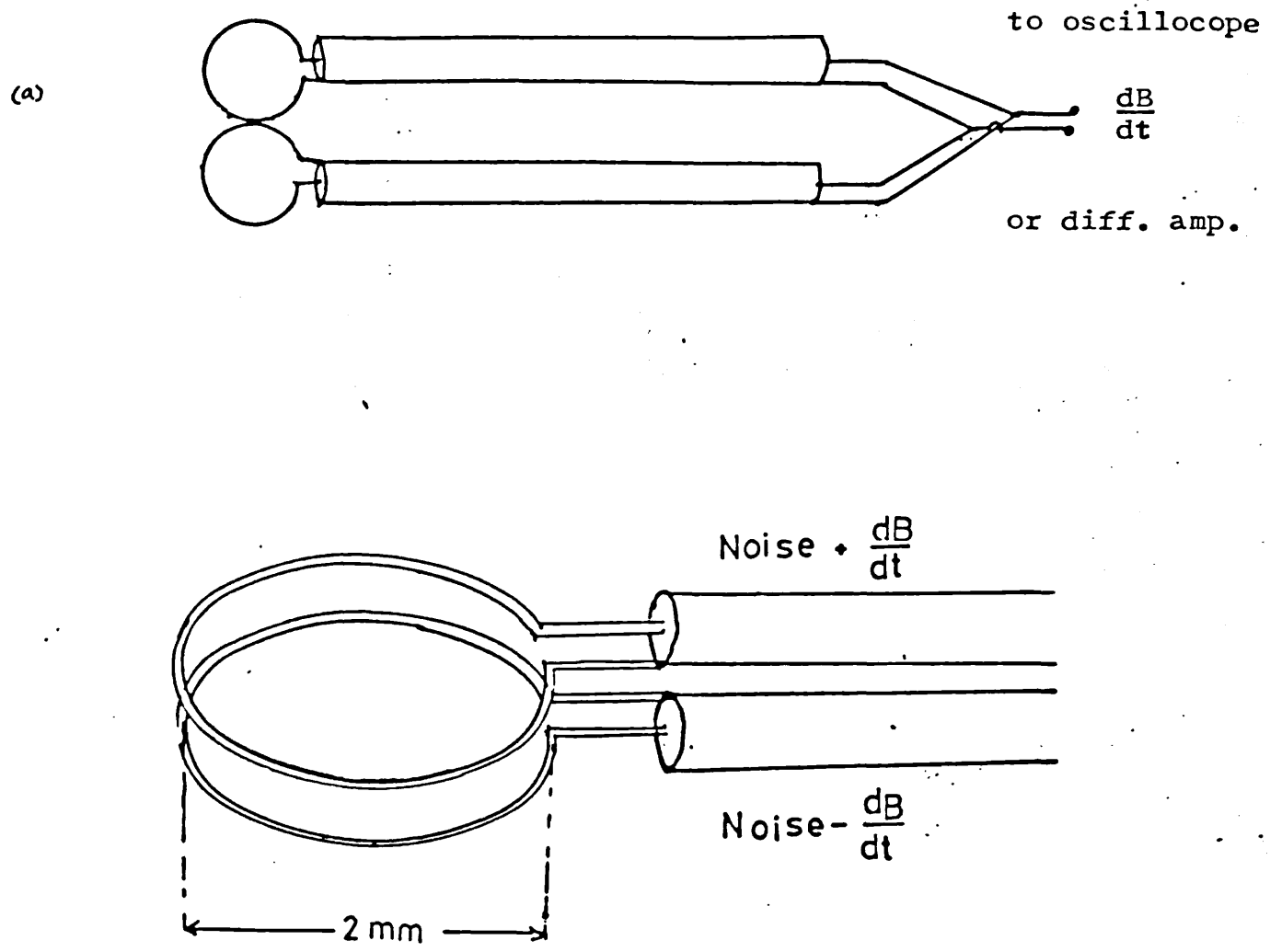

Figure 4.18.

Schematic configuration of double coil differential magnetic probe

oscilloscope, Tektronix 7409, then

$$V(t) = V_1(t) - V_2(t) = nA\left(\frac{dB}{dt} + \frac{dB}{dt}\right)$$

which gives the temporal variation of the magnetic field.

For accurate magnetic field measurements, the sensitivity of the probe was calibrated experimentally by using the circuit shown in Figure 4.19, by inserting the probe between two coils 2 cm diameter separated by 2 cm and connected in series with a 1 μf capacitor charged to 20 kV. When the circuit was closed by a spark gap, the accurate pulse of half peak duration 10^{-8} sec was produced. The current passing through the two coils was measured with a probe type Tek. CT5, allowing the sensitivity of the magnetic probe to be found. It was 0.31 V/G/nsec and the time response of the probe $\frac{L}{R}$ was calculated to be 26 psec.

For measuring the magnetic field near the focal spot on the target the probe was mounted at 45 degrees to the optical axis. It could be easily moved to different distances from the target. The value of the magnetic field can be deduced from oscillogram on the oscilloscope by integrating the area under the peak of the pulse and multiplying it by the sensitivity of the probe.

$$B \propto (V_1 - V_2)\, dt$$

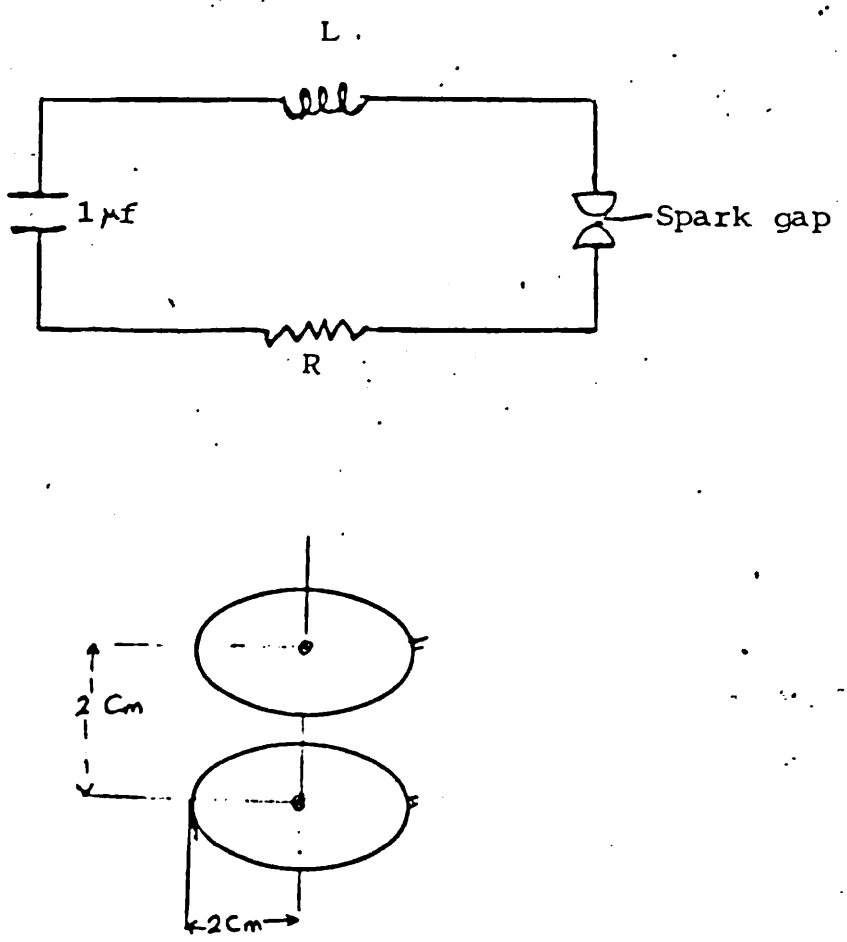

Figure 4.19.

The electric circuit used for calibrating the probe.

CHAPTER 5

EXPERIMENTAL RESULTS

5.1 INTRODUCTION

It was seen in Chapter 2 that there are several interaction processes which can occur on irradiating a solid target by high power laser radiation. The principal processes which are predicted are stimulated Brillouin scattering, stimulated Raman scattering, two plasmon decay and a resonance. Hence, it is expected that the plasma will contain ion acoustic waves of frequency ω_{ia}, plasmons of frequency $\omega_e \simeq \frac{\omega_o}{2}$ and multiples of these quantities.

The spectrometer was set up to record frequencies of ω_o, $\frac{3}{2}\omega_o$ and $2\omega_o$, the measurements being described below and the significance of the results being discussed in the following chapter.

5.2 INTEGRATED REFLECTIVITY MEASUREMENTS

The overall reflectivity was equated to the ratio of the backscattered radiation at all wavelengths to the incident laser irradiance and is plotted against irradiance in Figure 5.1. This was measured by time calibrated photon drag detectors, Rofin models 7411 and 7415, the latter having X100 amplifier, model 7402, which received radiation reflected from Kcl beam splitter as shown in Figure 4.2. It is assumed that the reflection from the two faces are equal. The signal of

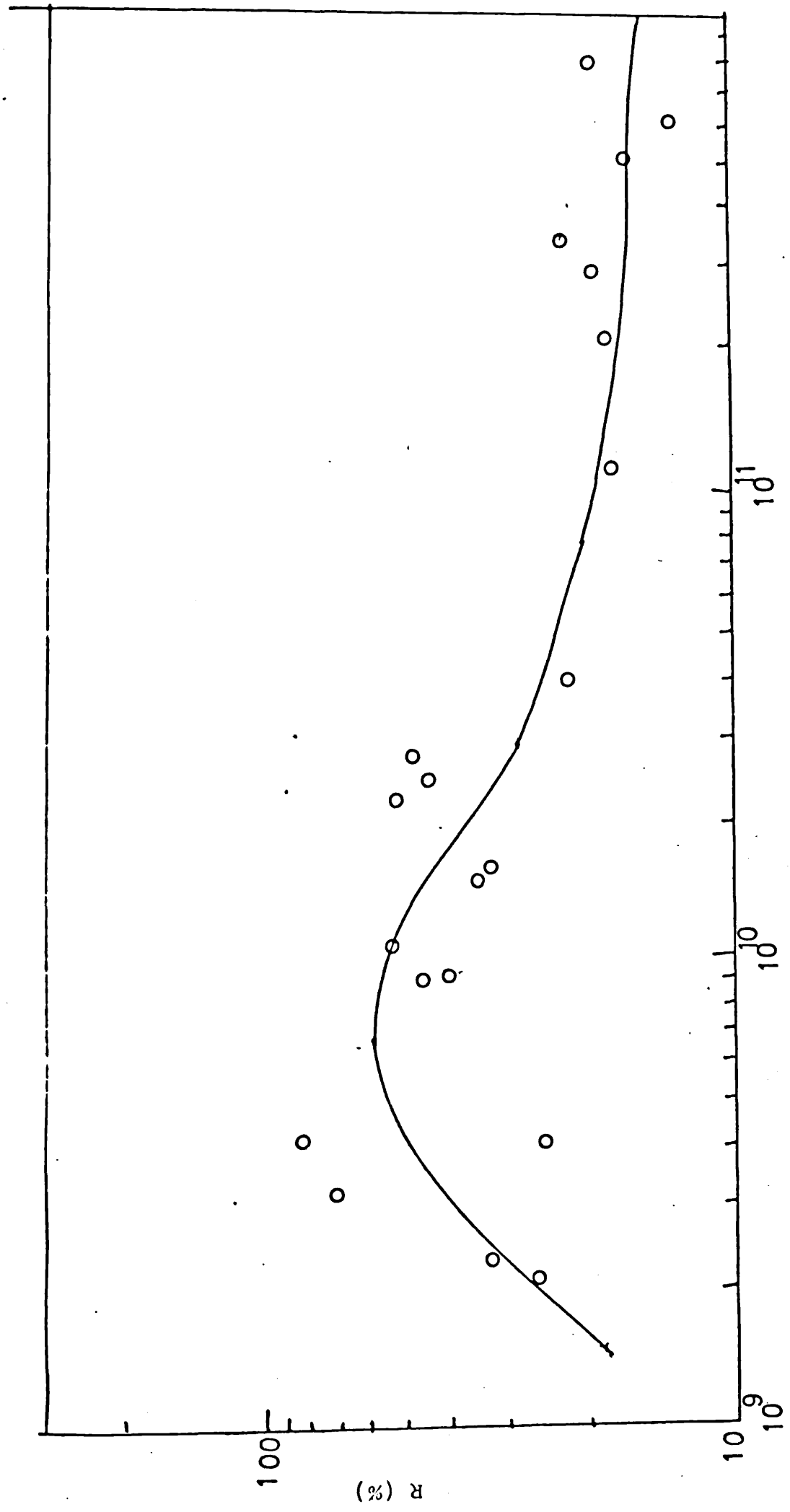

Figure 5.1:

Reflectivity of the plasma vs. Irradiance

incident and backscattered were received simultaneously on a Tektronix 556 double beam oscilloscope.

In Figure 5.2, it is seen that the backscattered intensity increases at a constant rate with increasing laser irradiance up to approximately 2×10^{10} W/cm^2 over this region, the scattered intensity I_s is related to irradiance I_o as

$$I_s = \text{const. } I_o^{1.28} \text{ Watts}$$

Above this value, the backscattered radiation increases rather more slowly and the scattered intensity is related to the irradiance by $I_s = \text{const } I_o^{0.8}$.

The reflectivity of the plasma which is defined by

$$R = \frac{I_s}{I_o}$$

is plotted against the incident irradiance in Figure 5.1, where it is seen that the reflectivity of the plasma attains a maximum value of 53 % at an irradiance of 1×10^{10} W/cm^2. Above this value, the reflectivity falls with increasing irradiance to about 10%.

5.3 BACKSCATTERED RADIATION AT ω_o

A portion of the collimated backscattered light was sampled with a beam splitter and analysed by the method discussed in Section 4.3. The profile of the laser line 10.6 μm and the backscattered radiation ω_o are both shown in Figure 5.3. It is seen that the laser line width plus the instrumental width is 21.0 Å.

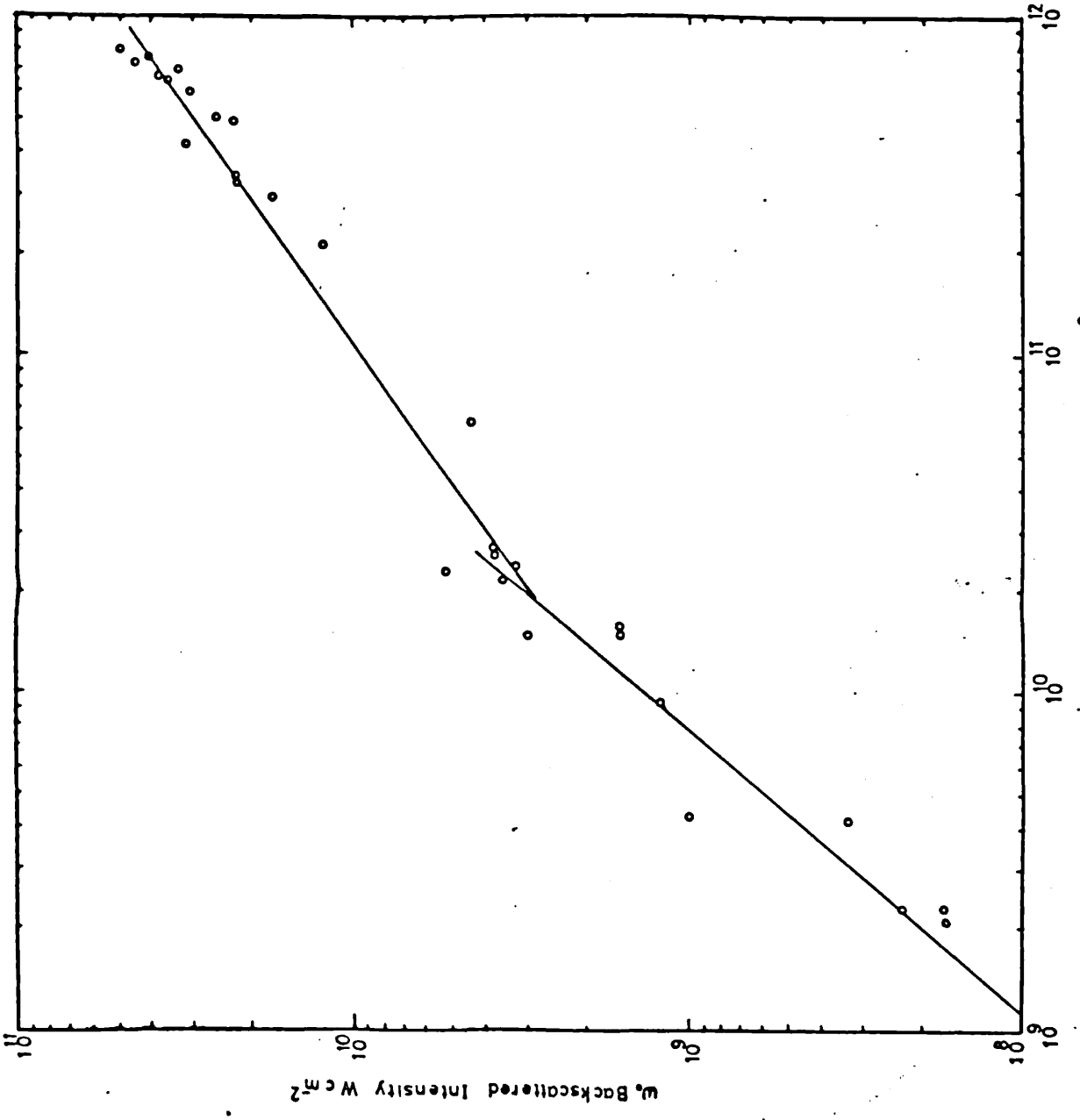

Figure 5.2.

Backscattered Intensity vs. Irradiance.

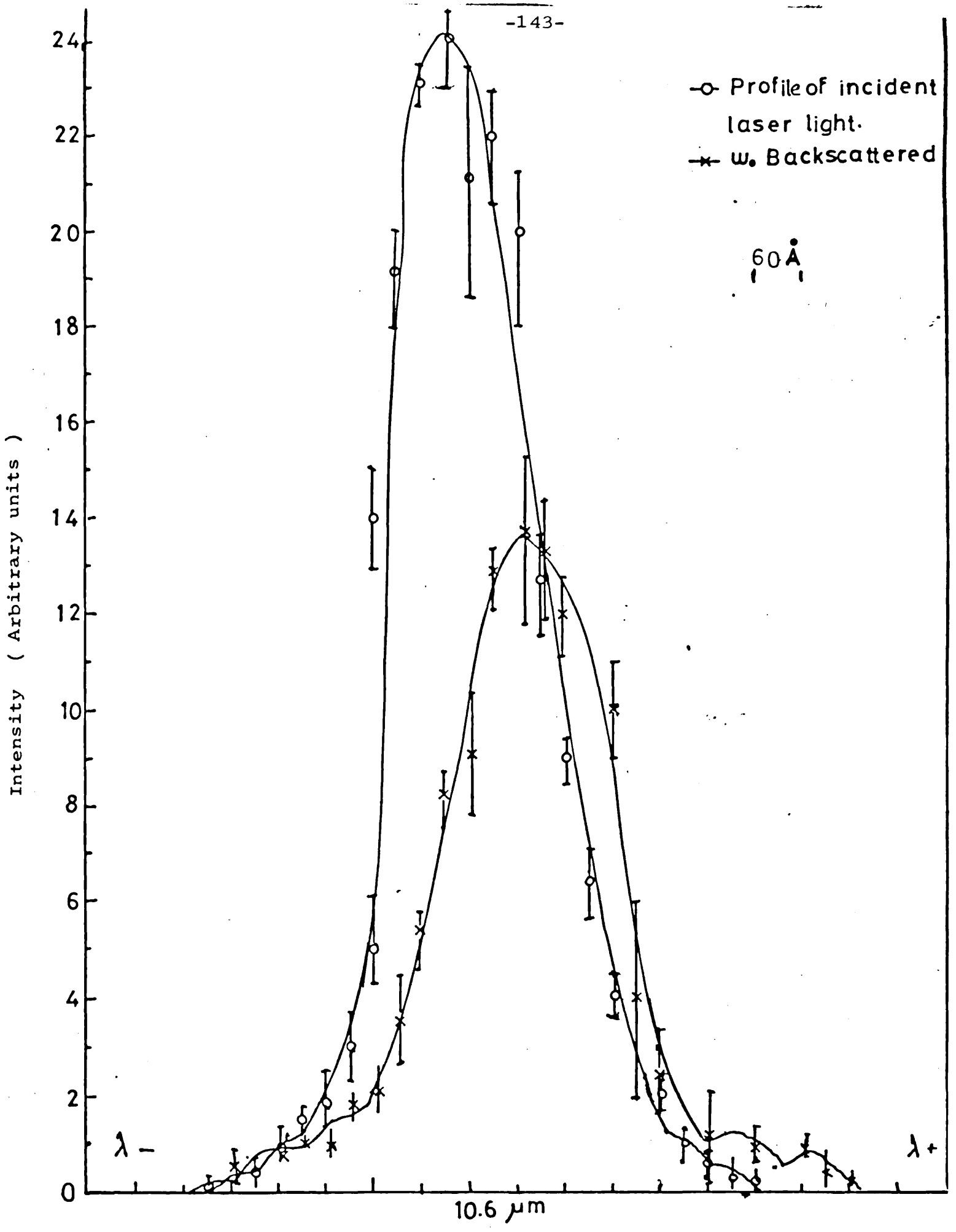

Figure 5.3.

Profile of the incident and backscattered ω_0

The fundamental ω_o of the backscattered radiation was displaced towards larger wavelengths by about 100 Å, depending on the irradiance. It was also broadened to 270 Å. After removing the effect of the instrumental broadening and the laser line width, the width is about 200 Å. The width of ω_o against laser irradiance was also plotted in Figure 5.4 and it varied with the laser irradiance linearly

The displacement of the spectral measurement from the wavelength of the incident radiation is plotted against irradiance in Figure 5.5. It was found that the relationship varied as

$$\Delta\lambda \propto I^{0.2}.$$

5.4 BACKSCATTERED RADIATION AT 2 ω_o

An example of the spectrum in the vicinity of 5.3 μm, a wavelength equivalent to 2 ω_o, is shown in Figure 5.6. It is seen to consist of a broad line slightly displaced towards wavelengths slightly greater than 5.3 μm and a satellite displaced by a further 0.1 μ_m (approximately). There is a shoulder on the long wavelength side of the main feature. Although a search was made over the range 5.1 to 5.45 μm, no other feature was found above the noise level.

This spectrum is obtained from many shots. Consequently, the breadth is an average value, consisting of the true breadth of 2 ω_o convoluted with the instrumental breadth, the width of the original laser line and the displacement from shot to shot.

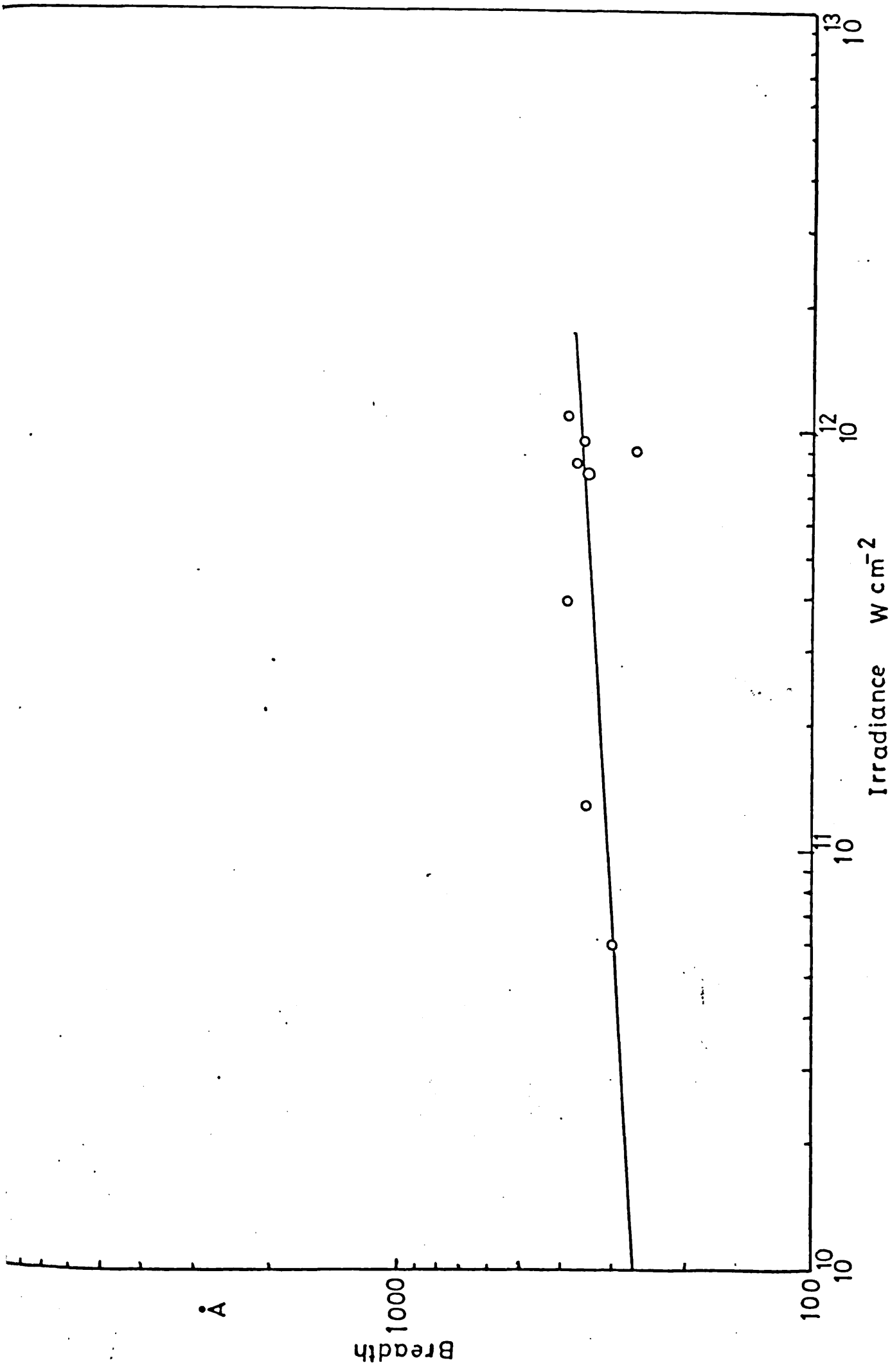

Figure 5.4.

Breadth of ω_0 vs. Irradiance

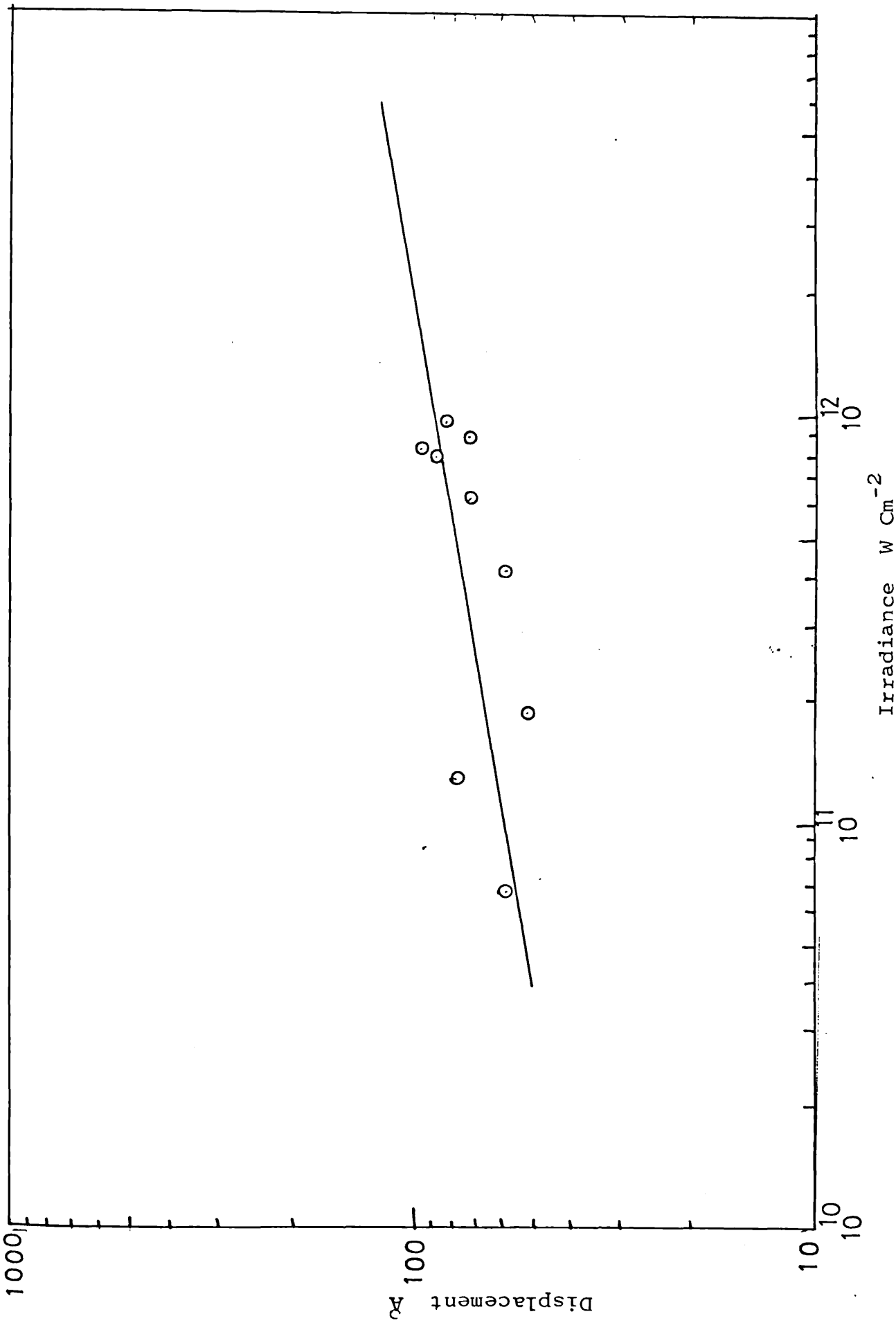

Figure 5.5:

Displacement of the backscattered ω_o vs. Irradiance

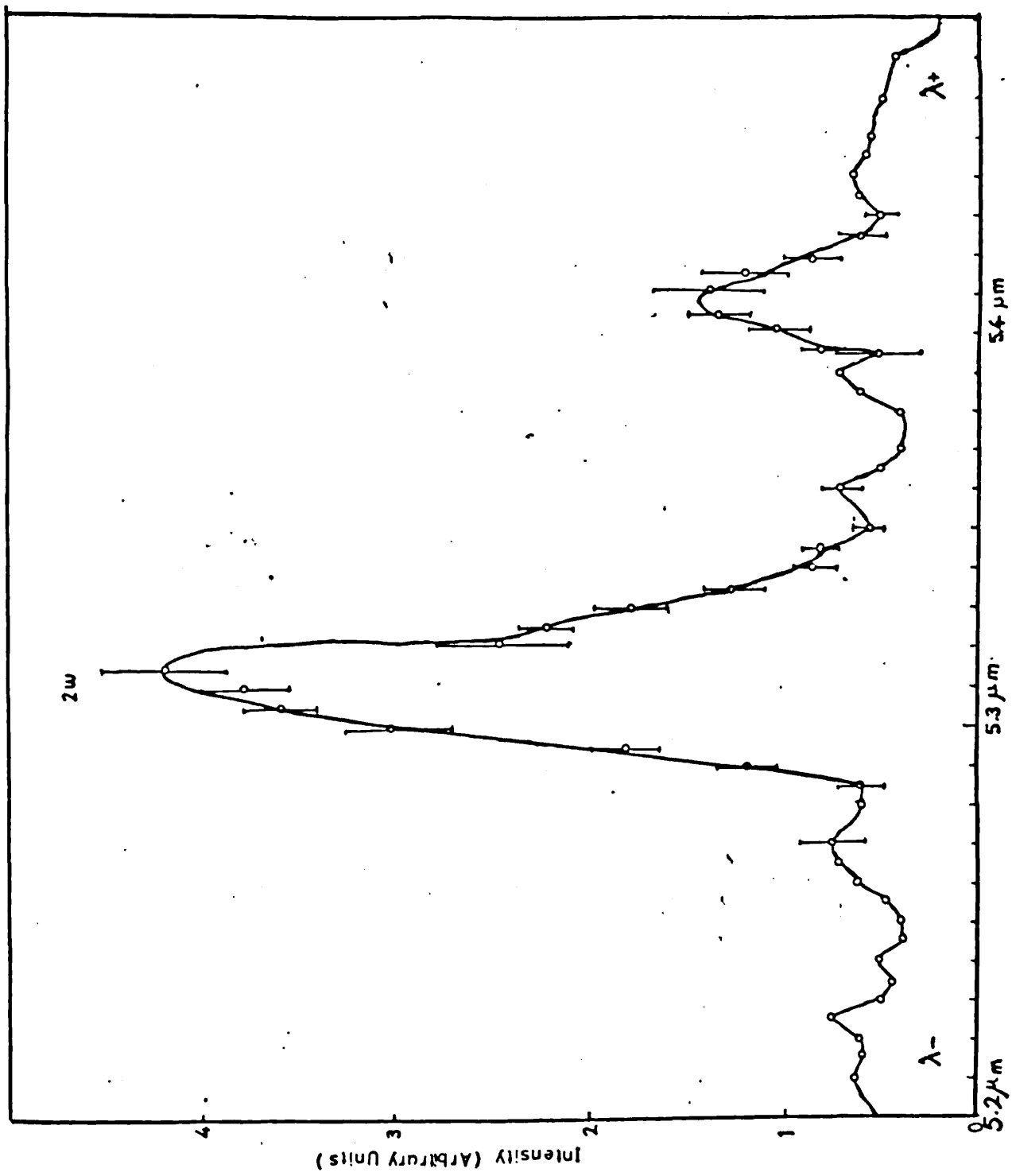

Figure 5.6.

Structure of 2ωo Backscattered

From successive measurements, it is possible to determine an average displacement of the main feature and the satellite, apparent breadths, and backscattered energy, using the spectroscopic system described in section 4.4.

The relative backscattered energy included in the main feature and the satellite are plotted against irradiance in Figure 5.7. To test whether this relationship of scattered energy to irradiance was linear or quadratic, a least square fit was made of both laws. The resulting equations and correlation coefficient are shown in Table 5.1 and it is seen that the linear relationship is the best fit.

TABLE 5.1

Plot	Intercept	Slope	Correlation Coefficient
linear	-0.3	$0.23\ 10^{11}$	0.956
quadratic			0.868

i.e. $E(2\ \omega) = -0.3 + 0.23\ 10^{-11}\ I(\omega_o)$ W cm^{-2}

On an arithmetic linear plot of the back scattered energy against irradiance, as shown in Figure 5.7., it is seen that the threshold power for the generation of $2\omega_o$ is $1.2\ 10^{11}$ W cm^{-2}.

The displacement of the harmonic feature from the precise value of $2\ \omega_o$ is plotted against irradiance on a log log scale in Figure 5.8. On a linear plot, there is a

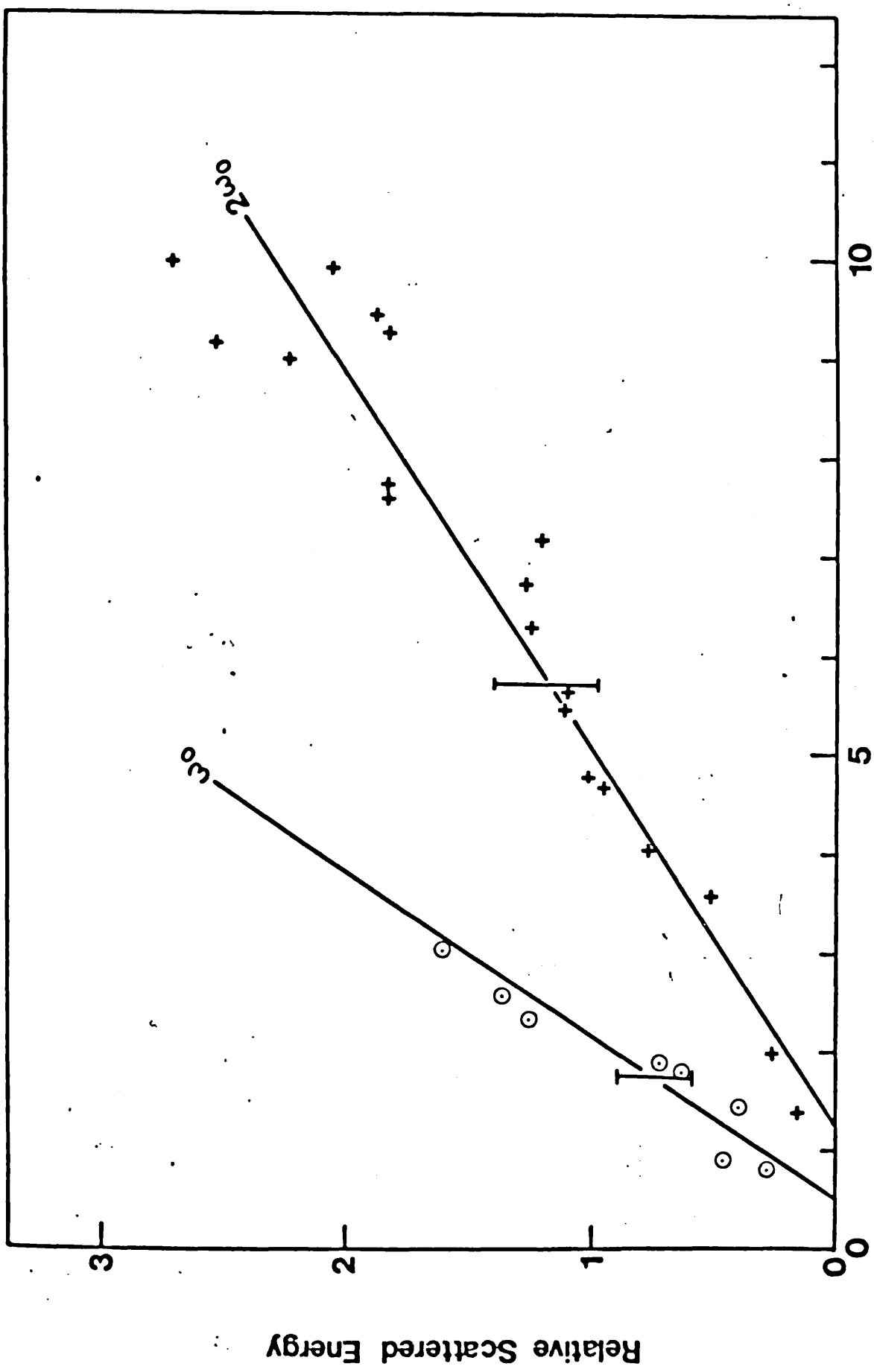

Figure 5.7.

The relation between Relative Scattered Energy
Vs. Irradiance

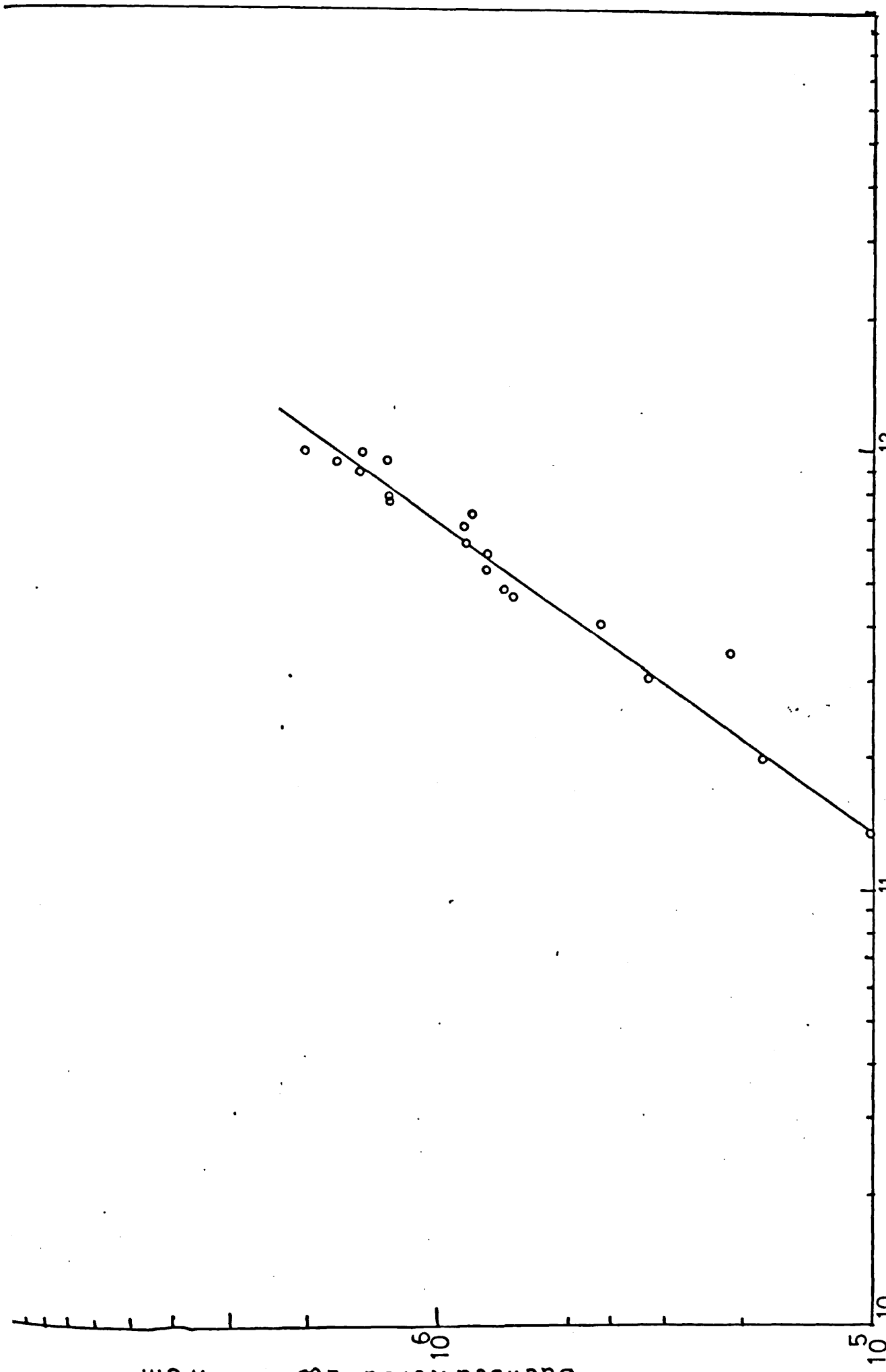

Figure 5.7a.

Backscattered Intensity at 2ω vs. Irradiance.

finite displacement at zero irradiance. The displacement is measured from the true value of 2 ω_o (= 5.32 μm) to the peak of the line. The displacement follows a linear relationship

$$\Delta \lambda = 10 + 2.5\ 10^{-10}\ I_o \text{ micron}$$

There is a finite displacement of 0.006 μm at the threshold irradiance with a smaller displacement increasing with irradiance.

The breadth $\Delta \lambda_{\frac{1}{2}}$ of the feature near 2 ω_o is shown in Figure 5.9 as a function of increasing irradiance. The value $\Delta \lambda_{\frac{1}{2}}$ is the full width half maximum (FWHM) derived after unfolding the instrumental width $\Delta \lambda_I$. This latter value is a convolution of the incident laser line width and the spectroscopic slit width. Experimentally it is equated to the FWHM value of a laser line, such as that shown in Figure 5.3. Deconvolution is obtained as an approximation

$$\Delta \lambda_{\frac{1}{2}} = \left[\Delta \lambda^2_m - \Delta \lambda_I^2\right]^{\frac{1}{2}}$$

where $\Delta \lambda_m$ is the measured FWHM value measured for the $2\omega_o$ line in a plot such as that shown in Figure 5.3.

Similar values of radiant emittance, displacement and breadth are also obtained for the satellite line at 2 ω_o + 0.1 μ_m approx. and are plotted in Figures 5.10, and 5.8 .

The displacement of 2 ω_o towards the red from the original 5.3 μ_m wavelength is plotted against irradiance

in Figure 5.8. There is a finite displacement at the threshold irradiance and a small increase in displacement with increasing irradiance.

In Figure 5.9 is the relation of the width of 2ω against the irradiance, which also slightly increases by the irradiance as $\delta\lambda \alpha \ I_{in}^{0.09}$.

5.4.1 Satellite line $\Delta\omega$

The satellite line $\Delta\omega$ is displaced from the main feature at $2\omega_0$ by about 0.1 μ_m, as seen in Figure 5.5. The relative intensity is plotted against the laser irradiance in Figure 5.10. It becomes apparent above the threshold for 2ω, but the extrapolation from a regression fitted to the experimental point does not permit a threshold for the $\Delta\omega$ line to be determined, the error in the graph is merely statistical errors which are $\simeq$35%.

The displacement of $\Delta\omega$ from 5.3 μ_m is plotted against irradiance in the same figure of the displacement 2ω, it seems that both displacements have first value at the irradiance threshold $\sim 1.1 \times 10^{11}$ W cm^{-2}.

The empirical equations derived from these quantities from linear regression are:-

$E_s = 0.25 + 0.5\ 10^{-11} I_o$ from figure 5.10. with $\pm$ 30% error. With no threshold apparent

Displacement	$\Delta\lambda_s = 0.1$ m	$\pm$ 25%	Figure 5.8.
Breadth	$\Delta\lambda_{\frac{1}{2}s} = 0.02$	$\pm$ 30%	Figure 5.6.

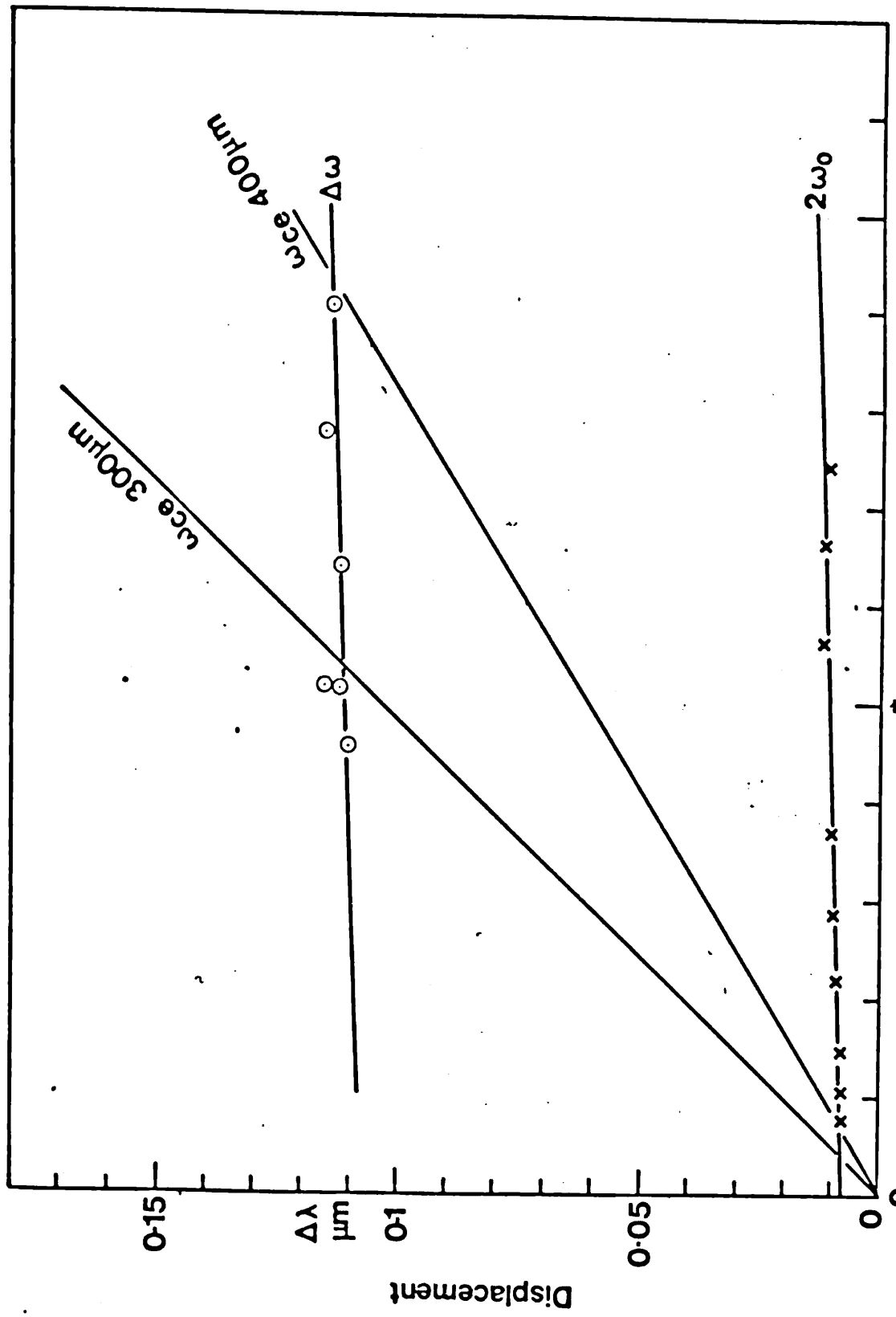

Figure 5.8

Displacement of Second harmonic 2ω, Satellite line Δω and Electron Cyclotron ω_{ce}

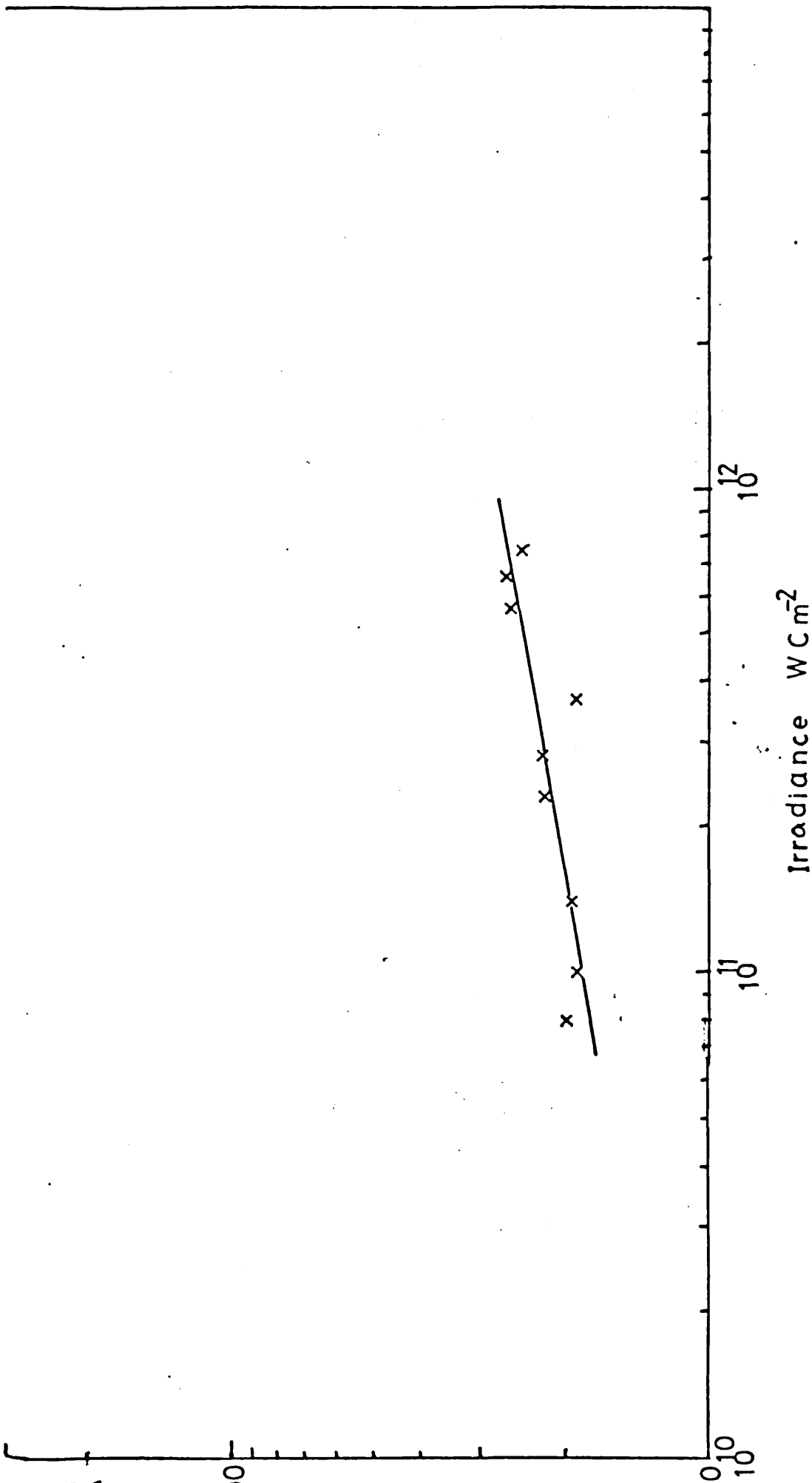

Figure 5.9.

Line Width of 2ω vs. Irradiance

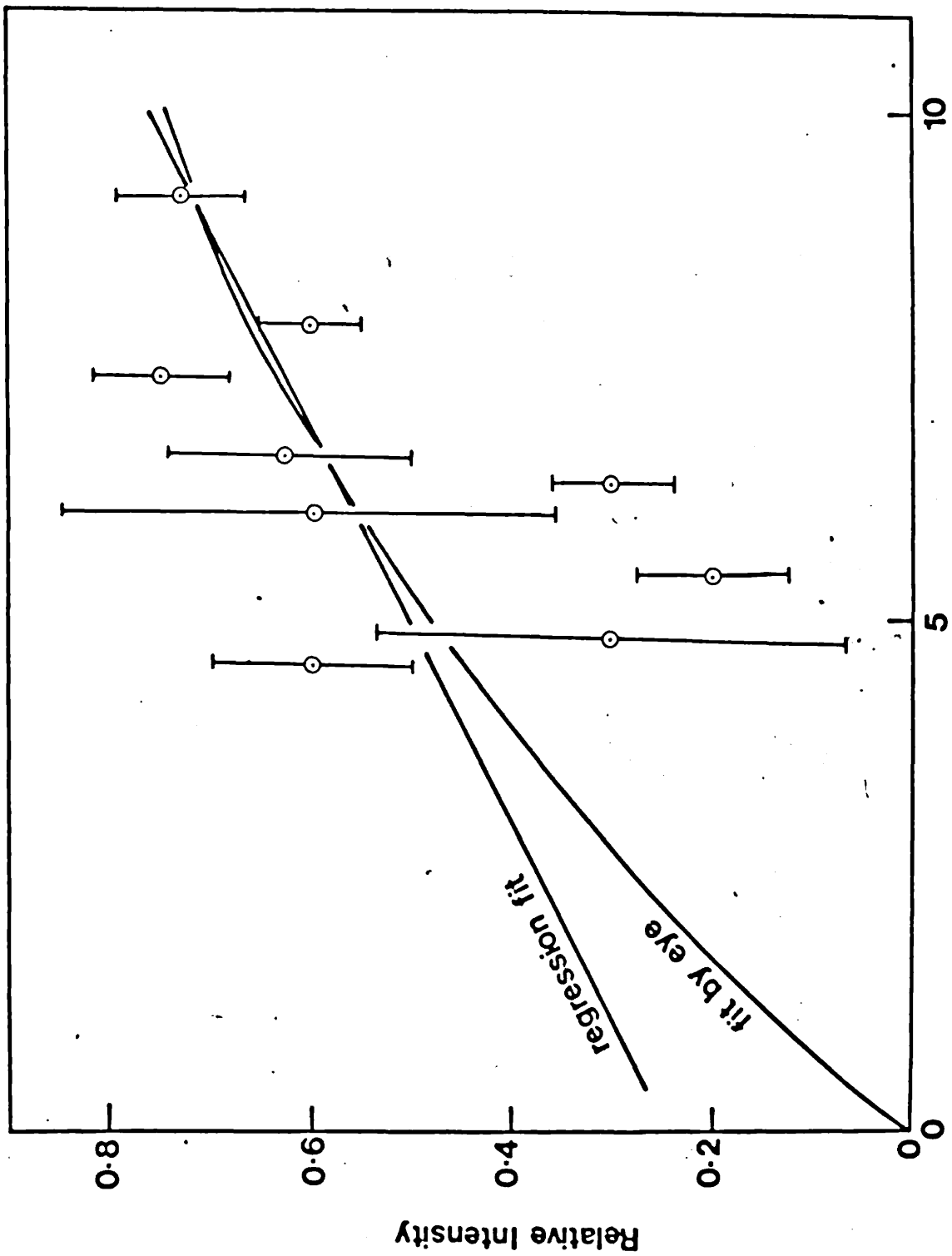

Figure 5.10.

Relative Intensity of the satellite line $\Delta\omega$ vr. Irradiance.

5.5 RADIATION SCATTERED AT $\frac{3}{2}\omega_o$

The emittance of the radiation scattered backwards at $\frac{3}{2}\omega_o$ was determined with a diode and filter as described in section 4.5, and is plotted against incident irradiance in Figure 5.11. There is a threshold irradiance at $0.9\ 10^{10}$ W cm^{-2}. The emittance of the target is about 10^{-2} that of $2\omega_o$ and varies as

$$E_{\frac{3}{2}\omega_o} = 0.3 - 0.2\ 10^{-11}\ I_o \text{ W cm}^{-2}$$

Because of the low intensity of the backscattered light, it was not possible to determine the spectral distribution. Hence, no relationship can be presented for the variation of displacement or breadth with irradiance.

5.6 TEMPERATURE MEASUREMENT

An estimate was made of the temperature of the electrons in the plasma by determining the relative intensities of two regions of the X-ray spectrum using the pinhole camera method described in section 4.5.2.1. Some spatial resolution could be achieved, but it was considered sufficient for our purposes to quote a spatially averaged number.

An experimental study was made of the relationship between focussed irradiance on the target surface and electron temperature and the results are plotted in Figure 5.12. The maximum temperature achieved at an energy of 30J from the laser is $1.4 \text{ kev} \pm 200$ eV. The measurements have been

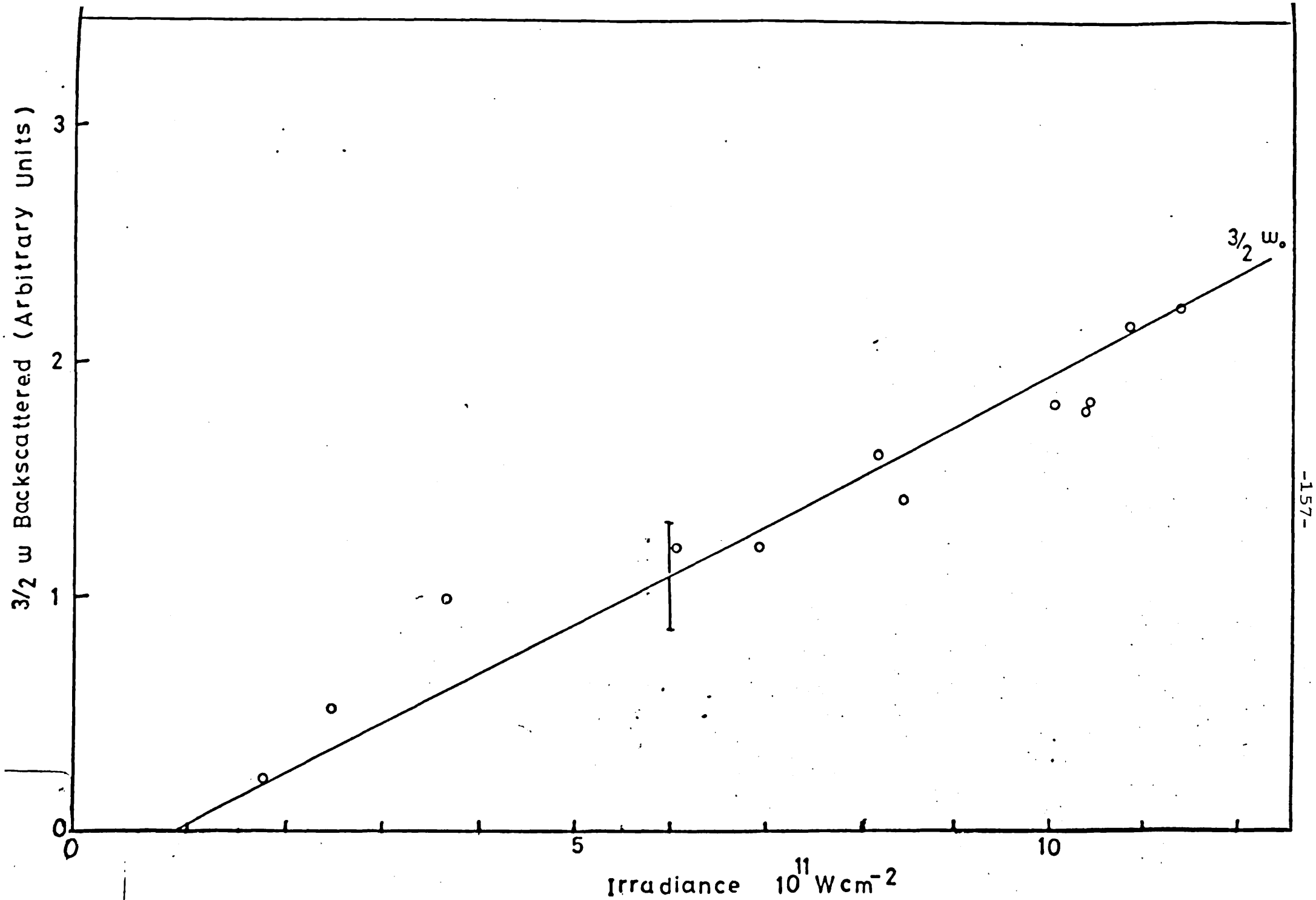

Figure 5.11.

Relative Intensity of 3ω/2 ω₀ Irradiance

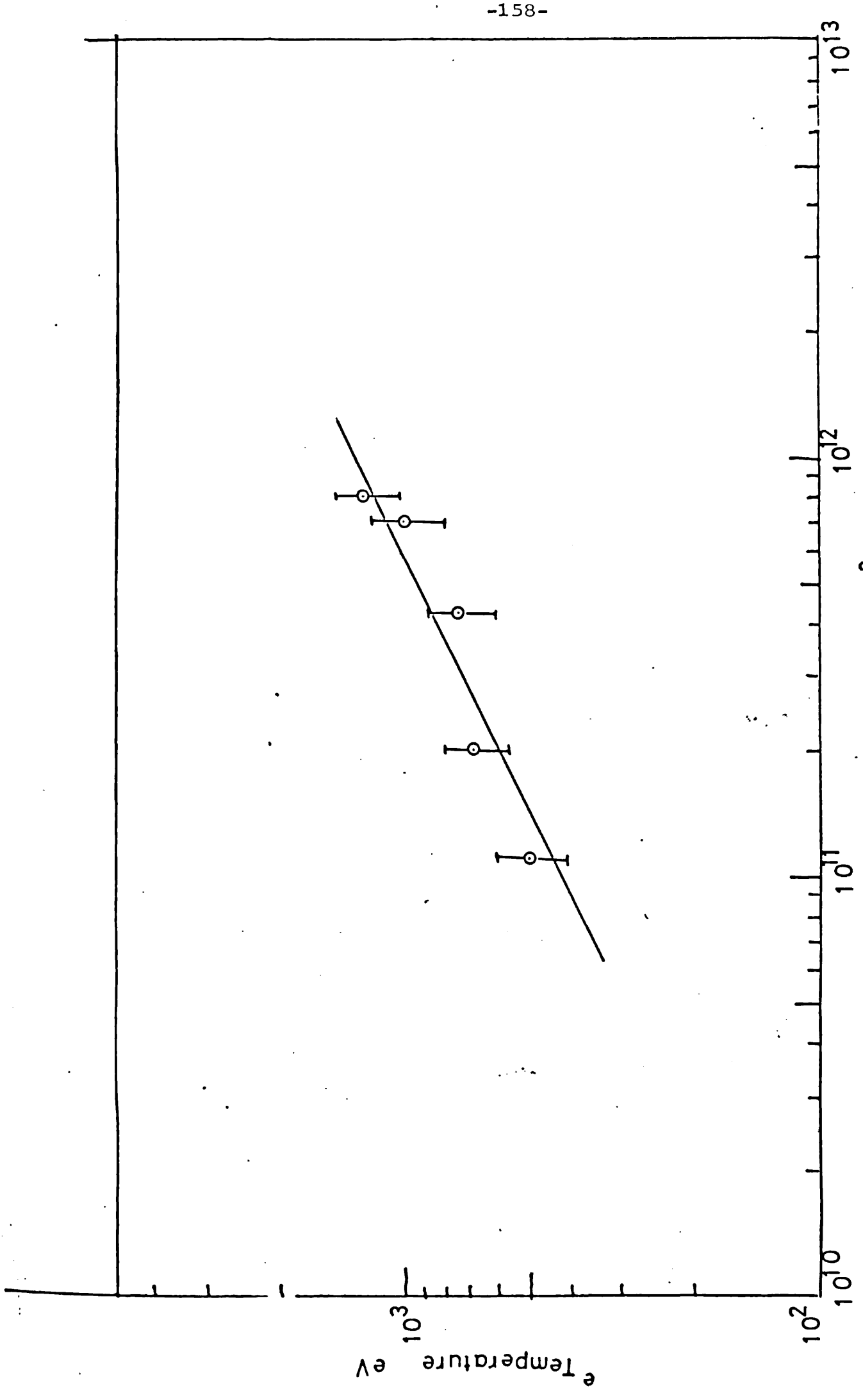

Figure 5.12.

Electron Temperature (from X-ray measurment) vs Irradiance.

carried out with three foil thicknesses 3 μ_m, 6 μ_m and 8 μ_m. The temperature obtained with the different pairs of foils were found to agree with15-20% errors.

5.7 MAGNETIC FIELD MEASUREMENTS

The magnetic field was determined by the magnetic probe described in section 4.6 with sensitivity 0.31 V/G/n sec and time response of 26 p sec.

Figure 5.1 3 shows a typical dB/dt signal which measured the temporal derivative of the magnetic field. It consists of pulses of rise time 10 n sec and fall time 60 to 70 n sec. The duration of the pulse (80 n sec) is appreciably larger than the laser pulse duration, but it is followed by a negative signal of about 4 n sec duration. The peak magnetic field against the laser irradiance was plotted in Figure 5.14 for several values of the distance, r, from the target r = 11, 5 mm and 3.5 mm. The slope increases from 0.5 KG/7 x 10^{11} W cm^{-2} at r = 11 mm to 2.8 KG/7 x 10^{11} W cm^{-2} at 3.5 mm. The peak magnetic field varies with irradiance I_o as

$$B \propto I_o$$

From plots such as those of Figure 5.14 it is possible to obtain a linear regression of B on various functions of r. In Figure 5.15 the relationship of B to $1/r$ is plotted. It is seen that

$$B = a r^{-0.5} \qquad r > 5 \text{ mm}$$

$$B = a r^{-1.4} \qquad r < 5 \text{ mm}$$

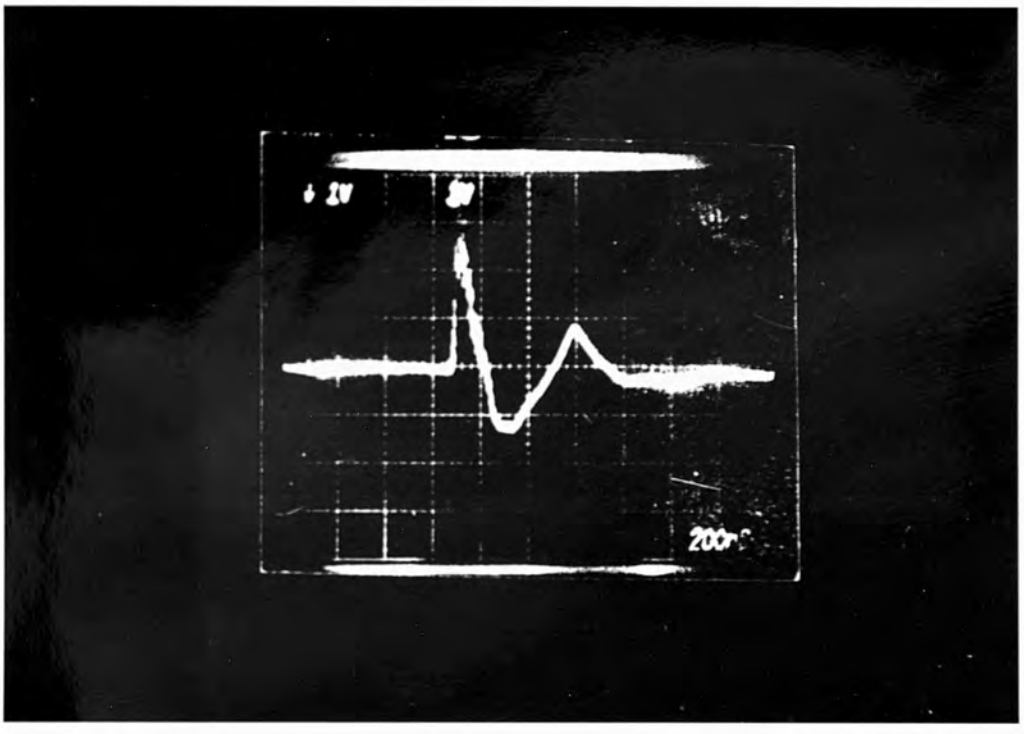

Figure 5.13.

Temporal derivative of the magnetic field $\frac{dB}{dt}$ at r=1 cm and irradiance I=5 10^{11} W cm^{-2}

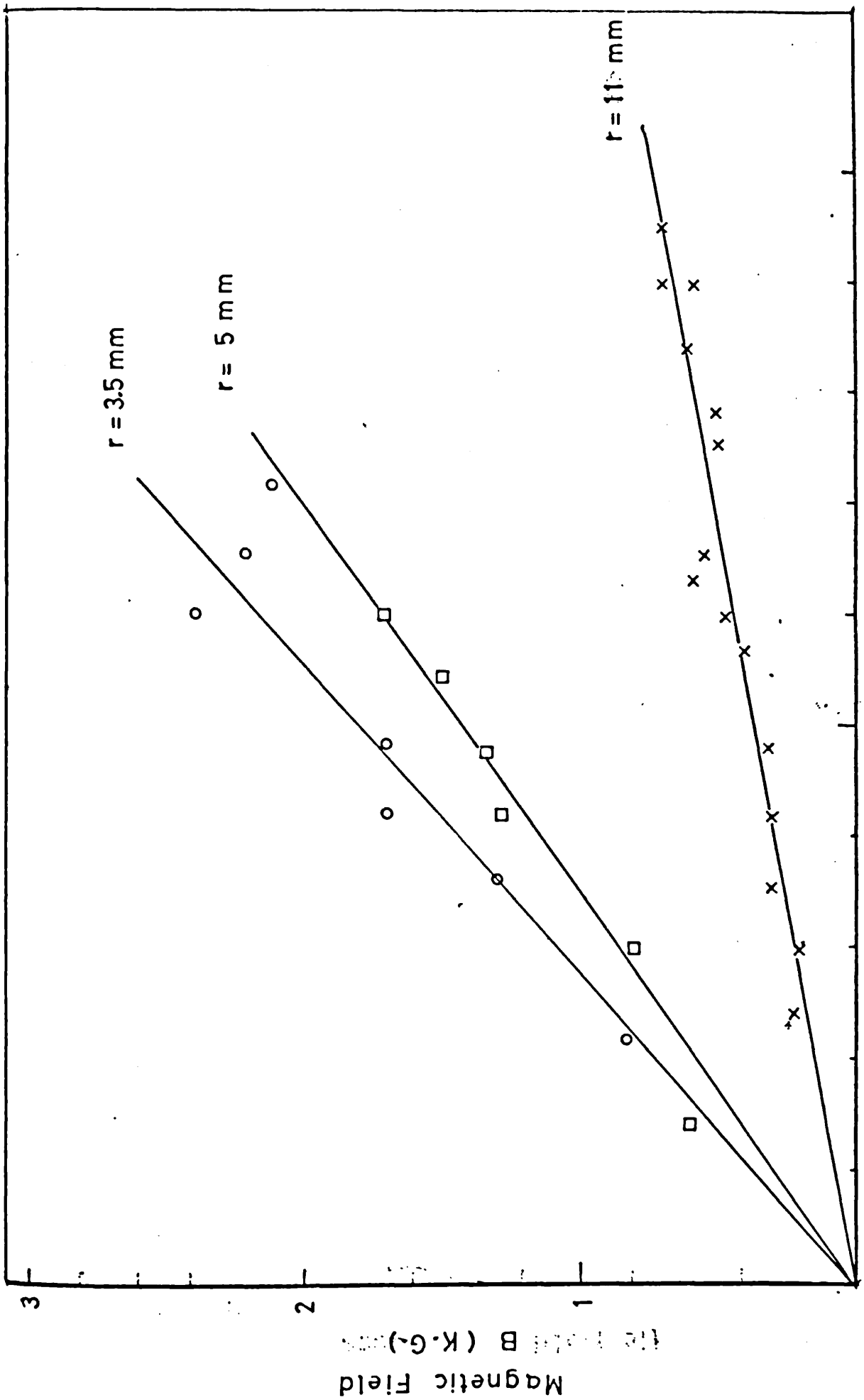

Figure 5.14.

The relation between the peak magnetic field and Irradiance at different distance r

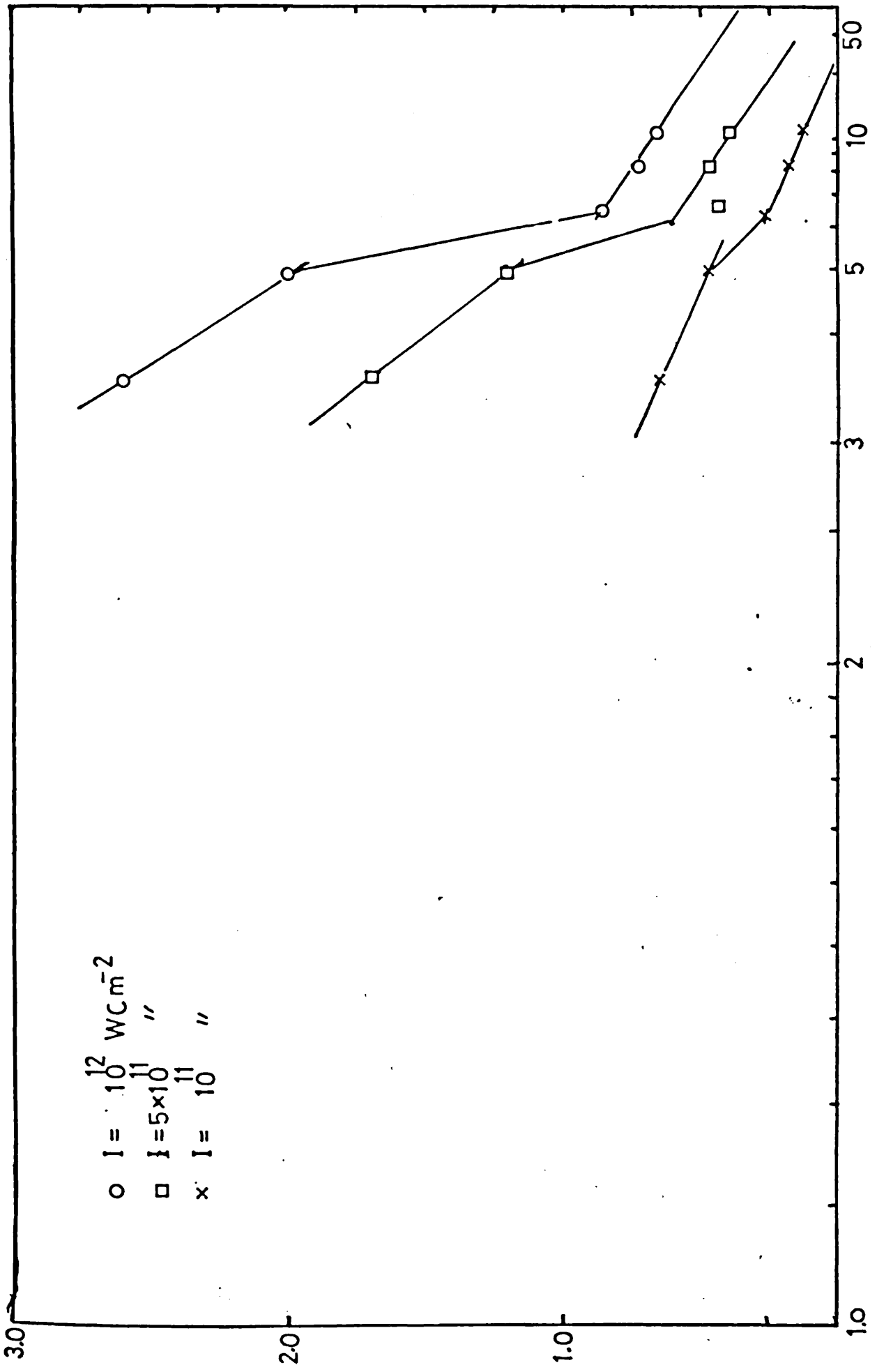

Figure 5.15.

Magnetic field B vs. 1/r for diffrent Irradiance

CHAPTER 6

DISCUSSION OF EXPERIMENTAL RESULTS

6.1 INTRODUCTION

Measurements of the radiation scattered as a result of CO_2 laser radiation interacting with a dense plasma were described in the previous chapter. It was seen that there were strong features at ω_0, $2\omega_0$ and $\frac{3}{2}\omega_0$, but also the spectrum at $2\omega_0$ was accompanied by a satellite.

The significance of the measurements made on these spectra and their relation with parametric processes occurring in the plasma will now be discussed. Measurements of temperature and magnetic field will be used in interpreting the results.

6.2 REFLECTED RADIATION

It was seen in Chapter 5 that the back scattered intensity was considerably lower in the harmonics than at the incident frequency. By taking into consideration detector responsivity and the attenuation factor of the filters for each wavelength, the intensities of these harmonics are seen to vary as:-

I (incident)	I (reflected)	$I_{2\omega}$	$I_{\frac{3}{2}\omega}$
1	0.1	10^{-6}	10^{-8}

Before studying these conversion ratios in detail, it is valuable to examine the reflectivity integrated over all wavelengths. In Figure 6.1 the ratio of reflected to incident energy is plotted against irradiance. It is seen that the relation is non monotonic. A large part of the energy is reflected back at the frequency ω_o, when the irradiance is low, reaching a maximum at 7.10^9 W cm^{-2}. The reflectivity then falls to a few percent at an irradiance of 2×10^{10} W cm^{-2}.

Also in Figure 6.1 is a curve showing the reflectivity expected if the only processes occurring are inverse Bremsstrahlung, according to the equation given by Dyer et al (1974).

$$R = \exp\left(-1.8 \cdot 10^{-3} Z \ln\Lambda L/\lambda^2 T^{\frac{3}{2}}\right)$$

where Z is the average charge of the ions

λ is the laser wavelength

T is the electron temperature

L is the density scale length

$\ln\Lambda$ is the coulomb logarithm

Comparing the two curves indicates that other processes occur. It will be seen in section 6.3 that a parametric process exists which has a threshold irradiance of $2.2\ 10^{10}$ W cm^{-2} and is responsible for reflecting a large proportion of the incident energy. The temperature has been determined in section 5.6. However, this does not explain reflection at an irradiance of less than 10^{10} W cm^{-2}.

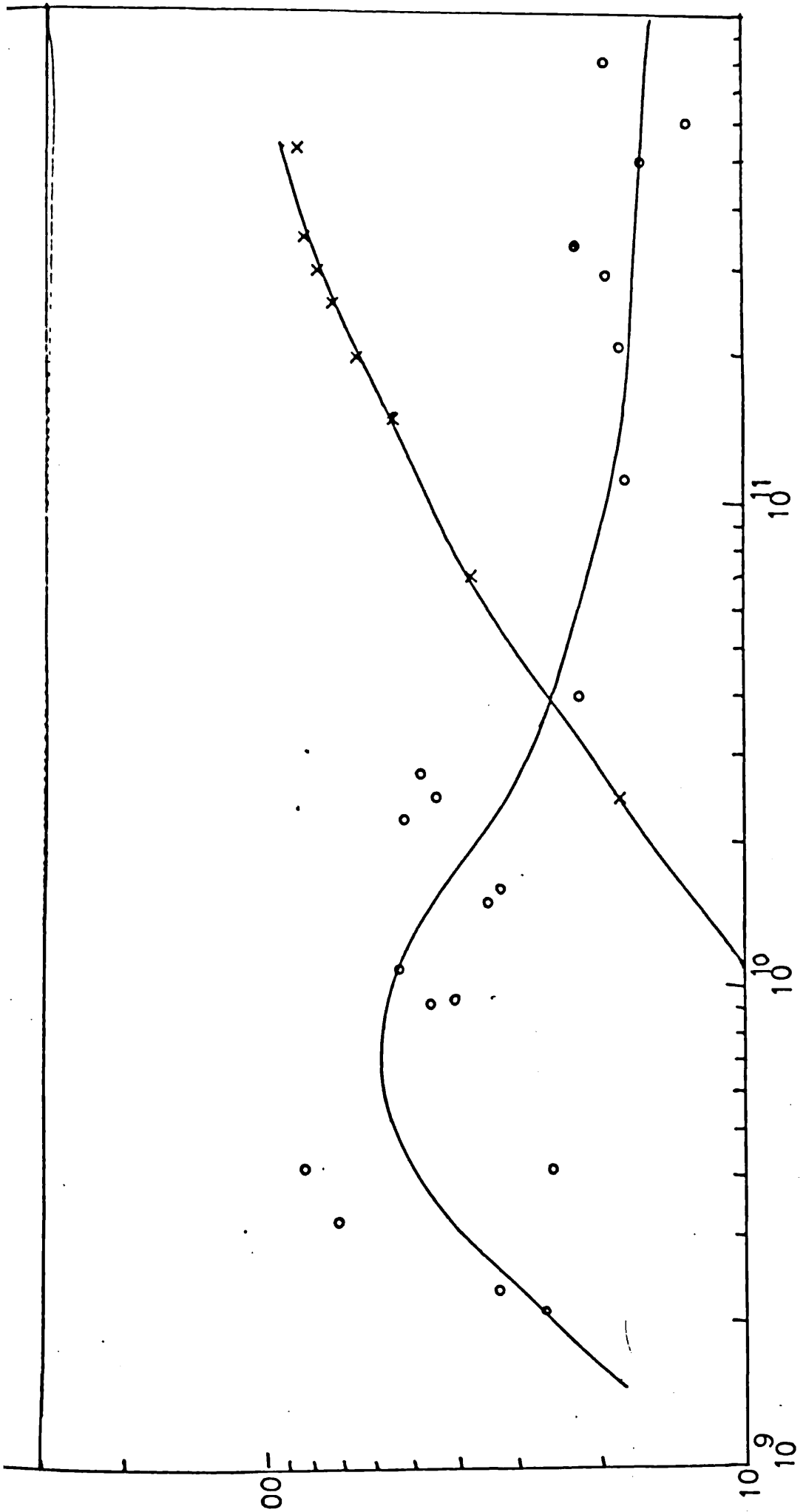

Figure 6.1.

Reflectivity of the plasma vs. Irradiance
-o- Measured reflectivity
-x- Calculated reflectivity

The falling reflectivity above 10^{10} W cm^{-2} indicates that there is anomalous absorption.

6.3 BACKSCATTERED RADIATION AT ω_o

The relationship of the intensity of the backscattered radiation and irradiance with a spectrometer has been seen in Figure 5.1. The results have been used to calculate a conversion ratio which is plotted in Figure 6.2. The scattering at ω_o is attributed to stimulated Brillouin scattering, as described in section 2.5.

The backscattered intensity varies with the incident irradiance as

$$I_{sc} \propto I_o^{\alpha}$$

for the irradiance below 10^{10} W cm^{-2}

$$\alpha = 1.2$$

and above this irradiance

$$\alpha = 0.7$$

showing that there is a transition from one process to another at about 2×10^{10} W cm^{-2}.

The threshold value at which the parametric instabilities develop is given by Nishikawa(1968) as

$$I_{th} \simeq 1.7 \times 10^9 \, (n_e/10^{19})^{3/2} \, (10^4/T_e)^{\frac{1}{2}} \text{ W cm}^{-2}$$

using the value of temperature given from X-ray measurements T_e = 400 eV and the electron density at the turning point

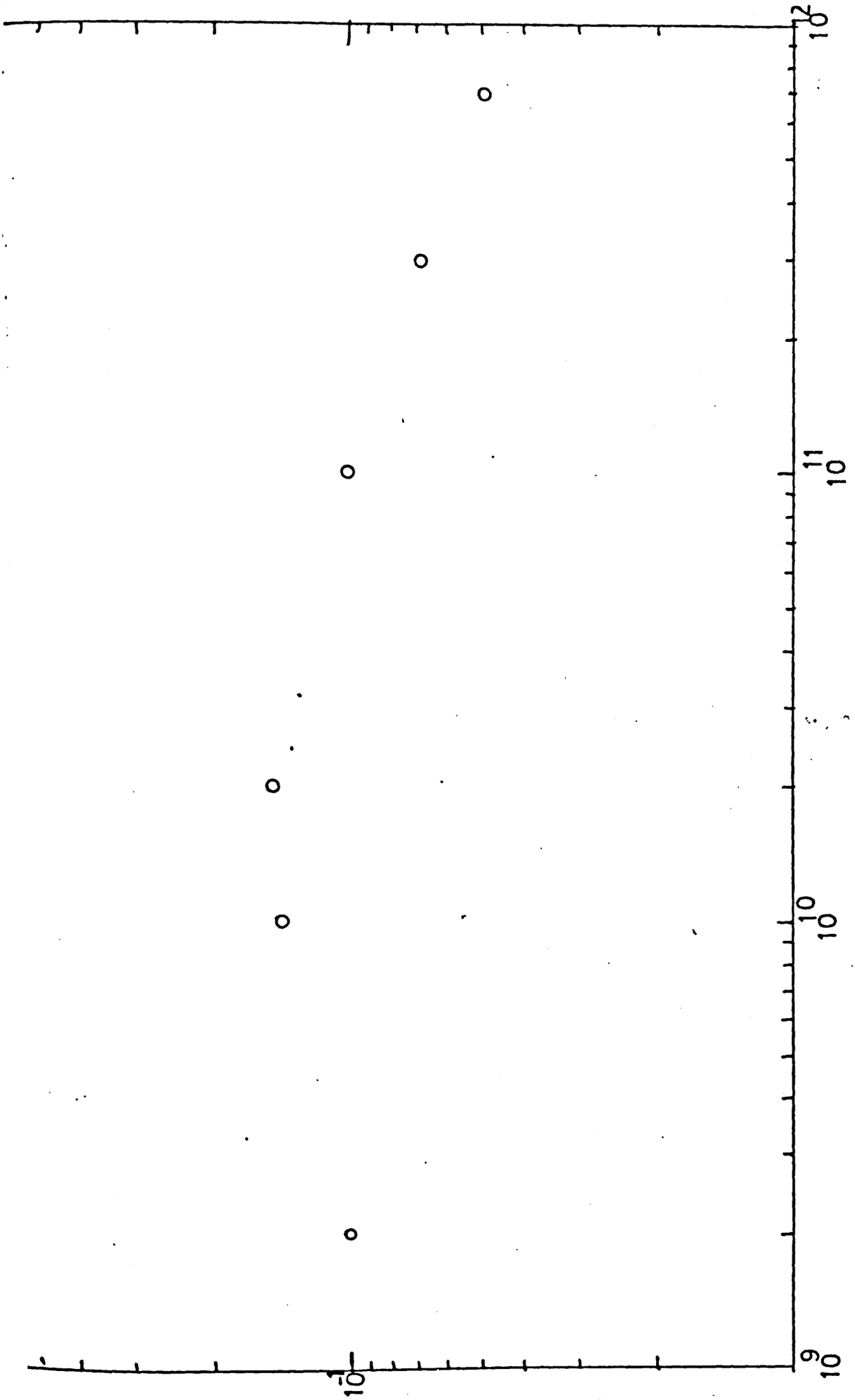

Figure 6.2:

Conversion ratio vs. Irradiance for ω_o

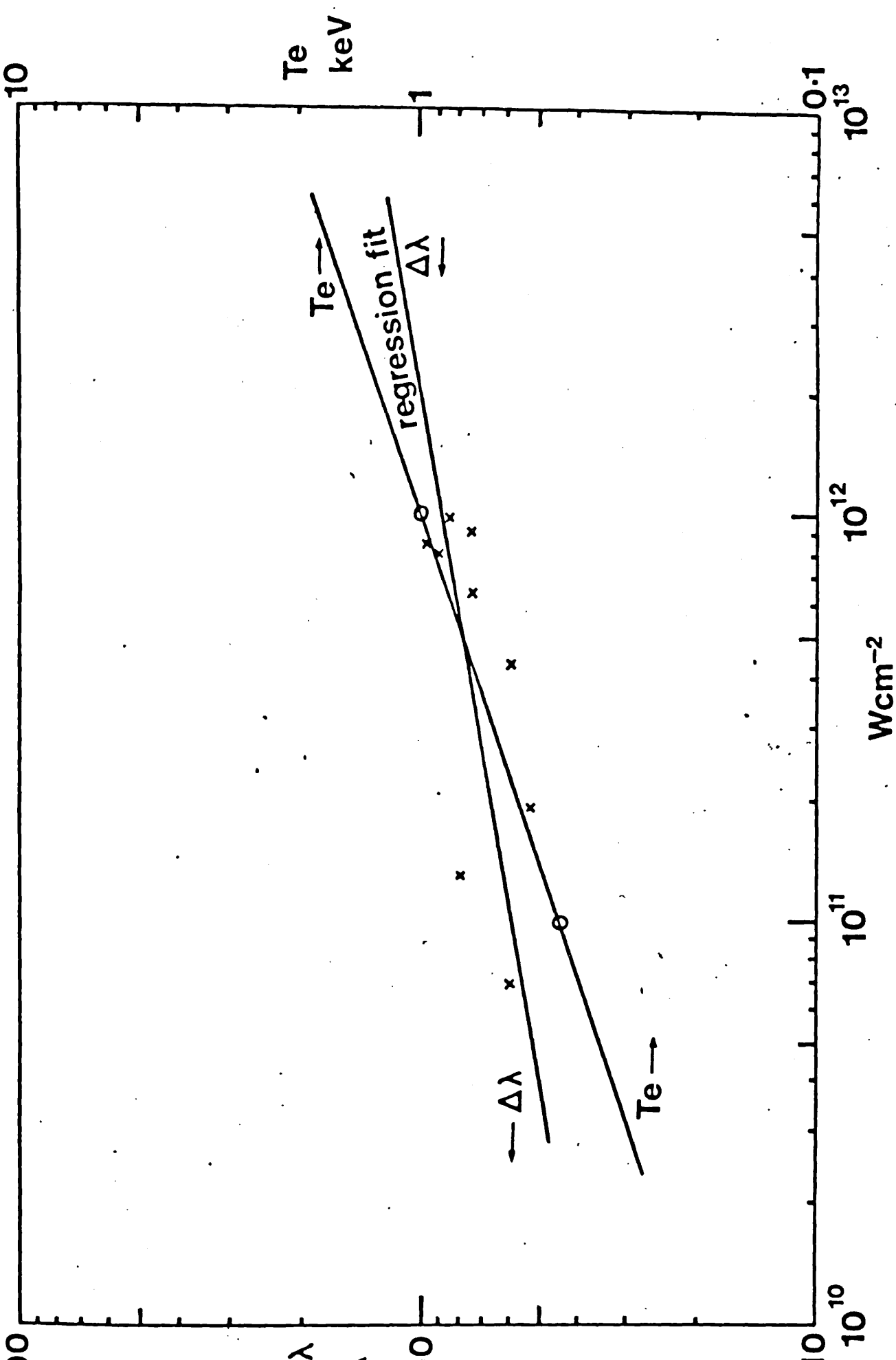

Figure 6.3.

Estimated electron temprature from (S.B.S) vs. Irradiance.

$$n_e = n_{ce} \cos^2 \theta \qquad \text{(Thomson et al (1975))}$$

where θ is the incident angle. The specification of the lens used gives a maximum angle of 7.6 degrees. The threshold irradiance would be $I_{th} \simeq 9 \times 10^9$ W cm^{-2} which is in reasonable agreement with the experimental value. It is noticeable that below 10^{10} W cm^{-2} the absorption of the laser radiation is due to inverse Bremsstrahlung which saturates near this value. Above this value the absorption increases, which is possibly due to excitation of other parametric processes.

6.3.1 Displacement of ω_o

It is noticeable from Figure 5.3 that the profile of backscattered ω_o displaced towards red from the original value of ω_o.

According to the theory of Brillouin scattering, the displacement $\Delta\omega$ towards lower frequencies is due to scattering from an ion acoustic wave. The displacement of the backscattered radiation ω_o is shown in Figure 5.5. The displaced value of $\omega - \omega_o$ is given by the dispersion relation for ion acoustic waves, ie:-

$$\Delta\omega_o = 2 K_o C_s$$

and

$$\Delta\lambda = \frac{2\pi c}{\omega_o^2} \Delta\omega$$

It is then possible to estimate the temperature of the plasma from the displacement, since $C_s = \left(\frac{KT_e}{m_i}\right)^{\frac{1}{2}}$. The

estimated temperature is also plotted in Figure 6.3. It is seen that the temperature varies as

$$T_e \propto I^{0.46}$$

ie a much slower increase than measured by the X-ray absorption technique, which gave:-

$$T \propto I^{0.70}$$

6.4 THE SECOND HARMONIC FEATURE

A spectral profile of the second harmonic radiation of the incident laser and its structure was shown in Figure 5.6, where it was seen that the structure consists of a central feature displaced towards longer wavelengths from the original $2\omega_o$ by about 120 Å. This main feature is also broadened by up to 120 Å (FWHM). There is a shoulder towards the real side of this feature starting at about 200 Å from the central frequency. Displaced by about 0.01 μ_m towards longer wavelength from the main feature there is a satellite $\Delta\omega$.

Experimental observation of emission from a laser produced plasma near the second harmonic of the laser frequency shows a spectrum which broadened and shifted towards the red side of the original harmonic, Bobin et al (1975), Burnette et al (1977) and Key et al (1977).

6.4.1 The Intensity of the Second Harmonic $2\omega_o$

It is seen from section 5.4 that there is a linear relationship between the laser irradiance and the back-scattered intensity at 2ω, with a threshold of 1.2×10^{11} W cm^{-2}. Previous investigations have shown varying relationships between the scattered energy at $2\omega_o$ and the incident laser irradiance I_o. Eidmann and Sigel (1975) found a quadratic law. Fabre et al (1975) found a variation with $I_o^{1.5}$ and the result published by Baldis et al (1979) varied as $I_o^{2.4}$.

Absorption due to interactions has been shown by Vinogradov and Pustovalov (1973) to be proportional to the radiation flux, the maximum absorption occurring when

$$\left(\frac{3}{4}\frac{\omega_o}{c} L\right)^{2/3} \sin^2 \theta = 0.5 \qquad (6.1)$$

Ginzburg (1964).

where θ is the angle of incident of the radiation at the plane. From the specification of the focussing lens this equation can be satisfied if the plasma density scale length is $L = 440\ \mu m$.

It has been seen in Chapter 2 that the Langmuir wave can produce a harmonic at 2ω either by coalescing with a transverse wave $t_2 = t_{\omega_o} + t_{\omega_o}$ or with another Langmuir wave $t_2 = t_{\omega_o} + L$. The matching conditions for ω and K may be satisfied near the critical surface over a very small region of the plasma and in the presence of ion acoustic oscillations. The conditions for the existence

of a parametric process and the threshold conditions are given by Rosenbluth (1972) as

$$\left(\frac{V_o}{C}\right)^2 K_o L > 1$$

Assuming a linear density gradient

$$n = n_o \left(1 - \frac{Z}{L}\right)$$

where n is the refractive index

Z is the penetration distance.

The ray penetrates to a distance

$$Z = L (1 - \sin \theta)$$

With the focussing lens f4 used the maximum value that θ could take was 7.6 degrees, then the value of Z was 300 μm.

It has been seen in Figure 5.7 that above an irradiance of $1.2 \cdot 10^{11}$ W cm^{-2} the intensity of $2\omega_o$ is monotonically increasing. The conversion ratio, energy of 2ω/incident energy, is obtained from the plot of $I_{2\omega}$ against irradiance irradiance and is shown in figure 6.4. It is seen that I_2 varies linearly with I_o following the relation,

$$I_{2\omega} \propto I_{\omega_o}^{1.33}$$

starting at threshold value of 1.2×10^{11} W cm^{-2}.

Using the threshold relation for ω_o given by Liu (1976) for stimulated Brillouin scattering

$$\frac{2}{3}\left(\frac{V_o}{V_{th}}\right)^2 K_o L > 1$$

where V_{th} is the thermal velocity and V_o is the quiver

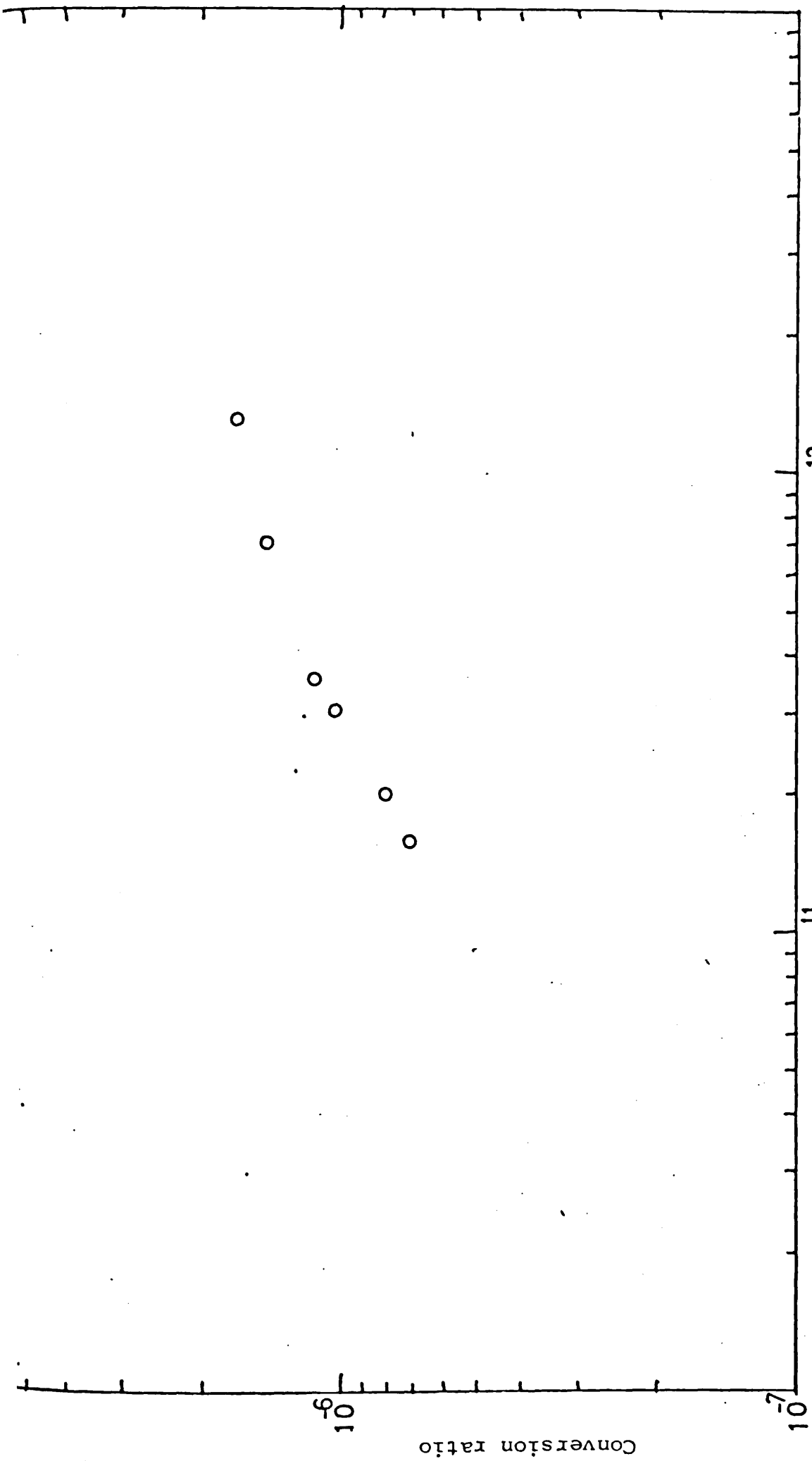

Figure 6.4: Conversion Ratio vs. Irradiance for $2W_o$

velocity, a value of the density scale length may be estimated to be $L = 510\ \mu m$.

The conditions for optimum generation of the second harmonic is a function of the incident angle θ. According to Erakhin theory (1969) the maximum intensity of $2\omega_o$ appears if

$$\frac{\omega L}{c} \sin^3 \theta \simeq 0.5$$

The plasma density scale length determined to be $L \simeq 370\ \mu m$. This value of scale length is consistent with the result given by other workers.

Condition of maximum absorption	440 μm
" of S.B.S. ω_o	510 μ_m
" " maximum generation for 2ω	370 μm
" " " "	$3/2\omega$ 560 μm
Fabre et al (1976)	300 μm and 400 μ_m
Tonon and Rabeau (1973)	100 μm
Walker et al (1978)	500 μ_m and 600 μ_m

The straight line plotted in Figure 6.5 on regression fits. For the 2ω line the correlation coefficient is found to be 0.956 , whereas if regression on I_o^2 is calculated the correlation coefficient falls to 0.868. We conclude that for an irradiance between the threshold value and 10^{12} W cm^{-2} there is an almost linear relationship between backscattered energy at 2ω and the incident irradiance. This is probably due to the fact that this mechanism occurs near the critical surface where $\omega_o > \omega_{pe}$ and there is a

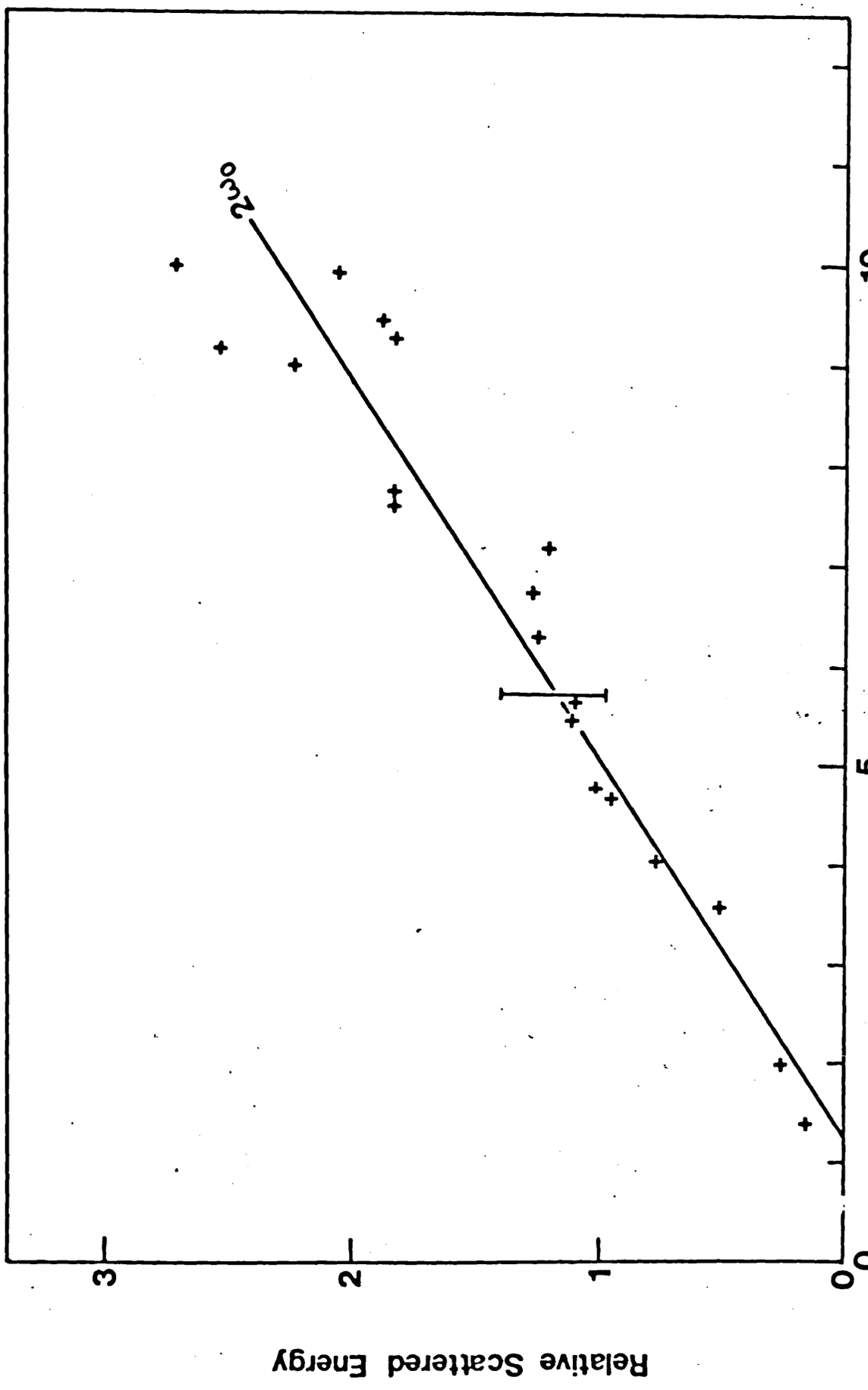

Figure 6.5: The relative backscattered energy vs. Irradiance

resonance absorption besides the two plasmons coupling which gives the second harmonic backscattered.

6.4.2 Displacement of 2ω

Theoretical explanations of the main 2ω feature have assumed that the second harmonic is the result of the interaction of an incoming photon and a plasmon produced near the critical surface, either by decay instability, Bobin et al (1973), or by resonance absorption, Vinogradov and Pustovalov(1973). Because steepening of the density profile occurs during laser plasma interaction the decay instability is inhibited and resonant absorption becomes dominant for generating the plasma wave near the critical surface.

The expression derived by Silin for the frequency shift of $2\omega_o$ caused by parametric resonance and given by Krokhin (1975) is

$$\Delta\omega = \sqrt{3}\,\omega_{pi}\left[\frac{V_{th}^2}{C^2} + \frac{1}{4}\,\frac{V_o}{C^2}\,\frac{\omega_o}{\Delta\omega_o}\right]^{\frac{1}{2}} \qquad (6.6)$$

where ω_{pi}, ω_o are the ion plasma frequency and incident laser frequency respectively. V_{th} and V_o are the electron thermal and quiver velocities and C is the light velocity. $\Delta\omega_o$ is the difference between the laser frequency ω_o and local plasma frequency $\omega_{pe}(Z)$ in

$$\Delta\omega_o = \omega_o - \omega_{pe}(Z)$$

with Z being the coordinate of the point of interaction in the linear density profile. Then

$$\omega_{pe}(Z) = \omega_o \left(\frac{Z}{L}\right)^{\frac{1}{2}}$$

and Z is the location of the first field maximum. Hence, from Ginzburg (1961)

$$Z = 1.02 \left(\frac{\lambda L}{2}\right)^{2/3}$$

where L is the electron density scale length. In equation (6.6) the first term is equal to KC_s since the wave number is $\sqrt{3}\,\omega_{pi}/C$, Melrose and Stenhouse (1979). The second term is a correction for the displacement of the turning point from the exact location of the critical density.

Since the interaction is expected to take place near to the critical density surface a correction must be made for the refractive index n (Z) of the plasma. Then

$$\Delta\omega = \frac{2\pi C}{n(Z)\,\omega_o^2}\,\Delta\omega_o \qquad \ldots(6.8)$$

Values of the density scale length in plasmas produced by CO_2 lasers have been determined experimentally as 100 μm Tonon and Rabeau (1973), 500 and 600 μm Walker et al (1978), or obtained from the irradiance at the threshold of the parametric processes as 440 and 560 μm. It will be seen in section 6.4 that a value of 500 μm may be derived from the threshold value. The temperature used for this purpose is the one measured in section 5.6. It is seen in Figure 6.6 that the resulting line falls very close to the experimental points.

The displacement is seen in equation (6.6) to be dependent on temperature. The estimated displacement is

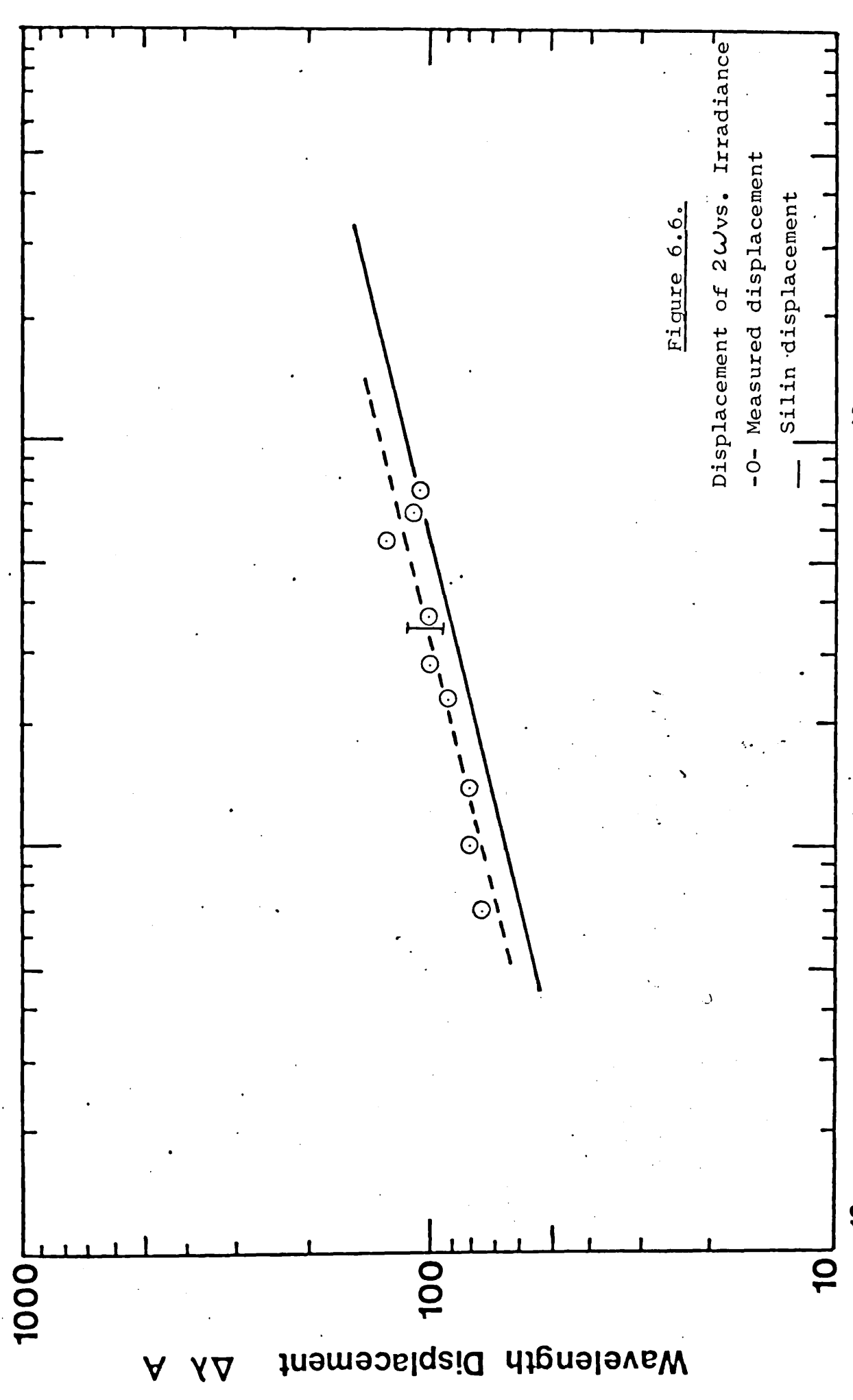

Figure 6.6.

Displacement of 2ω vs. Irradiance
-O- Measured displacement
— Silin displacement

dependent, to a lesser extent, on the position of the interaction in the plasma, although the value of the refractive index is rather critical. It should be noted that the density at the derived value of Z is considerably less than the critical density.

6.4.3 Line Shape

It is noticeable that there is a shoulder towards the red side of the original second harmonic line which shifts by up to 200 Å from the $2\omega_o$. It is assumed by Cairns (1979) that the spectral broadening and shift is seen in second harmonic emission if the plasma waves are excited by resonance absorption near the critical surface. If the ion acoustic wave which must propagate outwards to give a red shift has a wavelength close to the wavelength of a plasma wave in the vicinity of the critical surface, then it can transfer energy effectively into lower frequency modes and the envelope of the resulting mode intensities bears a close resemblance to the experimental observations.

Another explanation of this shoulder is probably due to super-elastic scattering, which consists of four waves coupling, which means that the backscattered second harmonic 2ω is shifted to the red from the original $2\omega_o$ by frequency equal $2\omega_i$, where ω_i is the ion acoustic wave.

$$2\omega = 2\omega_o - 2\omega_i$$

This may be possible, since if we take the shift of the shoulder from the original line and take into account the Doppler

shift towards blue. This shift is nearly twice the shift of the main 2ω line from the same reference $2\omega_o$. This was explained by Bobin (1975) as a result of two electron temperature cold and hot electrons.

6.4.4 Contribution of Doppler Shift

The harmonic line is displaced from the precise value of $2\omega_o$ ($5.3\mu_m$) towards the red, which is due to an interaction with an ion acoustic wave. However, the plasma is expanding, causing the interaction required to travel towards the laser, resulting in a displacement towards shorter wavelengths due to a Doppler shift. An estimate was made of the plasma velocity in the interaction region, assuming that the threshold irradiance for this interaction is approximately equal to the lowest irradiance at which the $2\omega_o$ spectrum is observed, Lee et al (1974). The frequency of the radiation ω_o incident on the plasma moving with velocity V suffers a Lorentzian displacement to

$$\omega'_o = \omega_o \gamma (1 + \beta)$$

where $\beta = V/C$ and $\gamma = (1 - \beta^2)^{\frac{1}{2}}$

This radiation produces a doubled frequency $2\omega'_o$ within the plasma which, in turn, radiates at a frequency $2\omega'_o$.

In the laboratory frames of reference, the frequency measured is $2\omega_o$, where

$$2\omega'_o = 2\omega_o (1 - \beta)$$

with matching $2\omega'_o$ to $2\omega_o$ leads to a value for β

$$\beta = \frac{\Delta}{4\omega_o + \Delta\omega}$$

$$\Delta\omega = 2\omega_o - 2\acute{\omega}_o$$

and $$\Delta\omega = \frac{2\pi c}{\lambda^2}\Delta\lambda$$

values of the plasma velocity were assumed to get the corresponding value of $\Delta\lambda$. The maximum value at 10^8cm s^{-1} is $\simeq$ 29 Å, which is small compared with the red shift in the $2\omega_o$ spectrum.

6.4.5 The Satellite Feature

It was seen in the previous section that the displacement of the $2\omega_o$ feature was fitted closely by a theory due to Silin. We now examine the feature $\Delta\omega_o$.

In Figure 5.8 the displacement of $\Delta\omega$ from 5.32 μ_m is plotted against the irradiance along with the displacement of the main feature $2\omega_o$. A displacement from 5.3 to 5.4 μm is equivalent to $\Delta\omega \approx 10^{12}$ rs^{-1}. It is seen that both displacements have a finite value at the irradiance threshold for $2\omega \sim 1.2 \times 10^{11}$ W cm^{-2}. The relative intensity of the $\Delta\omega$ feature is plotted in Figure 5.10. It becomes apparent above the threshold for 2ω but extrapolation from a regression with I_o the experimental point does not permit a threshold for $\Delta\omega$ to be determined. This saturation could be due to inverse Bremsstrahlung absorption of the back scattered $\Delta\omega$.

This feature is not in fact produced by the diffraction

grating. The monochromator was aligned for $2\omega_o$ to fall in the first order. Hence, the $4\omega_o$ harmonic in the second order would overlap. However, Baldis et al (1979) have shown that the intensity of $4\omega_o$ is two order of magnitude smaller than the intensity of $2\omega_o$ in a CO_2 laser plasma interaction. The difference in intensities of $2\omega_o$ and $\Delta\omega$ here is about 1.5. The $\Delta\omega$ feature is not a grating ghost, since nothing is observed near to ω_o when the incident laser radiation was resolved by the spectrograph.

Kruer and Estabrook (1977) show that self generated magnetic field can introduce light absorption and harmonic generation. The absorption and harmonic generation occur due to electrostatic waves resonantly generated by the oscillation of electrons driven by the $V_o \times B_o/C$ force where V_o is the quiver velocity of an electron in the laser light field and B_o is the self generated magnetic field. This kind of resonance absorption occurs even for normal incidence in the condition of $\omega_{ce} << \omega_{po}$, where ω_{ce} is the electron cyclotron frequency.

In Figure 5.8 the displacement of the satellite line $\Delta\omega$ is equivalent to about $B \simeq 4 \times 10^5$ Gauss.

Measurements of the magnetic field were discussed in section 5.7. By extrapolation, the field may be estimated at various positions within the plasma and its variation with irradiance determined. Plots of the displacement due to the cyclotron frequency in the vicinity of $300\mu_m$ and $400\mu_m$ from the target are shown in Figure 5.8. The dis-

placement equivalent to ω_{ce} reaches values similar to those of $\Delta\omega$ but increases much more rapidly.

Generally the satellite line is shifted from the main line at $2\omega_o$ by frequency which was too large to be considered as being due to ion acoustic waves. This magnetic field effect may have been observed by Bobin (1977).

6.5 HARMONIC GENERATION AT $\frac{3}{2}\omega_o$

It has been seen in Chapter 5 that the intensity back scattered in the form of $\frac{3}{2}\omega_o$ is about 10^{-8} of the incident laser irradiance. Figure 5.11 shows also the relation between the irradiance and the back scattered $\frac{3}{2}\omega_o$. The straight line is a regression plot which gives a threshold of 1×10^{11} W/cm^2. There is a rapid increase of the back scattered radiation at low irradiance $1 - 4 \times 10^{11}$ W/cm^2 after which saturation occurs.

The harmonic generation $\frac{3}{2}\omega_o$ results from the scattering of the incident laser wave on plasmons of frequency $\frac{\omega}{2}$. These plasmons may result from two plasma decay or from the stimulated Raman instability. The instability threshold for two plasmon parametric processes given by Rosenbluth for an inhomogeneous plasma is

$$\frac{2}{3}\pi^2\left(\frac{e}{m\,c^2}\right)^2\left(\frac{m_e^2}{T_e}\right)\frac{I\,L}{\omega_o} \gg 1$$

for plasma temperature of 500 eV and plasma scale length of 600 μm. The irradiance threshold calculated for this result is 1.4×10^{11} W/cm^2, which is in good agreement with the experimental value. For the Raman instability the

threshold irradiance would be 1.2 10^{12} W cm^{-2} for these values of temperature and scale length.

The spectral profile was not determined.

6.6 ELECTRON TEMPERATURE

Independent measurements of the temperature made with the aid of an X-ray pinhole camera (section 5.6, Figure 5.10) are compared with the estimation obtained from the displacement of the radiation backscattered at ω_o. The assumption, including these estimations, was given in section 6.3.

It is seen in Figure 5.12 that the value of X-ray temperature varies with the irradiance as $T_e \propto I_{in}^{0.70}$ whereas that from the Brillouin processes is $T_e \propto I_{in}^{0.46}$.

Krokhin (1965) and Caruso et al (1966) set up a one dimensional plane approximation which leads to a relationship between the temperature and the irradiance on the plasma as

$$T_e \propto I^{0.5} t^{0.25}$$

where t is the laser pulse duration time and I is the irradiance. The constant of proportionality is determined from the absorption coefficient. This model may not be applicable for a long duration pulse because the expansion of the plasma is three dimensional. Also, there is a reduced value of the absorption coefficient. Theoretical models treating this saturation have been developed by Basov et al (1968) and Pugll (1970), leading to

$$T_e \propto I^{4/9} r^{2/9}$$

In this case the time during which a plasma is being heated

is r/V_{th} where r is the local spot radius and V_{th} is the thermal flow velocity. Bobin et al (1969) obtain a relationship as

$$T_e \propto I^{2/3}$$

In the electron temperature values deduced from X-ray absorption in thin foils the diameter of the X-ray emitting region of the plasma was deduced from a pinhole photograph, as shown in Figure 3.15. The diameter emitting from the region is between 150 - 180 μm.

The electron temperature obtained from X-ray measurement shows nearly the same behaviour as that given from the red shift.

Two regions of electrons observed by Gitomer and Henderson (1979) follow

$$T_h = \text{const } (I\lambda^2)^d \; T_c^q$$

with $d = 0.67$ $\quad I\lambda^2 < 10^{15}$

or $d = 0.25$, $\quad I\lambda^2 > 10^{15}$

T_c is background electron temperature near to the critical surface

$$0.25 < d < 0.3 \qquad 0.33 < q < 0.50$$

$$I\lambda^2 = W\mu m^2 \text{ cm}^{-2}$$

6.7 MAGNETIC FIELDS

The magnetic field shown in Figure 5.13 was seen and

contains three components, B_1 (+ v_e) B_2 (- v_e) and B_3 (+ v_e). The B_1 components have a fast rise time and fast decay following the laser pulse. The magnetic field component is then explained as the consequences of a current flowing from the target towards the probe. The second signal B_2 goes negative and may be attributed to fast ions. The third component B_3 may be due to slow electrons. The magnetic field determined at various distances r from the target was shown in Figure 5.14. The maximum magnetic field in this case is $\simeq$ 10 KG.

The saturation field magnitude given by Max et al (1978)

$$B = 3.3 \left(\frac{T_e}{1\ \text{KeV}}\right)^{\frac{1}{2}} \left(\frac{10\ \text{m}}{L}\right) \left(\frac{A}{Z+1}\right)^{\frac{1}{2}}$$

where L is the plasma scale length. Values of this field are plotted in Figure 6.7 and is seen to be in good agreement with the experimental values.

From the relation which has been plotted between the peak magnetic field and the irradiance it was found that

$$B \propto T^{0.5}$$

since $T \propto I^{0.47}$ (X-ray)

Then $B \propto I^{0.27}$

In Figure 5.14 the peak magnetic field is plotted against the laser irradiance for several values of the distance r from the focal spot. It is noticeable to obtain a linear regression of B on various functions of r, the relationship of B to $\frac{1}{r}$ is plotted in Figure 5.15 It is seen that

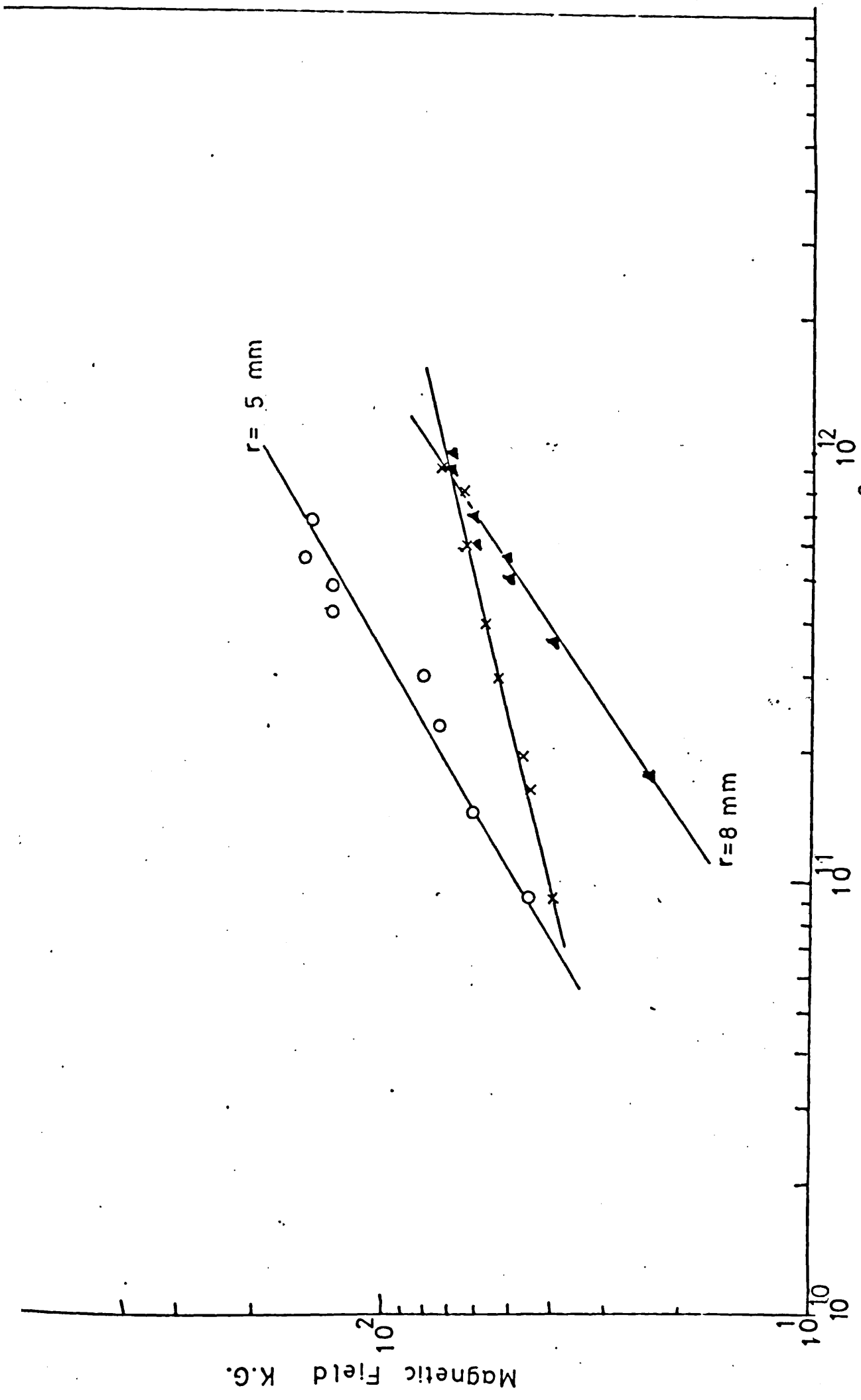

Figure 6.7.

Magnetic field vs. irradiance
-x- Calculated values

$$B = a\, r^{-0.5} \qquad \text{for } r > 5 \text{ mm}$$

$$B = a\, r^{-1.4} \qquad \text{" } r < 5 \text{ mm}$$

These results are in accordance with those of Kitigama et al (1979) and suggest the existence of a current sheet which travels a maximum distance of about 5 mm from the target surface before disruption.

Resonance absorption enhanced by existence of self generating magnetic field: In ordinary resonance (B = 0) and oblique incident with p-polarized component in the plane of incident the electric field oscillates along the density gradient. If magnetic resonance occurs even at normal incidence, the transverse electric field oscillates normally to the density gradient, but the $V_o \times B_o$ force induces electron oscillations along the density gradient. In either case, these oscillations along the density gradient produce a charge separation and drive a plasma wave. Transverse waves can propagate up to the appropriate cut-off density and tunnel through to drive plasma waves at the resonance density. These waves are then dampened with a consequent heating of the plasma. In this case upper hybrid waves may be involved in a magnetic resonance. This could explain the linear relationship of the intensity of $2\omega_o$ and $\frac{3}{2}\omega_o$ with the laser irradiance.

CHAPTER 7

CONCLUSIONS

The experimental investigations described here have been carried out with a CO_2 laser which provided a rather large duration pulse and a range of energies from 1 to 30 Joules. Only one material, carbon, has been used as a target; nevertheless, the results give a valuable insight into the physics of the interaction of intense coherent radiation with a dense plasma. Most of the experimental data are explained by existing theory, but it is seen in one or two instances that further theory needs to be developed. Where the experimental results conflict with those of other workers, or are not consistent with existing theory, explanations have been provided.

Measurements of the radiation backscattered through the focussing lens integrated over the wavelength range λ to $\lambda/2$ and the duration of the laser pulse enabled a measurement of plasma reflectivity to be made. It was seen in Figure 5.1 that the reflectivity attains a maximum value of 52% at 10^{10} W cm^{-2}. Below this value, the backscattered intensity increases with irradiance as $I_{sc} \propto I_o^{1.2}$. Above 10^{10} W cm^{-2} the backscattered intensity increases rather slowly as $I_o^{0.7}$. The reflectivity falls from the maximum value to 10% at the high irradiance of 10^{12} W cm^{-2}. It is concluded that anomoulous absorption accompanies a parametric process, stimulated Brillouin scattering, which

has a threshold irradiance of about 10^{10} W cm^{-2}. Measurements of the electron temperature support the view that classical reflection occurs at the critically dense surface and absorption is caused by inverse Bremsstrahlung which falls to 50% at an irradiance of 2×10^{10} W cm^{-2}. The increasing electron temperature, together with the low measured plasma reflectivity, suggest that nonlinear mechanisms are dominant above 10^{10} W cm^{-2}.

Parametric processes have been investigated mainly by observing the associated spectra. The intensities relative to the incident radiation recorded at the different scattered frequencies are of the order

ω_o	10^{-1}
$\frac{3}{2}\omega_o$	10^{-8}
$2\omega_o$	10^{-6}
$\Delta\omega$ satellite	10^{-7}

These figures confirm that the dominant reflection process is stimulated Brillouin scattering. The threshold irradiance for S.B.S. was found to be 3×10^{10} W cm^{-2}, which is two times higher than the value reported by Yamanaka (1977). An estimate of the density scale length made from the theoretical expression for the threshold intensity is 510 μ_m, which is plotted in Figure 7.1 and is in good agreement with values found by other workers.

The displacement of the backscattered wavelength from

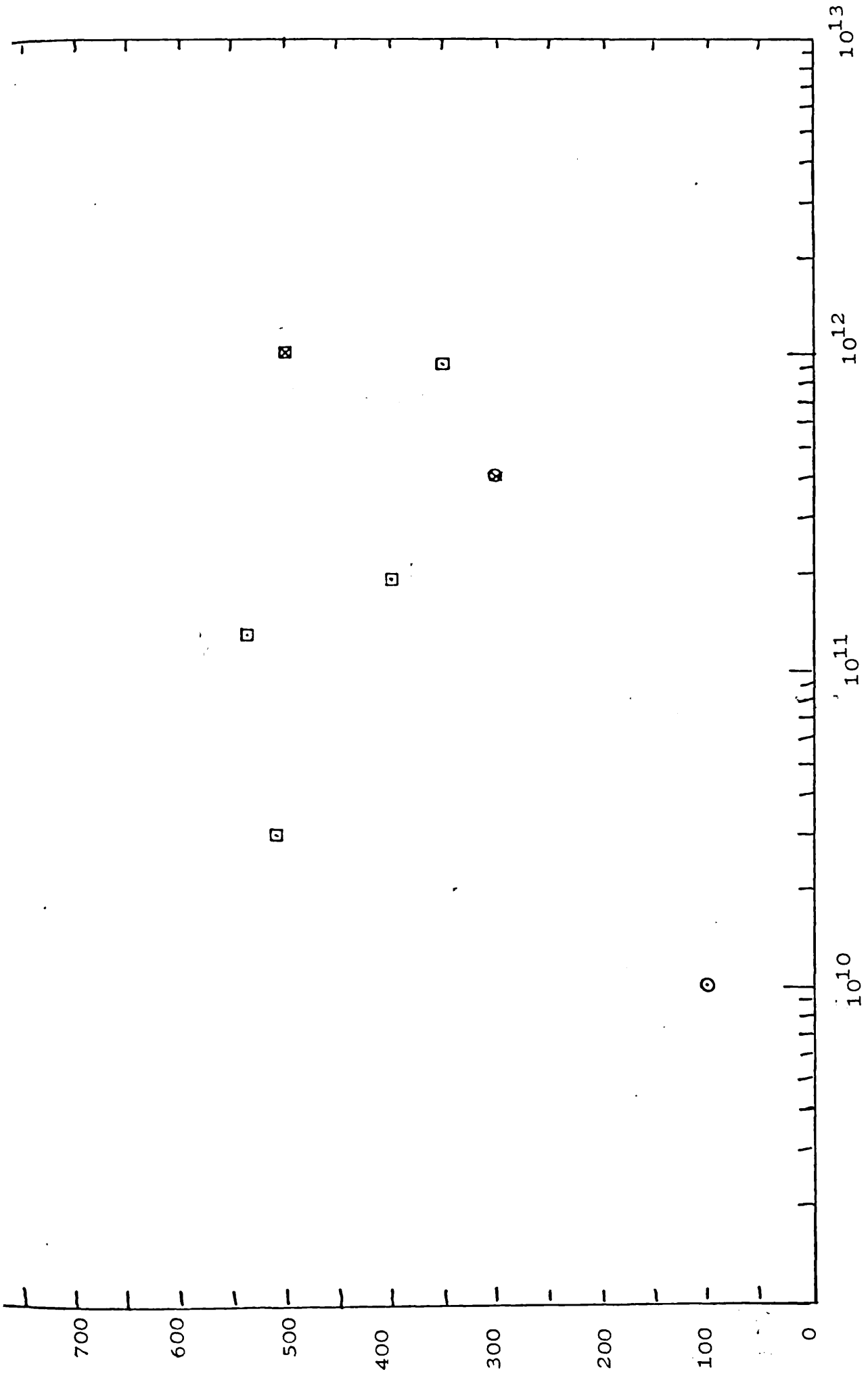

Figure 7.1.

Plasma density scale length

□ Experimental scale length

⊙ Tonon and Rabeau (1973) ⊗ Fabre et al (1976)

⊠ Walker et al (1978)

the value of the original wavelength of 10.6 μ_m is related to the frequency of the ion acoustic waves driven in the plasma. Then an estimate of the electron temperature may be made. The electron temperature, so derived, is plotted along with values derived from measurements of the X-ray continuum against irradiance in Figure 7.2.and compared with other experimental values. The dependence on irradiance is in the following proportion:-

T_e	$I^{0.46}$	Brillouin shift
T_e	$I^{0.7}$	X-ray measurement
T_e	$I^{0.67}$	Gitomer and Henderson
T_e	$I^{0.6}$	Fabre Hot
T_e	$I^{0.32}$	Fabre Cold

The agreement is sufficiently clear to support the argument that ω_o is scattered by an ion acoustic wave travelling through the under-dense plasma.

The structure of the backscattered radiation at frequency 2ωwhich was shown in Figure 5.6 consists of the main feature shifted towards red, with a shoulder towards red and a satellite line. This spectrum provides further evidence of the existence of ion acoustic waves near to the critically dense region. When the displacement of the harmonic from the exact value of $2\omega_o$ is compared with the theory which attributes the shift to scattering by an ion acoustic wave (Silin (1965)), good agreement is found.

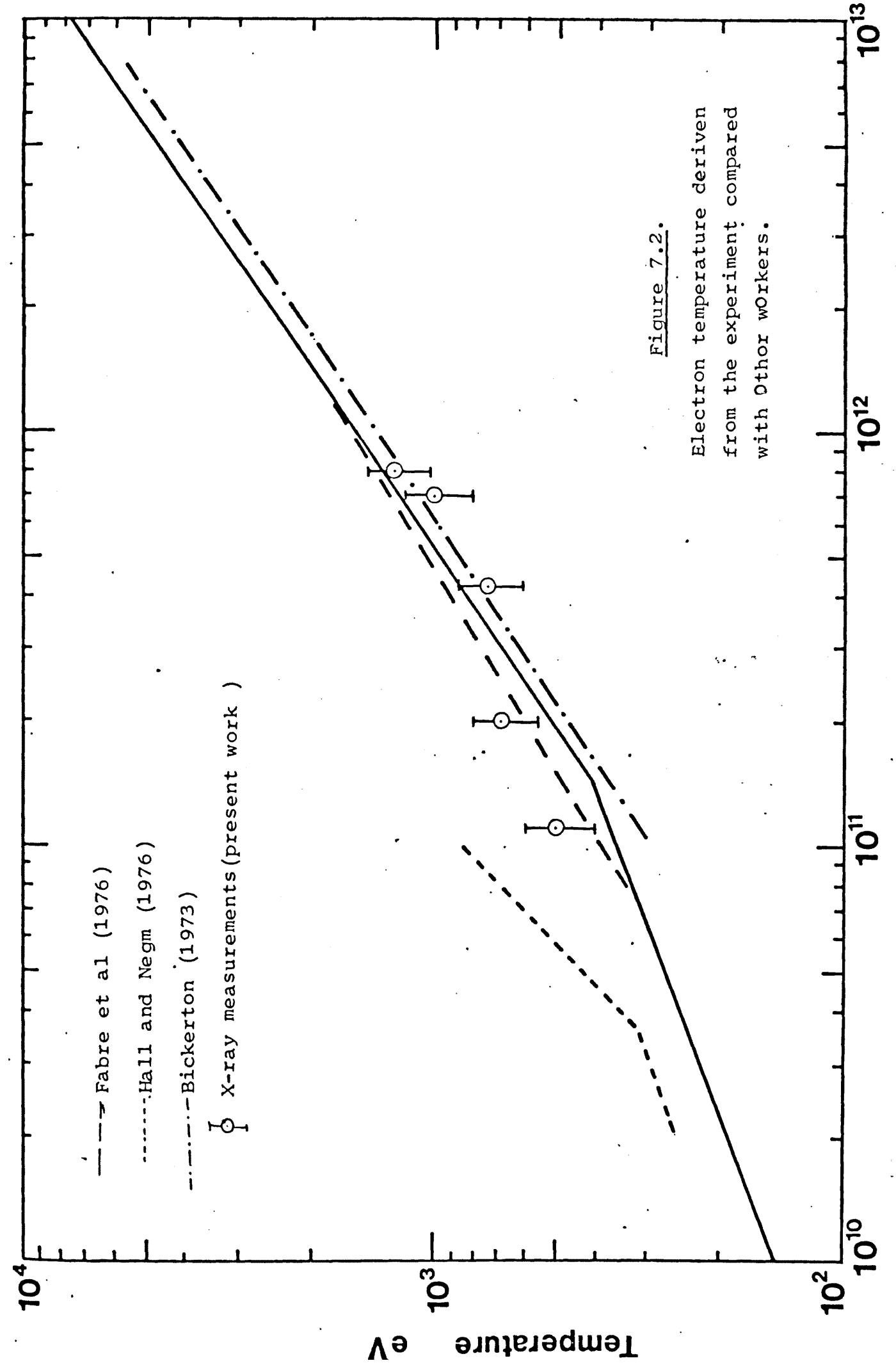

Figure 7.2.

Electron temperature deriven from the experiment compared with Othor workers.

The calculations require the value of the electron temperature, scale length and an estimate of the position of the turning point. These values were determined during the course of the experiments. The intensity of the back-scattered 2ω varies linearly with the irradiance, a result which is consistent with the theory of Hammerling (1977), but is not in agreement with the experimental results of Sigel (1975), Fabre (1975) or Baldis (1977). It is possible that slope is linear at 7×10^{11}, but quadratic at higher irradiance. The threshold at 1.5×10^{11} W cm^{-2} is due to the two plasmon decay. An estimate was made of the density scale length, and again is seen in Figure 7.1 to agree reasonably well with the results of the other workers.

The shoulder observed towards the red side of the main feature is in agreement with the observation of Bobin et al (1973), Burnettet al (1977) and Fabre (1977). It may be due to four wave processes. More data are required to test this hypothesis, and to compare with the predictions of Cairns (1979) or Yamanaka (1974).

The satellite to the $2\omega_o$ harmonic has been attributed to the presence of the upper hybrid frequency (Maki and Niu (1979))

$$\omega_{UH} = (\omega_{ce}^2 + \omega_{pe}^2)^{\frac{1}{2}}$$

However, when measurements of magnetic field at short distances from the plasma were used to estimate the cyclotron frequency near to the critically dense layer, it was found that the rate of increasing of the satellite displacement

with irradiance was too low. A further explanation is that a plasma wave is driven at a distance

$$Z = 1.03 \left(\frac{L}{\lambda}\right)^{\frac{1}{2}}$$

The satellite is then caused by resonance with a frequency (Ginzburg (1962))

$$\omega_{pe}(Z) = \omega_o \left(\frac{Z}{L}\right)^{\frac{1}{2}}$$

The satellite spectrum is then produced by a process

$$T(\omega_o) + L(\omega_p) \longrightarrow T(2\omega_o)$$

resulting in a displacement $\Delta\omega = \omega_{pe}$.

A correction needs to be made to the plasma permittivity which is not:-

$$\xi = 1 - \left(\frac{\omega_{pe}}{\omega_o}\right)^2$$

but

$$\xi = 1 - \frac{\omega_{pe}}{\omega(\omega_o \mp \omega_{ce})}$$

It is interesting to see in Figure 5.10. that the intensity of the satellite line when plotted against irradiance shows no threshold, a result which is consistent with the existence of pure resonance.

The other harmonic that was observed was backscattered $\frac{3}{2}\omega_o$ with a threshold irradiance of 1.2×10^{11} W cm^{-2}. The estimated density scale length of 550 μ_m is also plotted in Figure 7.1.

The method of recording spectra has dissuaded us against measuring the line breadth since the observed breadth is a convolution of the true line breadth plus the averaged effect of displacement. It is hoped that future measurements will be possible with a system which permits real time spectral resolutions.

It appears that $\frac{3}{2}\omega_o$ is also attributable to two plasmon decay.

It has been noticed that the red shift of the fundamental and the harmonic 2ω backscattered is due mainly to stimulated Brillouin scattering and is dependent on ion mass. By using different Z materials, further information about the mechanics of the shift may be obtained. Also, it would be valuable to use an ion collector to know the degree of ionization which gives accurate temperature measurements from the frequency shift.

Since resonance absorption depends on the angle of incidence of the laser light on the target, it would be interesting to do some experiments with different degrees of roughness of the target surface and also with variation of the angle of incidence of a smooth plane target.

An attempt should be made to find a satellite feature near the $\frac{3}{2}\omega_o$.

To enable further X-ray measurements to be made, a more sensitive system is in construction based on a pin hole camera followed by an image convertor.

The density distribution of the plasma created by a CO_2 laser should be measured by ruby laser scattering at 45^o or near the forward direction.

APPENDIX A1

A1.1 THEORY OF THE COMPENSATED MAGNETIC PROBE

The compensated probe was first described by Serov et al (1975). If the probe is connected as shown in Figure 4.13, the signal to the oscilloscope from the first cable is

$$V_3 + V_1 = V_C R_{01}$$

and from the second cable is

$$V_4 - V_1 = V_C R_{02}$$

Because the cables are identical

$$V_3 = V_4$$

If the signal from the two cables is fed through a differential amplifier, the resulting signal due to the magnetic field is

$$V_1 + V_2 = V_C R_0$$

or $$nA \frac{dB}{dt} + nA \frac{dB}{dt}$$

The induced electromagnetance in the probe is given by

$$\oint E \cdot dl = - \frac{d\Phi}{dt}$$

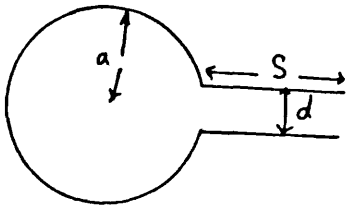

Figure A1.1

Writing the magnetic flux through the coil as the product of its area and the magnetic induction we obtain:-

$$\emptyset = (\pi a^2 + \text{s.d.})B$$

Hence the signal expected is

$$V = (\pi a^2 + KS.d.)\frac{dB}{dt}$$

permitting B to be obtained by integrating the signal. The factor K is a correction term for the fall off of the field in the direction of S. The response time is

$$L/R_O$$

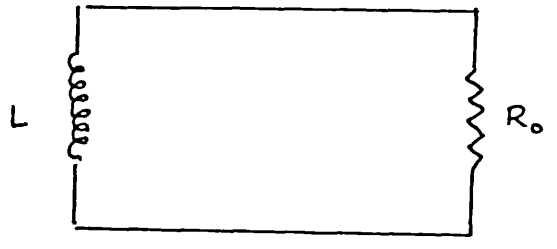

Figure A1.2

A1.2 COIL IMPEDANCE

For a single turn coil of radius a, of wire radius p as shown in Figure A1.1 , the self inductance L is given by Grover (1946) as

$$L = L_1 + L_2 - M$$

single turn loop $L_1 = 0.004\,\pi\, a \left[\ln\left(\frac{8a}{\rho}\right) - 1.75 \right] \mu H$

parallel pair $L_2 = 0.0042 \left[\ln \frac{d}{p} - \frac{1}{4} - \frac{d}{S} \right] \mu H$

mutual inductance $M = f\left(\frac{\delta}{2a}\right) \mu H$

Due to the second coil at an axial distance δ , f is given by Table 16 of the above reference. For 2 mm diameter coils of 28 SWG wire (0.38 mm dia) separated by 0.5 mm, these are negligible by comparison.

A1.3 SPURIOUS SIGNALS

The main interfering signal occurs on the cable joining the probe to the oscilloscope. Other spurious signals arise when X-rays, UV radiation and particles strike the probe surface and cause secondary emission. Assuming this signal

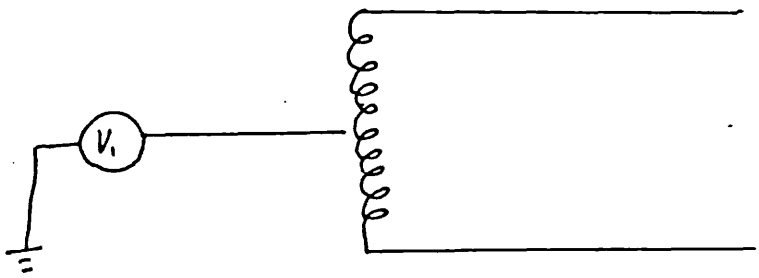

Figure A1.3

to be equivalent to a voltage generator between earth and the probe, compensation should ensure that the signal at the oscilloscope becomes:

$$V_{CR_O} = (V_1 + V_1) + (V_2 - V_1) = V_1 + V_2$$

the first 15 cm of the cable is covered with PTFE and a plastic sleeve is placed over the probe coil to reduce this spurious signal.

A1.4 ENVIRONMENTAL REQUIREMENTS

The probe is subjected to intense radiation which may cause damage. Furthermore, the current in the probe could reach a value which caused excessive heating of the coil.

Taking the worst possible case, we assume that all the energy W_o from the laser is re-radiated over 2π by the target, thereby exposing the probe to an irradiance $W_o \frac{\omega}{2\pi}$ where ω is the solid angle subtended by the probe surface at a distance V from the target

$$\omega = \frac{4 \pi a' \rho}{V^2}$$

It is assumed that the probe is damaged if it receives instantaneously sufficient energy to melt the wire. For metal of specific heat C_s, latent heat C_L and melting point T, density m and ambient temperature T_o, the closest position of the probe to the target is given by

$$r_{min} = \left(\frac{W_o \rho}{\pi a^2 m \left[C_s (T - T_o) + C_L \right]} \right)^{1/2}$$

value for copper - diameter 0.15 mm.

A1.5 EFFECT OF CABLE

The signal is attenuated in passing through a cable of length 1 by a fraction

$$\frac{V_o}{V_1} = \exp(-\alpha 1)$$

where α is the attenuation in db/meter. In the cable used here, α = 0.12 db/m, resulting in V_o/V_1 = 0.887 over 10 meters. Unless the cable is correctly terminated by a 50 Ω resistance at the oscilloscope, the inductive termination 2p results in a reflectivity of

$$\rho_r = \frac{Z_p - 50}{Z_p + 50} = -0.996$$

Consequently, a 50 nsec signal of 0.887 V_o at the oscilloscope would be followed by a second one of - 0.685 V_o after a period of 80 nsec.

The cable causes slight integration of the signal since its time constant R_C = 2.4 nsec.

An integrating circuit requires a time constant C_R at least 5 times the signal duration, or about 250 nsec, and results in an attenuation of

$$\frac{V_o}{V_1} = (1 + \omega^2 C^2 R^2)^{-\frac{1}{2}}$$

Making R = 50 ohm requires C = 5 nf and results in an attenuation of $6.35 10^{-2}$.

A1.6 PROBE SPECIFICATION

Coil	Material	Copper resistivity $1.78\ 10^{-6}$ ohm cm	
	Coil radius	=	1.0 mm
	Wire radius 305 6	=	0.15 mm
	Length for wire leads s	=	10 mm
	Spacing of wire leads d	=	1 mm
	Spacing of coils	=	0.1 mm
	Resistance of coil	=	$1.3\ 10^{-6}$
Probe	Self inductance of coil L_1	=	0.273 nH (1 GHz)
	Mutual inductance of coil Pair M	=	1.4 nH
	Total self inductance	=	1.27 nH
	Rise time of coil due to own resistance	=	10^{-3} sec
	Rise time of coil with load equal to cable impedance	=	26 psec
	Sensitivity of coil at 1 GHz	=	4.210^{-9} V/T/sec
Cable	No RG174A impedance		50 Ω
	No R27390		50 "
	R20470		50 "

A1.7 CONCLUSION

If the probe is compensated against electrical interference from the laser capacitors bank and spark gap it can give an accurate measurement for the magnetic field created from the laser produced plasma. It is a simple method compared with the Faraday rotation technique.

R E F E R E N C E S

1. Afanas'ev,Yu.V., Krokhin,O.N. and Sklizkov ,G.V. IEEE J. Quantum Electron., QE-2, p483 (1966)
2. Alexandrov,V.V., Anisimov,S.I., Brenner,M.V., Velikhov,E.P., Vikharev,V.A., Zatov,V.P., Kovalskii,N.G., Perament,M.P., Yaraslavskii,A.I. Sov. Phys. JETP, 71 p1826 (1976)
3. Aliev,Yu.M. and Silin,V.P. Sov. Phys. JETP, 21 p601 (1965)
4. Andrick, A., Donner, D., and Ehrhordt, H.,Phys. Lett.,29A p346 (1969).
5. Anderson, A.D., and Elton, R.C., N R L Report, 6541(1967)
6. Baldis,H.A., Burnett,N.M., Enright,G.D. and Richardson,M.C. App. Phys. Lett., 34 p327 (1979)
7. Baldis,H.A., Pepin,H., Johnson,T.W. and Parbhckor, K.J. Phy. Rev. Lett., 35 p37 (1975)
8. Boness,M.J.W. and Schudz,G.J. Phy. Rev. Lett., 21 p1031 (1968)
9. Basov,N.G. and Krokhin,O.N. Sov. Phys. JETP, 19 p123 (1964)
10. Basov,N.G., Gribkov,V.A., Krokhin,O.N. and Sklizkov , G.V. Sov. Phys. JETP, 27 p4 (1968)
11. Basov,N,G., Bereghin,I.A., Backo,V.A., Donilychev, V.A., Zvarykin ,V.P., Ignatev,V.V., Khalin,I.V. and Chugunov,A.Yu. Sov. Tech. Phys. 1(12) p473 (1975)
12. Beaulieu,A.J. App. Phys. Lett., 16 p504 (1970)
13. Beck,R., English,W., Gürs,K. "Table of Laser lines in gases and vapours", Springer-Verlag Berlin (1976)
14. Bugaev, .P.,et al. Sov. Tech. Lett. , 1, (5), p226 (1976)
15. Bezzerides,B., DuBois,D.F. and Forslund,D.W. Phys. Rev. A16 p1678 (1977)
16. Bickerton,R.J. Nuc. Fusion, 13 p457 (1973)
17. Bird,R.S.,McKee,L.L., Schwizke,F.S. and Cooper, A.W. Phys. Rev., A7 p1328 (1973)
18. Biskamp,D. and Welter,H. Phys. Rev. Lett., 34 p313 (1975)
19. Bobin,J.L., Decroisette ,M., Meyer,b. and Vitel, Y. Phys. Rev. Lett., 30 p594 (1973)
20. Bobin,J.L. Plasma Physics Non-linear theory and experiment Ed. H. Wilhelmsonn pp.102-21 (1976)

21. Bobin,J.L., Delobeau,F., DeGiovanni,G., Fauquignon, C. and Floux,F. Nuc. Fusion, 9 p.115 (1969)

22. Brederlow,G. et al. IEEE/OSA Clea Conf. Digest, 42 (1975)

23. Büchl,K., Eidmann,K., Salzmann,H. and Sigel,R. App. Phys. Lett., 20 p.3 (1972)

24. Budden,K.G., "Radiowaves inmthe ionospere ", Cambridge U.P. Cambridge, England (1966)

25. Bunkin,F.V. and Prokhorov,A.M. Sov. Phys. JETP, 19 p.739 (1964)

26. Bunkin,F.V. and Prokhorov,A.M. Sov. Phys. JETP, 19 p.109 (1964)

27. Burnett,N.H., Baldis,H.A., Richardson,M.C. and Enright,G.D. App. Phys. Lett., 31 p.172 (1977)

28. Burnett,.N.H., Baldis,H.A., Enright,G.D., Richardson, M.C. and Corkum,P.B. J. App. Phys. 48(9)Sept 77.

29. Bychenkov,V.Y., Silin,V.P. and Tikhonchuk,V.T. Preprint No. 94 of Lebedev Phys. Institute Moscow (1977)

30. Cairns,R.A. J. Plasma Phys. 22 p.149 (1979)

31. Caruso,A., Bertotti,B. and Giupponi,P. Nuovo Cimento, 45B, P 176, (1966)

32. Datskevich,N.P., Karlavo,E.K., Karlov,N.V., Kovol, Chuk,B.M., Konev,Yu.B., Kanonis,N.N., Kochetov, I.V., Kuzmin,G.P., Mesyut,G.A., Kikifanov,S.M., Pevgov,V.G. and Prokharov,A.M. Sov. J. Quantum Electron., 7(2) p.258 (1977)

33. Dawson,J.M. Phys. Fluids, 7(7) 981 (1964)

34. Dawson,J.M., Kaw,P. and Green,B. Phys. Fluids, 12 p.875 (1968)

35. Dawson,J.M. and Johnston,T.W. Phys. Fluids, 16 p.722 (1973)

36. Decroisette,M., Meyer,B. and Vitel,Y. Phys. Lett., 45A(6) 443 (1973)

37. Denisov,N.G. Sov. Phys. JETP., 4 p.544 (1957)

38. Donaldson,T.P., Hutcheon,R.J. and Key,M.H. J. Phys. B6, p.1525 (1973)

39. Donaldson,T.P. J. plasma. Phys., 20 p.1279 (1979)

40. Dougherty,J.P., Pugh,E.R., Douglas-Hamilton,D.H. Annual Gaseous Electronic Conf., Oct. 1972, Laser Focus 7 p.4 (Dec. 1971), 8 p.29 (1972)

41. Dougherty,J.P., Pugh,E.R. and Douglas-Hamilton,D.H. 24th Gaseous Elect. Conf. Gaisville

42. Dovit,J. "Laser induced damage in optical materials" Ed. Glass,A.J. and Guenther,A.H. NBS spec. publ. 387 p.170 (1973)

43. Drake,J.F., Kaw,P.K., Lee,Y.C., Schmidt,G., Liu, C.S. and Rosenbluth,M.N. Phys. Fluids, 17 p.778(1974)

44. Dubois,D.F. and Gilinsky,V. Phys. Rev. A135 p.1519 (1964)

45. Dubois,D. and Goldman,M.N. Phys. Rev. Lett. 14 p.544 (1965)

46. Duc Long,N., Prabhakav,K.J. and Johnston,T.W. 7th Eur. Conf. on Controlled Fusion and Plasma Physics., Vol.1, p.73 (1975) (Lausanne)

47. Duley,W.W. "Co_2 Laser Effect and Application" (ed by Yoh-Han) Academic press (1976)

48. Dumanchin,R. and Rocca-Serra,J.C.R. Acad. Sci., 269 p.916 (1969)

49. Dumanchin,R., Fancy,J.C., Bauchinet,G. and Rocca-Serra,J. IEEE. J. Quantum Electron. QE-8, p.163 (1972)

50. Dumanchin,R., Lovauni,B.M., Chan,M., Neul-auer,M. and Rocca-Serra,J. IEEE. J. Quantum Electron. QE-6, p.4 (1970)

51. Dupree,T.H. and Tidman,D.A. Phys. Fluids., 8 p.1860 (1969)

52. Dyer,P.E., James,D.J., Ramsden,S.R. and Skipper, M.A. Phys. Lett. 48A p.311 (1974)

53. Dyer,P.E. and James,D.J. J. App. Phys. 46 p.1679 (1975)

54. Dyer,P.E., James,D.J., Ramsden,S.R. and Skipper, M.A. App. Phys. Lett., 24 p.316 (1974)

55. Dyer,P.E., James,D.J. and Ramsden,S.R. J. Phys., E5 p.1162 (1972)

56. Eidmann,K. and Sigel,R. " Laser Interaction and related phenomena ", Vol.3B Ed. Schwarz,H.J. and Hora,H. pp.667-90 (1973)

57. Eidmann,K.E. and Sigel,R. Phys. Rev. 34 p.799 (1975)

58. Eidmann,K.E., Bredlerlow,G., Brodmann,R., Petsch, R., Sigel,R., Tsakiris,G., Volk,R. and Witkowskis PLF 15, (1979)

59. Elton,R.C. and Anderson,A.D. NRL Report 6541 (1967)

60. Elton,R.C. NRL Report 6738 (1968)

61. Elton,R.C. and Roth,N.V. App. Opt., 6 p.2071(1967)

62. Erokhin,N.S., Moiseev,S.S. and Mukhin,V.V. Nucl. Fusion., 14 p.333 (1974)

63. Erokhin,N.S., Zacharov,V.E. and Moiseev,S.S. Sov. Phys. JETP., 29 p.101 (1969)

64. Fabre,E., Garbon,C., Popovics,C., Poquerusse,A., Stenz,C. and Virmont,J., "Proc. 6th Conf. on Plasma Phys. and Controlled Fusion Research", Berchtesgaden (1976) IAEA., 2 p.597 (1977)

65. Fabre,E., Popovics,C. and Stenz,C., "VIIth Conference on laser plasma interactions ", Lousanne, p.80 (1975)

66. Fabre,E., Garbon,C., Popovics,C. Poquerusse,A., Stenz,C. and Virmont,J., " Plasma Phys. and Controlled Nuclear Fusion Research ", (1976) Vol. II IAEA.,p 597 (1977)

67. Farkas,G.Y., Horváth,Z.Gy., and Kertesz, I., Phys. Lett., 39A p.231 (1972)

68. Forslund,D.W, Kindel,J.M. and Lindman,E.L. Phys. Rev. Lett., 30 p.739 (1973)

69. Fenstermacher,C.A., Nutter,M.J., Leland,W.T., and Bayer,K., Appl. Phys. Lett., 20 p.56 (1972)

70. Fermi,E., Z. Phys. 71 p.250 (1931)

71. Galeev,A.A., Onrevskii,V.N. and Sagdeev,R.Z., JETP. Lett., 16 p.136 (1972)

72. Ginzburg,V.L. " The Propagation of Electromagnetic Waves in Plasma ", Pergammon Press, Oxford (1964)

73. Ginzburg,V.L. " The Propagation of Electromagnetic Waves in Plasmas ", Pergammon Press (1961)

74. Ginzburg,V.L. " The Propagation of Electromagnetic Waves in Plasmas ", 2nd Edition, Oxford Pergammon Press (1970)

75. Gitomer,S.J. and Henderson,D.B. Phys. Fluids, 22 p.364 (1979)

76. Gold,A. and Bebb,H.B. Phys. Rev. Lett., 14 p.60 (1965)

77. Goldman,M.V. and DuBois,D.F. Phys. Fluids, 8 p.140 (1965)

78. Goldman,M.V. Appl. Phys. 38 p.95 (1966)

79. Goldman,M.V. Appl. Phys. 38 p.117 (1966)

80. Goldman,L.M., Soures,J. and Lubin,M.J. Phys. Rev. Lett., 31 p.1184 (1973)

81. Grover,F.W. " Inductance Calculations. Working Formulas and Tables ", Dover Publications. (1946)

82. Haas,R.H., Shay,H.D., Kruer,W.L., Boyle,M.J., Phillion,P.W., Rainer,F., Rupert,V.C. and Kornblom,H.N., Phys. Rev. Lett., 39 p.1539 (1977)

83. Haas,R.H. and Holzrichter,J.F., J. Opt. Soc. Amm., 67 p.717 (1972)

84. Hall,T.A. and Negm,Y.Z., Opt. Comm., 16 p.275 (1976)

85. Haugh,A.F. and Polk,D.H., Phys. Fluids, 9 p.10 (1966)

86. Hammelling, P., plasma Phys., 19, p669 (1977)

86. Hill,A.E., Appl. Phys. Lett., 12 p.324 (1968)

87. Hiroatsu,Maki, and Keishiro, Niu, J. Phys. Soc. (Japan), 46 p.653 (1979)

88. Jackson,E.A., Phys. Rev., 153 p.235 (1967)

89. Jahoda,F.C., Little,E.M., Queen,W.E., Sawyer, G.A. and Stratton,T.F., Phys. Rev. 119(3) p.843 (1960)

90. Johns,T.W. and Nation,J.A., Appl. Phys. Lett., 20 p.495 (1972)

91. Kaw,P.K. and Dawson,J.M., Phys. Fluids, 12 p.2486 (1969)

92. Key,H.M. et al, Rutherford Labratory Report, p77/B(1977)

93. Kidder,R.E., "Physics of high energy density ", (Ed. P. Caldirola and H. Knoepfel) p.306 N.Y. Academic Press (1971)

94. Kitigqma,Y., Thein,Aye, Yamada,Y., Yokayoma,M. and Yamanaka,C., J..Appl. Phys. 50(8) p.5206 (1979)

95. Korobkin,V.V. and Serov, R.V., EKSP. Teor. Fiz. Plasma Red., 4 p.103 (1966) , JETP Lett., 4 p.70 (1966)

96. Krokhin,O.N., Sov. Phys., Tech. Phys., 9 p.1024 (1965)

97. Kruer,W.L. and Dawson,J.M. Phys. Rev. Lett., 25 p.1174 (1970)

98. Lovberg,R.H. "Plasma diagnostic techniques ", Ed. R.H. Huddlestone, p.69 (1965)

99. Lee,P., Giovanelli,D.V., Godwin,R.P. and McClean G.H., Appl. Phys. Lett., 24 p.406 (1974)

100. Leguy,F. and Leguy Sommaire,N. C.R. Acad. Sci., 259B p.99 (1964)

101. Linlor,W.I., Appl. Phys. Lett., 3(11) p.210 (1963)

102. Liu,C.S. in " Advances in Plasma Physics VI ", Ed. Simon,A. and Thompson,W.B., Wiley, N.Y. and London. p.121 (1976)

103. Liu,C.S., Rosenbluth,M.N. and White,R.B., Phys. Rev. Lett., 31 p.697 (1973)

104. Longaeler,S., Stadrek,W., Fishman,H., Grebensh-chikov,S. and Hinnov,E., Nuc. Fusion, 15 p.301 (1975)

105. MacDonald. " Microwave breakdown in gas ", New York. Wiley (1966)

106. Maker,P.D., Terhune,R.W. and Savage,C.M., 3rd. Int. Conf. Quant. Elec. Paris (1963)

107. Mandel'shtam,S.L., Fashinin,P.P., Prokhorov,A.M., Paizer,YN.P. and Sukhodrev,N.K. Sov. Phys. JETP., 22 p.91 (1966)

108. Manes,K.R., Ahlstrom,H.G., Haas,R.A. and Halzrichter,J.F., J. Opt. Soc. Amm. 67 p.717 (1977)

109. Martin,G., Richardson,J.A., Alcock, Kurt Leopold, and Peter, Bunty,N. IEEE. J. Quantum Elect. QE-9 p.236 (1973)

110. McClung,F.J. and Hellwarth,R.W. J. Appl. Phys. 33 p.828 (1962)

111. McLean,E.A., Stamper,J.A., Ripin,B.H., Griem,H.R., McMahon,J.M. and Bodner,S.E., Appl. Phys. Lett., 31 p.825 (1977)

112. Melrose,D.B. and Stenhouse,I.E., Astron. and Astrophys., 73 p.151 (1979)

113. Mitchell,K.B., ET AL., Appl. Phys. Lett., 27 (1) p.11 (1975)

114. Mizui,J., Kang,H.B., Yamaguchi,T.S., Yoshida,K., Yamanaka,T. and Yamanaka,C., J. Phys. Soc.(Japan) 41 p.1334 (1976)

115. Morgan,C.G., Rep. Prog. Phys., 38 p.621-65 (1975)

116. Morse,R.L. and Nielson,C.W., Phys. Fluids, 16 p.909 (1973)

117. Mulser,P., Z. Naturforsch, 25A, p282 (1970)

118. Nemchinov,I.V., Appl. Math. and Mech. 31. p.320 (1967)

119. Nuckolls, J.,Wood,L., Theissen,A., Nature, 239. P.139 (1972)

120. Nighan,W.L., Phys. Rev., 2A p.1989 (1970)

121. Nishikawa, J. Phys. Soc.(Japan) 24 p.916(1968)

122. Oraevski,V.N. and Sagdeev,R.Z., Sov. Phys. JETP., 32 p.1291 (1962)

123. Pan.Y.L., Bernhardt,A.F. and Simpson,J.R., Rev. Sci. Inst., 43 p.662 (1972)

124. Pant,H.C., Opt. Comm., 16(3) p.396 (1976)

125. Patel,C.K., Phys. Rev. Lett., 12 p.588 (1964)

126. Pearlman,J.S., Thomson,J.J. and Max,C.E., Phys. Rev. Lett., 38 p.1397 (1977)

127. Pert,G.J., J. Phys. A5 p.506 (1977)

128. Piliya,A.D., Sov. Phys. Tech. Phys. 11 p.609 (1966)

129. Ping Lee,D.V., Giovanielli,R.P., Godwin,P., and McCall,G.H., Appl. Phys. Lett., 24 p.406 (1974)

130. Puell,H., Z. Naturforsch, 25A, p1807 (1970)

131. Rosenbluth,M.N., Phys. Rev. Lett., 29 p.565 (1972)

132. Rosenbluth,M.N. and Sagdeev,R.Z., Comments Plasm. Phys. Controlled Fusion, 2 p.129 (1973)

133. Reody,J.F., J. Opt. Soc. Amm., 53 p.514 (1963)

134. Richardson,M.C., Alcock,A.J., Leopold,K. and Burtyn,P., IEEE. J. Quantum Electron. QE-9 p.236 (1973)

135. Raven,A., Willi,O., Rumsby,P.T., Phys. Rev. Lett., 41 p.554 (1978)

136. Schulz,G.J., Phys. Rev., 135A p.988 (1964)

137. Seguin,H. and Tulip,J., Appl. Phys. Lett., 21 p.414 (1972)

138. Serov,R., Richardson,M.C. and Burtyn,P., Rev. Sci. Inst., 45(7) p.886 (1975)

139. Serov,R. and Richardson,M.C., Appl. Phys. Lett., 28(3) p.115 (1976)

140. Shearer,J.W., Phys. Fluids, 14 p.183 (1971)

141. Shen,Y.R., Rev. Mod. Phys., 48 p.1 (1976)

142. Sharma,R.D. and Brau,C.A., J. Chem. Phys., 50 p.924 (1969)

143. Silin,V.P., Sov. Phys. Solid-State 12 p.2886 (1971)

144. Silin,V.P. , Erokhin, O.N., Pustovalov,V.V., JETP, Lett., 22, p21 (1975)

145. Silin,V.P., Sov. Phys. JETP., 21 p.112 (1965)

146. Silin,V.P., Nauka Moscow (1973)

147. Simmons,W.W., ET AL., IEEE/OSA-CLE Conf. Digest 31 (1975)

148. Sobelev,N.N. and Sakovikov,V.V., Sov. Phys. Uspekhi 10 p.153 (1967)

149. Somerville,J.M., " The Electric Arc ", (Wiley, New York, p.101 (1959)

150. Sprangle,P. and Granatstein,V.L., Appl. Phys. Lett., 25 p.377 (1974)

151. Stamatakis,T. Phd. Thesies London Univ. (1977)

152. Stamper,J.A., Papodopalos.,K., Sudan,R. ., Dean, S.O., McClean,E.A. and Dawson,J.M. Phys. Rev. Lett., 26 p.1012 (1971)

153. Stamper,J.A.,and Ripin,B.H., Phys. Rev. Lett., 34 p.135 (1975)

154. Stern,R.A., Phys. Rev. Lett., 14 p.538 (1965)

155. Stratton,T.F. in " Plasma Diagnostic Techniques", Ed. Huddleston,R.H. and Leonnard,S.L., Chap. 8 (Academic, N.Y. 1965)

156. Taylor,R.C. and Britteman,S., Rev. Mod. Phys., 41 p.26 (1969)

157. Thomson,J.J., Claire Ellen,M.X. and Kent Eastabrook, Phys, Rev. Lett., 35(10) p.663 (1975)

158. Thomson,J.J., Faehl,R.H. and Kruer,W.L., Phys. Rev. Lett., 31 p.918 (1973)

159. Tidman,D.A., Phys. Rev. Lett., 32 p.1179 (1974)

160. Tonon,G. and Rabeau,M., Plasma Phys. 15 p.871 (1973)

161. Vinogradov,A.V. and Pustovalov,V.V., Sov. Phys. JETP., 36 p.492 (1973)

162. Yamabe,C., Setayoma,E., Yakayama,M. and Yamanaka, C., Phys. Lett., 50A p.349 (1974)

163. Yamanaka,C., Yamanaka,T., Sasaki,T., Mizui,J. and Kong,H.B., Phys. Rev. Lett., 32 p.1038(1974)

164. Yamanaka,C., Jap. J. Appl. Phys. 16 p.131 (1977)

165. Young,F.C. and Ripin,B.H., Bull. Am. Phys. Soc., 22 p.1112 (1977)

166. Walker,A.C., Stamatakis,T. and Spalding,I.J., J. Phys. D, 11 p.2285 (1978)

167. Willett,C.S. " An Introduction to Gas Lasers; Population Inversion Mechanisms ", Pergamon Press. p.266 (1974)

168. Witte,K.J., Brederlow,G., Eidmann,K., Volk,R. E., Hohla,K. and Brodman,R., " High power laser and applications ", Ed. Kompa,K.L. and Walther,H., Springer Series in Optical Science, Berlin (1978)

169. White, R.B., Liu, C.S., and Rosenbluth, M. N., Phys. Rev. Lett. 31, 520, (1974)

*170. Max, C. E., Manheimer, W. M., and Thomas, J. J., phys. Fluids 21, 128 (1978).